The University of Cape Town

DIVISION OF BIOMEDICAL ENGINEERING, DEPARTMENT OF HUMAN BIOLOGY

Dissertation submitted in partial fulfilment of the requirements for the degree
MSc (Med) Biomedical Engineering

THE DESIGN, CONSTRUCTION AND TESTING OF A HERMETICALLY SEALED BREAST PLATFORM FOR DUAL-MODALITY MAMMOGRAPHY

AUTHOR: R.V. SMITH (SMTRAP002)
SUPERVISOR: DR KIT VAUGHAN

FEBRUARY 2014

Best viewed in colour

This page is intentionally blank

DECLARATION

I, Raphael V Smith, hereby declare that the work on which this dissertation is based is my original work (except where acknowledgements indicate otherwise) and that neither the whole work nor any part of it has been, is being, or is to be submitted for another degree in this or any other university. I empower the university to reproduce for the purpose of research either the whole or any portion of the contents in any manner whatsoever.

The Harvard referencing style was used for citation and referencing. Each contribution to, and quotation from the work(s) of other people has been cited and referenced.

Raphael Smith

Cape Town, February 2014

ABSTRACT

Breast cancer claims nearly half a million lives annually. At present, early detection and treatment are the most effective means of reducing mortality. Even though mammography is the gold standard in breast cancer screening, it does not perform well in the case of dense breasts. Conversely, ultrasound is well suited to the imaging of dense breasts when used as an adjunct to mammography, and has been shown to significantly improve the sensitivity (from 76.0% to 97.7%) and specificity (from 98.2% to 99.7%) of breast cancer screening.

However, when ultrasound is used as an adjunct to X-ray mammography in either hand-held or automated mode, the patient typically lies in a prone position. The disadvantages of this approach include: variable image quality; poor co-registration of X-ray and ultrasound images; and increased costs and patient anxiety. In response to these shortcomings, the Aceso full-field digital mammography and automated breast ultrasound (FFDM+ABUS) system aims to acquire both X-ray and 3D ultrasound images simultaneously. The Aceso has been developed by the Cape Town based company CapeRay Medical (Pty) Ltd.

The focus of this thesis is the design, construction and testing of a novel breast platform wherein the challenges of combining FFDM and ABUS have been addressed, in a clinically suitable package. This approach has been attempted by several companies including Xdata, General Electric and Fischer. However, these systems are not clinically suitable and have not progressed beyond the working prototype stage.

In the final design of the breast platform, the constraints of the mammographic arrangement were considered, as were the clinical and ergonomic requirements of breast imaging and the transmission characteristics of ultrasound.

The final design is a hermetically sealed breast platform (HSBP). The breast platform houses the scanning X-ray detector, the scanning ultrasound transducer and the scanning mechatronics. Additionally, the entire breast platform is filled with non-conductive white pharmaceutical oil 15, submerging the internal components. The oil acts to acoustically couple the ultrasound transducer to a 6 mm thick TPX (polymethylpentene) compression plate which in turn is acoustically coupled to the breast. The TPX is hermetically attached to the breast platform housing using a novel stitched bond to compress an O-ring.

The functionality of the HSBP was verified in a series of laboratory tests, wherein the front-edge X-ray imaging dead space was established to be less than 5 mm, as required by the IEC. Additionally, the HSBP contributes only 6 mm to the 78 mm lateral dead space for dual-modality imaging.

The effect of the HSBP on the X-ray image quality was evaluated through the measurement and computation of the modulation transfer function (MTF), noise power spectrum (NPS) and detective quantum efficiency (DQE) as per the IEC 62220-1-2 standard. The TPX and mineral oil were found to act as radiographic filters, thus decreasing the MTF by 13% @ 5 lp/mm and the NPS by 38% @ 5 lp/mm. The significant reduction in radiographic noise increased the overall image quality, as measured by the DQE, by ~4% @ 5 lp/mm.

The Aceso and HSBP were used to successfully acquire dual-modality images of a stereotactic phantom. This demonstrated the successful integration of FFDM and ABUS in a clinically suitable package. However, poor performance of the ultrasound transducer precluded further image quality testing. Therefore the effect of the HSBP on the ultrasound image quality was studied using hand-held ultrasound transducers.

It was found that high frequency ultrasound (≥5.5 MHz) does not provide the required penetration depth of ~90 mm. However, low frequency ultrasound (≤3.5 MHz) does and at 3.5 MHz the HSBP decreased the ultrasound image quality only slightly. The transverse resolution was reduced by 5.5%, the penetration depth was reduced by 3 mm and the axial geometrical conformity featured a 3% negative error. In contrast, the lateral resolution was improved by 6% and several other ultrasound image quality metrics were unaffected by the HSBP.

In conclusion, FFDM+ABUS has been successfully achieved with the novel HSBP. Additionally, the HSBP has been shown to improve the X-ray image quality and degrade the ultrasound image quality only slightly. These findings have important implications for the future of breast cancer screening.

ACKNOWLEDGEMENTS

I would like to acknowledge the contributions of the following:

Dr Kit Vaughan for serving as my supervisor, for providing guidance in the early stages of this thesis and for giving me the opportunity to work on this project.

Professor Tania Douglas for her willingness to help and for her assistance in the early stages of this thesis.

The past and present staff of CapeRay for their contributions to the research, for their outstanding workmanship and for their support, enthusiasm and friendship.

The NRF, CapeRay and the trusties of the KW Johnston Scholarship for their financial assistance.

My Mother and Father for their contributions to the editing of this thesis and for their love and support throughout my studies.

My family and friends for their interest, patience and support.

My fiancé Melissa Efthymiades for her tireless editing, for her love, support and encouragement, for her understanding, patience and forgiveness and for the countless meals, cups of tea and hours of company.

TABLE OF CONTENTS

LIST OF FIGURES

LIST OF TABLES

LIST OF ABBREVIATIONS

ABUS	Automated breast ultrasound
BRCA	BReast Cancer
CC	Craniocaudal
DQE	Detective Quantum Efficiency
FEA	Finite Element Analysis
FFDM	Full Field Digital Mammography
FPC	Flexible Printed Circuit
FWHM	Full Width Half Maximum
GS	Grayscale
HHUS	Hand-held ultrasound
HSBP	Hermetically sealed breast platform
HVL	Half-Value Layer
IEC	International Electrotechnical Commission
MLO	Mediolateral Oblique
MTF	Modulation Transfer Function
NPS	Noise Power Spectrum
PSF	Point Spread Function
SRS	System Requirement Specification
TDI	Time Delay Integration
TDLU	Terminal Duct Lobular Unit
TPX	Polymethylpentene trade name
2D	Two-Dimensional
3D	Three-Dimensional

Chapter 1: INTRODUCTION

1.1 BACKGROUND

1.1.1 BACKGROUND TO THE ACESO

In 2008, more than 1.38 million new breast cancer cases were reported and more than 458 000 women died from breast cancer, worldwide (Ferlay et al., 2010). In South Africa, 5 871 new breast cancer cases were recorded in women in 2006 (National Cancer Registry, 2006).

Mammography is the gold standard in breast cancer detection and several studies have shown mammographic screening reduces mortality by 25-30% in women over the age of 50 (Schopper & de Wolf, 2009). However, there are many who dispute the effectiveness of mammography, claiming it can be more detrimental than beneficial (Bleyer & Welch, 2012). Such claims arise from the three primary shortcomings of mammography: radiation exposure; unsatisfactory sensitivity (a measure of true positive diagnoses); and unsatisfactory specificity (a measure of true negative diagnoses). Further, the sensitivity decreases for dense breasts, typical in women under the age of 50 (Carney et al., 2003).

Radiation exposure is of particular concern for those with an increased lifetime risk of cancer due to BRCA gene mutations, since such mutations are exacerbated by ionising radiation (Kuhl et al., 2005). Low sensitivity, especially in dense breasts, results in the percentage of *interval cancers* – cancers clinically detected between mammographic screening sessions – being as high as 36-56% (Kuhl et al., 2005). Low specificity results in high call-back rates and avoidable biopsies which are costly, increase radiation dose, and cause unnecessary patient anxiety. These factors raise many questions about the efficacy of mammographic screening.

In response to these shortcomings many new technologies have been developed to reduce radiation dose and increase sensitivity and specificity. Low-dose full-field digital mammography (FFDM) and automated breast ultrasound (ABUS) are two such technologies. A particular advantage of ABUS is the proficiency with which it images dense breasts. In an exemplary study by Giuliano & Giuliano (2012), 3418 asymptomatic women were screened using ABUS as an adjunct to FFDM. The study showed an increase in sensitivity from 76.0% to 97.7% and specificity from 98.2% to 99.7%.

This increase in performance is the motivation behind the development of the Aceso dual-modality, low-dose full-field digital mammography and automated breast ultrasound (FFDM+ABUS) system. The system is being developed by the Cape Town based start-up, CapeRay Medical.

CapeRay has its roots in the De Beers mining company. In the 1980s De Beers estimated that 20% of its uncut diamonds were being stolen by its workers. To curb this trend they developed a very low-dose digital X-ray scanner to scan its workers on a daily basis. In 1999 De Beers and the University of Cape Town (UCT) secured funding from the Innovation Fund to develop the Lodox full-body X-ray scanner for medical applications.

Additionally, UCT and De Beers set up a joint venture – African Medical Imaging (Pty) Ltd (AMI) – to exploit the Lodox technology for other medical imaging applications. One such application was breast screening mammography (Lease et al., 2002). Prototype A, shown in Figure 1.1, was developed by AMI to test the scanning mammography technology.

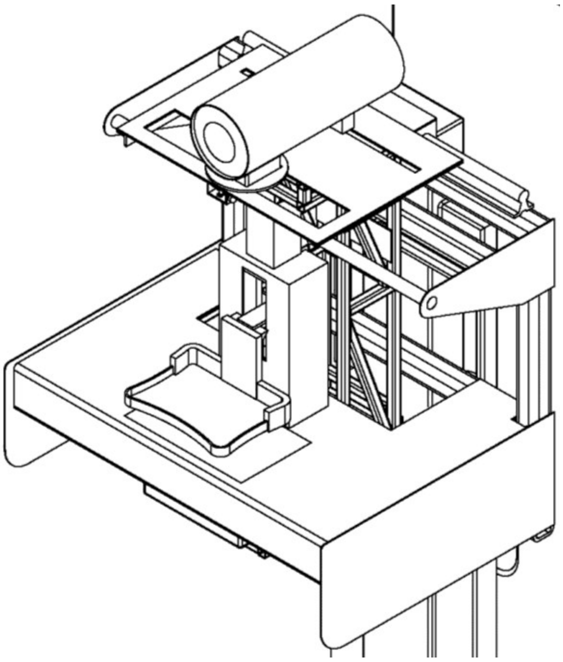

Figure 1.1: **AMI Prototype A. The X-ray source and detector move on a scanning gantry which is uncoupled from the static compression plate and paddle.**

In 2010 African Medical Imaging changed its name to CapeRay Medical and, with venture capital funding from the Industrial Development Corporation, it set its sights on developing the PantoScanner platform. The PantoScanner platform may be classed into three different products: the Soteria, an entry level X-ray only system implementing the Lodox scanning technology; the aforementioned dual-modality Aceso; and finally the Aegle which adds digital breast tomosynthesis to the functionality of the Aceso. The development strategy began with the Soteria and in 2012 a prototype Soteria, shown in Figure 1.2, was tested in a clinical trial.

Figure 1.2: **CapeRay Soteria. A prototype version of the Soteria; the X-ray only variation of the PantoScanner.**

In a parallel development stream, several students and engineers began to investigate the feasibility of incorporating ABUS into the Soteria X-ray architecture. This preliminary work is well documented in an unpublished honours thesis by Russell (2010).

With the goal of testing the Aceso in a clinical trial in late 2013, the aim of the present work – which began in early 2012 – was to pick up where the previous research had left off and successfully integrate the proposed ABUS system into the existing X-ray architecture.

1.1.2 MAMMOGRAPHY SCREENING

As shown in Figure 1.3, screening mammography exams typically involve two X-rays of each breast. Craniocaudal (CC) scans are parallel to the spine while mediolateral oblique (MLO) views are at an angle to the spine. In the MLO view the platform is angled so as to be parallel to the pectoral muscle (typically 30-60 degrees). Breast compression is used to immobilise the breast, to reduce the thickness of the breast and the overlapping of structures, and – in the case of film-mammography with low dynamic range – to ensure a uniform tissue thickness. The thickness of a compressed breast is typically less than 8 cm.

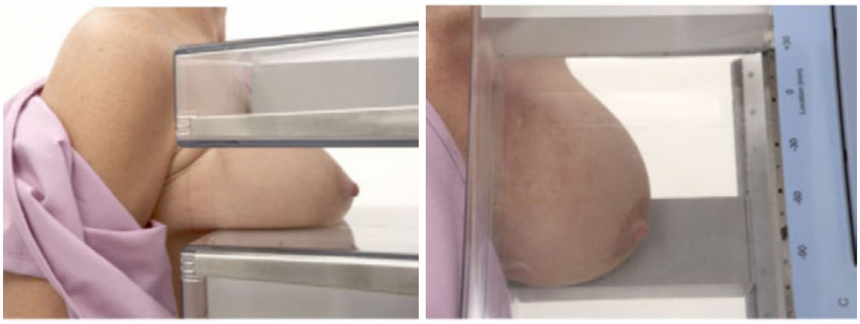

Figure 1.3: Breast Compression for CC and MLO Views. Left – side view of craniocaudal (CC) compression. Right – side view of mediolateral oblique (MLO) compression (Adapted from Schilling et al., 2011).

A mammogram is performed by a radiographer (a trained medical technician) whilst a radiologist (a specialist medical doctor) is responsible for clinically reviewing the X-ray images. A representative set of X-ray images is shown in Figure 1.4.

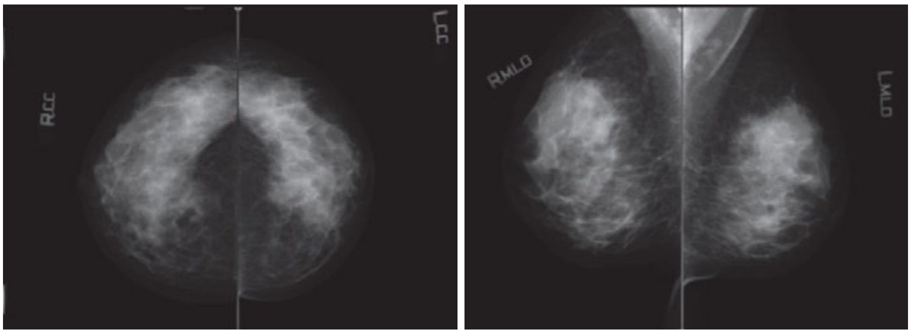

Figure 1.4: CC and MLO Mammography X-rays of the Left and Right Breasts (Adapted from Baert et al., 2010).

The findings of a mammogram are typically reported using BI-RADS (Breast Imaging-Reporting and Data System). BI-RADS classifies the results of a mammogram in two categories (see Table 1.1): *assessment* – an indication of the findings of the mammography; and *composition* – a classification of the mammographic breast density.

Table 1.1: Breast Imaging-Reporting and Data (BI-RADS) System Categories (Vaughan, 2011).

Assessment		Composition	
Category	Description	Category	Description
0	Incomplete	1	Almost entirely fat
1	Negative	2	Scattered fibro-glandular densities
2	Benign findings	3	Heterogeneously dense
3	Probably benign	4	Extremely dense
4	Suspicious abnormality		
5	Highly suggestive of malignancy		
6	Known biopsy-proven malignancy		

Breast density, or more specifically radiological breast density, is determined by the ratio of fatty to fibrous/epithelial tissue. The quantities of each tissue type and hence the breast density vary from woman to woman and depend on a complex array of interrelated factors that are not fully understood. However, breast density typically decreases with age, number of live births and menopause. It is worth noting that increased breast density has been associated with an increased risk of breast cancer, making the imaging of dense breasts all the more important (Boyd et al., 2011).

Fatty tissue is a poor attenuator of X-rays whereas fibrous connective tissue and epithelial tissue are strong attenuators of X-rays. Hence, as the amount of fibrous and epithelial tissue increases the overall attenuation, or radiography density, increases (see Figure 1.5). In dense breasts cancerous legions are easily hidden by the radiographic shadows of the high attenuation tissue.

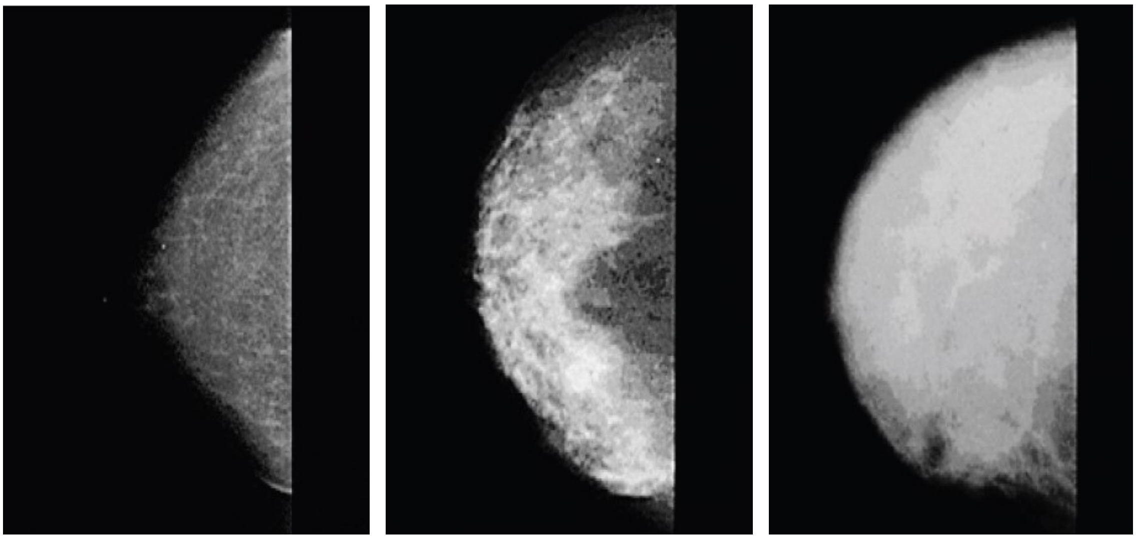

Figure 1.5: Examples of Mammographic Density. Left – BI-RADS 1; centre – BI-RADS 2; right –BI-RADS 4 (Adapted from Boyd et al., 2011).

If a radiologist's report indicates a suspicious lesion (BI-RADS assessment above 2) or dense breasts (BI-RADS composition above 2) the patient is typically referred for an investigative breast ultrasound or *call-back*. In a simplistic ultrasound model, sound waves are able to penetrate through dense tissue. However, a portion of the wave is reflected at the interface of different tissue types. These reflections are used to create the ultrasound image. As a result, ultrasound is a powerful tool for identifying masses in dense breast, where mammography falls short. It is also useful in distinguishing whether a suspicious lesion is a dense mass or a fluid filled cyst and what further action, if any, is required. As a result, hand-held ultrasound (HHUS) has been used as an adjunct to screening mammography for more than half a century (Dempsey, 2004; Harper & Kelly-Fry, 1980) and has significantly improved the breast cancer detection rate (Berg et al., 2008; Nothacker et al., 2009; Schaefer et al., 2010).

1.1.3 BREAST ULTRASOUND AND DUAL-MODALITY MAMMOGRAPHY

One of several methods for performing HHUS (hand-held ultrasound) is known as the clock face method (see Figure 1.6). The breast is scanned as a series of circles with the nipple at the centre and the probe directed radially from the nipple (longitudinal scan). If a suspicious legion is detected, the probe is rotated through 90° and a transverse scan is captured. Regions of interest are defined by a clock position and distance from the nipple i.e. 11 o'clock 5 cm from the nipple.

Simpson et al.(2008) present a case study of a 62-year-old asymptomatic woman who presented for a routine mammogram. CC and MLO mammograms of the right breast (see Figure 1.7) indicate a heterogeneously dense breast without suspicions findings. In the subsequent HHUS exam (recommended based on breast density), a suspicious legion was found at the region of interest indicated in Figure 1.6. Figure 1.8 shows the transverse and longitudinal ultrasound scans wherein the suspicious masses are easily identified.

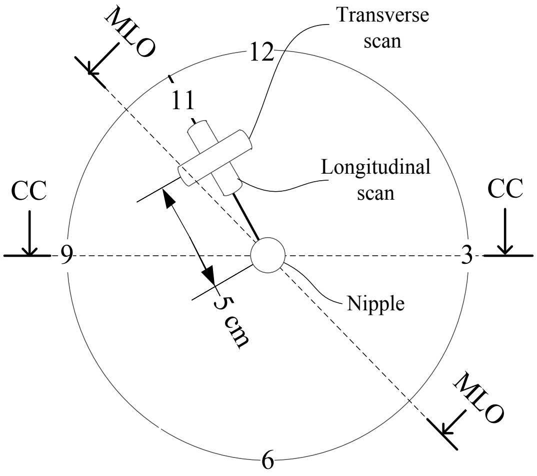

Figure 1.6: **Clock Face Representation of Hand-Held Breast Ultrasound Scan Location. In the supine position, regions of interest on the breast are based on a clock face (12 o'clock lies in the sagittal plane). A longitudinal and transverse scan at 11 o'clock, 5 cm from the nipple is shown. The sections produced by CC and MLO mammographic views are also shown.**

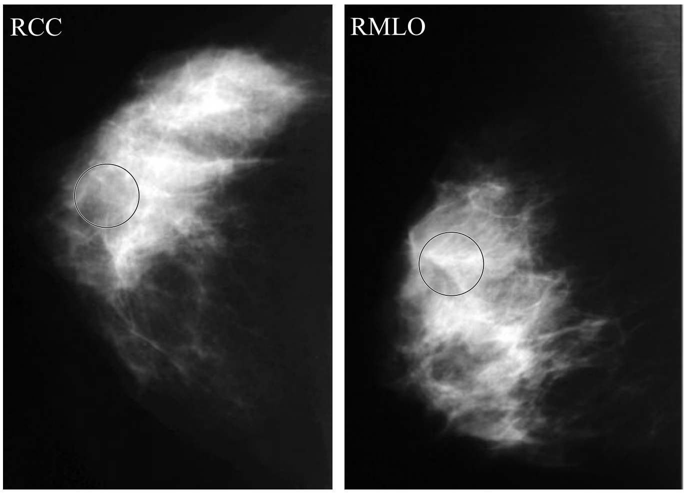

Figure 1.7: **CC and MLO Screening Mammogram of Heterogeneously Dense Breast without Suspicious Findings. The encircled areas are the approximate projections of the region of interest shown in Figure 1.6 (Adapted from Simpson et al., 2008).**

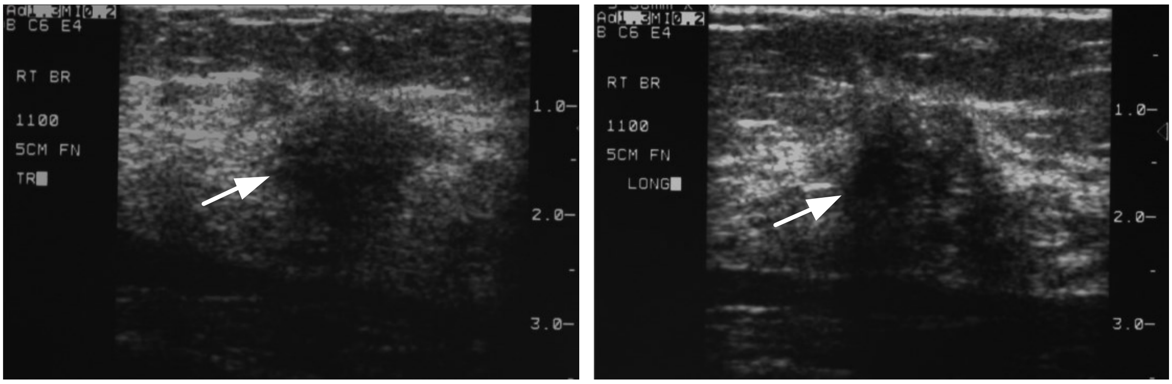

Figure 1.8: **Breast Ultrasound of 1.5 cm Irregularly Marginated, Hypoechoic Mass. The transverse (left) and longitudinal (right) ultrasound scans of the region of interest, shown in Figure 1.6, clearly shows a legion undetected by the corresponding mammogram (Adapted from Simpson et al., 2008).**

While breast ultrasound is clearly an indispensable adjunct to mammography, HHUS has several shortcomings: (1) manual scanning of the breast is highly dependent on the skill of the operator; (2) co-registration of the mammogram and the ultrasound is difficult because the ultrasound is gathered at a different time, with the breast in a different position and from a different angle (Novak, 1983); and (3) call-backs increase financial cost and patient anxiety.

ABUS resolves the first of these issues (1 in the previous paragraph) by standardising the ultrasound scan quality. However, ABUS scans are typically performed with the patient in the prone or supine position. Also, international guidelines recommend that breast ultrasound is only used for follow-up examinations in the case of dense breasts and/or suspicious mammographic findings (Albert & Schulz, 2004; SIGN, 2013; Smith & Saslow, 2003). As a result, the latter two shortfalls (1 and 2 in the previous paragraph) remain (Romilly-Harper et al., 1995).

The dual-modality Aceso aims to overcome the above limitations by capturing X-ray and ultrasound images simultaneously, automatically and under immobilising compression.

1.1.4 ARCHITECTURE OF THE ACESO

The architecture of the Aceso and the entire PantoScanner range are well defined in a continuing series of patents (Evans et al., 2013a, 2013b; Vaughan & Evans, 2013). Figure 1.9 shows a schematic front view of the Aceso (the breast has been sectioned at the chest wall). The functions of the Aceso may be grouped into three subsystems: the X-ray system, the ultrasound system and the breast compression system. Each system is discussed in turn below.

Considering the X-ray system, an X-ray cone is generated by the X-ray tube (18). The cone is collimated into a fan-beam (F) by a *collimator* (20) and the X-rays are detected by a detector (37) called the *Pandia*. The collimator and the Pandia scan across the imaging window along axes A-A and B-B respectively, thereby imaging the entire breast (32). This X-ray architecture is known as low-dose slot-scanning and produces high quality images at low doses owing to a significant reduction in X-ray scatter when compared to conventional cone-beam architectures (Åslund et al., 2006; Baldelli et al., 2011; Lai et al., 2008).

The ultrasound system is made up of a long linear *ultrasound transducer* (36) that scans the breast (32) from below, through the *compression plate* (30). It scans along the same axis as, but is independent of, the Pandia.

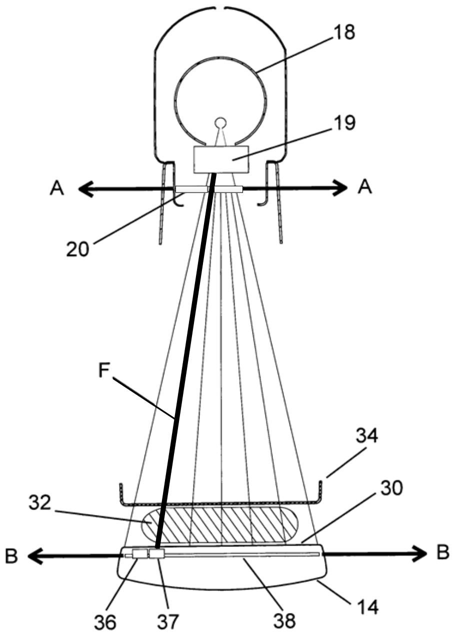

Figure 1.9: **Front View of the Aceso Architecture. A compressed breast (32) is shown, sectioned at the chest wall (Vaughan & Evans, 2013).**

The compression system compresses the breast between a *compression paddle* (34) and the compression plate (30). According to the regulations, the compression force may be as high as 200 N (IEC, 2011).

The subject of this research, the *breast platform* (14) is topped by the compression plate and houses the Pandia, the ultrasound transducer and the mechatronics for the two independent scanning mechanisms.

The X-ray, ultrasound and compression systems are housed by the *C-arm* (22) (see Figure 1.10). To facilitate CC, MLO and other views, the C-arm is able to rotate about the axis D-D from -180° to +180° relative to the vertical. Additionally, to accommodate women of varying height as well as women in wheelchairs, the C-arm moves vertically along the axis E-E.

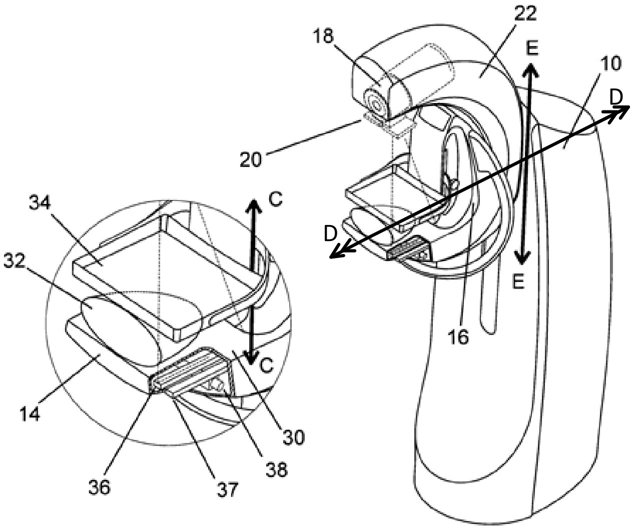

Figure 1.10: **Isometric View of Aceso Architecture with Detail (Vaughan & Evans, 2013).**

The slot scanning architecture requires precise alignment of the collimator and Pandia. As shown in Figure 1.11, the fan-beam is not a square distribution. As a result, any misalignment of the Pandia reduces the net X-ray exposure and subsequently reduces the dose efficiency of the system. Additionally, time varying misalignment results in image striping (variations in image intensity in the scan direction). This requirement for precise alignment limits the allowable deflection of the C-arm and places high tolerances on the repeatability and precision of the scanning mechanisms.

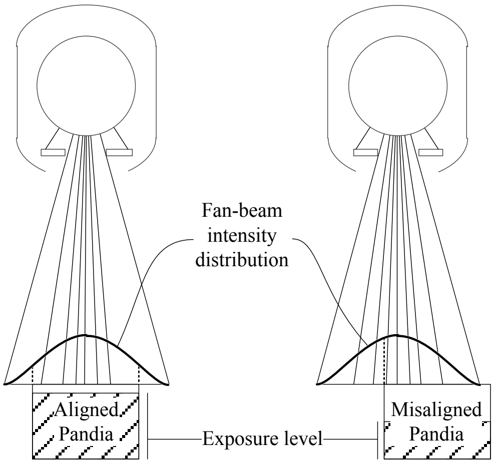

Figure 1.11: Effect of Collimator-Pandia Misalignment on Detection Efficiency. Front view. Left – the correctly aligned Pandia is aligned with the centre of the fan-beam, right – the misaligned Pandia misses a large portion of the impinging X-rays.

1.1.5 THE COUPLING PROBLEM

Acoustic energy at the ultrasonic frequencies used in medical imaging (1-10MHz) is not effectively transmitted by air. Hence, to implement the ultrasound architecture described in the preceding section, the transducer must be *acoustically coupled* to the underside of the compression plate. That is to say, the transducer must be in direct physical contact with the compression plate or a coupling material which, in turn, is in direct contact with the compression plate. Additionally, a coupling liquid/gel must be used at material interfaces to fill microscopic pores and guarantee the absence of air. This is akin to the use of coupling gel in standalone medical ultrasound exams.

A lubricating couplant must be employed between the moving transducer and the stationary compression plate to prevent frictional damage. Lubricating the underside of the compression plate presents several challenges. Firstly, any inconsistencies in the lubricant thickness will result in X-ray imaging artefacts. Secondly, as the transducer scans across the platform, lubricant will collect at its leading edge. Under the influence of gravity, this collection is likely to fall off the underside of the compression plate; the management of such spillage inside a precision medical device is no trivial task. Thirdly, a means of replacing lost lubrication is required to ensure the long term functioning of the system. Such a means, which must also make contact with the compression plate, would lead to an undesirable decrease the useful imaging area.

The task of maintaining an effective acoustic couple is further complicated by the deflection of the compression plate due to breast compression. The magnitude and distribution of this deflection depends on the compression force, breast size, breast density and the breast position (CC versus MLO). The ultrasound probe is a straight, non-compliant, delicate transducer. Hence, a compliant compression-plate-to-transducer mechanical and acoustic coupling is required to take up the deflections.

Finally, any materials in the acoustic pathway (including the compression plate) must have suitable acoustic properties. More specifically, the characteristic speed of sound in the material (c) and its acoustic impedance (Z) – the product of c and the material's density (ρ) – should be similar to those of breast tissue to ensure optimal acoustic energy transmission and imaging performance.

Several groups including General Electric (GE), Fischer, Hologic, Xdata Corporation, Siemens, Magnaflux, Imperium, Fujifilm and the United States Surgical Corporation have tackled the coupling problem. Many potential solutions to this problem have been proposed but none have overcome the full array of challenges presented above (Dines et al., 2005; Fischer & Mertelmeier, 2011; Flaherty et al., 1969; Lasser et al., 2005; Sendai, 2012; Shmulewitz, 1996; Sinha et al., 2007a; Suri et al., 2005, 2013).

Although outside of the scope of this research, an additional coupling problem known as the *peripheral volume issue* is included here for the purposes of completeness. It pertains to the peripheral curvature of a compressed breast. As shown in Figure 1.12, in this peripheral region a large air gap exists between the compression plate and the breast. In order to properly image this portion of the breast with ultrasound, this gap must be filled with a couplant. This aspect of the problem is more a question of ergonomics and forms part of the Aceso industrial design task.

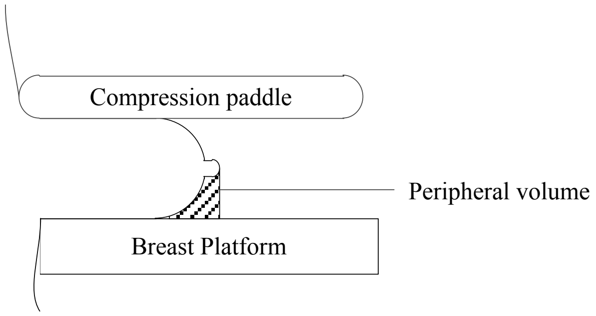

Figure 1.12: The Peripheral Volume Issue. The air gap present around the periphery of a compressed breasts shown.

1.2 MOTIVATION

The need for an improved breast cancer screening device – as embodied by the Aceso – is made apparent in the literature and in the concerted efforts of several groups to develop FFDM+ABUS systems. The advantages of FFDM+ABUS include reduced radiation dose and increased sensitivity and specificity which in turn, reduce costs, patient anxiety and ultimately, breast cancer mortality.

Despite these advantages; to date, no commercial FFDM+ABUS systems are in existence. This is attributed to the myriad of challenges that must be solved in combining ABUS and FFDM. The most challenging of these is the coupling problem.

1.3 OBJECTIVE

The objective of this thesis is to design, manufacture and test a novel breast platform for FFDM+ABUS wherein the problem of acoustically coupling the ultrasound transducer to the compression plate is resolved.

The breast platform must form the lower breast compression surface. It must also provide a means for the independent translation of the X-ray detector and the ultrasound transducer. A further requirement, of primary importance, is ensuring the integrity of the X-ray and ultrasound image quality.

1.4 SCOPE

The scope of this research is limited to the design, manufacture and testing of the compression platform for the Aceso dual-modality mammography system.

The architecture of the X-ray system and the ultrasound system are outside the scope of this research. The peripheral volume problem is also outside the scope of this research. Additionally, several aspects of the design such as system interfaces are constrained by high level design decisions.

The breast platform must fulfil all the Aceso User Requirement Specifications (Baasch, 2013b) and the Aceso System Requirement Specifications (Baasch, 2013a) as well as the necessary regulatory requirements, collated in the Aceso Regulatory Requirements Review (Goemans, 2013). Moreover, the Aceso project timeline and budget must be adhered to.

1.5 OVERVIEW OF THIS DOCUMENT

As far as possible, the structure of this document tracks the research and design methodology. As a guide to the design, construction and testing of the breast platform, some further background and a review of the relevant theory and literature are presented in Chapter 2. Having fully contextualised the problem, the design requirements are presented in Chapter 3. Also in Chapter 3 several theoretical concepts are developed. Based on prototypes of these concepts, a single concept is selected for further development. Using experimental, computational and theoretical testing, the design is developed and detailed in Chapter 4. Chapter 5 focuses on evaluating the performance of the design and is divided into four parts: Part I – manufacturing and assembly; Part II – Laboratory testing; Part III – X-ray image quality testing; and Part IV – ultrasound image quality testing. In Chapter 6 the results are discussed and conclusions drawn. Several recommendations for future work are also included.

Chapter 2: REVIEW OF THE LITERATURE

2.1 OVERVIEW OF THIS CHAPTER

To contextualise the research problem and provide insight into the physiological characteristics of breast cancer, this chapter begins with a review of breast anatomy followed by the pathological changes caused by breast cancer (see section 2.2). It is these changes that breast cancer screening aims to detect.

Section 2.3 introduces screening mammography and several X-ray image quality metrics. The metrics are used to assess the X-ray imaging performance of the final design.

The theory of ultrasound transmission is presented in section 2.4.2. This theory is used in the optimisation of the compression plate. To evaluate the performance of the ultrasound imaging, several metrics are once again employed. These are discussed in section 2.4.3.

A fundamental understanding of the ergonomic constraints of mammography allows the designer to find innovative design solutions. Accordingly, the ergonomics of mammography are considered in section 2.5.

With this foundation, a detailed review of relevant research and patents is presented in 2.6.

2.2 THE PATHOLOGY OF BREAST CANCER

2.2.1 ANATOMY OF THE BREAST

The anatomy of the breast is considered for two reasons: firstly, the anatomical locations where cancers originate and metastasise define the mammographic regions of interest; and secondly, the different breast tissue types play an important role in the ultrasound coupling problem.

The functional unit of the breast is called the terminal duct lobular unit (TDLU) (see Figure 2.1). The lobules (glandular epithelial tissue) are responsible for the production of breast milk. The milk collects through a system of epithelial tributaries (acini, terminal ducts and lactiferous ducts) into a lactiferous sinus which passes through the nipple.

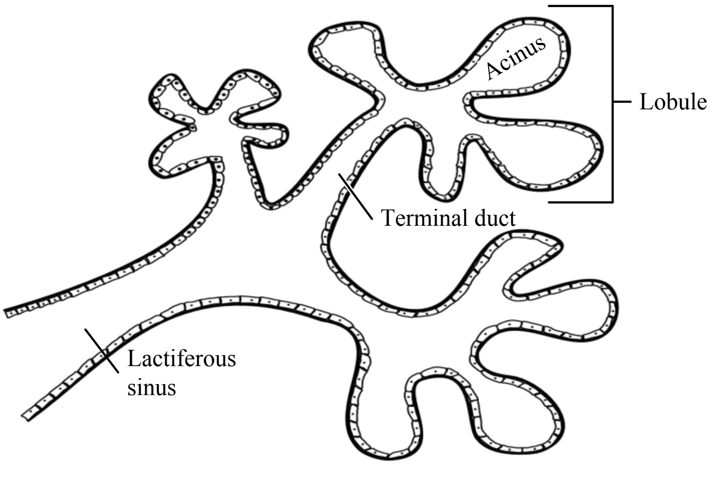

Figure 2.1: Terminal Duct Lobular Unit. The functional unit of the breast, comprised of the acinus, lobule, terminal duct and lactiferous sinus are shown (Adapted from D'Orsi, 2010).

Each breast contains several TDLUs as shown in the sectioned view of the breast in Figure 2.2. The TDLUs are encased in fibrous connective tissue, all of which is separated from the skin by a layer of fatty adipose connective tissue. The adipose tissue is interleaved with fibrous suspensory Cooper's ligaments which support the structure of the breast. Posteriorly, the pectoralis muscles separate the breast from the chest wall.

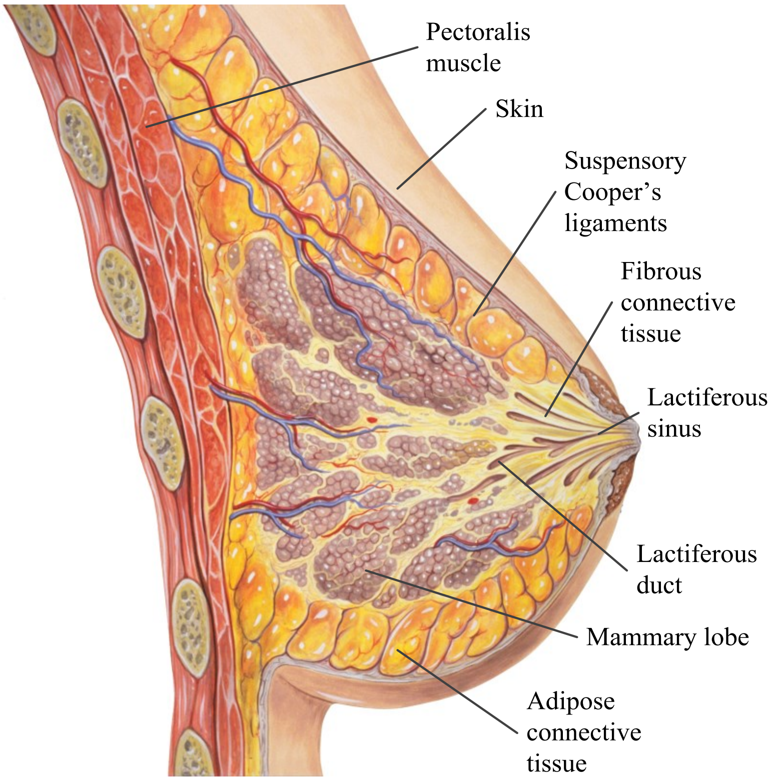

Figure 2.2: Medial Section of Left Breast (Adapted from Lynch, 2006).

The lymphatic system of the breast is shown in Figure 2.3. Breast cancers often metastasise (spread), via the lymphatic system, to the lymph nodes in the armpit. For this reason, it is preferable to image as much of the axillary tissue (tissue of the armpit) as possible.

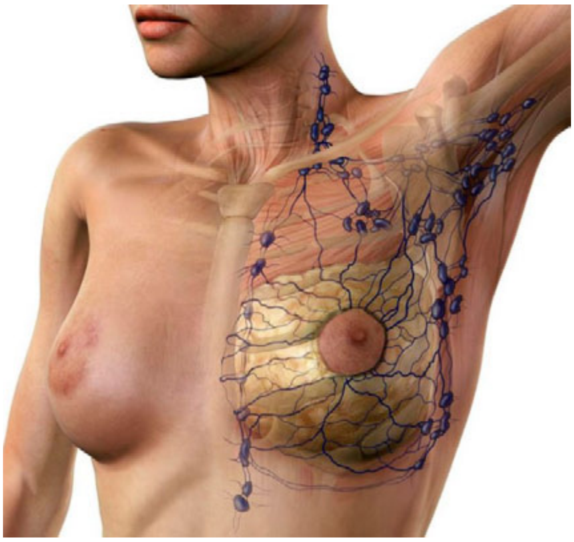

Figure 2.3: Lymphatic Drainage of the Breast (Reporduced from D & L Graphics, 2014).

2.2.2 BREAST CANCER

Cancer is characterised by the abnormal multiplication and spread of cells in the body. This abnormal behaviour is the result of a genetic mutation that disrupts the cellular mechanisms of apoptosis (the means by which a cell commits suicide when it is no longer needed) and differentiation (the means by which a cell determines what type of cell it should be) (Guyton, 1982).

This uncontrolled multiplication of cells typically results in a tumour. Benign tumours occur when the uncontrolled cell multiplication is limited and does not spread from one site to another. However, in the case of cancer, tumours – called malignancies – grow quickly and metastasise throughout the body (Weinberg, 2013).

The growth and metastasis of cancer is quantified by its stage which varies from stage 0 to stage IV. The stage is determined based on three sub-stage criteria: (1) **T**-stage is based on the size of the **T**umour; (2) **N**-stage is based on the presence and location of lymph **N**ode spread; and (3) **M**-stage is based on the presence or absence of **M**etastases.

Stage 0 breast cancer is known as carcinoma[1] in situ[2]. There are two types of stage 0 breast cancer: ductal carcinoma in situ (DCIS) and lobular carcinoma in situ (LCIS). The former is more common (Hirshaut & Pressman, 2009). As shown in Figure 2.4, in both cases, the cancerous cells have not spread beyond the duct or lobe in which they originated and are hence non-invasive. When in situ breast cancers begin to invade the surrounding tissue they are termed invasive. Stages I through IV cancers are all invasive. The aforementioned staging criteria are presented in Table 2.1 for breast cancer stages 0 through IV.

Stage at diagnosis (a measure of cancer metastasis) is known to be one of the most important factors in determining the likelihood that a breast cancer patient will survive (Carter et al., 1989; Richards et al., 1999; Sant et al., 2003). Accordingly, the purpose of breast cancer screening is to detect malignancies as early as possible, typically before the onset of any signs or symptoms.

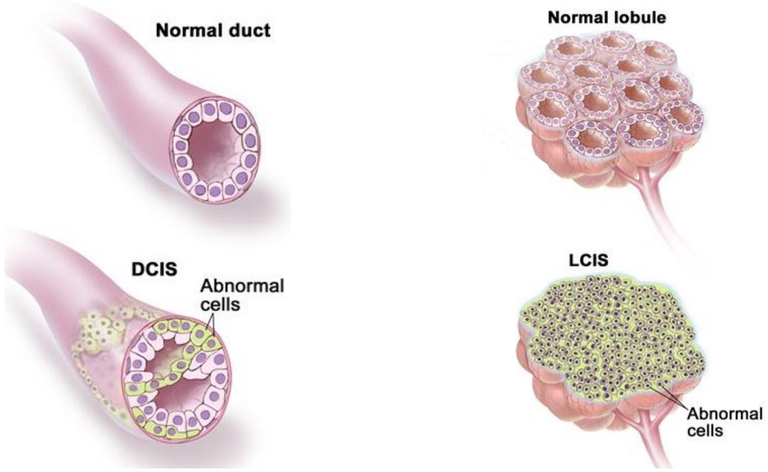

Figure 2.4: In Situ Cancers of the Breast Ducts and Lobes (Adapted from National Cancer Institute, 2013).

---

[1] Cancers originating in the epithelial cells of the lobules or ducts of the breast are called carcinomas.

[2] Cancers that have not invaded beyond an anatomical landmark called the basement membrane are known as *in situ* cancers.

Table 2.1: **The Stages of Breast Cancer. Left – The four TNM stages of breast cancer, right – description of T, N and M staging criteria (Hirshaut & Pressman, 2009).**

Stage	T	N	M
0	Tis	N0	M0
I	T1	N0	M0
IIA	T0	N1	M0
	T1	N1	M0
	T2	N0	M0
IIB	T2	N1	M0
	T3	N0	M0
IIA	T0	N2	M0
	T1	N2	M0
	T2	N2	M0
	T3	N1	M0
	T3	N2	M0
IIIB	T4	N0	M0
	T4	N1	M0
	T4	N2	M0
IIIC	Any T	N3	M0
IV	Ant T	Any N	M1

TNM descriptions	
T	Tumour size
Tis	In situ ductal or lobular carcinoma
T1	< 20 mm
T2	>20 mm and <50 mm
T3	>50 mm
T4	Any size which has: infiltrated the pectoral muscle/ chest wall; invaded the lymphatics of the skin; or infiltrated the skin itself.
N	Node spread
NX	Indeterminable
N0	None
N1	Yes. Nodes are not fixed in place the cancer.
N2	Yes. Nodes are fixed to one another or surrounding tissue/ blood vesicles or lymph nodes of the sternum show mammographic evidence of cancer.
N3	Yes. Cancer is present in the lymph nodes just above or below the collarbone.
M	Spread to distant site
M0	No
M1	Yes

2.3 SCREENING MAMMOGRAPHY AND X-RAY IMAGE QUALITY

From Table 2.1 it is clear that breast cancer screening should be capable of detecting mass legions, 20 mm or smaller. However, the detection of microcalcifications places much higher demands on the sensitivity of mammography.

Microcalcifications are calcium deposits as small as 100 µm in diameter (see Figure 2.5). They can and do occur naturally. However, clusters of microcalcifications may be indicative of pre-cancerous changes and such clusters accompany more than 50% of breast cancers. The detection of microcalcifications requires high spatial resolution, contrast sensitivity and signal-to-noise ratio (Baert et al., 2010).

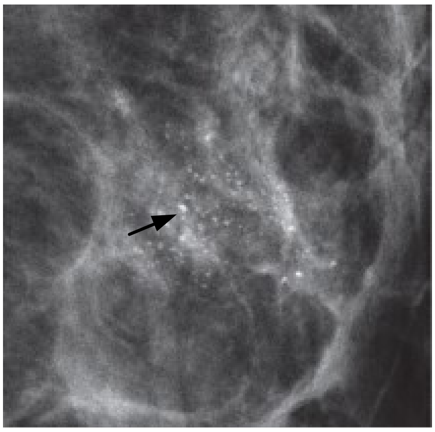

Figure 2.5: **Screening Mammogram Showing a 40-mm DCIS with Microcalcifications (Adapted from Baert et al., 2010).**

Figure 2.6 illustrates the loss of diagnostic information resulting from low resolution and poor contrast sensitivity (centre) as well as a low signal-to-noise ratio (right). To ensure the Aceso X-ray system can provide the required spatial resolution, contrast sensitivity and signal to noise ratio and to assess the effect of integrating ABUS into the X-ray system, some quantitative measure of X-ray image quality is required.

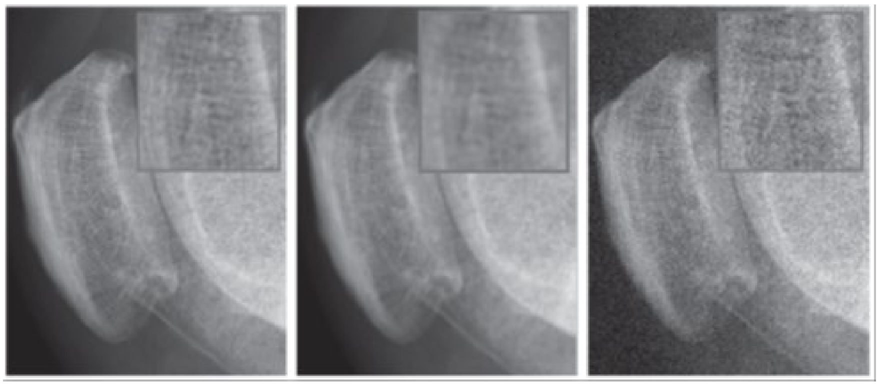

Figure 2.6: **Section of a High-Resolution of a Radiograph of the Knee. The three images show the effect on the original (left) of added blur (centre) and added noise (right) (Reproduced from Samei, 2003).**

Suri et al. (2005) made use of three metrics to evaluate the X-ray image quality of their FFDM+ABUS system: modulation transfer function (MTF), noise power spectrum (NPS) and detective quantum efficiency (DQE). These quality assurance metrics are used extensively and are endorsed and/or required by several regulatory authorities (Greiter & Hoeschen, 2010; NHS Breast Screening Programme, 2009; Samei, 2003; Smith, 2003; Stierstorfer & Spahn, 1999; Williams et al., 1999). The methods and formulae used in the computation of these metrics have been standardised and published by the International Electrotechnical Commission (IEC, 2007).

MTF. MTF, a measure of spatial resolution and contrast sensitivity, is the ratio of the output amplitude of a sinusoidal fluctuation to the input amplitude. For an ideal system it has a value of 1. Any system input may be decomposed into a series of sinusoidal contributions using a Fourier series as shown in Figure 2.7 (Palm, 2000). The MTF describes the efficiency with which each sinusoid is transferred to the output. As shown in Figure 2.7, the efficiency typically decreases with increasing spatial frequency. The net system output is the superposition of all the output sinusoids and, accordingly, contains less of the high frequency information. As a result, the contrast of an object at the output will decrease as the object becomes smaller. In this manner, MTF gives an indication of the effective spatial resolution and contrast sensitivity of the system.

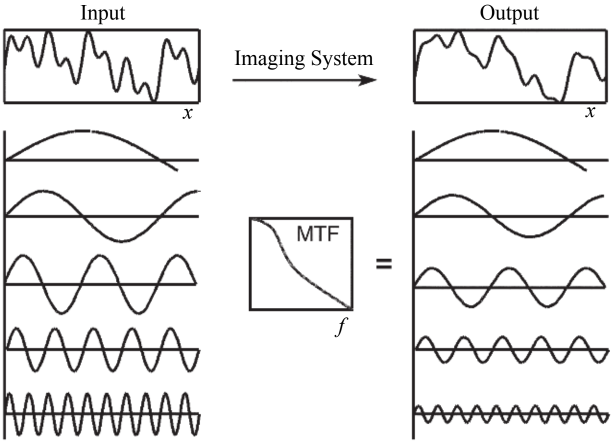

Figure 2.7: **Schematic Depiction of MTF. As shown by the MTF, the input to output transmission efficiency decreases with increasing spatial frequency (Adapted from Samei, 2003).**

NPS. Noise, or more specifically radiographic noise, refers to unwanted variations within an image that do not stem from the imaging subject. This added information can affect the image quality by drowning out small, low contrast features and masking larger features through edge distortion as shown in Figure 2.6 (Rose, 1948). NPS is the spectral decomposition of the noise as a function of spatial frequency. As shown in Figure 2.8, the NPS describes the spatial frequency variation as well as the magnitude of the system noise. The latter is computed from the area under the curve. The NPS is obtained through a Fourier transform of the fluctuations in a uniform image, known as a gain image.

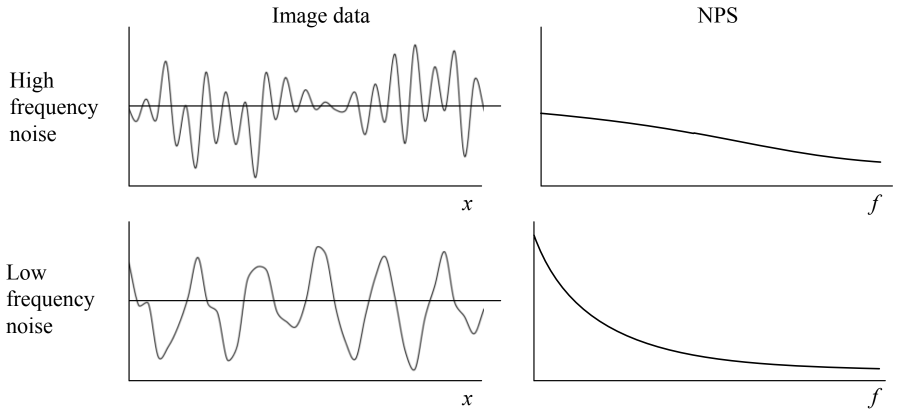

Figure 2.8: Schematic Depiction of NPS. The NPS is shown for high (above) and low (below) frequency noise.

DQE. The DQE is a function of MTF and NPS and is a measure of signal-to-noise ratio and dose efficiency. Mathematically, it is given by:

$$DQE(x,y) = MTF^2(x,y)\frac{NPS_{in}(x,y)}{NPS_{out}(x,y)}, \tag{2.1}$$

where MTF and NPS_{out} are the aforementioned MTF and NPS, respectively and x and y are coordinates in the two-dimensional image space. NPS_{in} is the NPS of the radiation field resulting from the radiation source (IEC, 2007). An ideal imaging system has DQE = 1 at all spatial frequencies. However, in addition to the decrease in MTF with increasing special frequency, each component in the X-ray imaging system (compression paddle, compression plate, detector etc.) decreases the signal to noise ratio because of added blur and detector inefficiencies (Samei, 2003). Therefore, NPS_{out} is always less than NPS_{in}. The ratio of the two gives an indication of how effectively the system has converted the available radiation into imaging information. Hence, DQE is a measure of dose efficiency. More specifically, a system with a higher DQE will achieve equivalent imaging performance at a lower dose (Aufrichtig & Xue, 2000).

In summary, measurement and computation of the MTF, NPS and DQE before and after the addition of the ABUS design features will quantify the effect of such systems on the Aceso X-ray image quality. Specifically, changes in terms of spatial resolution, contrast sensitivity, signal to noise ratio and dose efficiency will be highlighted. Additionally, the methods and calculations given in the aforementioned IEC standard (IEC 62220-1-2) provide a suitable guide for the computation of said metrics.

2.4 ULTRASOUND

2.4.1 THE COUPLING STACK

Figure 2.9 is a front view section through the Aceso showing the architecture of the ultrasound system, as introduced in section 1.1.5. The breast is compressed between the compression paddle and the compression plate with a thin layer of couplant between the compression plate and breast. A compliant material is used to take up the flexion of the compression plate and provide a planar scanning surface for the ultrasound transducer. Couplant is necessarily used at the material interfaces. The various materials between the transducer and the probe are henceforth referred to as the *coupling stack*.

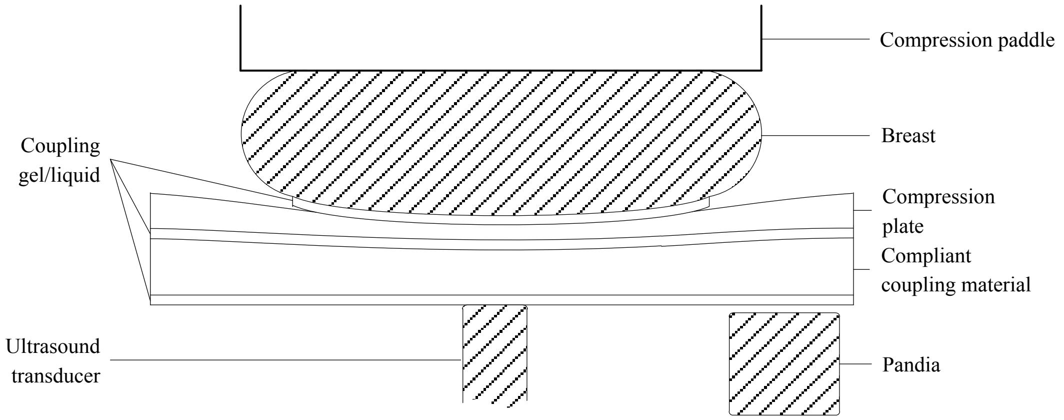

Figure 2.9: Front View of the Aceso Ultrasound Architecture

As ultrasound waves travel from the transducer, through the coupling stack to the breast and back, three processes take place: attenuation, reflection and refraction. The design of the stack requires careful consideration of these processes to ensure an elegant and optimised solution.

2.4.2 TRANSMISSION THEORY

Attenuation. Attenuation results from the cumulative effects of scattering and absorption. The latter is caused by the conversion of sound energy to other forms of energy. Attenuation causes the amplitude *A(x)* of an acoustic wave to drop off exponentially according to:

$$A(x) = A_0 10^{\frac{dB(x,f)}{20}}, \tag{2.2}$$

where A_0 is the intensity of the wave at some reference point and *dB(x,f)* is the attenuation. The attenuation is typically a linear function of the distance *x* from the reference point and the ultrasound wave frequency *f* given by:

$$dB(x,f) = \alpha \cdot x \cdot f, \tag{2.3}$$

where *α* is the characteristic attenuation coefficient of the material (Azhari, 2010). Usually α is reported in units of [dB/cm/MHz] and typical values for α are available from a variety of sources. Onda Corporation of Sunnyvale, California, has one of the most extensive collections of freely available material acoustic properties (Pedersen, 1999).

Based on the above relationship between attenuation and frequency, it seems pertinent to use as low a frequency as possible. However, this must be balanced with the relationship between resolution and frequency. Figure 2.10 shows that as frequency decreases so too does the wavelength and hence the spatial resolution. As such, the attenuation and resolution requirements must be carefully balanced.

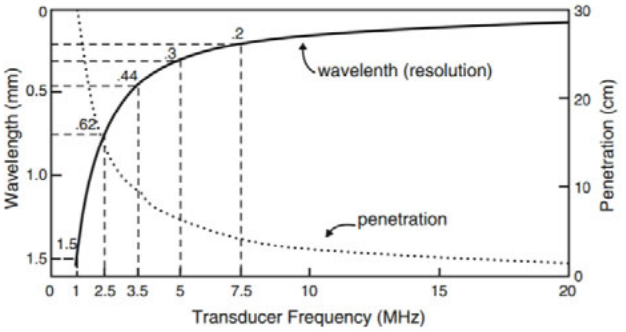

Figure 2.10: **Relationship Between Frequency, Resolution and Penetration (Reproduced from Chan & Perlas, 2011).**

Reflection. Figure 2.11 shows the reflection (*R*) and refracted transmission (*T*) of an incident (*i*) ultrasound wave at the boundary of two mediums. In the case of the coupling stack it is assumed that $\theta_i = \theta_R = \theta_T \approx 0$ because the ultrasound beam is perpendicular to the plane of the stack. For this special case, the reflection (A_R) and transmission (A_T) ratios are given by:

$$R = \frac{A_r}{A_i} = \frac{Z_2 - Z_1}{Z_2 + Z_1} \tag{2.4}$$

and

$$T = \frac{A_T}{A_i} = \frac{2Z_2}{Z_2 + Z_1}\,. \tag{2.5}$$

Z_1 and Z_2 are the acoustic impedances of the first and second mediums respectively (Azhari, 2010). Acoustic impedance is given mathematically by $Z=c\rho$, where c is the speed of sound in the medium and ρ is the density. However, in practice, acoustic impedances may be taken from the aforementioned collection of data provided by the Onda Corporation.

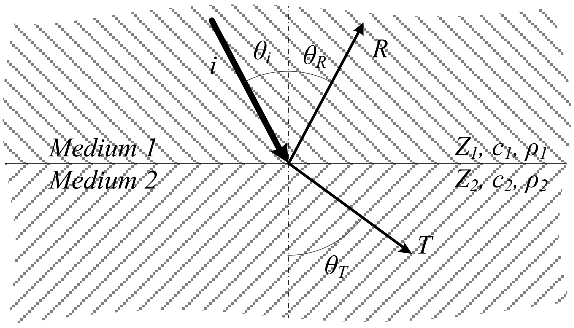

Figure 2.11: **Schematic Representation of Ultrasound Reflection and Refraction**

Refraction. In all cases $\theta_i = \theta_R$ however, as a result of refraction, the angle of the transmitted wave is given by the relationship:

$$\frac{c_1}{\sin\theta_i} = \frac{c_2}{\sin\theta_T}\,, \tag{2.6}$$

where c_1 and c_2 are the speed of sound in the two mediums (Azhari, 2010).

To optimise the design of the coupling stack, attenuation, reflection and refraction should be carefully considered. The maximum acoustic energy output of the ultrasound system is limited by the ultrasound electronics (and regulatory health and safety limits). These limits have been optimised for systems without the added burden of a coupling stack. Therefore it is necessary to minimise the loss of acoustic power caused by the coupling stack. Attenuation and reflection are the most pertinent considerations in this respect.

To this end, the attenuation of the materials used in the coupling stack should be minimised to ensure the efficient transmission of the ultrasound. To minimize the loss of acoustic energy due to reflections, it is necessary to minimize the difference in acoustic impedances between interfacing materials. This process is known as acoustic matching.

Although the incident angle was neglected in the calculation of R and T above, it should not be neglected in the context of beam-forming where refraction can have substantive effects on the image quality. Because the ultrasound beam is formed by a series of waves, and because only the wave directly below the focal spot travels perpendicular to the scanning plane, refraction through the coupling stack will result in spatial distortions and a reduction in focus. Hoctor & Thomenius (2003) have patented a beam former algorithm that corrects for the refraction effects of scanning through a coupling stack. However, such considerations form part of the ultrasound system design and fall outside the scope of this research. Nevertheless, in assessing the effect of the imaging stack on the ultrasound imaging performance it is useful to anticipate some detrimental effect on spatial resolution and geometric conformity (see section 2.4.3). Moreover, the variation in c from medium to medium should be minimised (see equation (2.6)) and the angle of incidence should be kept as close to zero as possible.

It is important to note that all material acoustic properties are affected by the exact material composition as well as the manufacturing process and so the actual values of the attenuation coefficient and acoustic impedance may well vary from the reported theoretical values. Additionally, the transmission theory presented here is intended to act as a design guide rather than an empirical computation. The reader is referred to Azhari (2010) for a more extensive and in-depth review of the subject.

2.4.3 ULTRASOUND IMAGE QUALITY

Although the need for ultrasound quality assurance was recognised more than 30 years ago (Erikson et al., 1976), the field still suffers from a fair degree of ambiguity. The rapid and continuing evolution of ultrasound technology, together with the subjective assessment of image quality, complicates the task of creating an applicable set of standards. Nevertheless, several institutions including the American Association of Physics in Medicine (AAPM) have produced quality control test procedures and several research groups continue to work on this problem (Goodsitt et al., 1998).

A review of the literature showed that ultrasound image quality is typically measured using the following six metrics: *elevation focus; contrast resolution; penetration depth; dead zone; spatial resolution; and geometric conformity* (Browne et al., 2004; Dudley & Griffith, 2001; Goodsitt et al., 1998; Sipilä et al., 2011; Thijssen et al., 2002, 2007; Tradup et al., 2003).

Before addressing each parameter in turn, it is necessary to introduce the general purpose ultrasound phantom. Such phantoms are typically constructed from tissue mimicking materials populated with several *target groups*. The targets are cylinders or wires that run the full width of the phantom. Each target group is used for one or more image quality measurement. With reference to Figure 2.12 the following groups are used in the measurement of the six image quality metrics: vertical group; horizontal group; grayscale group; dead zone group; and resolution array group.

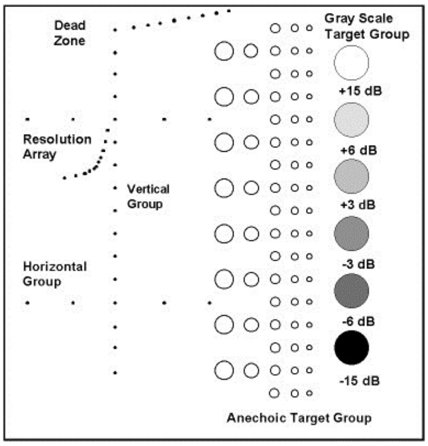

Figure 2.12: Layout of the ATS 539 Multipurpose Ultrasound Phantom

Elevation Focus. With respect to Figure 2.13, the elevation thickness of an ultrasound beam varies with distance, along the axial axis, from the probe. Knowledge of this parameter is particularly important in 3D ultrasound applications as it defines the resolution in the scan direction. Figure 2.14 is a beam width contour plot for a typical transducer. The beam width at any axial distance is defined by the lateral distance at which the signal intensity drops off by -6 dB. In the figure, this is indicated with a dashed line. The axial distance at which the beam is narrowest is known as the elevation focus depth.

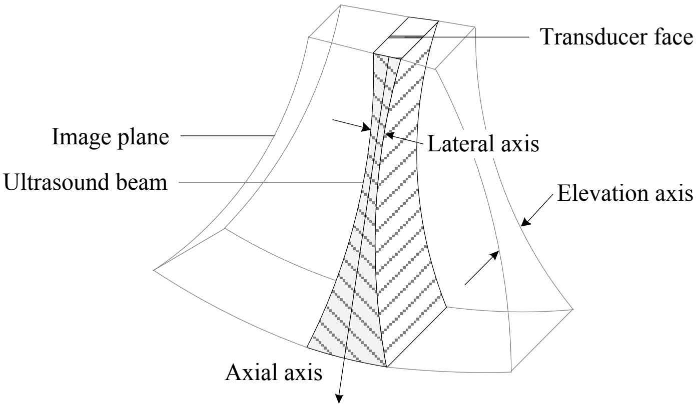

Figure 2.13: Schematic Representation of an Ultrasound Beam Showing the Three Spatial Axes

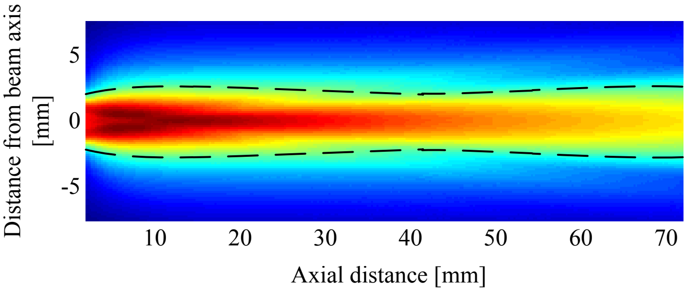

Figure 2.14: Ultrasound Beam Width Contour Plot. The dashed line illustrates the -6dB drop-off, or the effective width of the ultrasound beam.

Contrast Resolution. Contrast resolution or contrast sensitivity is defined as the smallest detectable difference in attenuation between an object of interest and the background material. This is an important parameter as it gives an indication of the sensitivity of the ultrasound system to anatomical tissue structures of similar impedance. Figure 2.15 shows a scan of three grayscale targets. The leftmost target has a relative attenuation of -15dB and is clearly visible. However, the target on the right has a relative attenuation of -3dB and is only just discernible.

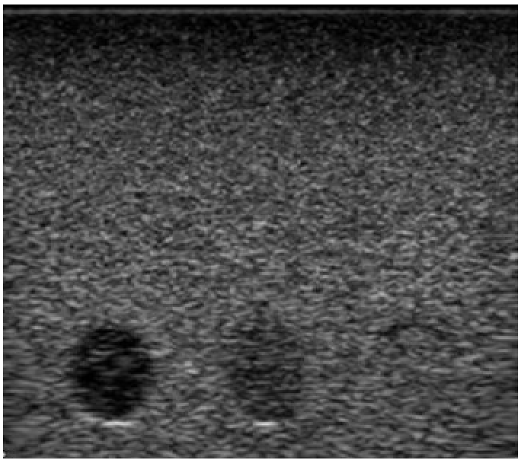

Figure 2.15: Ultrasound Scan of Grayscale Targets in a General Purpose Phantom. The impedance values of the targets from left to right are -15dB – 6dB and -3dB.

Penetration Depth. Penetration depth is a measure of the maximum depth at which echoes due to scatter in the background medium are detected. The penetration depth is measured as the depth at which the echo level has dropped off by -6 dB from the maximum. This parameter gives an indication of the maximum depth at which diagnostic quality images can be obtained. In the clinical setting, the background scatter is called *tissue grain*.

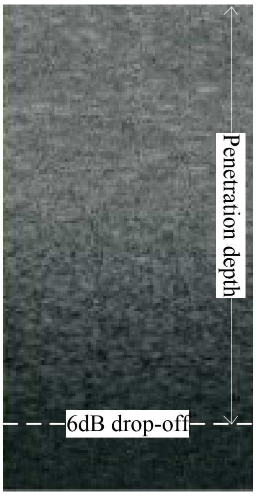

Figure 2.16: Ultrasound Scan of Homogenous Tissue Mimicking Phantom Material

Dead Zone. The dead zone is applicable when imaging structures close to the surface of the tissue. Using the dead zone target group of the phantom, one can easily discern the depth above which structures are not imaged by counting the number of visible targets and comparing that number to the known number of targets.

Spatial Resolution. Spatial resolution is the minimum distance at which one can differentiate two point targets. This is an especially important performance measure for the imaging of small structures such as microcalcifications. It is defined by the lateral and axial resolutions and can be measured using the resolution array and counting the number of discernible targets. Alternatively, it is precisely measured using the point-spread-function (PSF). The PSF is computed from the lateral and axial width of the -6 dB drop off of a point target. This width is typically called the full width half maximum (FWHM) (see Figure 2.17).

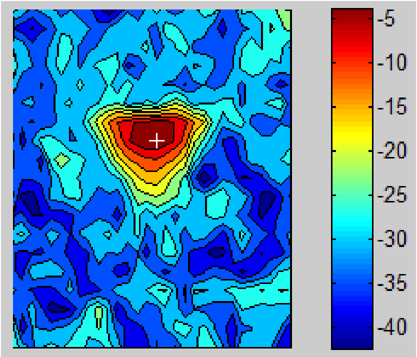

Figure 2.17: Point Target Contour Plot. The colour scale represents the dB drop-off from the maximum. This gives an indication of the spread of a point and hence the potential special resolution.

Geometric Conformity. Ultrasound is frequently used to take geometrical measurement of size and position. To ensure the necessary accuracy, measurements are taken of the horizontal and vertical target groups using digital callipers and compared to the known spacing of the targets.

To address the subjective assessment of the image quality parameters, several computational software packages have been developed that produce accurate, repeatable, objective and quantitative image quality metrics (Browne et al., 2004; Thijssen et al., 2007).

A free version of the software by Thijssen et al. (2007) – quality assurance for ultrasound (QA4US) – as well as a guide to its use is available from the Medical Ultrasound Imaging Centre, Radboud University, (MUSIC, 2012). This package may be used to quantitatively assess the impact of the coupling stack on the ultrasound image quality.

2.5 ERGONOMIC CONSIDERATIONS

Ergonomics is important for the comfort and safety of the patient and the mammographer. Further, good ergonomics should facilitate a consistently high quality image.

From an ergonomics point of view, the Aceso system is essentially a mammography unit. That is to say, the ergonomics are inherited from mammography rather than sonography and the additional workload required by the ultrasound functionality should be minimised.

The British National Health Service Breast Screening Programme published an extensive report on the ergonomics of mammography (Gale et al., 2007). The report raises two ergonomic considerations of particular relevance to the current work: The first pertains to the active imaging area of the system and the second pertains to the overall size of the compression platform.

Active Imaging Area. Figure 2.18 shows the features present in CC and MLO views when a breast has been well-positioned by the radiographer. In the CC view the pectoral muscle is visible. Although this is not a necessity, it provides a useful anatomical reference indicating the extent of the retromammary coverage. In the MLO view, a full field of view is indicated by the presence of the axillary tissue, the pectoral muscle and the inframammory fold (IMF). The axilla and IMF are imaged to detect lymphatic metastasis as discussed in section 2.2.2. The presence of the pectoral muscle once again gives an indication of the posterior tissue coverage (Bassett et al., 2010).

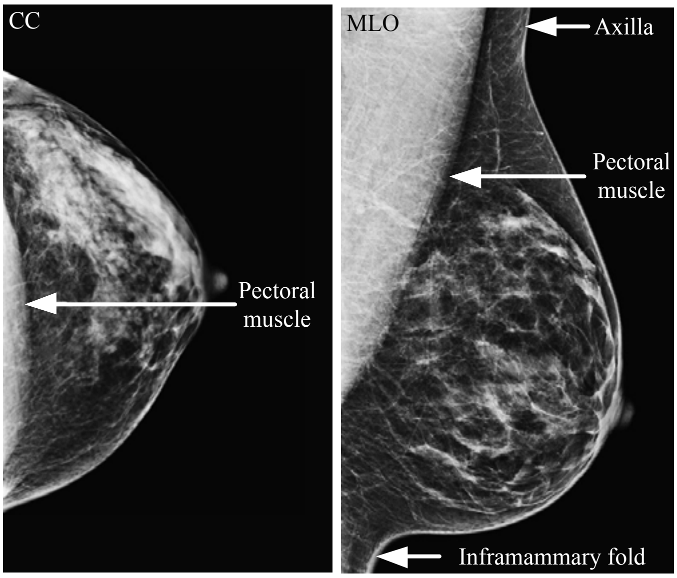

Figure 2.18: Optimal Positioning Features of CC and MLO Mammography (Adapted from Bassett et al., 2010).

Compression Platform Size. An important property of the compression platform, which is mentioned in the report, is its depth. Figure 2.19 shows a side view of the Hologic™ Selenia® compression platform which is considered relatively thick at ~10 cm. Thick compression platforms make it difficult to position larger, pregnant or wheelchair bound women because the platform must fit between the breast and the abdomen (Kailes & Lee, 2009).

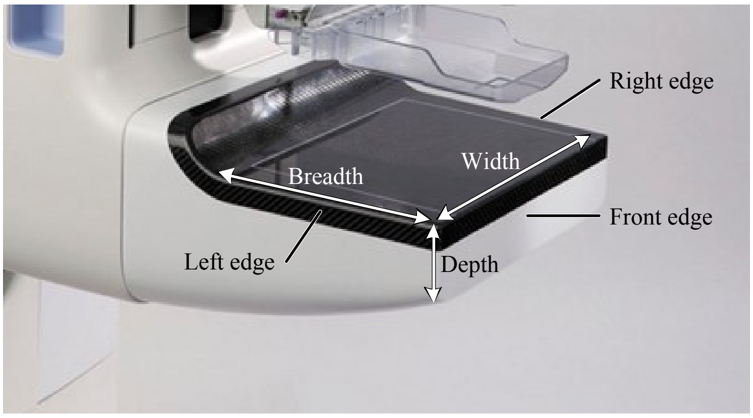

Figure 2.19: Hologic™ Selenia® Compression Platform (Adapted from Hologic, 2013).

The active imaging area must be large enough to accommodate the majority of women so as to avoid multiple scans due to lack of coverage. However, excessively large platforms complicate the task of the mammographer who must manoeuvre around the larger obstacle (Kailes & Lee, 2009). The size of the digital imaging area has been inherited from the size of X-ray films. Simmons et al. (2013) report that the smaller 18 × 24 cm cassettes are used 80% of the time while the larger 24 × 30 cm are used 20% of the time. The width of the Aceso breast platform (not the imaging area) is set to 300 mm by Aceso User Requirement Specification URS-24 (Baasch, 2013b).

Dead Space. The space between the active imaging area and the platform edge is known as the dead space. Optimisation of the platform requires the dead space to be minimised. Figure 2.20 shows how the lateral dead space (the active imaging area ends at the white line) reduces the portion of the axilla that can be imaged. Similarly, dead space at the front edge of the platform reduces retromammary coverage. The front-edge dead space is regulated by several authorities and, in the case of the IEC, may be no more than 5 mm (IEC, 2011). However, the lateral dead space is unregulated and systems such as the Selenia Dimensions from General Electric have lateral dead spaces of 30 mm or more.

In summary, the design of the breast platform should aim to minimise the imaging dead space as a matter of priority. Additionally, the dead space at the front-edge may be no more than 5 mm.

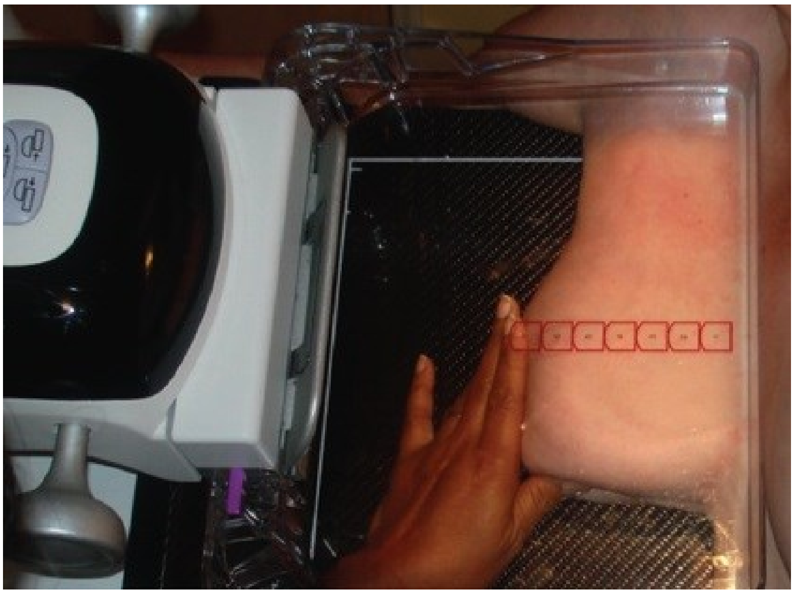

Figure 2.20: Compression of the Breast for a Right Mediolateral Oblique Scan (Reproduced from Simmons et al., 2013).

2.6 PRIOR ART AND RESEARCH IN THE FIELD

2.6.1 INTRODUCTION TO THIS SECTION

In this section several patents and accompanying journal articles are reviewed, in loose chronological order. To start, the basic characteristics of ABUS systems and the development thereof are discussed in a review of several early designs. Next, the work of four major contributors to FFDM+ABUS is considered in turn. The first is a patent by Shmulewitz which addresses many of the technical challenges raised in section 1.1.5. The second is a patent by Dines et al. who developed the Shmulewitz concept into a working prototype. Under the auspices of the third contributor – General Electric – several groups conducted research on a system similar to that of Dines et al. The relevant design characteristics of the General Electric system are presented, followed by a review of the X-ray and ultrasound image quality studies conducted on the system. Finally, the work of the fourth major player – Fischer – is presented. Fischer is the first to make significant progress with a system wherein the breast is imaged from below the compression plate. Again, the technical details of the system are presented first, followed by the X-ray and ultrasound image quality evaluations.

With the aim of finding innovative solutions to the coupling problem, an in depth patent review was conducted in and outside the medical imaging arena. A list of useful references is given at the end of this section and one particularly pertinent concept is discussed in detail.

2.6.2 THE DEVELOPMENT OF AUTOMATED BREAST ULTRASOUND SYSTEMS

Figure 2.21 shows one of the earliest ABUS systems (left) developed by Kossoff, Jellins, and their associates at the Australian Commonwealth Acoustic Laboratories Incorporated in 1969 (Dempsey, 2004; Harper & Kelly-Fry, 1980; Jellins et al., 1977). A compliant water-bag is lowered onto the breasts and the ultrasound transducer is suspended in the water from above. Details of an equivalent system are given in a patent by Flaherty & O'Connor (1969). The patent indirectly addresses coupling and matching, stating that the bag is made from thin vinyl and that olive oil or petroleum jelly is used as a coupling agent between the breasts and the bag.

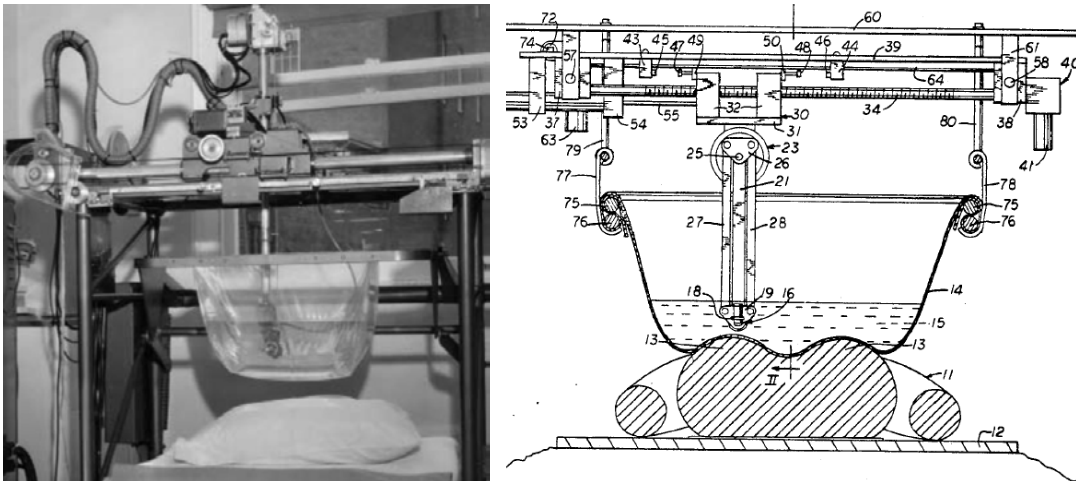

Figure 2.21: Early Supine Automated Breast Ultrasound Systems. A compliant water-filled bag is placed on the breast. The transducer is submerged in the water to achieve the necessary acoustic coupling. Left (Reproduced from Dempsey, 2004), right (Reproduced from Flaherty & O'Connor, 1969).

The Flaherty & O'Connor patent also details a prone scanning arrangement which is the forerunner of several ABUS systems (see Figure 2.22 left). In this arrangement, the ultrasound transducer is simply coupled to the breast using a water bath. This approach elegantly avoids the need for additional materials between the transducer and the breast.

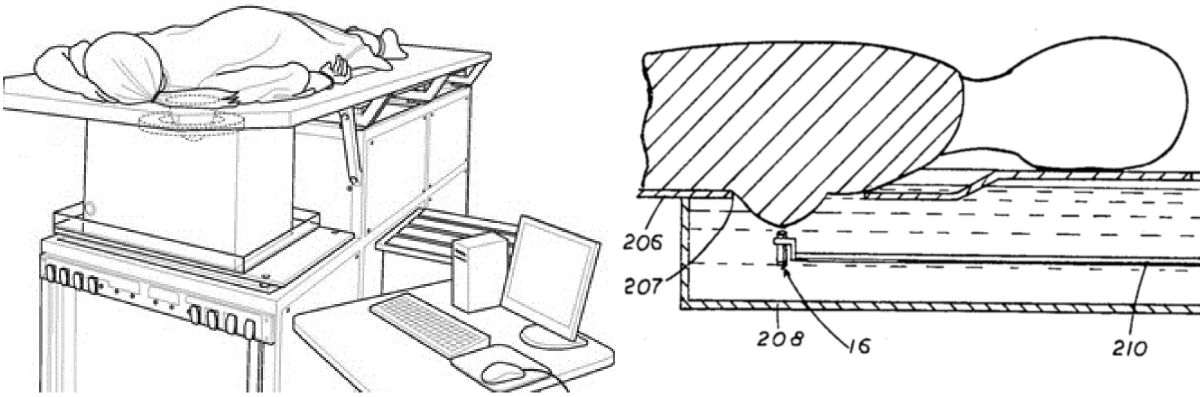

Figure 2.22: Prone Automated Breast Ultrasound Systems. In prone systems, the breast passes through a hole in the examination table into a water tank which couples the ultrasound transducer to the breast. Left – a modern prone ABUS system (Reproduced from Delphinus Medical Technologies, 2014). Right – a patent illustrating a prone ABUS system (Reproduced from Flaherty & O'Connor, 1969).

Prone and supine systems dominate the modern ABUS landscape (Dempsey, 2004). When compared to the mammographic arrangement, tissue management and acoustic coupling are significantly simplified: in the prone position the breast extends under gravity and in the supine position the breast tissue flattens out onto the chest wall; and in both cases, gravity acts so as to fill the anatomical contours with couplant (see Figure 2.21 and Figure 2.22). However, neither architecture successfully immobilises the breast, and hence both are prone to motion artefacts. Additionally, the scan position is less convenient than the upright position used in conventional mammography and the form factor of the 3D ultrasound volume differs from the mammographic case, preventing co-registration of suspicious lesions (see section 1.1.3).

The patent by Jones (1971) addresses some of these issues by adding compression to the prone architecture. The compression paddles are described as a polymeric film pulled taught on a rigid frame. By setting the thickness of the film to less than a quarter of the acoustic wave length the platform is made acoustically transparent (Azhari, 2010).

Figure 2.23 illustrates a patent application by Kossoff & Robinson (1983) which is one of the earliest attempts at ABUS in the mammographic arrangement. The system is embodied as either a point transducer which scans in two directions (left) or linear transducer, scanning in one direction (right). The latter resembles the Aceso ultrasound architecture. The patent specifies a “flat, ultrasonically transparent and rigid” compression plate (12). Rigid polycarbonate plastic is recommended as a suitable material, despite its high attenuation coefficient and high acoustic impedance.

As couplant, Kossoff & Robinson specify that coupling gel and/or oil is to be applied to the upper and lower surfaces of the platform prior to each examination. The impracticality of this is alluded to by a further suggestion that grooves may be used to continuously feed fluid to the appropriate surfaces; neither concept is explored in any detail.

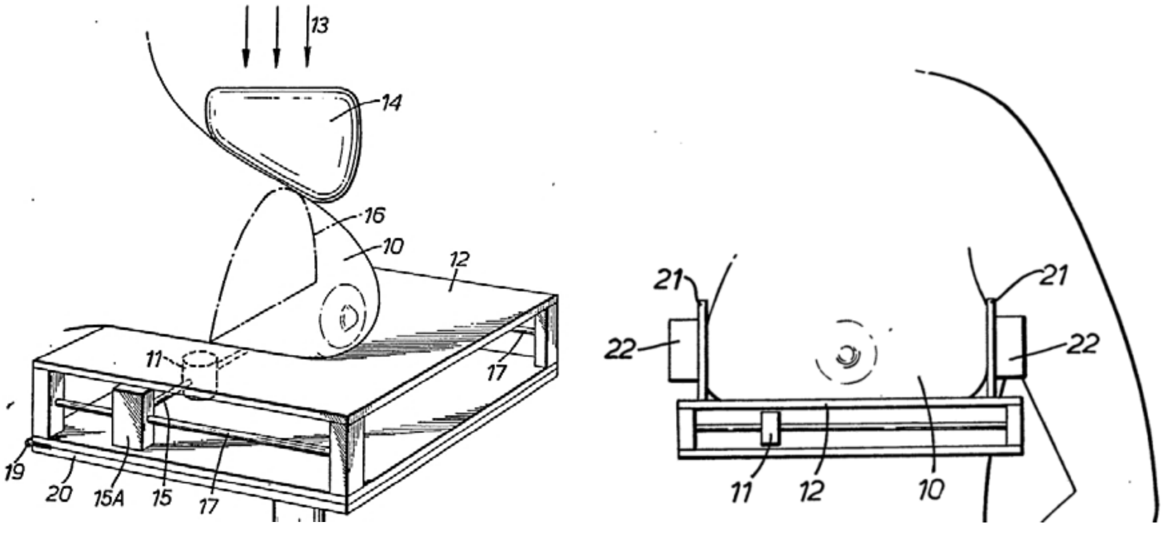

Figure 2.23: Patent for Automated Breast Ultrasound in the Mammographic Arrangement (Reproduced from Kossoff & Robinson, 1983). Left – point transducer with rastering. Right – linear transducer with scanning.

A later patent by Green & Taenzer (1984) is shown in Figure 2.24. In this design, the compression plates are acoustically coupled to the transducer using fluid filled compartments, devoid of air. However, the patent fails to detail the material used for the acoustic windows. Also, the complex system of actuating lenses and mirrors seems somewhat elaborate.

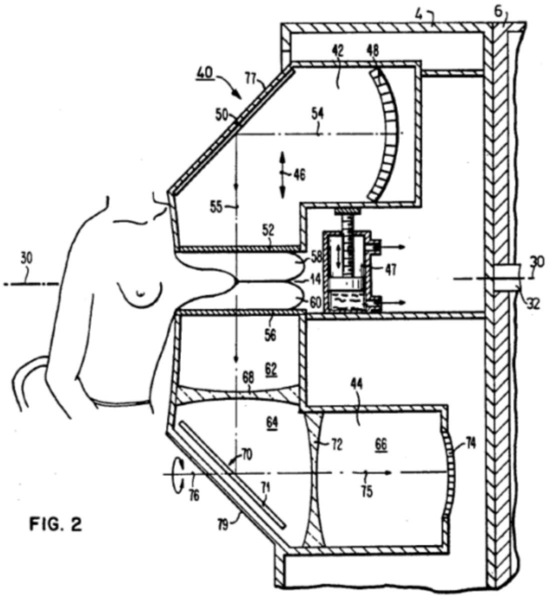

FIG. 2

Figure 2.24: Patent for Automated Breast Transmission Ultrasound in the Mammographic Arrangement (Reproduced from Green & Taenzer, 1984).

2.6.3 THE SHMULEWITZ PATENT

The Shmulewitz patent was one of the first to show X-ray and ultrasound in a single dual-modality system (Shmulewitz, 1996). Two embodiments, shown in Figure 2.25, are presented. In the first instance (left) the breast is scanned from above, through the compression paddle (15). This arrangement is henceforth referred to as the compression *paddle* architecture. In the second instance (right) the breast is scanned from below the compression plate (56). This arrangement is henceforth referred to as the compression *plate* architecture. In the description of the former embodiment the patent addresses many of the technical challenges of FFDM+ABUS raised in section 1.1.5.

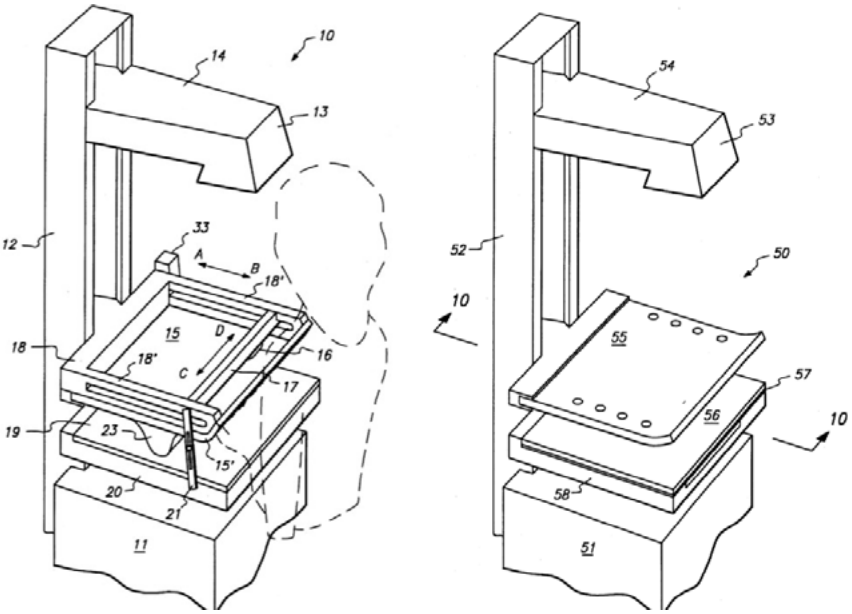

Figure 2.25: Patent for a Dual-Modality Mammography and Automated Breast Ultrasound System. Left – the rastering ultrasound transducer (16) scans the breast through the compression paddle (15) from above. Right – a two-dimensional ultrasound array (57) scans the breast from below the compression plate (56) (Reproduced from Shmulewitz, 1996).

The transducer is coupled to the compression paddle by a wetted sponge designed to take up any deflection of the paddle. Shmulewitz indicates that the deflection should be no more than 1° from the horizontal (~2.5 mm deflection for a 300×300 mm paddle). Kapur et al. (2004) explain that this limitation prevents significant spatial variations in the paddle-to-transducer distance and orientation. This in turn prevents spatial variations in the refraction artefacts (see section 2.4.2). Such spatial variations – which would vary between subjects and mammographic views – cannot be corrected through beam-forming. Shmulewitz found that common engineering materials with the required rigidity had unacceptably high attenuation and impedance characteristics.

In one embodiment of the design, Shmulewitz negates the acoustic properties of the paddle material by implementing the aforementioned taught-film paddle. He finds that Kapton® film yields a transmission loss of less than 3dB. In an alternate embodiment, Shmulewitz recommends plates of TPX® approximately 6 mm thick are used to give the required mechanical, X-ray and ultrasound characteristics. TPX® is the trade name used by Mitsui Chemicals for polymethylpentene. The material properties of TPX® are unique in that it has high mechanical rigidity but is radiolucent and sonolucent and has low acoustic impedance.

2.6.4 XDATA CORPORATION

In 1979 Kris Dines created the Xdata Corporation and pursued the compression paddle architecture with the MammoSonic3D. The design was first patented in 1998 (Dines et al., 2005). This work was conducted with guidance from Elizabeth Kelly-Fry who has been working in the field since the late 1960's (Dempsey, 2004; Harper & Kelly-Fry, 1980; Kelly-Fry et al., 1972).

As shown in Figure 2.26, the MammoSonic3D features a commercial ultrasound transducer (32) mounted in a rastering gantry (76) which in turn mounts to a custom compression paddle (78). Dines experimented with compression paddles constructed from several materials and thicknesses. He settled on a 3 mm polycarbonate compression paddle, claiming the mechanical strength of polycarbonate allows a reduction of thickness that counteracts its high attenuation coefficient and high acoustic impedance. However, Kapur & Carson (Kapur et al., 2004) report that the MammoSonic3D suffered from unresolved reverberations and defocusing as a result of the thick compression paddle.

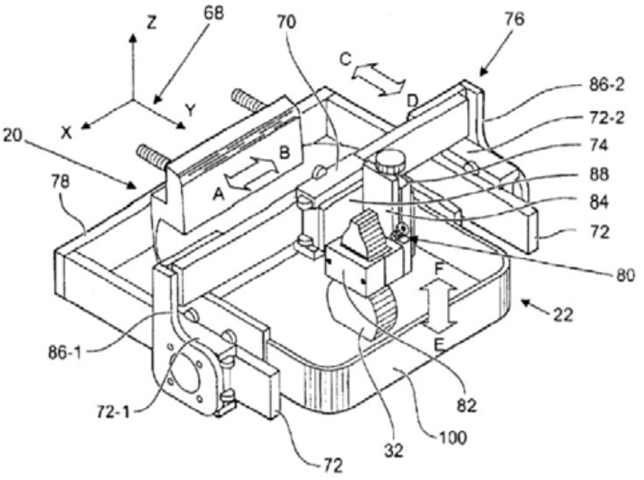

Figure 2.26: Xdata's MammoSonic3D Automated Breast Ultrasound Mammographic Compression Paddle (Reproduced from Dines et al., 2005).

A significant limitation of the compression paddle architecture is the need for a transducer-to-probe couplant. As discussed in section 1.1.5, the couplant will likely lead to X-ray imaging artefacts. Dines acknowledges this, stating the couplant must be cleaned from the platform before X-ray images are taken. A further issue is the choice of couplant. A liquid couplant would be easy to apply and would ensure the absence of air bubbles. However, it would spill out in the MLO view. If a gel couplant were used, it would be difficult to ensure bubble-free application and the gel build-up at the leading edge of the probe would need to be spread level at the end of each scan to maintain the coupling. Ultimately, this approach is more or less functional, but impractical in the clinical environment.

2.6.5 GENERAL ELECTRIC

A patent by Kapur & Thomenius (2005), assigned to General Electric, details a gel pad replacement for the paddle-to-transducer couplant, thereby enabling MLO scans. However, the concept failed to catch on and liquid/gel couplants continued to be used in later research (Dines et al., 2005; Kapur & Thomenius, 2005; Sinha et al., 2007a).

In further work conducted under the auspices of General Electric, Kapur et al. (2004) continued to refine the compression paddle architecture. Interestingly, the paddle was allowed to deflect as much as 10mm; and a compliant probe mounting was used to maintain a constant paddle-to-transducer distance and orientation. Shown in Figure 2.27 (left), the compliant mounting is the subject of another patent held by General Electric (Lokhandwalla & Kapur, 2007). A shortcoming of this design is the time varying angular orientation of the ultrasound transducer which complicates the task of 3-D volume reconstruction.

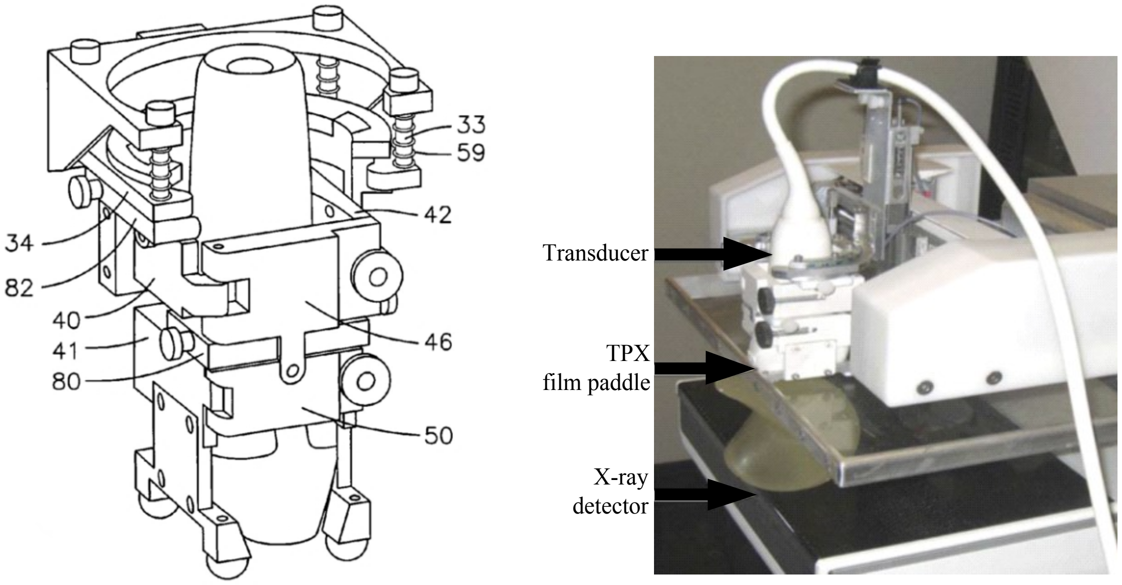

Figure 2.27: Compliant Ultrasound Transducer Assembly. Left – the bearings at the base of the device maintain contact with the scanning surface while the springs (33) take up deflections in the surface (Reproduced from Lokhandwalla & Kapur, 2007). Right – A thin film TPX compression paddle is shown with the complaint transducer assembly (Reproduced from Sinha et al., 2007b).

Kapur et al. evaluated the effect of TPX® on the X-ray image quality by computing the system MTF with a 2.5 mm LEXAN® compression paddle and a 4.5 mm TPX® paddle. The thickness of the TPX® was selected to yield the same radiographic half value layer (HVL) as the LEXAN® paddle. The MTF was found to coincide within 1%.

Kapur et al. also evaluated the ultrasound imaging performance using a 3.2 mm TPX® compression paddle. The TPX® reduced the lateral resolution, contrast and signal power by 86%, 3.5 dB and 8 dB, respectively. By implementing beam-former corrections these were reduced to 7%, 0.5 dB and 3 dB respectively (Booi et al., 2007). To further improve the ultrasound image quality, Kapur et al. recommends: reducing the plate thickness; increasing the gain and acoustic output power; and choosing an impedance-matched material to further minimize reverberations. The ultrasound performance in clinical trials was also studied and the difference in contrast levels between the FFDM+ABUS system and HHUS was found to be within 2.2dB.

2.6.6 FISCHER

Fischer was another significant player in the FFDM+ABUS field. However, much of its intellectual property is now owned by Hologic. Fischer filed a patent in 2003 for a system featuring the compression plate architecture (Besson & Nields, 2005). The breast platform houses independent scanning assemblies for the X-ray (40) and ultrasound (50) (see Figure 2.28). The ultrasound armature is compliant, allowing the probe to adjust to the deflection of the compression plate (36). Additionally, a gel pad (55) is used as a compliant couplant to take up the deflection along the axis of the probe. TPX® is the recommended compression plate material and mineral oil is suggested as an additional lubricant between the compression plate and the gel pad.

Fischer's continued development of this concept led to a further two patents (Suri et al., 2011, 2013) and a journal article (Suri et al., 2005). In the prototype system (see Figure 2.29), the taught-film architecture is used for the compression plate (not shown) and a system developed by Philips was implemented for the compression-plate-to-transducer coupling (also not shown).

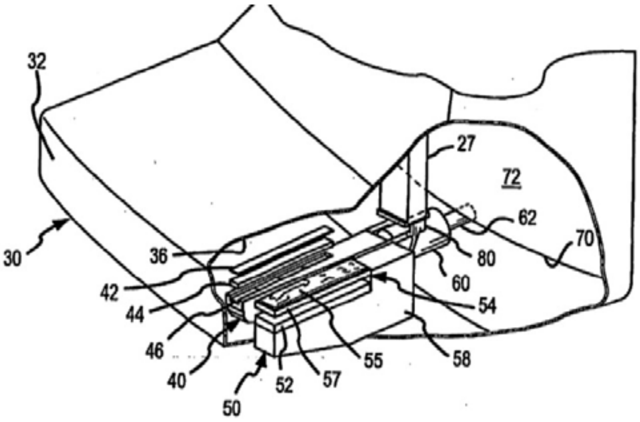

Figure 2.28: Fischer's 2003 Conceptual Breast Compression Platform (Reproduced from Besson & Nields, 2005).

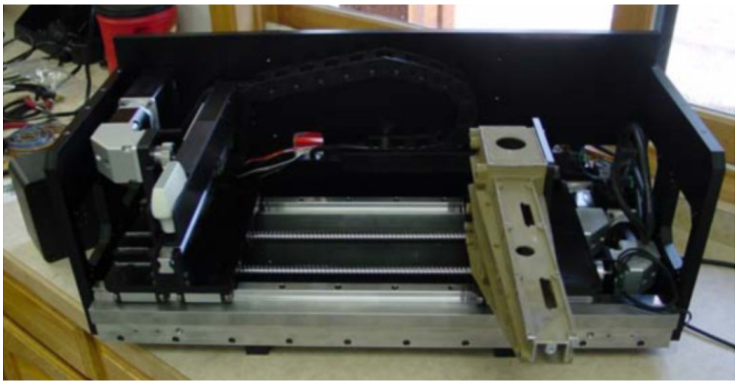

Figure 2.29: Fischer's 2004 Prototype Breast Compression Platform (Reproduced from Suri et al., 2005).

The Philips system, illustrated in Figure 2.30, comprises an oil-filled coupling chamber (101) which makes contact with the underside of the compression plate (14) by means of a flexible seal (106). The transducer is acoustically coupled to the compression plate via the oil-filled coupling chamber. A sponge (102) is used to reduce the free volume of fluid in the event of a leak. Channels (103) allow fluid to continually circulate through the coupling chamber. The fluid is sucked through the chamber and the resulting low pressure enhances the flexible seal.

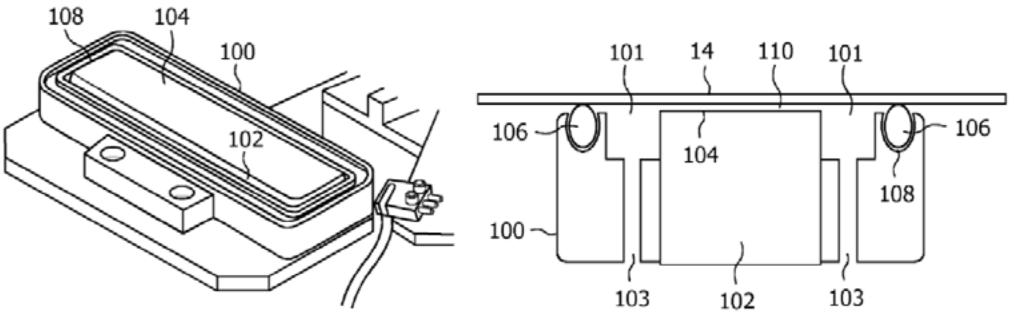

Figure 2.30: **Philips' Compression-Plate-to-Transducer Coupling System (Reproduced from Entrekin, 2011).**

This coupling system suffers from two limitations. The first is the height of the sealing assembly; in one of the Fischer priority documents the compression-plate-to-transducer distance is quoted as 19 mm. This increases the height of the compression platform and attenuates the ultrasound. The second limitation is the couplant which inevitably seeps and/or leaks out of the coupling chamber (see section 1.1.5). A couplant management system is presented in a patent assigned to U-Systems for a similar ABUS-only breast platform. Shown in Figure 2.31, the breast platform includes a system for the collection and recycling of the spilt couplant (Anderson et al., 2006). However, the system is not suitable in the presence of an X-ray detector as it fails to address the points raised in section 1.1.5.

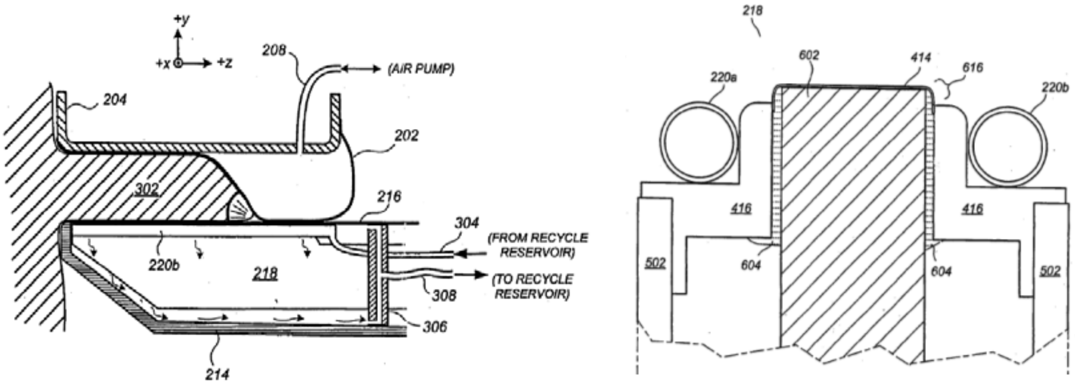

Figure 2.31: **U-Systems' Compression-Plate-to-Transducer Coupling System. The figure on the left illustrates a system for collecting and recycling coupling fluid which has spilling from the coupling chamber (220b) (Reproduced from Anderson et al., 2006).**

The system was nevertheless a functional prototype and Suri et al. (2005) used it in a series of X-ray and ultrasound image quality tests. In the X-ray image quality evaluation of the system, the MTF was found to increase slightly for the FFDM+ABUS case when compared to FFDM-only case (ΔMTF < 0.1 at 3 lp/mm). This unexpected result is attributed to geometric and characteristic differences between the machines used to acquire the two data sets. This experimental discrepancy brings into question the significance of the marginal increase in NPS and DQE recorded for the dual-modality case.

The ultrasound image quality of the FFDM+ABUS system was compared to that of HHUS using the PSF. The results showed no significant change in spatial resolution at the -6 dB drop-off. This is to be expected as a taught-film compression plate was used (see Figure 2.29). However, the transmission loss was found to be relatively high at approximately -6 dB. Suri attributed the high losses to reverberations within a 2 mm butadiene rubber standoff which was required to couple the system to the phantom.

2.6.7 INNOVATIVE SOLUTIONS TO THE COUPLING PROBLEM

Ultrasound coupling is a challenging design task, even outside the medical imaging arena and an extensive patent review revealed many innovative solutions. One particularly pertinent solution is presented in a 2004 patent application for a fingerprint scanner (Schneider et al., 2010). The system, illustrated in Figure 2.32, comprises a scanning ultrasound transducer (40) housed in a hermetically sealed housing. The housing is filled with a fluid that acts to couple the transducer to the scanning surface (16). This arrangement bears some similarity to the previously discussed patent by Green & Taenzer (1984).

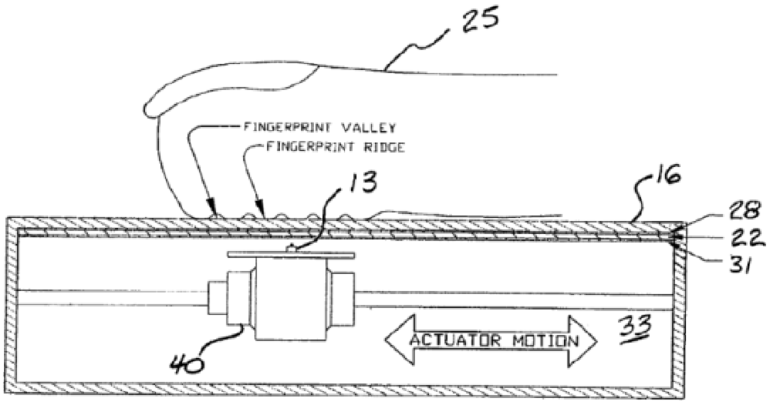

Figure 2.32: Ultra-Scan Corporation's Ultrasonic Fingerprint Scanner. The entire device is filled with a fluid (33) which couples the transducer to the scanning surface (16) (Reproduced from Schneider et al., 2010).

In addition to the array of coupling architectures discussed above the following references were found to be useful to a lesser extent: (Amara, 2012; Beyer & Derndinger, 1984; Crosby & Shmulewitz, 1998a, 1998b; Hayakawa & Matsui, 1996; Ishiyama & Takano, 1987; Nields & Ulatowski, 2000; Pretlow, 2005; Richter, 1998; Towfiq et al., 2013; Wang et al., 2013; Wendelken & Pope, 2006).

2.6.8 RECENT WORK IN THE FIELD

In the recent past there have been no significant publications indicative of substantial design progress by Xdata, General Electric, Fischer/Hologic or any other group. That said, all three companies continue to pay maintenance on their respective IP and the National Institutes of Health (NIH) in America continues to provide financial support to the development of FFDM+ABUS. It is thus likely that work on FFDM+ABUS systems continues to progress behind closed doors so as to protect the valuable IP.

2.7 SUMMARY OF THIS CHAPTER

Following an introduction to the anatomy of the breast, the important characteristics of breast cancer were briefly introduced.

This was followed by a discussion of screening mammography and X-ray image quality metrics. These metrics are to be used to determine the X-ray imaging performance of the final design. The IEC provides a useful standard, detailing the measurement and computation of said metrics.

The concept of a coupling stack was introduced in section 2.4.1. In the section that followed, ultrasound transmission theory – used in the optimisation of the coupling stack – was reviewed. In section 2.4.3 several ultrasound imaging metrics were explained and a tool for the measurement and computations thereof was presented.

In section 2.5 the ergonomics of mammography was reviewed and some important design constraints were identified.

Finally, in section 2.6 the development of FFDM+ABUS systems was investigated with a study of prior art and research in the field. Several innovative solutions to the coupling problem were identified as well as an array of unsolved technical challenges.

In conclusion the necessary background, design tools, and review material have been gathered; forming a firm foundation for the next stage of the design process: concept development.

Chapter 3: CONCEPT DEVELOPMENT AND PROTOTYPING

3.1 OVERVIEW OF THIS CHAPTER

This chapter begins with the development of the system requirement specification (SRS) for the breast platform, which fully defines the design task. This is followed by the development of several theoretical concepts. The manufacture and testing of a first prototype are detailed in section 3.4 and three further prototypes are presented in section 3.5.

3.2 SYSTEM REQUIREMENT SPECIFICATION

The SRS comprises: requirements, constraints and criteria. The requirements are definitive functions that the device must perform. The constraints define the limitations placed on the design such as cost, and regulatory requirements. Finally, the criteria are used to differentiate a poor design from an elegant one. Each item of the SRS is motivated by the information in the preceding chapters and/or high level Aceso specifications.

Table 3.1: Breast Platform System Requirement Specification

Requirements	
No	Description
RE01	The device must integrate ABUS into the existing Aceso FFDM architecture.
RE02	The device must form the lower breast compression surface supporting breast compression up to 200 N.
RE03	The device must provide a means for the independent translation of the X-ray detector and the ultrasound transducer.
RE04	The resulting X-ray and ultrasound images must be of diagnostic quality.
RE05	The device must function at C-arm angles between +180º and -180º.
Constraints	
No	Description
CO01	The X-ray architecture is fixed and must be implemented as described in section 1.1.4.
CO02	The ultrasound architecture is fixed and must be implemented as described in section 1.1.4.
CO03	The first active pixel of the X-ray detector may not be more than 5 mm from the outer front-edge of the breast compression platform.
CO04	The device must continue to support compression in the event of a power failure.
CO05	Operating temperature range: 10° to 40°C.
CO06	Shipping temperature range: -10° to 40°C.
CO07	The design must be completed by July 2013.
CO08	Manufacture and procurement must be completed by mid-September 2013.
CO09	The device must be commissioned by mid-October 2013.
Criteria	
No	Description
CR01	The image quality should be optimised.
CR02	The imaging dead space should be minimised.
CR03	The ergonomics should be maximised.
CR04	Ease of assembly/maintenance should be maximized.
CR05	Ease of manufacture should be maximized.

3.3 CONCEPT DEVELOPMENT

In this section, four conceptual systems are presented. Each concept is accompanied by a description and schematic representation. Furthermore, the advantages and disadvantages of each concept are discussed.

3.3.1 CONCEPT 1 – MINIMAL DEFLECTION PLATFORM

Description. The transducer makes direct physical contact with the underside of the compression plate. The compression plate is rigid and does not deflect under breast compression. The compression-plate-to-transducer interface is lubricated with coupling fluid via the sponge at the end of the platform. The sponge is supplied with lubricating/coupling fluid from a reservoir.

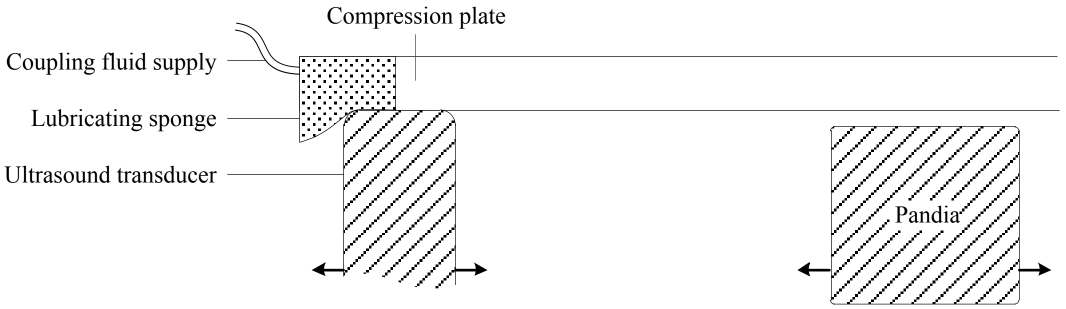

Figure 3.1: Design Concept 1 – Minimal Deflection Platform

Advantages. The advantage of this concept is its simplicity.

Disadvantages. This concept suffers from many of the shortcomings given in section 1.1.5. To achieve the required rigidity, the compression plate would need to be extremely thick or constructed from materials lacking the required X-ray and ultrasound characteristics. Also, lubricating couplant would build up on the underside of the compression plate, causing X-ray imaging artefacts and dripping onto the Pandia. Finally, the sponge would increase the imaging dead space.

3.3.2 CONCEPT 2 – COUPLING CHAMBER WITH A SLIDING SEAL

Description. This concept is adapted from the Philips patent (see section 2.6.6). The transducer is offset from the compression plate and any deflection is absorbed by the compliant sliding seal. The compression-plate-to-transducer coupling is achieved through a fluid-filled coupling chamber, circumscribed by the sliding seal. The coupling chamber is bled[1] using the couplant inlet and outlet lines.

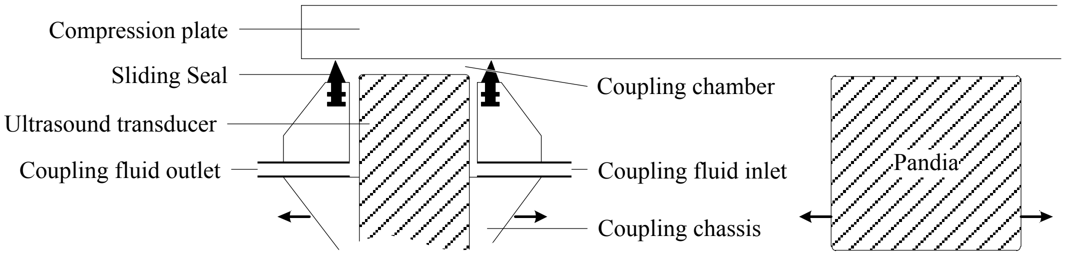

Figure 3.2: Design Concept 2 – Coupling Chamber with a Sliding Seal

Advantages. This concept accounts for the deflection of the compression plate and is also relatively simple.

---

[1] Bleeding, in a hydraulic context, refers to the removal of all air from the system.

Disadvantages. Couplant and/or air may seep through the seals. This would cause couplant to collect under the compression plate and/or bubbles to collect in the coupling chamber, affecting the X-ray and ultrasound image quality, respectively.

3.3.3 CONCEPT 3 – COUPLING CHAMBER WITH A STATIC SEAL

Description. Like concept 2, a coupling chamber is used for compression-plate-to-transducer coupling. However, concept 3 does not rely on a sliding sealing. Instead, a thin film keeps the coupling chamber – the region between the thin film and the compression plate – sealed off. The couplant is further contained by a static seal around the perimeter of the platform, where the deflection is negligible. The transducer enters the coupling chamber through a rectangular cut-out in the thin film. The transducer is sealed to the periphery of the cut-out thereby maintaining the integrity of the coupling chamber. As the transducer translates, lateral rollers disperse and collect the thin film, thereby keeping it taught. The Pandia is fitted with spring-loaded rollers that smooth the thin film so as to avoid X-ray imaging artefacts.

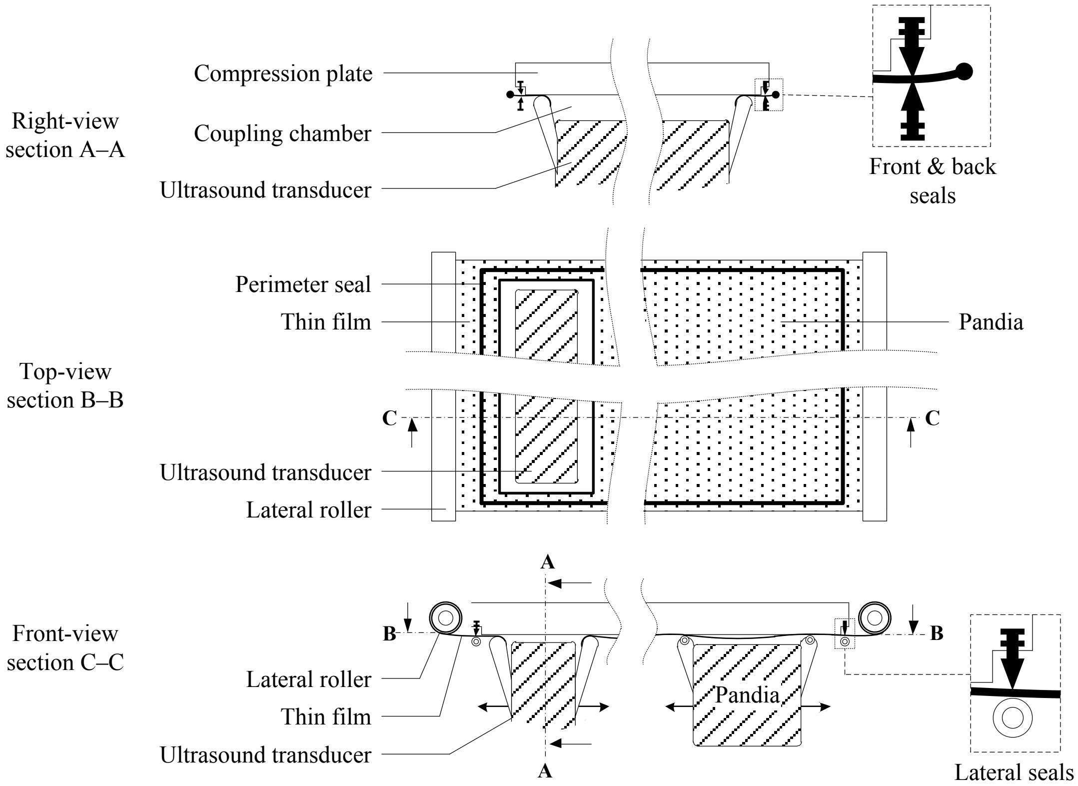

Figure 3.3: Design Concept 3 – Coupling Chamber with Static Seal

Advantages. This concept builds on the advantages of concept 2 by simplifying the sealing system and isolating the Pandia from the couplant.

Disadvantages. The significant disadvantage of this system is its complexity. Additionally, the seals and rollers increase the imaging dead space considerably.

3.3.4 CONCEPT 4 – HERMETICALLY SEALED BREAST PLATFORM

Description. Although this concept was developed before the patent by Schneider et al. was unearthed, the two concepts bare a distinct similarity (see section 2.6.7). In this concept the entire breast platform is hermetically [1] sealed with the Pandia, ultrasound transducer and scanning mechatronics inside. It is then wholly filled with a *non-conductive* coupling fluid.

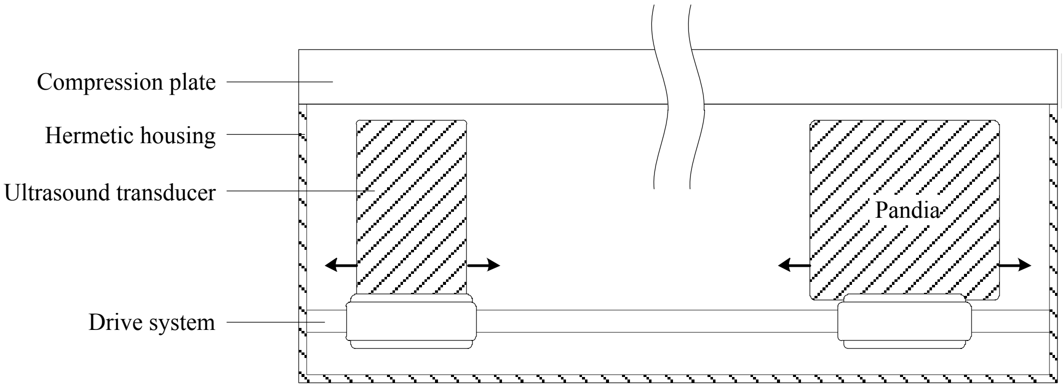

Figure 3.4: Design Concept 4 – Hermetically Sealed Breast Platform

Advantages. This concept is likely to provide a consistently high X-ray and ultrasound image quality. It accommodates platform deflection and minimises the imaging dead space.

Disadvantages. This concept is high risk: wetting the Pandia, ultrasound transducer and breast platform may cause irreparable damage. Also, achieving a hermetic seal is complicated by the power and signal cables for the Pandia, ultrasound transducer and scanning mechatronics. Moreover, maintenance of the internal components would be complex and messy.

3.3.5 CONCEPT SELECTION

Concept 1 was deemed unlikely to be successful and concept 3 and four were deemed overly complex. Hence concept 2, having already been demonstrated by Suri et al. (2005), was selected for further development and prototyping.

3.4 PROTOTYPE 1– A COUPLING CHAMBER WITH A SLIDING SEAL

A 3D rendering of prototype 1 is shown in Figure 3.5. A HHUS transducer is mounted in the coupling chamber which in turn is mounted on a rail system, allowing the assembly to translate as shown. The compression plate is mounted on the compression plate mount. The height of the mount can be adjusted, thereby varying the compression-plate-to-transducer distance and the compression of the sliding seal. The sliding seal is not shown in the figure.

The coupling chamber is bled using an inlet and outlet valve at the base of the chamber, with the entire assembly upside down. The pressure inside the chamber is raised and lowered by varying the height of the couplant reservoir relative to the height of the coupling chamber.

The performance of the prototype was evaluated in a series of laboratory experiments. Achieving a reliable sliding seal proved problematic. A successful sliding-seal must: slide smoothly without snagging; and seal without seeping. Several different seal materials were investigated. These included closed cell foam, hollow silicon section, windscreen wipers, and hollow foam section. The only promising material was the hollow foam; however, it too failed under certain conditions.

---

[1] Hermetic seals are impervious to gases and liquids.

A screen-shot from a video of the prototype in operation is shown in Figure 3.6. Translation of the transducer caused the sliding seal to deflect. As a result, couplant seeped out of the seal and air leaked in. Despite extensive testing a robust seal could not be achieved, an outcome alluded to by the Anderson et al. patent (see Figure 2.31). A further shortcoming of the concept was the imaging dead space resulting from the sliding seal.

Based on the couplant leakage and the large imaging dead space this concept was rejected as a viable option for the Aceso. Nevertheless, it was used extensively to study various couplants and compression plate materials. The results of this testing are incorporated into the final design presented in Chapter 4.

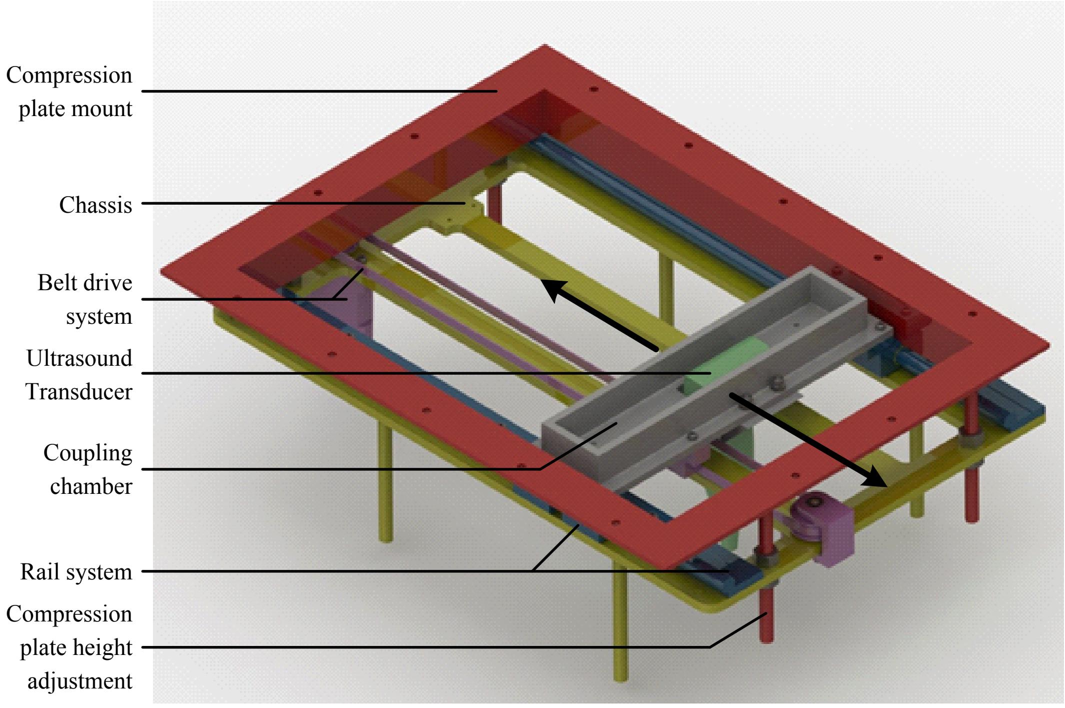

Figure 3.5: **Isometric Rendering of Prototype 1**

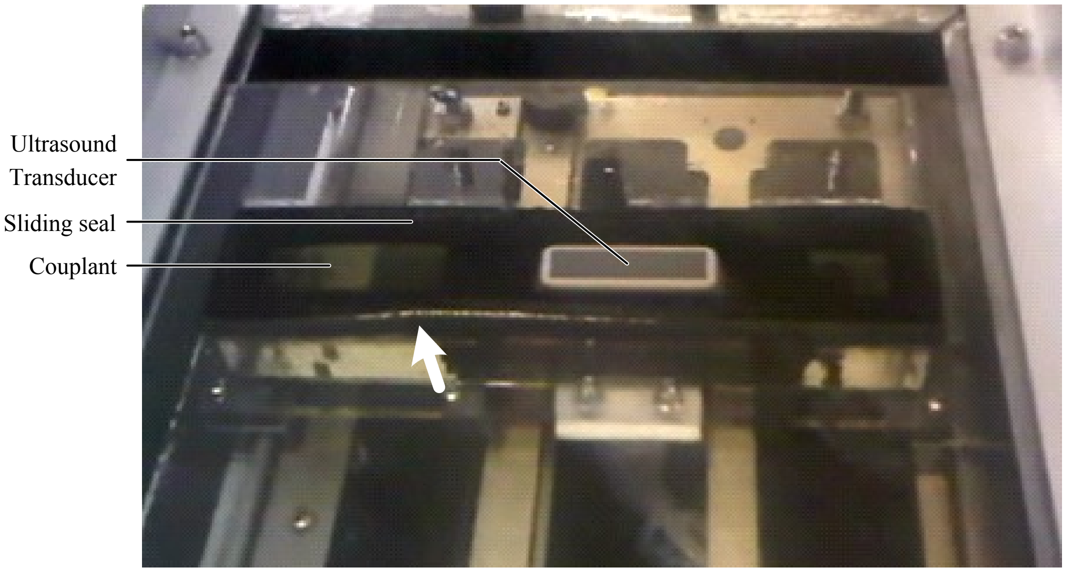

Figure 3.6: **Screen Capture of Prototype 1 in Operation. The sliding seal has deflected, resulting in fluid seeping out the seal.**

3.5 PROTOTYPES 2, 3 & 4 – A HERMETICALLY SEALED BREAST PLATFORM

Following the failure of prototype 1, it became clear that – as suggested by the review of the literature – a more advanced solution was required. With concepts 1 and 2 already rejected, concepts 3 and 4 were more closely examined in a thorough design review. It was decided that concept 3 would likely suffer from similar sealing issues as concept 2. Additionally, the static seals would exceed the limit on the front-edge-imaging-dead-space (CO03) with the lateral rollers leading to significant lateral dead space. Hence, concept 3 was also rejected.

At this stage it was decided that the feasibility of concept 4 should be re-evaluated. In an effort to de-risk the concept, a motor and motor controller from Soteria were submerged in a non-conductive couplant (see Figure 3.7 left). The motor was left to drive continuously for several days and no degradation in performance was detected. Additionally, research into liquid cooling revealed it to be used extensively in the *immersion cooling* of high performance computers and other electronic components (Bar-Cohen et al., 2006; Yokouchi et al., 1987). With the concept somewhat de-risked, the decision was made to progress to the prototyping stage.

Figure 3.7: Immersion cooling. Left - screen capture of the first test of a motor and controller in non-conducting couplant. Right – an immersion cooled server bank by Revolution Cooling (2014).

3.5.1 PROTOTYPE 2 – PROOF OF CONCEPT

The purpose of prototype 2 was to demonstrate the feasibility of concept 4 by submerging the Pandia, ultrasound transducer and scanning mechatronics in couplant. A further aim was the acquisition of a dual-modality image of a phantom, using a predated version of the Pandia and a HHUS transducer.

Prototype 2 is shown in Figure 3.8. The prototype comprised of a rail carriage, with independent Pandia and ultrasound drives, as shown in Figure 3.9 (left). The rail carriage was housed in a PMMA (Perspex) box (Figure 3.9 right). The housing was filled with couplant above the level of the compression plate so as to couple the ultrasound transducer to the compression plate.

A *homemade* phantom – created in collaboration with Patrick Muthui. – was manufactured using gelatine as a base material and small gelatine sweets as lesions. The sweets were positioned with wires. While the material properties (acoustic impedance, speed of sound, attenuation, etc.) of the phantom were somewhat random, it proved a useful tool in early imaging tests. Figure 3.10 shows the resulting X-ray (left) and ultrasound (right) images.

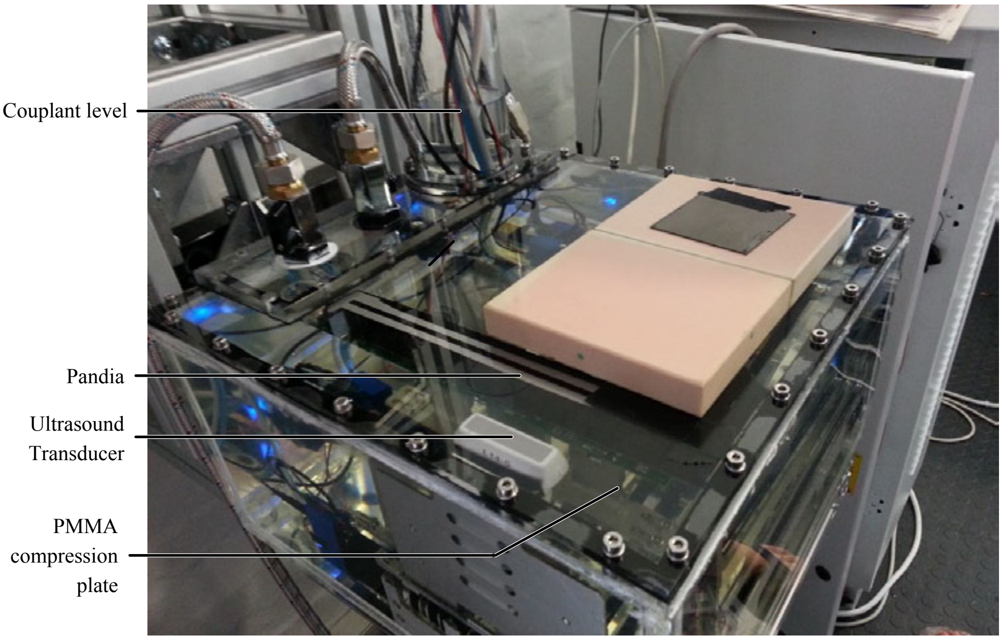

Figure 3.8: **Prototype 2 in Operation. The Pandia and ultrasound transducer are shown scanning radiographic tissue clocks from within the PMMA box which is filled with non-conductive mineral oil.**

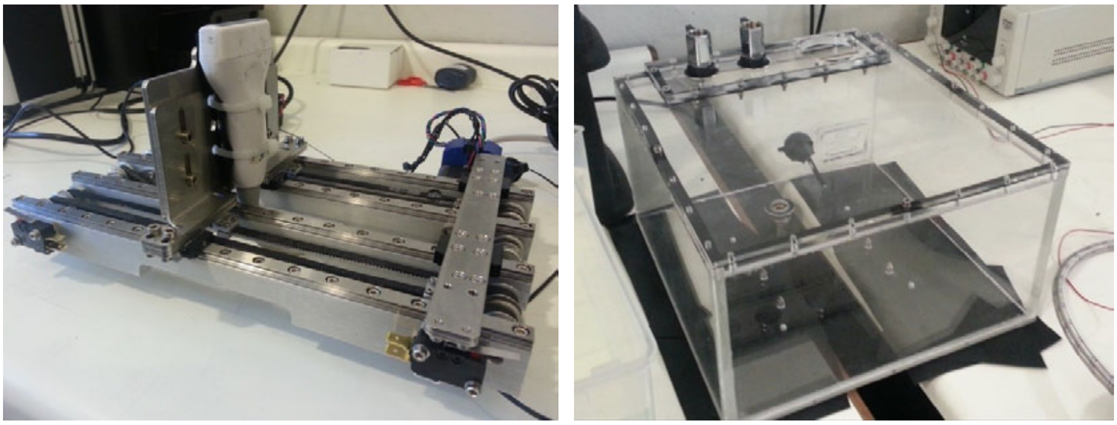

Figure 3.9: **Prototype 2 Rail Carriage and PMMA Housing. Left – the rail carriage is shown with a HHUS probe mounted on the ultrasound carriage. Right – the PMMA (Perspex) housing with bleeding valves.**

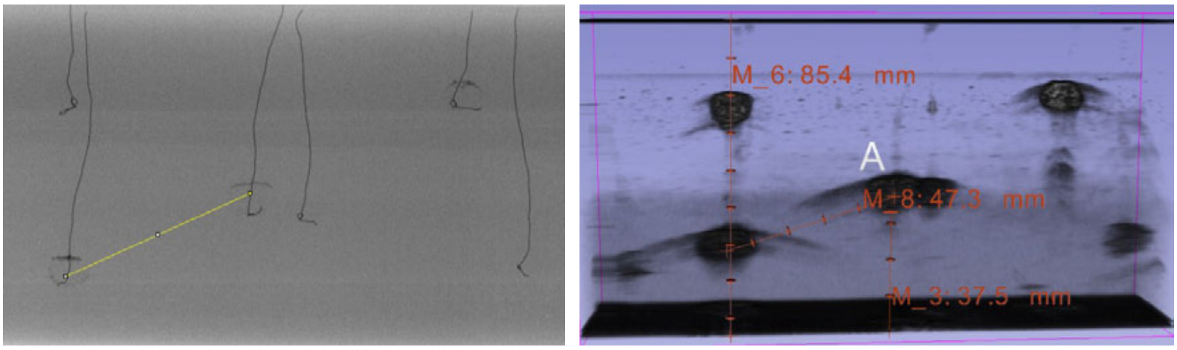

Figure 3.10: **Prototype 2 Dual-Modality Images of a Homemade Phantom. Left – an X-ray scan of the phantom. Right – a 3D reconstruction of the ultrasound images (reconstruction by Benjamin Irving). The same distance is being measured in both images.**

Based on a visual inspection only, both the ultrasound and X-ray images appeared to be of high quality. However, later, more formal testing indicated that the attenuation characteristics of the homemade phantom may have falsely inflated the imaging performance. Nevertheless, proof of concept was achieved and the decision was made to continue the development of the HSBP.

Concept 2.1 suffered from several shortcomings which highlighted many of the remaining design challenges. These included: (1) difficulty sealing the box; (2) leaking electrical connectors; (3) a front-edge dead space greater than 5 mm; (4) large deflections of the 3 mm PMMA compression plate; and (5) poor acoustic matching of the coupling stack.

It was decided that the resolution of these issues would most easily be achieved through the development of two further prototypes: prototype 3 and prototype 4. The purpose of the former was to test the mechanical aspects of the HSBP including (1-4) in the previous paragraph, while the latter prototype was designed and manufactured to evaluate various compression plate materials and couplants (5 in the previous paragraph).

3.5.2 PROTOTYPE 3 – MECHANICAL TESTING

Prototype 3 is shown from behind in Figure 3.11. The housing is made from carbon-fibre-reinforced-polymer (CFRP) and a 3 mm thick TPX platform. The housing is sealed posteriorly with a transparent polycarbonate back plate. Several hydraulic fittings allow the HSBP to be filled and bled. Additionally, a solenoid valve, connected to a reservoir, allows the internal pressure to be equalised. This prototype was used extensively in mechanical and thermal testing, and the relevant details of this testing are discussed in the final design of the HSBP presented in Chapter 4.

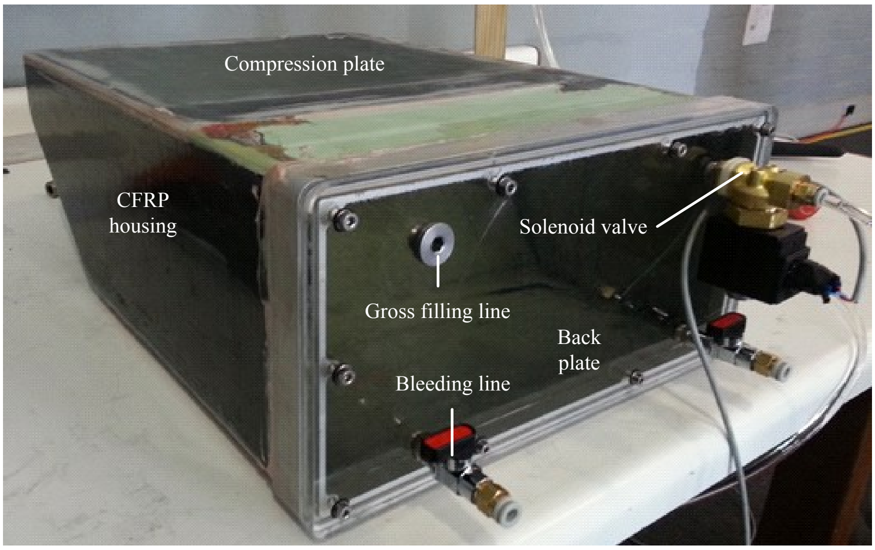

Figure 3.11: Prototype 3

3.5.3 PROTOTYPE 4 – COUPLING STACK TESTING

Prototype 4 is shown in Figure 3.12. The prototype is constructed from a low cost plastic container, which has been sealed with a stainless steel lid. In use, the container is filled entirely with couplant. An imaging window allows large and small compression plate samples to be tested. This system was used to test different couplants and compression plate materials. Once again, the relevant details of the testing are discussed in Chapter 4.

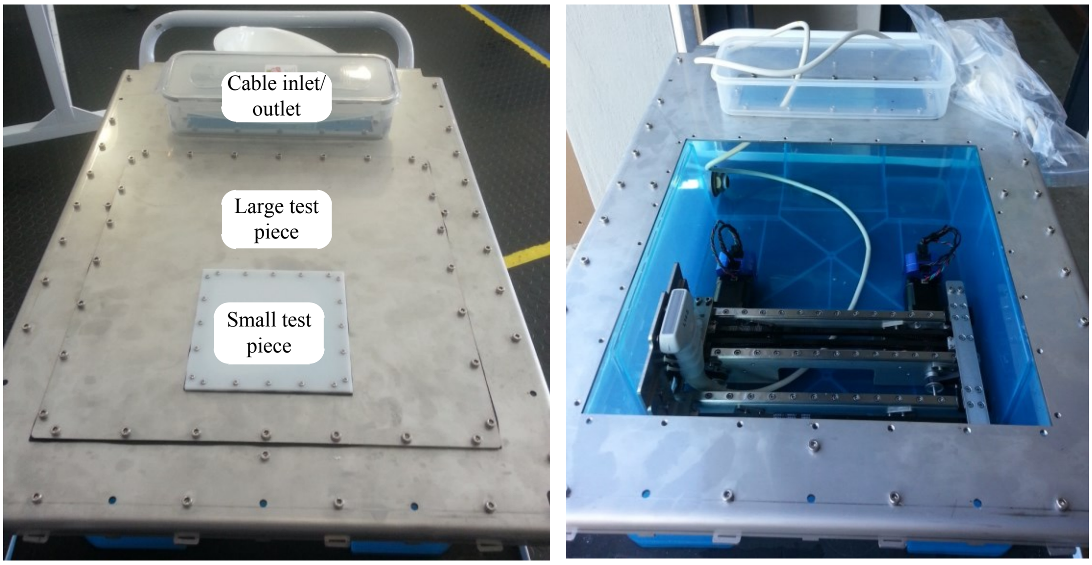

Figure 3.12: **Prototype 4. Left – the test rig is shown fitted with a small test piece. Alternatively it can accommodate a large test piece. Right – the test rig is shown with the test piece removed so as to show the internal scanning mechanism which was recycled from prototype 2.**

3.6 SUMMARY OF THIS CHAPTER

In section 3.2 the breast platform SRS was defined based on the information gathered in Chapter 2. The concept selection and prototyping process –which is summarised in Figure 3.13 – begins with the presentation of four potential design concepts in section 3.3. Concept 2 – a sliding seal – was selected for prototyping. However, the results of said prototyping (section 3.4) highlighted several issues which disqualified concept 2 and subsequently concept 3. With concept 1 rejected as unlikely to succeed, concept 4 – a hermetically sealed breast platform (HSBP) – was selected for prototyping, after de-risking the major concerns. A first prototype (2) demonstrated proof of concept. Subsequently, two further prototypes (3 & 4) were constructed to develop the mechanical design and optimise the coupling stack, respectively. All prototypes were used extensively throughout the design process and are discussed where appropriate in Chapter 4, wherein the final design of the HSBP is detailed.

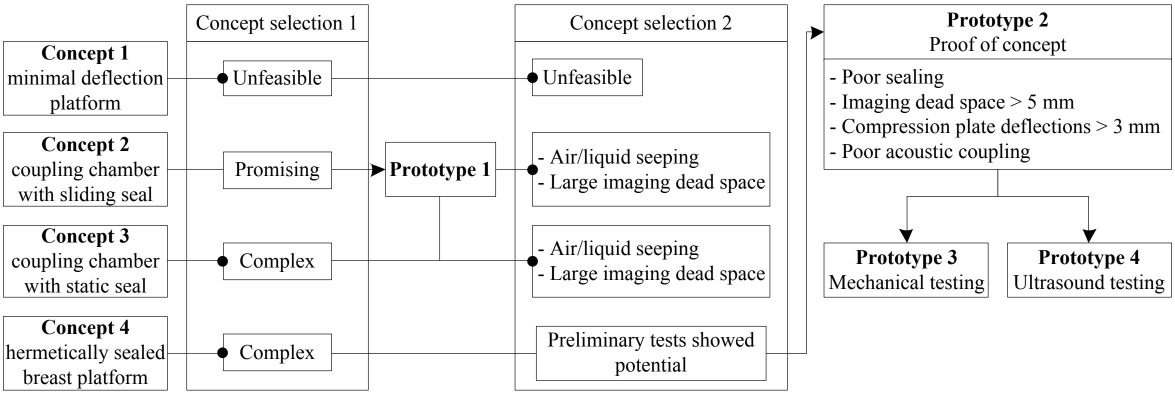

Figure 3.13: **Concept Selection and Prototyping Process**

Chapter 4: DETAILED DESIGN OF THE HSBP

4.1 STRUCTURE OF THIS CHAPTER

The final design of the HSBP is shown in Figure 4.1. It comprises five significant subsystems: (1) the rail carriage; (2) the housing; (3) the ultrasound carriage; (4) the Pandia carriage; and (5) the cable management chassis. The Pandia carriage and ultrasound carriage mount to, and are translated by, the rail carriage. The housing – featuring a TPX compression plate – is sealed posteriorly by a back plate. The back plate is the thoroughfare for all electrical and mechanical connections. The ultrasound carriage mounts the ultrasound transducer and multiplexing circuit board to the rail carriage. The Pandia carriage simply comprises the Pandia and a mounting bracket. Finally, the cable management chassis connects the rail carriage to the back plate and manages all dynamic and static cables.

The first three systems are discussed in sections 4.2, 4.3 and 4.4, respectively, while a discussion of the Pandia carriage and the cable management chassis is included in the description of the general assembly (section 4.5). The design process for each subsystem is the same as the design process for the HSBP as a whole. As such, the description of each subsystem is broken up into: system requirement specification; concept development and prototyping; and detailed design. Where appropriate, some sections are combined or curtailed for the purposes of concision.

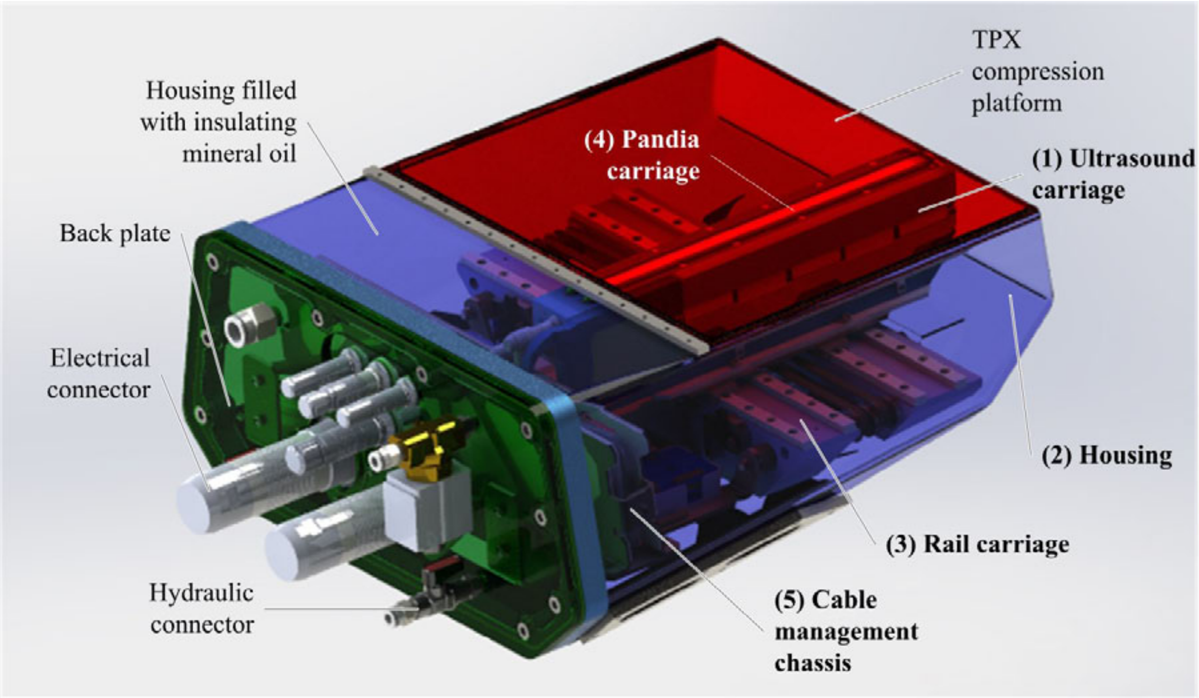

Figure 4.1: **Rear Isometric Rendering of the HSBP**

4.2 RAIL CARRIAGE

4.2.1 SYSTEM REQUIREMENT SPECIFICATIONS

The rail carriage must precisely and independently translate the Pandia and ultrasound carriages in the scan direction. The system requirement specification for the rail carriage is presented in Table 4.1

below[1]. Specifications requiring additional explanation are marked with an asterisk and explained below the table.

Table 4.1: Rail Carriage System Requirement Specification

Requirements		
No	Description	Inherits from
RCRE1	The rail carriage must independently and precisely translate the Pandia and the ultrasound transducer in the scan direction.	RE03
RCRE2	The rail carriage must function at C-arm angles between +180° and -180°.	RE05
RCRE3	The X-ray scanning speed must be >46 mm/s.	Inferred*
RCRE4	The rail carriage must precisely locate Pandia and ultrasound carriages relative to the HSBP housing.	CO03*
RCRE5	The HSBP must facilitate the duel-modality imaging of breasts with a compressed thickness of up to 8cm.	Defined by Aceso specifications
Constraints		
No	Description	Inherits from
RCCO1	The rail carriage assembly may not protrude beyond the front-edge of the X-ray and/or ultrasound carriages.	CO03*
RCCO2	The Pandia start position repeatability should be less than 20 µm.	Inferred*
RCCO3	All materials should be corrosion resistant.	Inferred*
RCCO4	EVA Robotics® stepper motor, encoder and controller stacks must be used as actuators.	Defined by Aceso specifications*
Criteria		
No	Description	Inherits from
RCCR1	The image quality should be optimised.	CR01
RCCR2	The imaging dead space should be minimised.	CR02
RCCR3	The ergonomics should be maximised.	CR03
RCCR4	Ease of assembly/maintenance should be maximized.	CR04
RCCR5	Ease of manufacture should be maximized.	CR05

RCRE3. The Pandia is a CCD detector implementing time-delay-integration (TDI) over each row of pixels (in the scan direction). As a result, the scanning speed of the detector must precisely match the clocking speed of the CCD. Failure to maintain the required speed will result in a reduction of image quality, due to blurring.

RCRE4 and RCCO1. Constraint CO03 states that the first active pixel of the Pandia must be within 5 mm of the outside front-edge of the HSBP. This constraint directly determines the allowable clearance between the Pandia and the inside front-edge of the HSBP housing. In section 4.3.3, this clearance is set at 0.5 mm. Such a small clearance requires the rail carriage to be precisely aligned to the inside front-edge of the housing to prevent collisions. The ultrasound carriage will also translate with 0.5 mm of the inside front-edge, so as to maximise the ultrasound imaging area.

RCCO2. Precise control of the Pandia's position is important in two respects. Firstly, any misalignment between the Pandia and the collimator will reduce the dose efficiency of the system (see section 1.1.4). Secondly, the flat-fielding process[2] requires the Pandia to start each scan in exactly the same position. With the CCD pixel size being 27 µm, the allowable uncertainty in the Pandia's position is limited to 20 µm.

RCCO3. Corrosion of materials inside the HSBP may release charge carrying particles into the non-conducting couplant which may damage the Pandia, ultrasound transducer and/or mechatronic systems.

---

[1] "RC" in the specification numbering is an abbreviation of rail carriage.

[2] Flat-fielding is a post-processing technique which corrects for the intensity distribution of the X-ray cone, differences in CCD pixel gain, and any other constant imaging artefacts.

RCCO4. The control system architecture of the Aceso requires the use of the *motor encoder driver* stacks from EVA Robotics®.

4.2.2 DETAILED DESIGN

Figure 4.2 shows the rail carriage assembly with some of the major components labelled. The Pandia drivetrain is shown in blue and the ultrasound drivetrain is shown in green. The scan direction is dictated by the TDI electronics of the Pandia. When viewing the machine from the front, the Pandia must move from right to left. Additionally, the workflow of the Aceso is such that the ultrasound scan takes place before the X-ray scan; hence, the ultrasound carriage is to the left of the Pandia carriage. This arrangement allows the radiographer to comfort the patient for as long as possible before retreating behind the radiation protection screen, for the exposure. Additionally, the X-ray tube can spin up during the ultrasound scan, thereby reducing the total breast compression time and minimising patient discomfort.

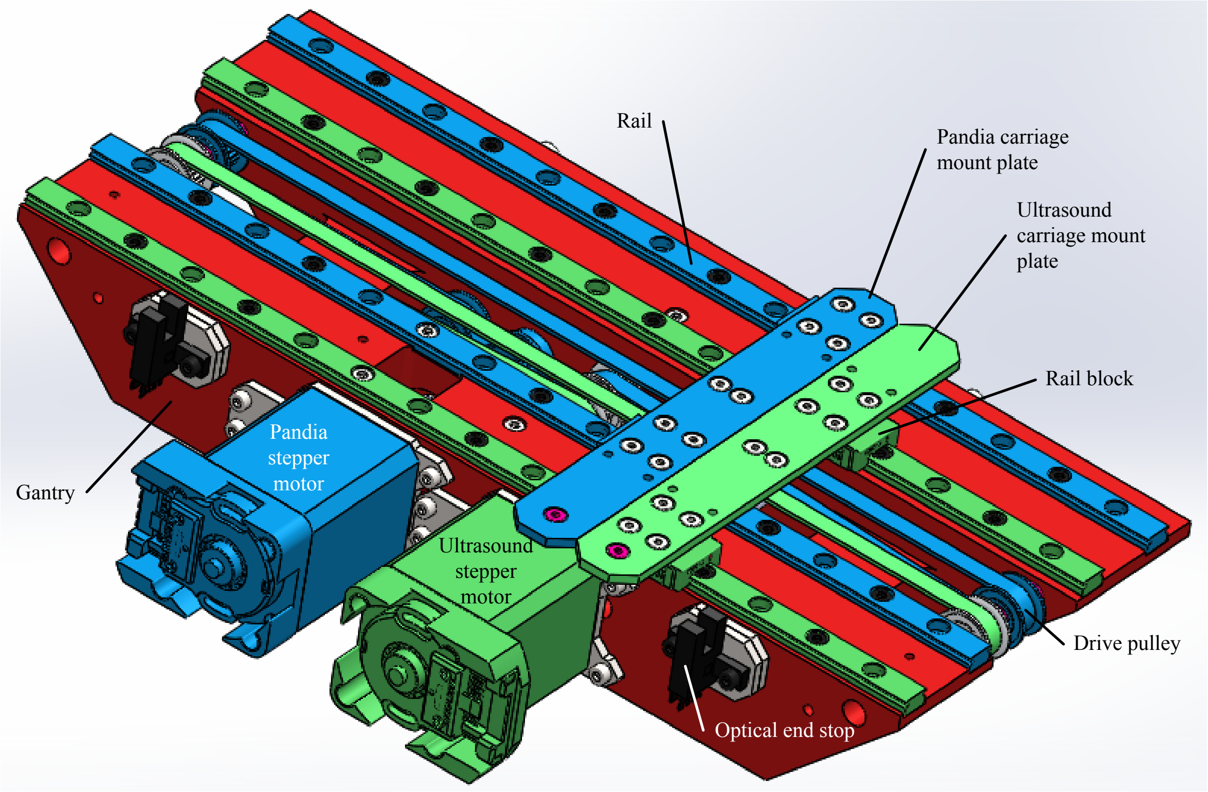

Figure 4.2: **Rail Carriage Assembly**

The drivetrains are required to convert the rotation of the stepper motors into the translation of the Pandia and ultrasound carriages. Worm gear drivetrains are typically used for this purpose. However, worm gears require the motor to be placed in line with the drivetrain which would result in an unacceptable lateral imaging dead space. The use of gears to reposition the motor relative to the worm gear was considered, but avoided due to the associated backlash – which is in conflict with RCCO2. Ultimately, a belt and pulley drive system was selected, which achieved the necessary conversion of rotation to translation with zero backlash and minimal imaging dead space. Figure 4.3 is a front view of the symmetrical drivetrain. Again, the Pandia drivetrain is in blue and the ultrasound is in green.

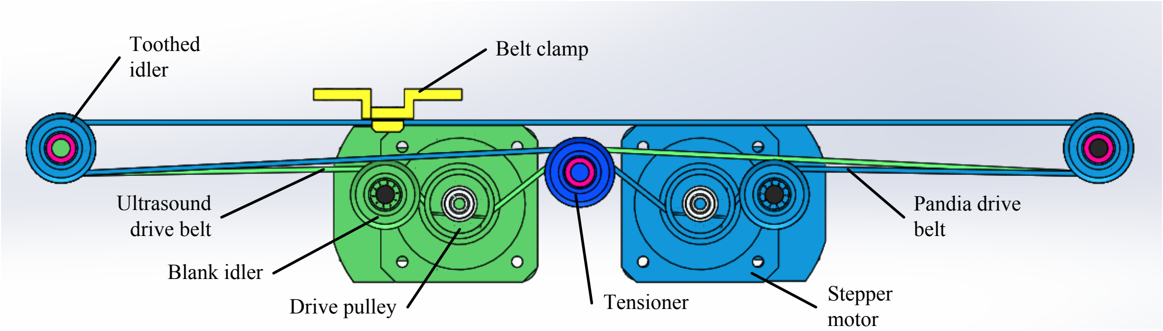

Figure 4.3: **Rail Carriage Drivetrain Front View**

Figure 4.3 and Figure 4.4 show the ultrasound drivetrain staggered behind the Pandia drivetrain. The blank idlers and the tensioner work together to ensure that at least six drive-pulley teeth make contact with the drive belt. This is the contact ratio recommended by the design manual.

Each drivetrain is connected to its respective mount plate by a belt clamp. The belt clamp also connects the two open ends of the discontinuous drive belt. Commercially available belt clamps typically grip five teeth at each end. However, this custom clamp only holds two teeth per end. The size of the belt clamp was minimised to reduce the imaging dead space. To verify the strength of the design, 100 N of tension was applied to the belt. The clamp arrangement did not fail under this load, which exceeds the operational conditions by a significant safety factor. Further to this, the Aceso control system software implements checks to ensure the belt clamp has not failed.

Although the use of stepper motors is a high level constraint, they suffer from characteristic vibrations (Guangxian et al., 2002). This may affect the performance of the CCD, due to TDI related blur. Preliminary imaging with prototype 2 showed that the effect of the vibrations could be eliminated by careful tuning of the controller gains. Hence, it was decided not to investigate alternate solutions. Nevertheless, a flexible couple is included to reduce the transmission of vibrations from the stepper motor to the drivetrain and to take up any misalignment between the motor and the drive shafts. Eccentricity due to misalignment plagued the rail carriage developed for prototype 2, resulting in X-ray image striping.

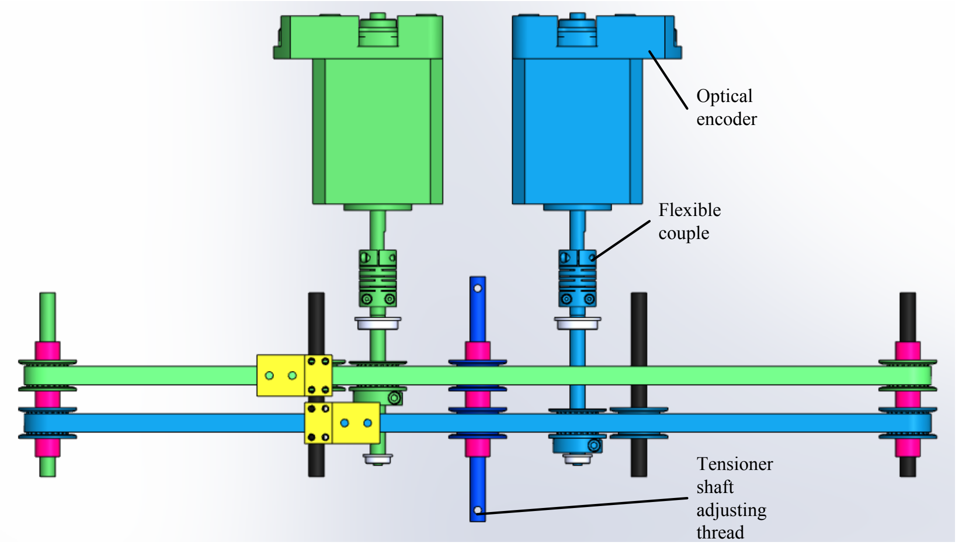

Figure 4.4: **Drivetrain Top View**

The stepper motors are mounted to the gantry via motor mount plates shown in yellow in Figure 4.5. In conjunction with the access cut-out, this allows the motors to be easily removed as per criterion RCCR4 (ease of assembly and manufacture).

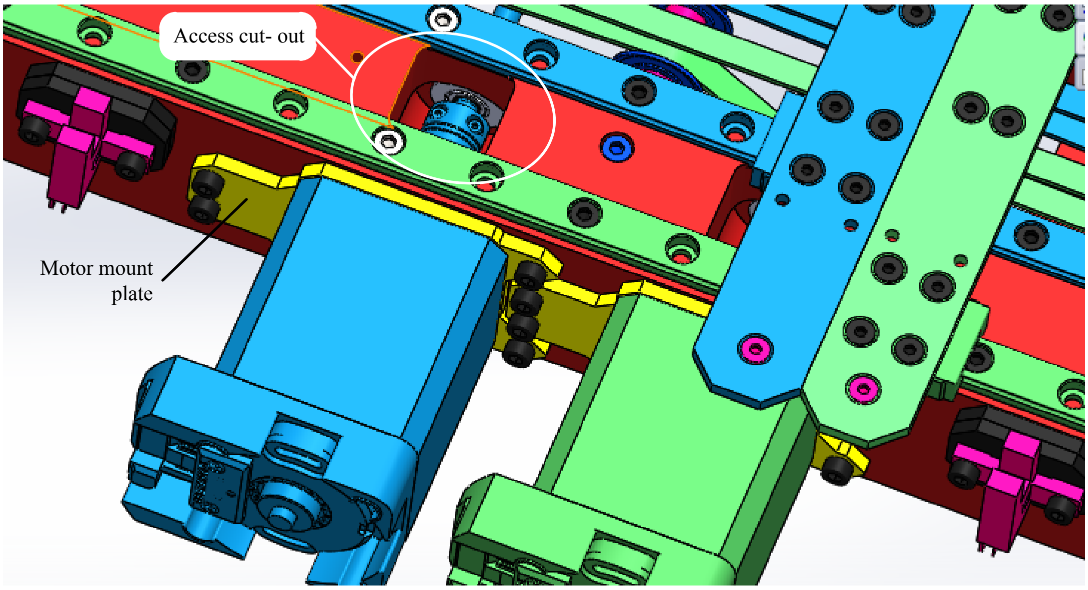

Figure 4.5: **Rail Carriage Motor Mount Plates and Access Cut-out**

Also in line with RCCR4 is the idler shaft assembly shown in Figure 4.6. The shaft slides into the gantry from the right with a sliding fit. Vesconite spacers and idlers are added and the shaft passes into the far side of the gantry. A grub screw is then used to hold the shaft in place. The idlers have built-in roller-pin bearings and do not rely on rotation of the shaft. Vesconite spacers are not necessary on the lower idlers as they are sufficiently close to the axially located drive pulleys (see Figure 4.3 and Figure 4.4).

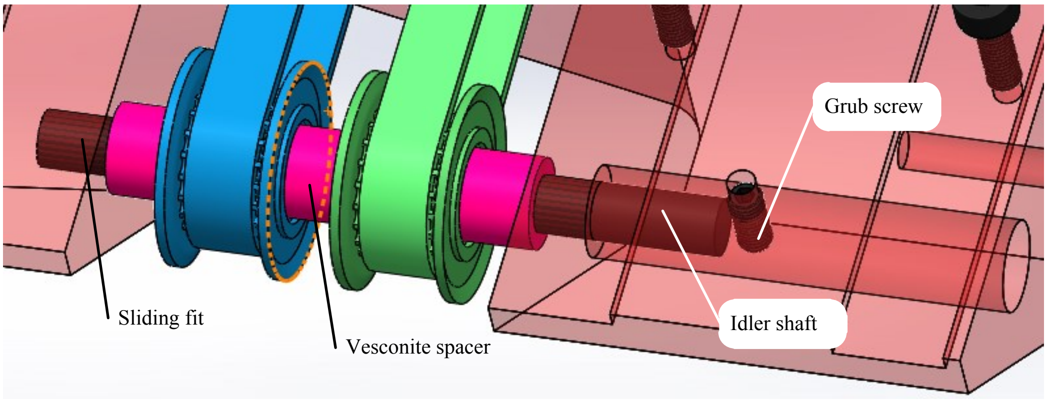

Figure 4.6: **Idler Shaft Assembly**

The assembly of the drive shaft is similarly simple (see Figure 4.7). The drive shaft, fitted with the circlip and the larger flange bearing, is inserted into the gantry from the left. It then slides through the drive pulley and the smaller flange bearing into the far side of the gantry. Finally, the drive shaft assembly is axially located by the flexible couple, which in turn is located by the motor shaft. All fits are sliding fits for ease of assembly.

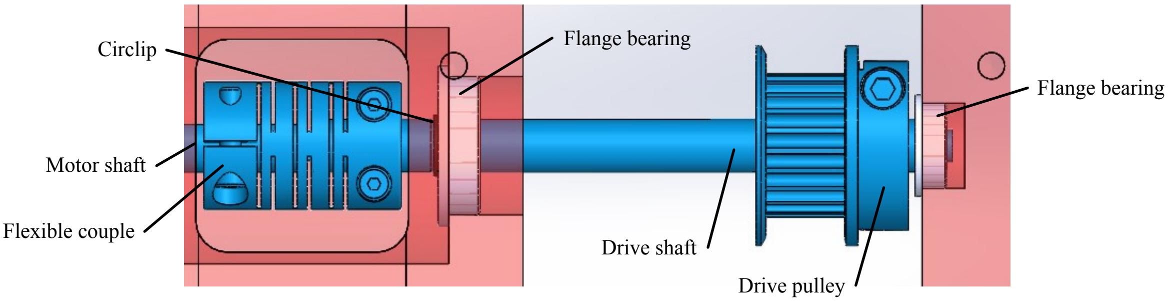

Figure 4.7: **Drive Shaft Assembly**

Figure 4.8 shows an exploded view of the toothed and blank idler assemblies. The idlers allow the two drive belts to move at different velocities while sharing a shaft. This design feature significantly reduces the lateral imaging dead space. To prevent vibrations of the drive belt, toothed stock is used where the idler runs on the toothed side of the belt and vice-versa.

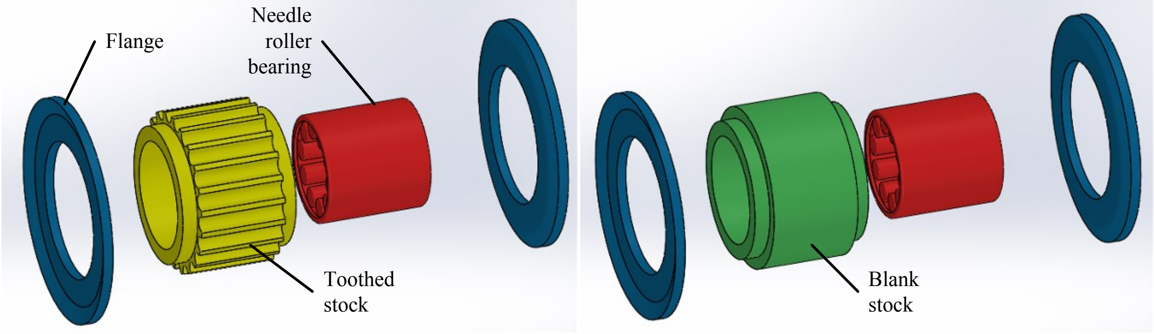

Figure 4.8: **Toothed and Blank Rail Carriage Idler**

Figure 4.9 shows the belt tensioner assembly which tensions both belts equally. The tensioning shaft is threaded at either end and is raised or lowered by rotating the adjusting screws. This in turn tensions or releases the drive belts. The tensioning shaft slides up and down, guided by a precision slot in the gantry. In addition, a support plate and locking nut prevents unwanted movement of the tensioning shaft. Movement of the shaft could introduce unacceptable backlash into the drivetrain.

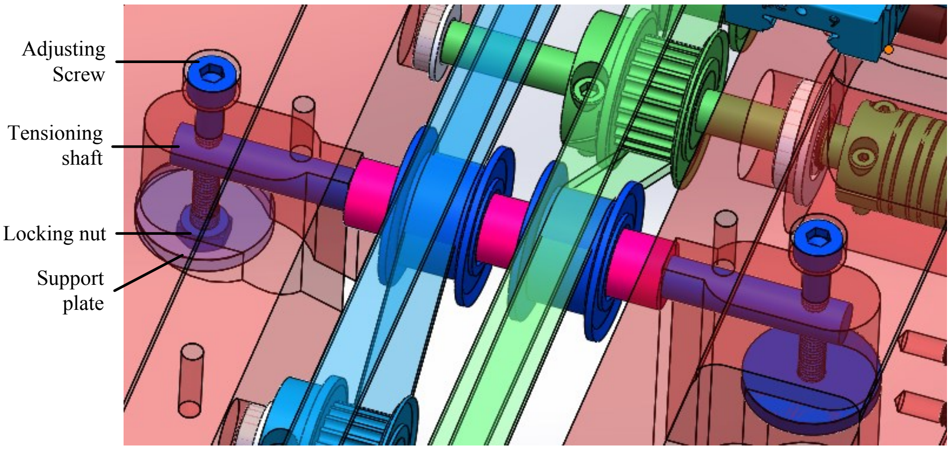

Figure 4.9: **Tensioner Assembly**

Figure 4.10 shows the mount plates for the Pandia and ultrasound carriages. Each mount plate connects its respective carriage to the corresponding rail blocks and belt clamp. The width of the mount plates has been designed to prevent collisions between the Pandia and ultrasound transducer, while simultaneously minimising the imaging dead space between the two detectors. Because the rail blocks are wider than the mount plates, four were used instead of two. This reduced the lateral imaging dead space by 10 mm.

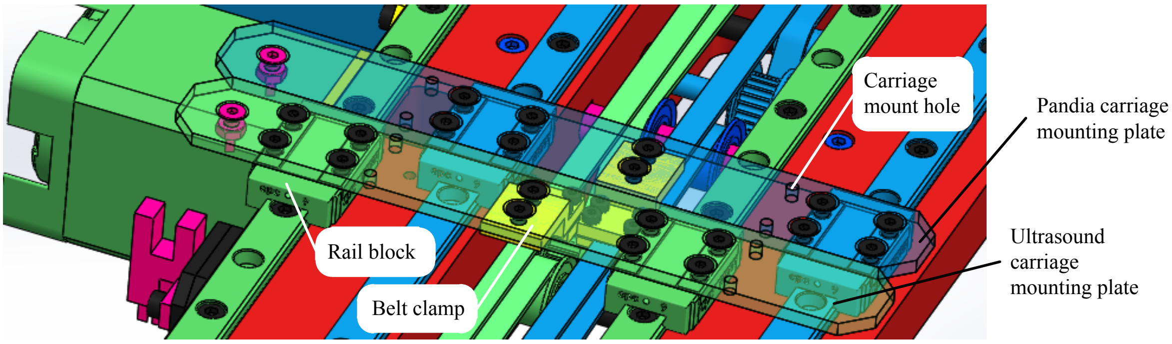

Figure 4.10: Carriage Mount Plates

A mechanical limit switch was used in prototype 2 as an absolute position reference. However, it was found to have an unacceptable uncertainty of more than 1 mm. Hence, optical end-stops were implemented in the final design, as shown in Figure 4.11. A modified M3 x 10 mm machine screw is used to trigger the end-stop. A triangular profile was added to the screw to ensure repeatable triggering (RCCO2).

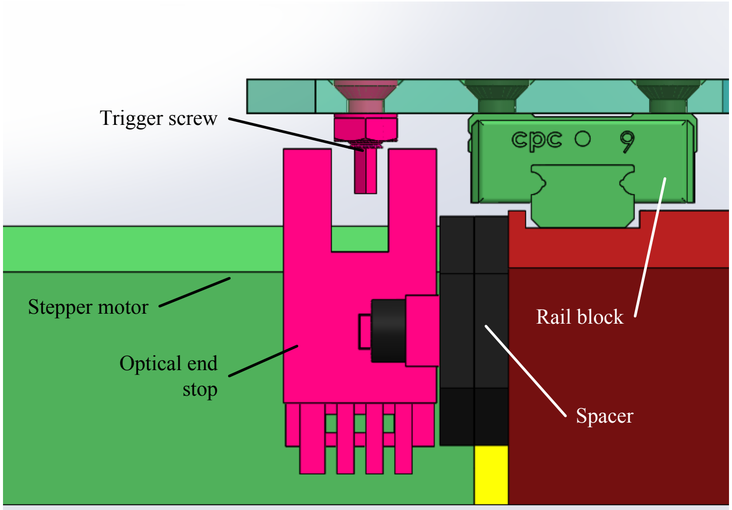

Figure 4.11: Optical End Stop

Figure 4.12 shows a bottom-front view of the rail carriage gantry. The gantry mounts to the HSBP housing with four fasteners on two reference surfaces. The fasteners pass through the HSBP CFRP housing and O-rings are used to maintain the hermetic seal. Figure 4.12 shows the O-ring seats on the two reference surfaces. The upper (pink) and lower (blue) surfaces are precision references. The upper surface ensures the Pandia and ultrasound transducer do not collide with the inside front-edge of the HSBP housing, while the lower surface ensures the scanners clear the underside of the compression plate. As per RCRE4 and RCCO1, the internal front-edge clearance is 0.5 mm, nominally. The lower reference surface has a perpendicular tolerance of 0.1 mm with respect to the upper surface. The mating surfaces in the HSBP housing have the same tolerance. This yields a positional uncertainty of

±0.4 mm, thereby ensuring a real-world clearance of at least 0.1 mm. Adjustment in the final position of the scanners using precision spacers makes this small clearance feasible.

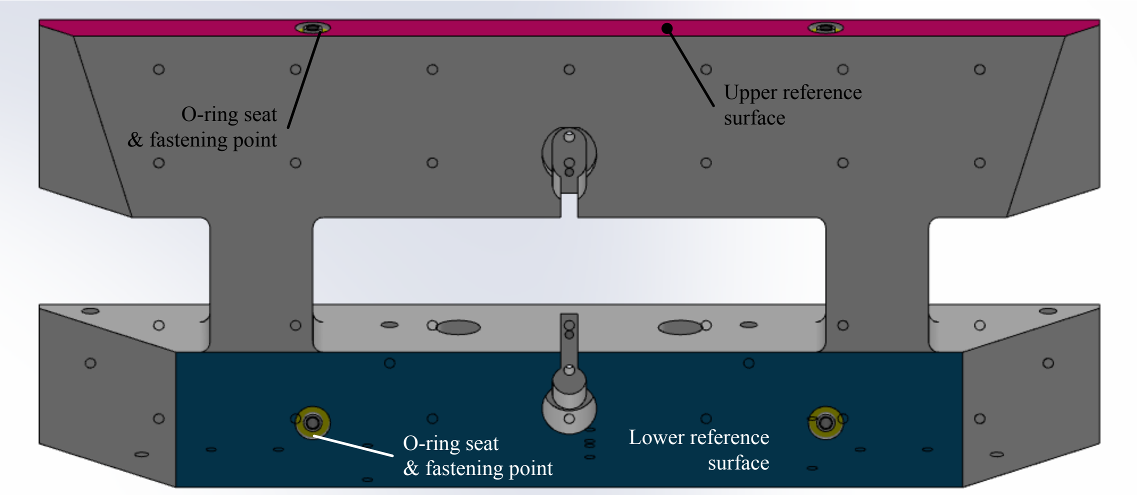

Figure 4.12: **Rail Carriage Gantry Bottom/Front View**

To ensure the Pandia and ultrasound carriages translate perfectly parallel to the upper reference surface – a necessity with 0.1 mm of clearance – the rail reference surfaces and the upper reference surface are machined in the same machining operation (see Figure 4.13).

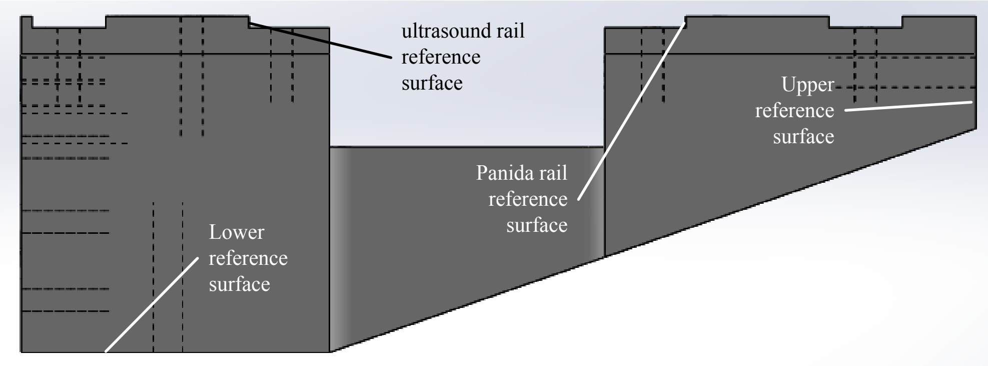

Figure 4.13: **Rail Carriage Gantry Side View**

The form factor of the gantry is designed to optimise the ergonomics of the HSBP. A particular example is the chamfers on the underside of the gantry. These significantly reduce the size of the HSBP – especially at the front-edge – while also ensuring the carriages can scan across the width of the compression plate. The optimisation of the gantry's depth and breadth was limited by the depth of the stepper motors and the cumulative breadth of the rail blocks and belt clamps, respectively (see Figure 4.10).

The torque sizing of the actuators is discussed next. To size the stepper motors the worst case loading scenario was considered. This occurs with the C-arm at ±90° at the end of the acceleration period when gravitational, inertial, fluid drag and cable forces are at a maximum (buoyancy is neglected).

The ultrasound carriage was used in the analysis as it is heavier than the Pandia carriage and, having a larger frontal area, is subjected to a large drag force. Because the ultrasound carriage runs ahead of the Pandia carriage, its maximum speed will be equal to that of the Pandia (46 mm/s), in the case of an

X-ray-only scan. Based on testing of Soteria and prototype 2, an acceleration of 240 mm/s^2 was used in the analysis.

At the time of design, the mass of completed ultrasound carriage was unknown. Hence a conservative estimate of 550 g was used. The frontal area of the ultrasound carriage is 0.0182 m^2 and the force required to translate the ultrasound cables was experimentally estimated at 5.5 N.

Computational fluid dynamics (CFD) was used to estimate the drag force on the ultrasound carriage. Figure 4.14 shows the simplified two-dimensional (2D) model that was used. The 2D slice represents a top view of the HSBP. In simplifying the model to the 2D case, it is implied that there is no fluid flow above or below the probe. This assumption adds a conservative safety factor. The analysis yielded a drag force of 6.5 N per metre of thickness into the page. A python script (see Appendix A) was used to validate the CFD and compute the required torque of 0.08 Nm, as tabulated in Table 4.2.

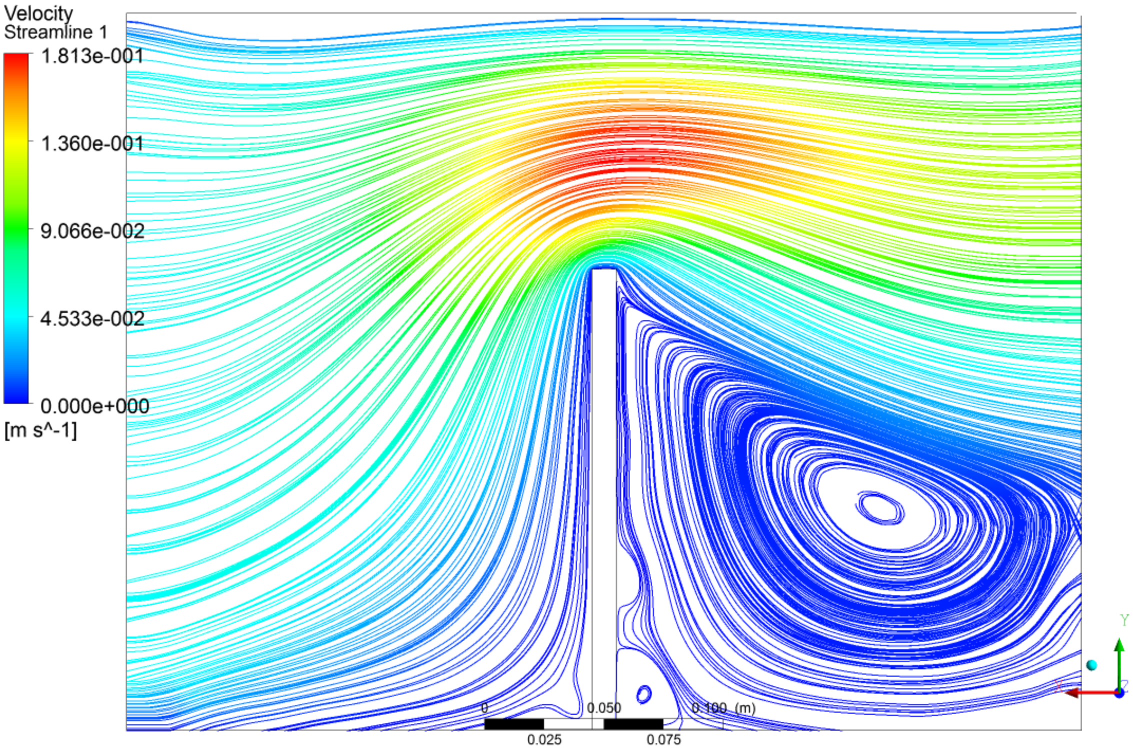

Figure 4.14: **CFD Analysis of the Drag Force on the Ultrasound Carriage**

Table 4.2: **Motor Sizing Calculation Results**

Variable	Value
Weight	5.4 N
Inertia	0.13 N
Fluid drag	0.42 N
Cable load	5.5 N
Total load	11.45 N
Required Torque	**0.08 Nm**

From the EVA Robotics® collection, the EvoDrive ST-17 motor-encoder-controller stack is used extensively in Aceso. Hence, it was the actuator of choice for the rail carriage. The torque-speed curve for the ST-17 is shown in Figure 4.15. At the required drive speed of 62.8 rpm (46 mm/s), the drive can supply approximately 0.4 Nm of torque. This exceeds the requirements by an order of magnitude. Nevertheless, a smaller EVA Robotics stack was not available at the time and so the ST-17 was implemented.

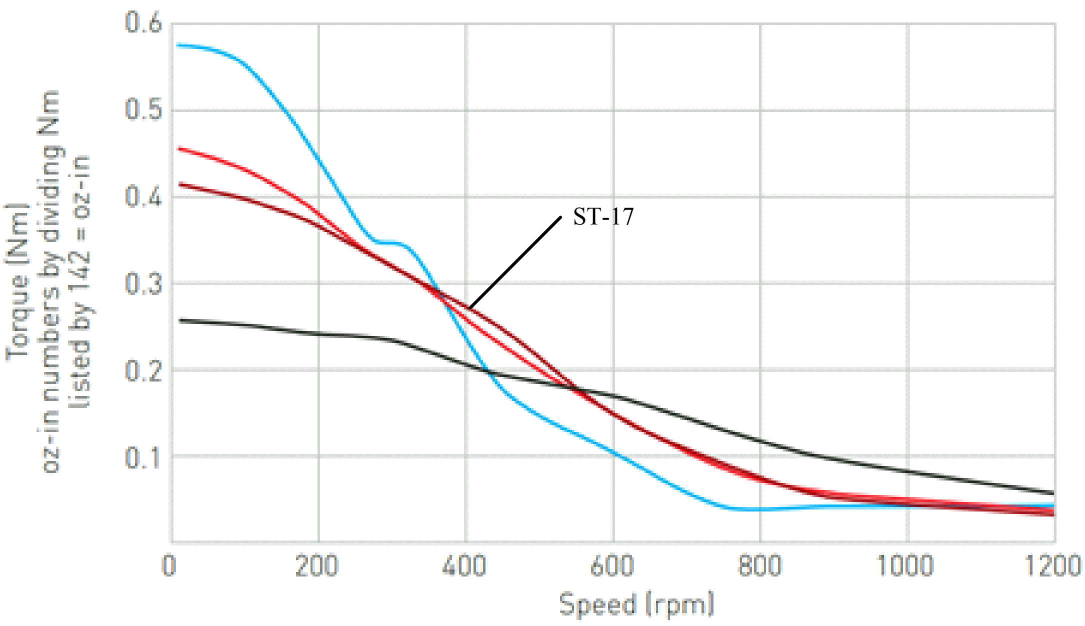

Figure 4.15: EvoDrive ST-17 Torque-Speed Curve (Reproduced from EVA Robotics, 2013).

As a conclusion to the design of the rail carriage, the choice of materials is briefly discussed. As per constraint RCCO3, all machined and sheet-metal components are non-corrosive stainless steel 403 or aluminium 6082. Being a preproduction prototype, the fasteners are expected to be removed and replaced on a regular basis. For this reason, stainless steel was selected for all threaded components. A few exceptions were made where weight and/or machining costs were of primary importance. The rail carriage gantry is an exemplary component that required extensive machining and was hence made from aluminium. Sheet metal components were made from stainless steel, which allows for smaller holes, tighter bend radii and more robust threads, when compared to aluminium. All fasteners are stainless steel.

The final design of the rail carriage built on the successes and failures of the prototype 2 rail carriage. As such, it was expected to perform well with minimal issues. The physical specifications of the rail carriage are given in Table 4.3 below.

Table 4.3: Rail Carriage General Physical Specifications

Variable	Value
Weight	4 kg
Width	310 mm
Height	56.5 mm
Depth	194.5 mm

4.3 HSBP HOUSING

4.3.1 SYSTEM REQUIREMENT SPECIFICATIONS

The HSBP housing must form the lower compression surface, as well as hermetically contain the non-conductive coupling fluid, provide suitable mountings for the internal systems and provide a means of mounting the HSBP to the C-arm. The system requirement specification is given in Table 4.4 with additional explanations provided below.

Table 4.4: HSBP Housing System Requirement Specifications

Requirements		
No	Description	Inherits from
HSRE1	The housing must form the lower breast compression surface, supporting breast compression up to 200 N.	RE01
HSRE2	The housing must hermetically contain the non-conductive coupling fluid.	Inferred*
HSRE3	The housing must provide suitable mountings for internal systems.	Inferred
HSRE4	The housing must provide a means of mounting the HSBP to the C-arm	Inferred
HSRE5	The compression platform must have dimensions 300 x 240 mm.	Defined by Aceso specifications
Constraints		
No	Description	Inherits from
HSCO1	The housing may not leak.	Inferred*
HSCO2	The first active pixel of the Pandia must be no more than 5 mm from the outside front-edge of the housing.	Inferred
HSCO3	The housing must continue to support compression in the event of a power failure.	Inferred*
HSCO4	The deflection of the compression plate may be no more than 3 mm.	Inferred*
HSCO5	The HSBP operating temperature range is 10ºC to 40ºC.	CO05
HSCO6	The HSBP shipping temperature range is -10 ºC to 40 ºC.	CO06
Criteria		
No	Description	Inherits from
HSCR1	The presence of air bubbles and other particles inside the filled housing must be minimised.	Inferred
HSCR2	The image quality should be optimised.	CR01
HSCR3	The imaging dead space should be minimised.	CR02
HSCR4	The ergonomics should be maximised.	CR03
HSCR5	Ease of assembly/maintenance should be maximized.	CR04
HSCR6	Ease of manufacture should be maximized.	CR05

HSRE2 and HSCO1. Because the C-arm can be rotated through ±180° it is essential that there is absolutely no air in the HSBP. The presence of any air may lead to bubbles which would create X-ray and ultrasound imaging artefacts.

HSCO3. The standards governing mammography do not allow for the automatic release of compression in the event of a power failure. The importance of this requirement is made clear in the course of this section.

HSCO4. As discussed by Shmulewitz (see section 2.6.3), deflections of more than 1° cause spatially varying refraction artefacts that cannot be corrected by ultrasound beam-forming. For a 300 mm compression plate, the 1° limit is equivalent to a maximum deflection of ~3 mm. Additionally, the Pandia must clear the compression plate by an amount equal to the deflection. A large clearance would attenuate the X-rays and exacerbate the geometric magnification[1].

4.3.2 CONCEPT DEVELOPMENT

Figure 4.16 shows the final housing design with all the major components labelled. The compression plate is bonded to the CFRP housing and a cross-brace is added to increase the rigidity of the assembly. Mount plates are bonded to the CFRP to facilitate the mounting of the HSBP to the C-arm. The CFRP is supported posteriorly by the seal rim, which also mates to the transparent back plate. The back plate is fitted with various hydraulic (blue) and electrical (pink) connectors.

---

[1] Geometric magnification is caused by the divergence of X-rays from a point source. It is analogous to the size of a shadow increasing as the subject moves closer to the light source.

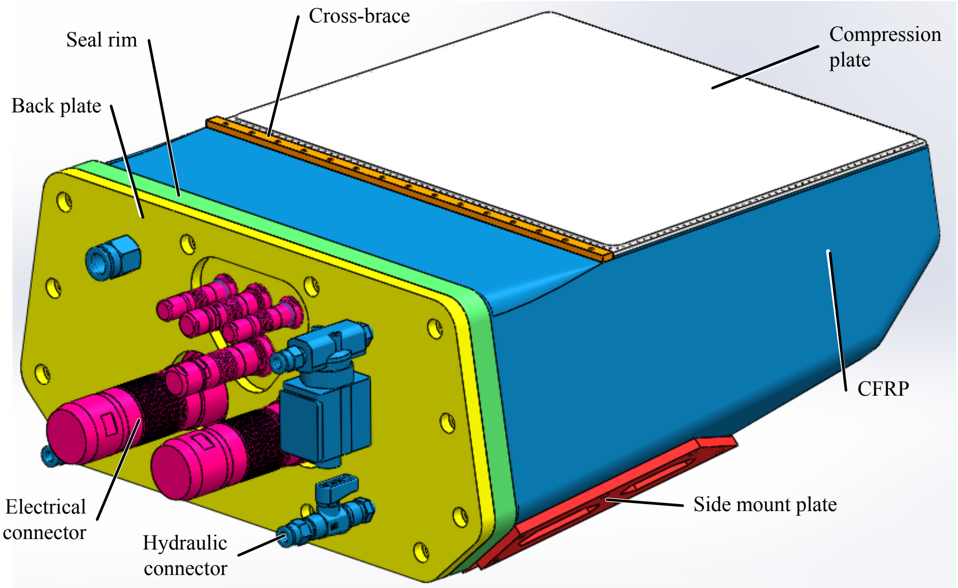

Figure 4.16: Housing Schematic

The starting point for the design of the housing system is the compression plate material. As discussed in Chapter 2, the X-ray, ultrasound and mechanical systems place conflicting requirements on the material properties of the compression plate. This conflict is represented graphically in Figure 4.17. As shown, optimal X-ray, ultrasound and mechanical characteristics cannot be achieved in a single material. However, some materials perform well in at least two respects.

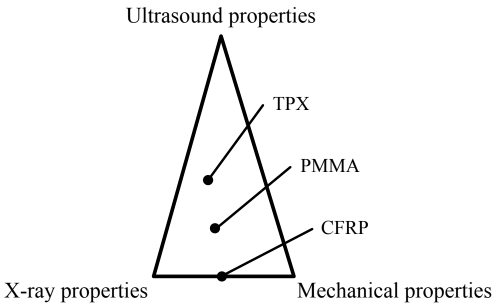

Figure 4.17: Compression Platform Material Optimisation Problem

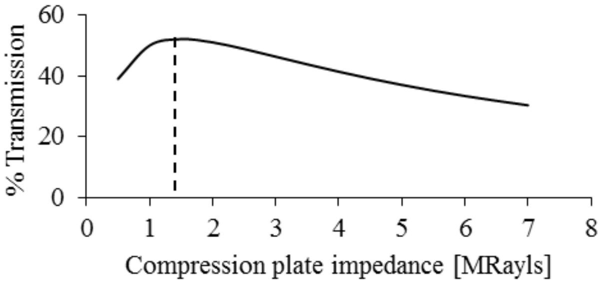

Figure 4.18: Plot of Transmission versus Compression Plate Acoustic Impedance

In preliminary testing, X-ray attenuation was found to be insignificant for most prospective materials, and their mechanical suitability was easily evaluated by inspection. However, determining the ultrasonic suitability of materials proved more complex.

Figure 4.18 shows the variation of the transmission coefficient as a function of the acoustic impedance of the compression plate. The transmission coefficient has been computed for ultrasonic waves on a round-trip from the transducer into the breast and back[1]. With the maximum transmission occurring at ~1.5 MRayls, the Laust Pedersen tables were used to identify potential compression plate materials. Although the attenuation coefficient and speed of sound were also considered, the reflective losses where quickly identified as the most pertinent consideration. Samples of several materials were

---

[1] This computation is based on the coupling stack in Figure 4.19 and formula (2.5).

acquired; however, TPX was quickly identified as the only material with acceptable mechanical rigidity. In addition to TPX, two further materials – CFRP and polymethyl methacrylate (PMMA or Perspex) – were selected for ultrasonic testing.

Breast compression plates are typically constructed from CFRP owing to its low X-ray attenuation and high stiffness. The stiffness allows for thin, rigid compression plates, reducing attenuation and geometric magnification. As indicated in Figure 4.17 and Figure 4.18, CFRP – with Z ≈ 7 MRayls – was not expected to perform well ultrasonically. Nevertheless it was decided to evaluate its suitability experimentally, owing to its X-ray, mechanical and manufacturing suitability.

PMMA is a readily available plastic offering low X-ray attenuation and relatively high mechanical strength. Ultrasonically, it performs better than CFRP with an acoustic impedance of Z ≈ 3 MRayls. Hence, it too was experimentally evaluated.

TPX is costly, difficult to manufacture and only available from international suppliers, in inconvenient thicknesses (<1 mm or >9 mm). Nevertheless, the literature and theoretical computations (Z ≈ 1.8 MRayls) suggested it was the only suitable material, and a TPX sample was acquired for experimental testing.

To assess the ultrasonic performance of each material, a custom ultrasound phantom was designed in collaboration with CIRS phantom manufacturers (Norfolk, Virginia USA). The custom phantom was necessitated by the problem of ultrasonic reverberations. Reverberations are caused by large reflections – due to poorly matched acoustic impedances – on both sides of the breast compression plate. This causes ultrasound waves to bounce back and forth within the compression plate, creating several versions of objects in the resulting ultrasound image. The acoustic impedance of standard ultrasound phantoms is typically designed to mimic breast *tissue* rather than breast *skin*. Hence, to properly evaluate the performance of the compression plate, a phantom was procured with a replaceable 2 mm thick skin-mimicking surface (see Appendix B).

The experimental setup for the ultrasonic materials testing is shown in Figure 4.19. The illustrated coupling stack is designed to replicate the clinical scenario (albeit upside-down). The urethane mimics mineral oil (the coupling fluid), the Zerdine mimics breast skin, and the phantom mimics breast tissue. The acoustic properties of the respective materials are listed in Table 4.5.

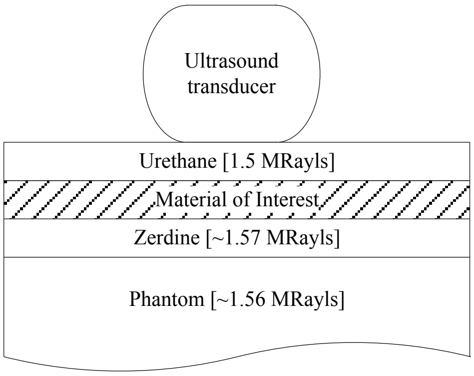

Figure 4.19: Compression Platform Ultrasound Testing Setup

Table 4.5: Acoustic Properties of Relevant Materials (Pedersen, 1999)

Material	Acoustic impedance [MRayls]	Acoustic attenuation [dB/cm/MHz]
Breast skin	1.57	0.7±0.7
Breast tissue	≈1.6	0.7±0.3
Urethane	1.5	0.5±0.3
Zerdine	1.57	0.5
CIRS phantom	1.56	0.5
Mineral oil	1.44–1.46	0.4
Perspex	3.1	0.64
TPX	1.8	2.92
CFRP	≈7.04	0.24

Figure 4.20 shows the results of the experimental testing of the three materials[1]. The leftmost image is a control with no compression plate present. The TPX case results in only a single reverberation. However, extensive reverberations result in the case of PMMA and CFRP. The reverberations have the additional effect of significantly attenuating the ultrasound. The reduction in penetration depth (see section 2.4.3) is approximately equal for all three materials even though the TPX is 6.5 mm thicker than the PMMA, and 8 mm thicker than the CFRP. These results are in agreement with the values in Table 4.5.

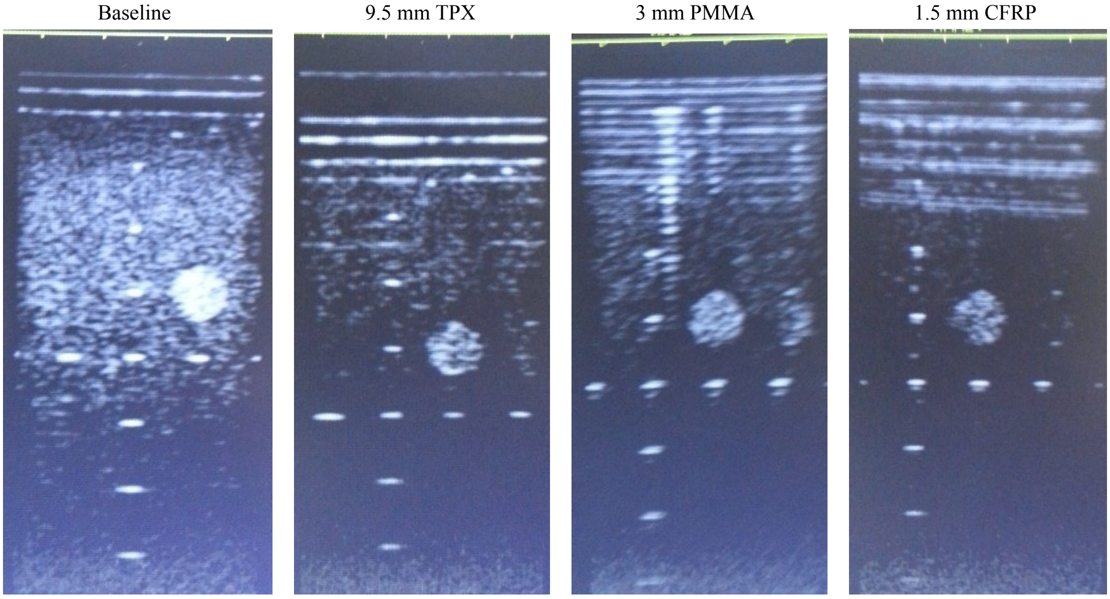

Figure 4.20: Ultrasound Scans Through Four Different Materials Using the Customised CIRS 40GSE Phantom

Based on these results it was clear that TPX was the only suitable platform material if high quality ultrasound was to be achieved. However, the ultrasonic attenuation of TPX is particularly high; and four times greater than breast tissue (see Table 4.5). To counteract this, the thickness of the compression plate would need to be minimised and the power of the ultrasound would likely need to be increased.

---

[1] These tests were performed at 8.5MHz using a Well. D WED-3100 ultrasound system and a L1-5 linear transducer.

The choice of coupling fluid was also studied. White pharmaceutical oil (mineral oil) is non-conducting, colourless, odourless, edible and acoustically suitable ($Z \approx 1.44$ MRayls). Also, it is conveniently available, at low cost, from local suppliers. The oil is available in two viscosities: 15 (low viscosity) and 68 (high viscosity). According to the Laust Pedersen tables the higher viscosity has a slightly higher acoustic impedance ($\Delta Z = 0.02$ MRayls). Therefore, the high viscosity oil was expected to perform better in terms of reflective losses. However, experimental testing showed that the low viscosity oil offered less cumulative attenuation (see Figure 4.21) and it was therefore selected as the HSBP coupling fluid.

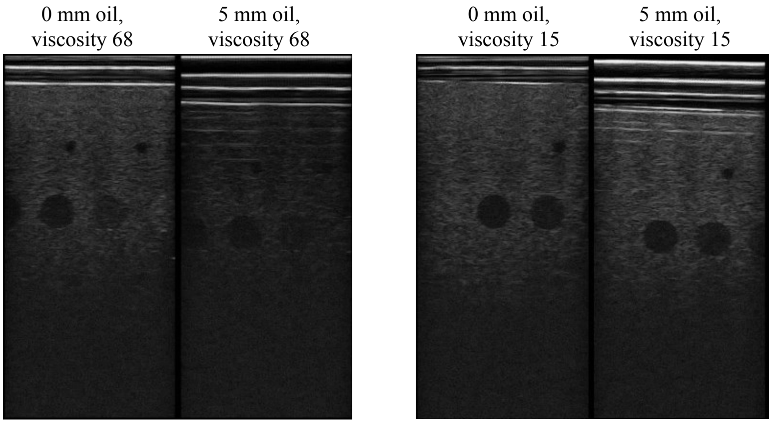

Figure 4.21: Effect of Mineral Oil Viscosity on Ultrasound Image Quality

To validate the choice of materials for the coupling stack the TPX and oil were X-rayed[1]. Figure 4.22 shows an X-ray of a sample of TPX. Both a 2 mm step and a 9.5 mm step in the TPX thickness are shown. The 2 mm step is barely visible, while the 9.5 mm step can only just be discerned. It was thus concluded that the TPX attenuation of X-rays is acceptable. Similar X-rays were acquired of the mineral oil but there was no obvious attenuation.

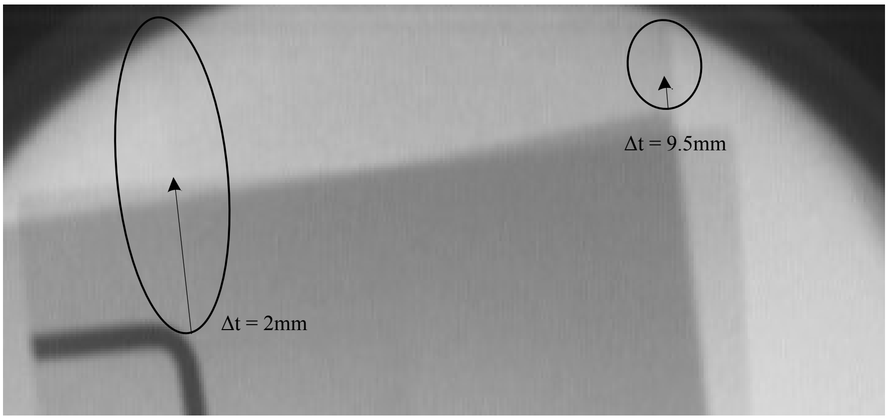

Figure 4.22: TPX Attenuation of X-Rays

The next consideration was the housing material. The 5 mm dead space limit (HSCO2) was a determining factor in this regard. The Pandia has a front-edge dead-space of 3.5 mm and a further 0.5 mm of clearance is required between the Pandia and the inside front-edge of the housing. Hence,

---

[1] A fluoroscopy machine (SIREMOBIL 4E from Siemens) was used to acquire the X-rays at unknown kV and mA values.

the maximum thickness of the front-edge of the housing is 1 mm. This is further reduced to 0.5 mm when the need for an aesthetic coat of paint is considered. CFRP was selected as the most suitable material due to its high strength, manufacturability, and chemical resistance. It has the additional and necessary advantage of being air-tight.

While both TPX and CFRP are impermeable to liquid and gas, creating an equally impenetrable bond between the two materials proved challenging. The most intuitive method of joining the two materials is a glued bond and this approach was used on prototype 3. At the time, it was already known that TPX was notoriously difficult to bond. With this in mind, the adhesives manufacturer Loctite® was consulted. They recommended a two-part primer and adhesive solution (Loctite® 770 and 401, respectively). At first, breast compression testing of prototype 3 indicated that the adhesive was successful. However, in later thermal testing, the temperature of the prototype was raised to 40°C and the bond began to fail. In further tests and consultation it was discovered that TPX exudes small quantities of oil at temperatures above 30°C. This oil caused all tested adhesive bonds to fail. The list of adhesives tested includes: the specialised adhesive from Loctite®; hot glue; epoxy resin; and urethane. All of these, and many others, easily pushed off by hand, at temperatures above 30°C. Other more exotic bonds were considered, including the development of a custom adhesive and using sonic welding. However, the Aceso project timeline did not allow for the necessary development time and a mechanical seal was selected as a more pertinent and robust solution.

It was decided that an O-ring would be used to make the hydraulic seal between the TPX and CFRP. However, a means of compressing the O-ring between the CFRP and TPX was required. At the front-edge, the bond volume was constrained to a tiny 4.5 x 8 x 310 mm channel; the result of the 5 mm dead space limit and geometric magnification considerations. Various clamping solutions were considered. Rivets and screws were considered first but rejected due to insufficient space and overloading of the materials. Custom CFRP hooks were also considered and even prototyped with limited success (Figure 4.23). However, this concept was ultimately rejected as too complex. Clamping rims were also considered; however, the rim would need to deflect no more than 0.1 mm to maintain the O-ring seal. This was not feasible for a rim which would need to be 300 mm long and less than 4 mm square.

Figure 4.23: CFRP Custom Hook Prototype

A prototype of the final and selected clamping concept – inspired by the stitching used on shoes to attach the outsole – is shown in Figure 4.24. The concept requires a series of 1 mm holes to be drilled around the perimeter of the CFRP-to-TPX bond. Thread is then used to *stitch* the two materials together thereby compressing the O-ring. Finally, the holes and the thread are sealed from inside the housing with epoxy resin.

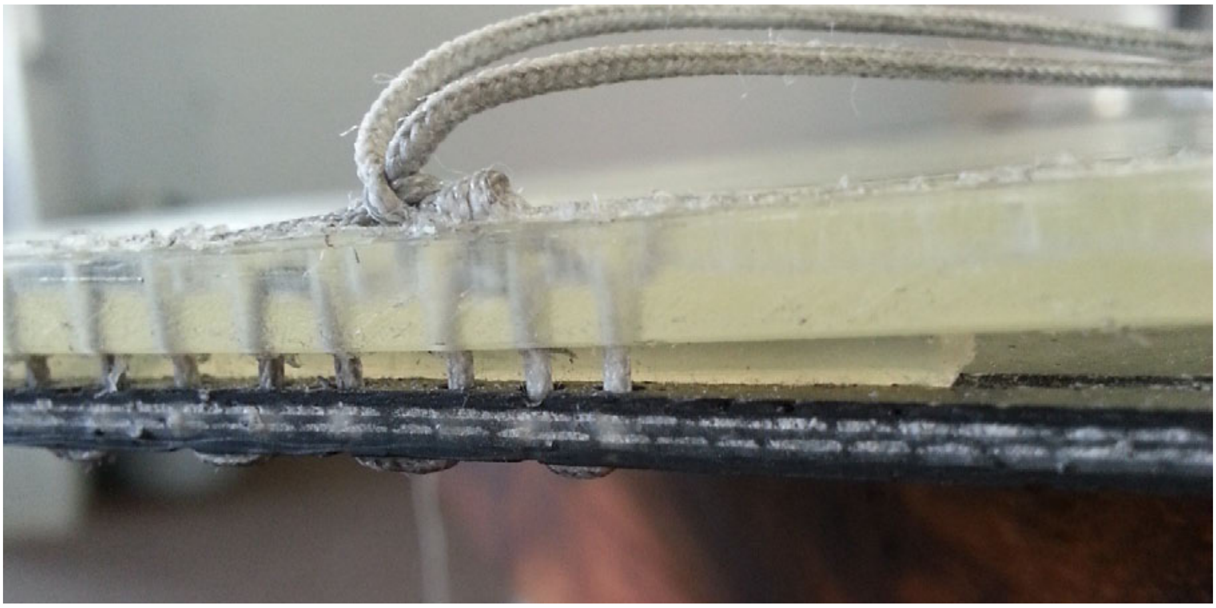

Figure 4.24: CFRP-TPX Stitched Seal Prototype

4.3.3 DETAILED DESIGN

The starting point for the detailed design of the housing was the exact thickness of the TPX compression plate; the subject of extensive testing. It was hypothesised that by making the CFRP housing rigid and holding the volume of couplant constant the TPX would be supported by the coupling fluid. This would prevent the TPX from deflecting under compression and allow for a thinner compression plate. To test this, a 3 mm thick TPX compression plate was implemented in prototype 3.

In thermal testing of the compression plate, the flexibility of TPX was found to increase significantly at ~40°C. Under compression, the TPX deflection was greater than 5 mm. The unexpectedly large deflections were found to be the result of the TPX assuming its second mode of bending. Figure 4.25 illustrates the first two bending modes. In mode 1, deflection is prevented because the required change in fluid volume is precluded by the rigid HSBP housing. However, in mode 2, the uncompressed portion of the compression plate deflects upwards allowing the compressed portion to deflect downwards without requiring a change in fluid volume.

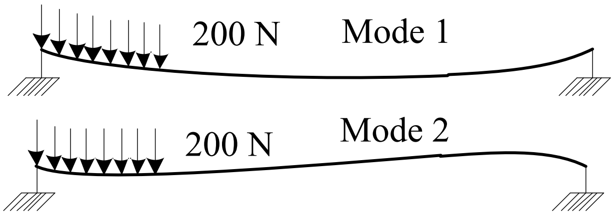

Figure 4.25: Side View of TPX Bending Modes

To accommodate the second mode of bending, a conservative design was implemented and the thickness of the platform was increased to be sufficiently rigid, even without hydraulic support. To minimize the geometric magnification, and account for the softening of TPX at ~40°C, the allowable deflection was set to a conservative 2 mm. Finite element analysis (FEA) was used to model the deflection. A uniformly distributed load of 200 N was applied to the compression plate surface while the perimeter was fixed. The results are shown in Table 4.6.

Table 4.6: TPX FEA Deflection Analysis Results

Thickness [mm]	Deflection [mm]
2	10
4	1.9
6	0.8
8	0.4

Although the 4 mm thick case meets the minimum requirements, it was decided that 6 mm TPX would be used instead. There are three justifications for this decision: (1) the reduction in TPX stiffness at ~40°C; (2) the FEA loading case was less concentrated than the clinical loading; and (3) implementing the stitched CFRP-to-TPX bond with less than 6 mm of material was not feasible.

To validate this decision, the effect of TPX thickness on the ultrasound image quality was studied[1]. Figure 4.26 shows the ultrasound scans of the custom CIRS phantom for various thicknesses of TPX[2]. There is a discernible step change in the penetration depth for the 6 mm case when compared to 2 mm and 4 mm. However, the reduction in image quality was deemed tolerable in light of the mechanical requirements. Additionally, the assumption was made that the penetration depth could be easily improved upon by decreasing the ultrasound frequency and/or increasing the transmission energy (see section 2.4.2).

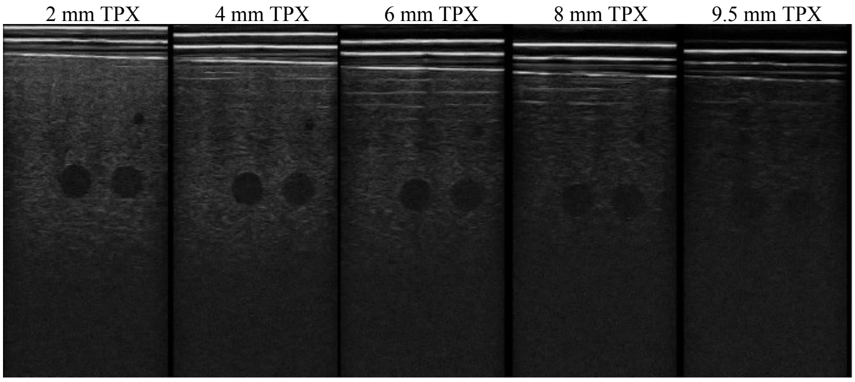

Figure 4.26: Effect of TPX Thickness on Ultrasound Image Quality

The detailed design of the stitched CFRP-to-TPX bond is discussed next. Figure 4.27 shows a section through the bond. The sealing O-ring sits in a seat, machined into the TPX. The stitching passes through 1 mm holes in the TPX and CFRP. The holes are spaced 5 mm apart (into the page) to ensure the O-ring is compressed along the length of the bond. The position of the Pandia is shown, illustrating the 0.5 mm limit on the Pandia-to-housing clearance. The 0.5 mm thick front-edge is also shown. The Pandia is 1 mm below the CFRP. This allows for a 0.5 mm clearance between the stitching and the Pandia and a 2 mm Pandia-to-compression-plate clearance as previously discussed. The portion of the TPX that contacts the patient has a radius of 4 mm. This dimension was maximised

---

[1] The effect on the attenuation of X-rays had already been shown to be insignificant and was not investigated further.

[2] The scans were performed at 10MHz using an Ultrasonix Modulo beam-former and a L14-5/38 linear transducer.

to reduce patient discomfort. The width of the bond is increased on the side and back edges of the TPX to allow for a more generous bend radius and bonding of the aesthetic skirt that clads the HSBP, a previously unmentioned component.

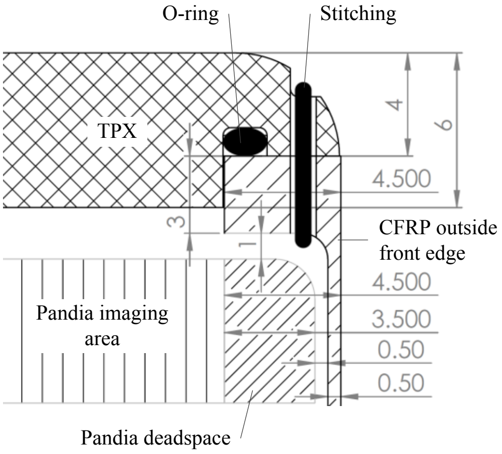

Figure 4.27: Front-Edge Geometry

Figure 4.28 shows the implemented stitching pattern; a variation of back-stitch. This pattern is self-locking. That is to say, as each loop is pulled tight it does not loosen. This ensures the O-ring is well compressed at the end of the stitching process. Epoxy resin is applied from inside the housing to seal the holes and thread.

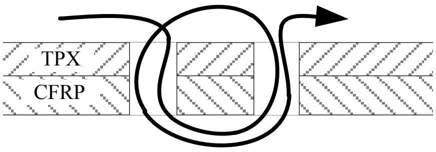

Figure 4.28: CFRP-TPX Stitching Pattern

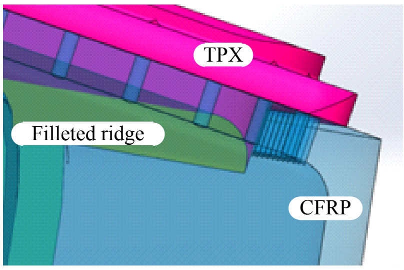

Figure 4.29: TPX Bubble Guide Fillet

Figure 4.29 shows a 3 mm filleted ridge that was added to the X-ray side of the TPX. This ridge allows any micro-bubbles that may collect on the underside of the TPX to run into the groove between the ridge and the CFRP when the C-arm is rotated to -90°. Due to the radiolucency of TPX, the change in thickness is not visible in X-rays.

Every effort was made to reduce the overall size of the HSBP. In collaboration with the manufacturer – Custom Works (Jeffreys Bay, South Africa) – the housing was designed to follow the contours of the internal components as closely as possible; the mouldability and strength of CFRP was useful in this regard. Conversely, the moulding process required draft angles, which increased the size of the housing slightly and complicated its geometry.

Mount plates are used to fasten the HSBP to the C-arm (see Figure 4.30). The plates – made from stainless steel to ensure the durability of the threads – are bonded to the CFRP with epoxy.

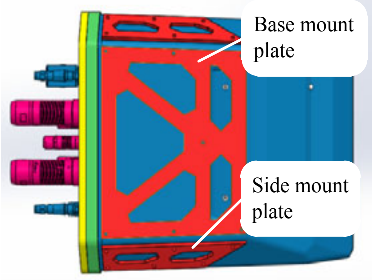

Figure 4.30: **HSBP Mount Plates**

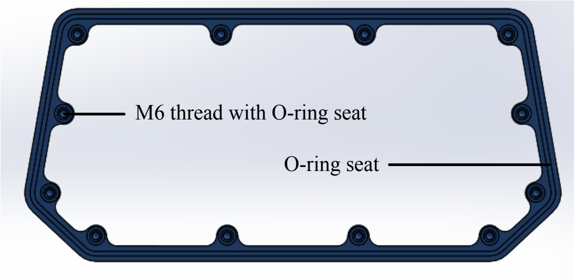

Figure 4.31: **Seal Rim Rear View**

A polycarbonate back plate is used to hermetically seal the housing. To achieve a robust seal and structurally support the open face of the housing, an aluminium seal rim (see Figure 4.31) is bonded to the CFRP. The back plate is clamped to the seal rim by 12 fasteners. FEA was used to compute the spatial frequency of the fasteners required to ensure O-ring compression. For simplicity, one long O-ring is used to seal the back plate and several smaller O-rings are used to seal each fastener hole. The fastening points are placed inside the HSBP to minimize its overall dimensions, an ergonomic criterion.

The back plate is the thoroughfare for all electrical and hydraulic lines (see Figure 4.32). Hermetically sealed electrical connectors are used for the electrical lines. One connector carries power and signal lines to the Evo controllers for the rail carriage, two further connectors carry Ethernet and power to the Pandia, and yet another connector carries power and control lines for the ultrasound transducer. Two large 55-way connectors carry the analogue ultrasound signals. All connectors were sourced from the Fischer range of hermetically sealed connectors.

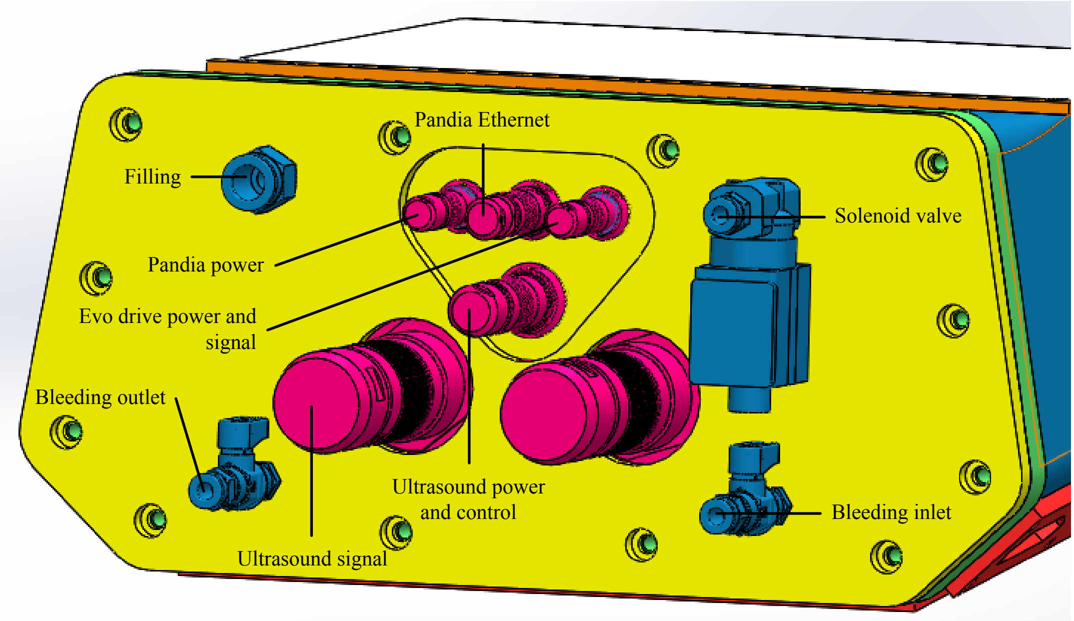

Figure 4.32: **Back Plate Electrical and Hydraulic Connectors**

The back plate has four hydraulic connections as shown in Figure 4.32. The filling, bleeding-inlet and bleeding-outlet connectors are used for filling and bleeding the HSBP. The fourth hydraulic connection – a solenoid valve – is necessitated by the difference in thermal expansion between the housing and the coupling fluid. To maintain atmospheric pressure inside the HSBP (a safety requirement) a flexible bladder is required to accommodate the resulting changes in volume. When unpowered, the solenoid valve allows fluid to flow freely between the bladder and the HSBP.

However, during breast compression the valve is electronically closed, fixing the internal fluid volume, thereby supporting the TPX compression plate. Although the TPX has been designed to deflect less than 2 mm even without hydraulic support, an uninterrupted power supply unit is used to ensure the valve remains closed in the event of a power failure, as per constraint HSCO3. Additionally, the normally-open solenoid valve allows for pressure equalisation due to temperature changes during transport without the need for a battery pack. This ensures that the unit is intrinsically safe.

An issue highlighted in the testing of prototype 3 was the management of small bubbles during the bleeding process. Figure 4.33 shows the inside face of the back plate. A 3 mm round-bottom-groove around the periphery of the plate is used to guide micro bubbles to the bleeding-outlet valve. Also shown in the figure, are the internal attachment points used to mount the cable chassis and two of the hermetically sealed electrical connectors.

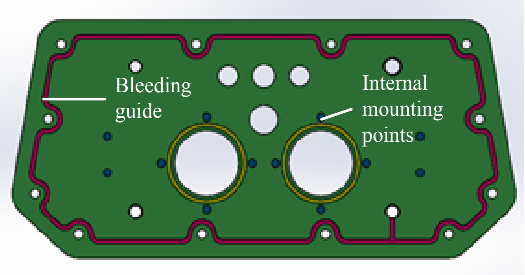

Figure 4.33: Back Plate Front View

Figure 4.34: Flexible Bladder

Thermal testing of prototype 3 showed a net flow in/out of the HSBP of 100 ml for every 10ºC change in temperature. As per HSCO5 and HSCO6, the HSBP may be subjected to a change in temperature of up to 50ºC. Therefore, the bladder must allow for a change in volume of up to 500 ml. Also the volume of fluid in the bladder at the time of filling and bleeding, as well as the expected operating conditions, must be carefully considered in determining the *pre-fill* of the bladder. The custom-made bladder, with a total volume of more than 700 ml, is shown in Figure 4.34. There are two ports on the bladder to facilitate bleeding. The bladder and the hydraulic line to the HSBP must also be air-free, as the bladder is mounted in the rotating C-arm.

Although prototype 3 was used to test many of the features of the HSBP housing, the final design featured several changes, untested systems, and new manufacturing techniques. As such, some manufacturing and assembly challenges were anticipated. Table 4.7 lists the physical specifications of the HSBP housing.

Table 4.7: Housing General Physical Specifications

Variable	Value
Weight empty with connectors	13.6 kg
Mineral oil volume	~13 *l*
Width (max)	353 mm
Depth (front-edge)	60 mm
Depth (max)	167 mm
Breadth (max) ex. connectors	366.5 mm
Breadth (max) inc. connectors	465.5 mm

4.4 ULTRASOUND CARRIAGE

4.4.1 SYSTEM REQUIREMENT SPECIFICATION

The ultrasound carriage is made up of a chassis, the ultrasound transducer and the multiplexing board. The multiplexer is used to switch the 64 analogue ultrasound lines between the 640 elements of the transducer. The design of the chassis, transducer and multiplexer was a highly iterative process with input from the transducer manufacturer (Apex Electronics, Shanghai) and the multiplexer designer (Samuel Ginsberg). However, only the design of the chassis is within the scope of this research.

The chassis must mechanically support the ultrasound transducer and the multiplexer while also managing the cables that service the multiplexer. Additionally, it must protect the multiplexer from X-ray scatter.

4.4.2 DETAILED DESIGN

Figure 4.35 shows the ultrasound carriage assembly. The ultrasound transducer and multiplexer – being mounted to the chassis – are electrically connected by flexible printed circuits (FPCs) which extend from the transducer into connectors on the multiplexer. A connector clamp plate prevents fluid drag on the FPCs from forcing open the connectors. In a later revision, the form factor of the clamp was expanded to fully shield the multiplexer. The ultrasound chassis base plate is used to mount the ultrasound carriage to its mount plate on the rail carriage.

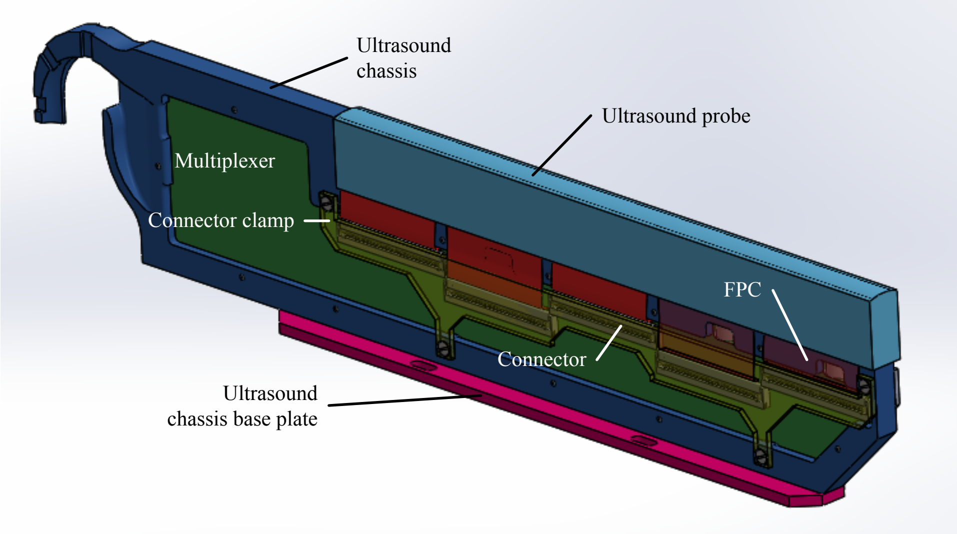

Figure 4.35: Ultrasound Chassis

The ultrasound carriage is the highest component in the HSBP and defines the overall thickness of the breast compression platform. As previously discussed, minimising this dimension is a primary ergonomic criterion. Hence, every effort was made in the mechanical and electrical design to minimize the height of the carriage. In particular, the front of the carriage was chamfered to reduce the front-edge thickness of the HSBP. Because of its intricate machining requirements, the material of choice for the chassis was aluminium.

Figure 4.36 shows the connection between the ultrasound probe and the chassis. A screw, hidden by the FPCs, passes through the chassis into the aluminium block at the bottom of the ultrasound probe.

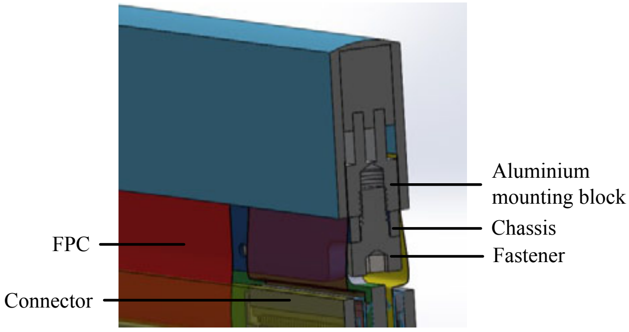

Figure 4.36: Ultrasound Probe Mounting

Figure 4.37 shows the seat in which the multiplexer sits. It also shows the series of M2 fasteners that are used to secure the multiplexer to the chassis. To maximise the usable area of the multiplexer, the width of the seat was minimized. To accomplish this, inconveniently small M2 fasteners were used. To prevent damage to the multiplexer, the seat is electrically insulated. This was achieved with a thin layer of epoxy resin, as anodising would likely damage the delicate M2 threads.

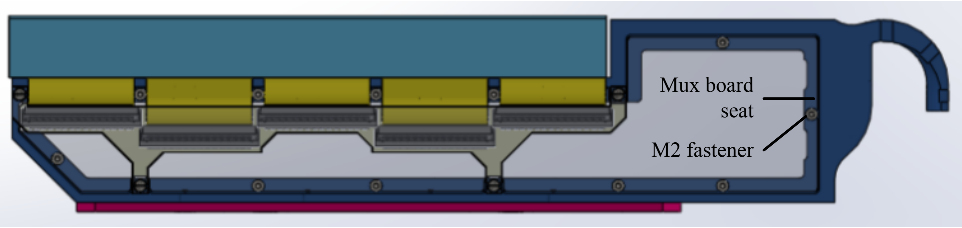

Figure 4.37: Ultrasound Carriage PCB Mounting

The base plate is bolted onto the chassis as shown in Figure 4.38. The sheet metal base is a cost effective alternative to a single-piece machined chassis. Also visible is the mounting slot in the base plate. This allows the transducer to be precisely located relative to the HSBP housing.

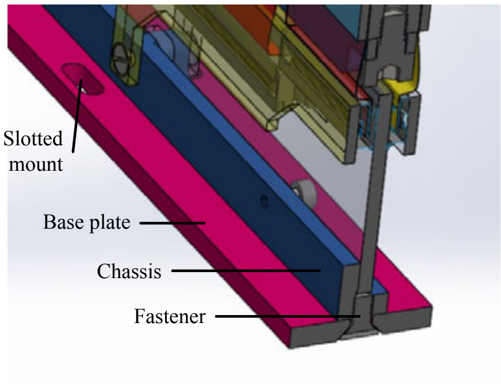

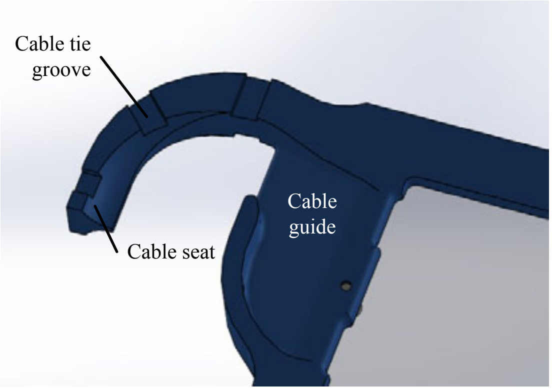

Figure 4.38: Ultrasound Carriage Base Plate Mounting

Figure 4.39: Ultrasound Chassis Cable Guide

Figure 4.39 shows the organically shaped cable guide which carefully bundles the delicate ultrasound lines. The hook allows the cable to be securely mounted to the carriage with cables ties. It also guides the cables into the cable management chassis. There is one semi-circular cable seat on each side of the chassis: one for the signal cable and one for the control cable.

A further feature of the ultrasound carriage is that it is no wider than the ultrasound transducer. As a result, the contribution of the ultrasound system to the lateral dead space has been fully minimized.

The ultrasound chassis, ultrasound transducer and multiplexer are all complex systems, none of which had been prototyped at the time of the design. As such, the performance of the carriage as a whole was the subject of some uncertainty. The physical specifications of the ultrasound carriage are given in Table 4.8.

Table 4.8: Ultrasound Carriage General Physical Specifications

Variable	Value
Weight (ex. multiplexer and probe)	313 [grams]
Width	10 [mm]
Base plate width	20 [mm]
Height	63.5 [mm]
Length	306 [mm]
Probe length	194.6 [mm]

4.5 HSBP GENERAL ASSEMBLY AND CABLE MANAGEMENT

In the general assembly of the HSBP, the management of cables is of primary importance. Conventional cable management systems, such as energy chains, were avoided, as their use would have necessitated an increase in the lateral dead space. Hence, a custom cable management system, shown in Figure 4.40, was implemented. The cable chassis – which connects the back plate to the rail carriage – comprises a back cable guide and a front cable guide. Together, they create a channel in which the cables for the Pandia and ultrasound transducer run. There are large cut-outs in the cable guides that allow one to see the translating carriages from outside the HSBP, via the back plate. Plastic coverings are used to provide smooth running surfaces for the cables. There are small cut-outs in the plastic that prevent the build-up of bubbles during bleeding. Flexible anti-vibration mounts are used for the cable-chassis-to-rail-carriage mounting. This allows the rail carriage to move relative to the back plate and to precisely mate to the reference surfaces in the CFRP housing.

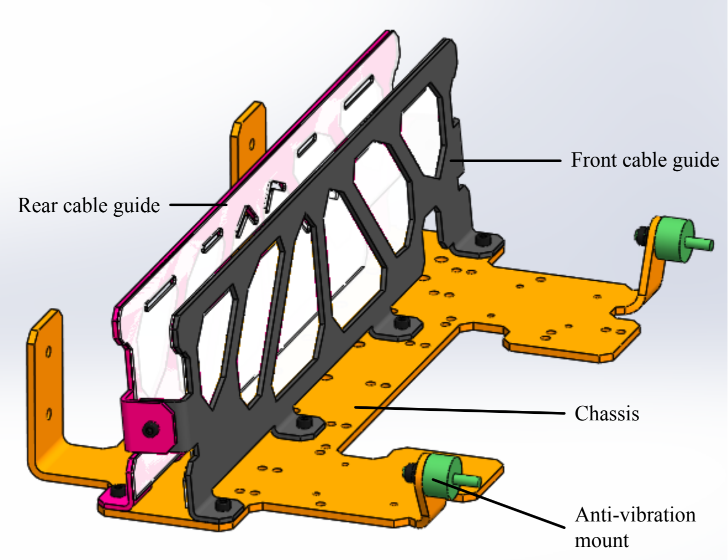

Figure 4.40: Cable Chassis

Prior to the final assembly of the HSBP, all subassemblies excluding the housing are assembled into the functional *drive assembly*, shown in Figure 4.41. This assembly allows the functionality of the Pandia, ultrasound transducer and mechatronics to be thoroughly tested before they are submerged in mineral oil. It is worth noting that the Pandia itself is hermetically sealed. This was done to protect the sensitive circuitry, CCD and scintillator from being damaged by the mineral oil – the likelihood of which is not yet fully understood.

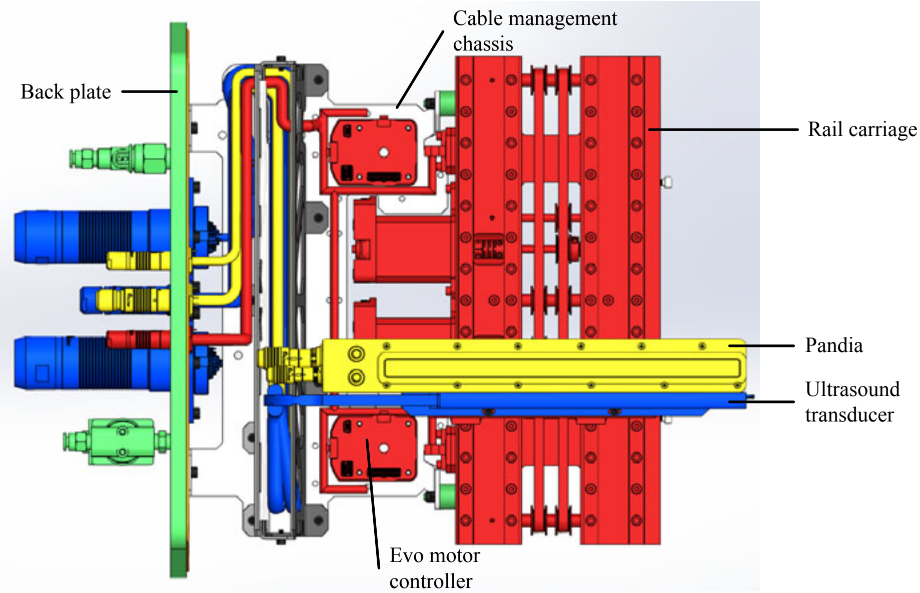

Figure 4.41: HSBP Drive Assembly

Figure 4.42 shows the cable management in detail. There are three sets of cables: the Pandia (yellow), ultrasound (blue) and mechatronics (red). All three sets pass directly from the hermetically sealed connectors onto the cable chassis (see Figure 4.43). The cables are held in place with cable ties (not shown) that pass through the numerous holes in the cable chassis. The mechatronics cable passes directly in and out of the guide channel. It then services the two Evo controllers and the optical end stops. The dynamic Pandia and ultrasound cables run in the guide channel. The ultrasound cables lie underneath the X-ray cables so they do not become entangled.

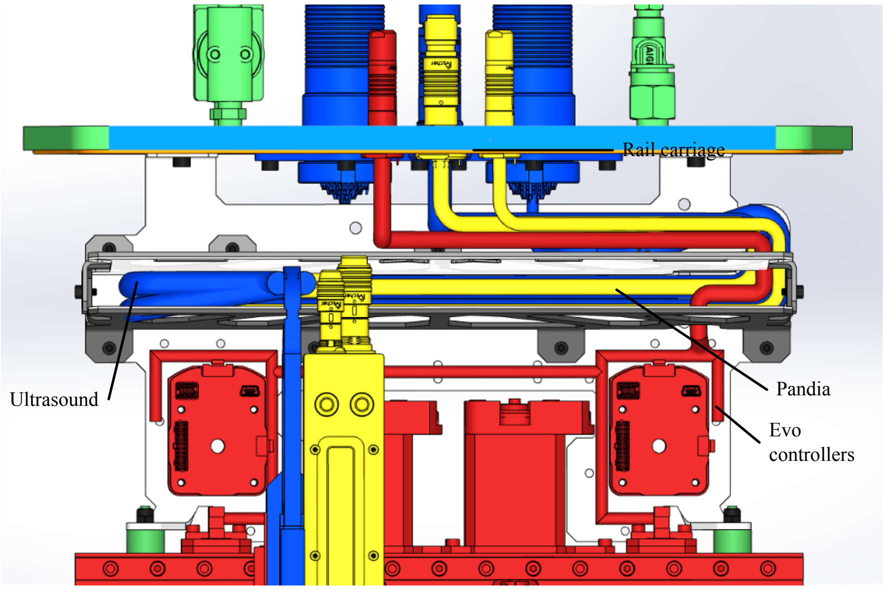

Figure 4.42: Cable Management Detail

The cable guides are at a slight angle to optimally use the space available inside the HSBP (see Figure 4.43). Also shown is the manner in which the Pandia and ultrasound cables are directed into the guide channel. The cable management chassis is constructed from stainless steel sheet metal to achieve the required hole sizes and bend radii.

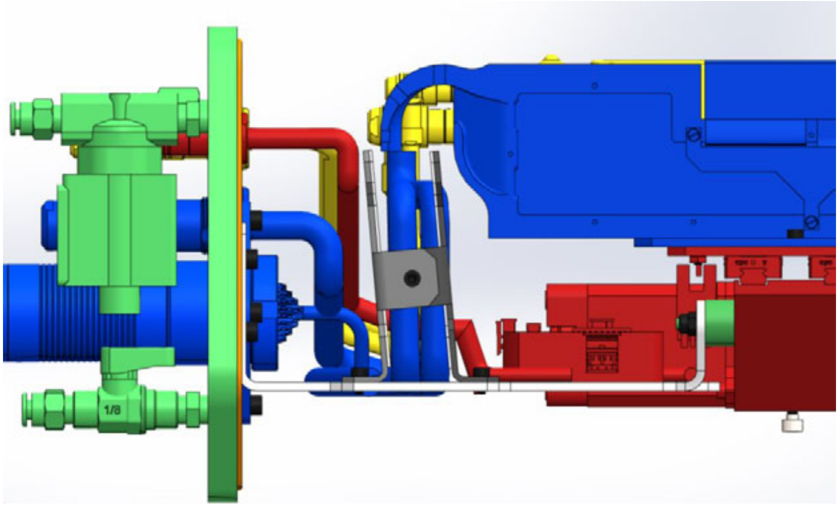

Figure 4.43: **Drive Assembly Side View**

In the final assembly of the HSBP, the drive assembly is placed inside the housing. To ensure proper alignment of the rail carriage, it is secured to the reference surfaces on the CFRP before sealing the back plate. At this stage, the X-ray and mechatronic functionality is tested one final time and a pressure test is used to ensure there are no leaks, before filling and bleeding the HSBP.

Selected manufacturing drawings are included in Appendix C and the physical specifications of the HSBP as a whole are presented in Table 4.9 below. With the design of the HSBP completed, the manufacturing packs were distributed to the various manufacturers and suppliers. In Chapter 5 the performance of the design is fully evaluated, beginning with a discussion of the manufacturing and assembly challenges.

Table 4.9: **HSBP General Physical Specifications**

Variable	Value
Weight empty (estimate)	10 [kg]
Weight full (estimate)	25 [kg]
Width (max)	353 [mm]
Height (max)	167 [mm]
Depth (max) ex. connectors	366.5 [mm]
Depth (max) inc. connectors	465.5 [mm]

Chapter 5: EVALUATING THE PERFORMANCE OF THE HSBP

This chapter focuses on evaluating the performance of the HSBP and is divided into 4 parts: In Part I, the ease of manufacture and assembly of the HSBP is analysed; in Part II the functional performance of the HSBP is assessed in terms of the SRS; in Part III the X-ray image quality is quantified using MTF, NPS and DQE; and in Part IV the ultrasound image quality is computed in terms of the six image quality metrics introduced in section 2.4.3. In each part, areas of success and failure are identified and where appropriate, design improvements and areas for development are highlighted.

5.1 PART I – MANUFACTURE AND ASSEMBLY

The HSBP drive assembly is shown in Figure 5.1. In this section the challenges in the manufacturing and assembly process and the resolution thereof, are discussed. Additionally, a determination is made regarding the extent to which criteria CR04 and CR05 – which pertain to ease of assembly and manufacturability – have been met.

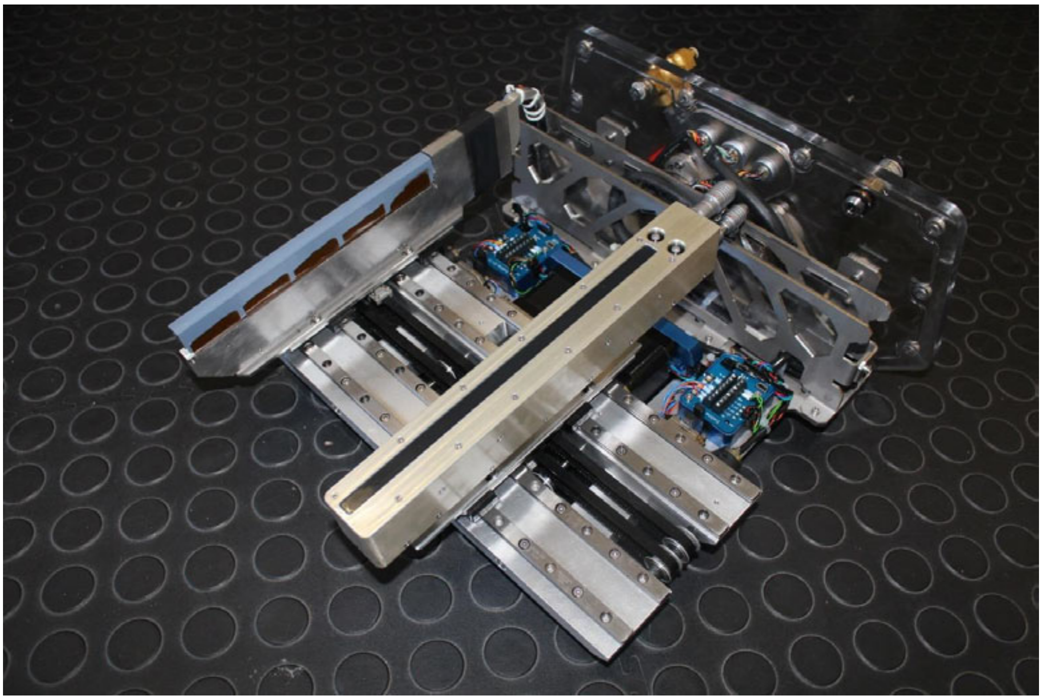

Figure 5.1: HSBP Drive Assembly

5.1.1 RAIL CARRIAGE

There were no significant challenges in the manufacture of the rail carriage. The workmanship of the manufacturers, TiTaMED, is acknowledged in this regard. The only problematic machining operation was the slot for the tensioning shaft (see Figure 4.9). It is recommended that a press-fit insert is used in future iterations.

Assembly of the rail carriage was similarly easy. One exception was the clamping of the drive belt. The clamping process is illustrated in Figure 5.2. Ultimately, fast-drying adhesive was used to temporarily secure the belt-ends to the clamp, so the assembly could be fastened.

One further issue, related to the HSBP drive assembly, is the accessibility of the motor and light-gate fasteners[1] (see Figure 5.3). The motors and light-gates are wired to the Evo controllers via the wiring harness on the cable management chassis. Hence, it is preferable that the light-gate and motors can be separated from the rail carriage, without detaching the cable management chassis or disassembling the wiring harness. This requirement is not facilitated by the current design. Therefore, it is recommended that future versions feature a single mount plate for both motors and light-gates. The mount plate should be secured by no more than four easily accessible fasteners. Overall, the manufacture and assembly of the rail carriage is considered exemplary. Some additional, photographs of the assembly process are included in Appendix D.

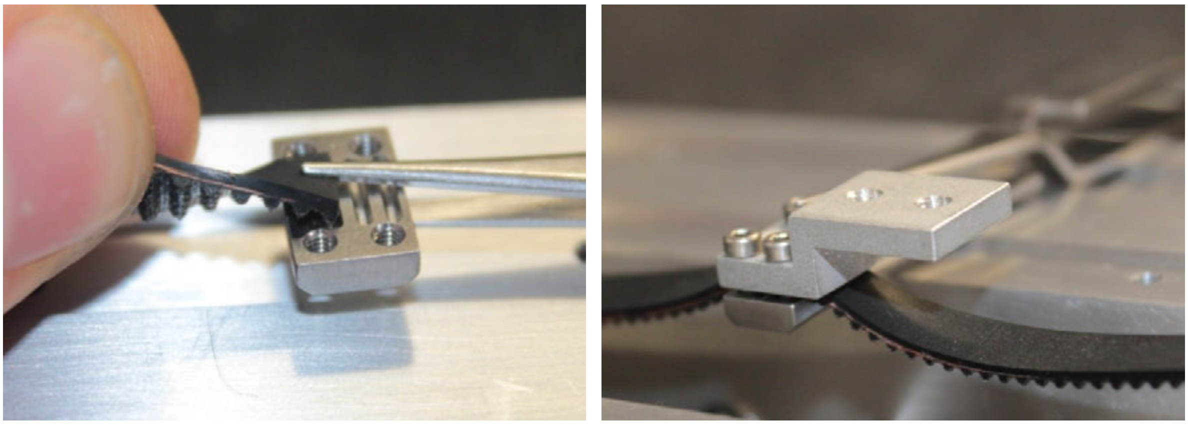

Figure 5.2: **Clamping of the Drive belt Left – the belt is held in place using adhesive. Right – the clamped assembly is shown.**

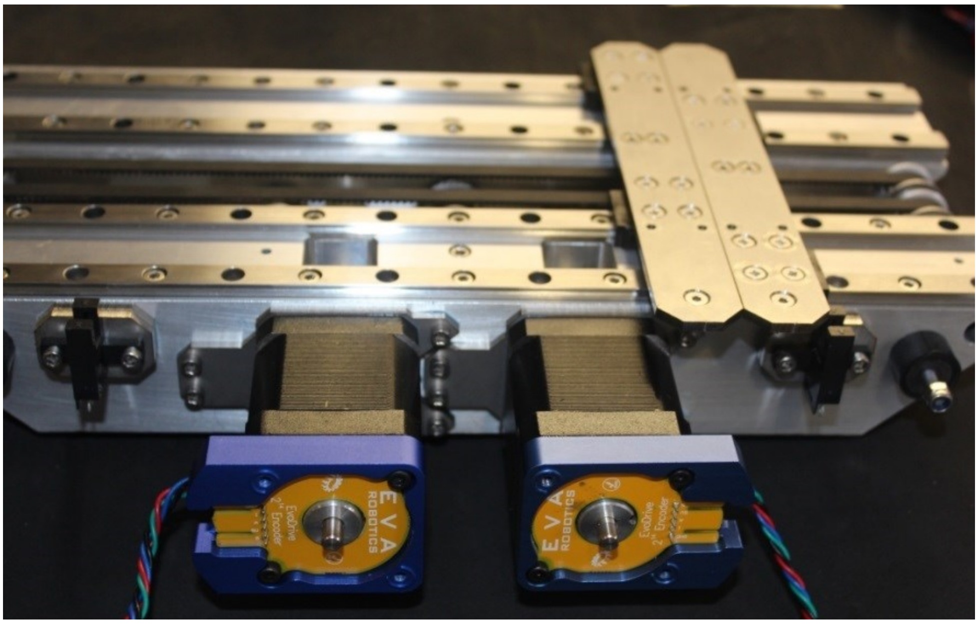

Figure 5.3: **Stepper Motor and Light-Gate Mounting**

5.1.2 ULTRASOUND CARRIAGE

The chassis – also manufactured by TiTaMED – was a challenging component to machine. The primary difficulty was the M2 fastening holes used throughout the component. This led to the

---

[1] The asymmetry of the motor mount plates is a legacy feature that has since been updated.

manufacturer requesting that M3 fasteners be used instead of the M2 fasteners. However, the space limitations on the multiplexer precluded this request and the M2 fasteners were retained.

The chassis and the multiplexer were assembled without any issues. However, the suppliers of the ultrasound transducer failed to manufacture it according to the agreed upon specifications. As illustrated in Figure 5.4, the FPCs were made 3 mm too short and the overall height of the transducer was ~1.5 mm too long. Additionally, the positioning of the mounting holes in the base of the transducer was incorrect.

Figure 5.4: **Ultrasound Transducer Manufacturing Errors Left – the FPCs are 3 mm shorter than specified. Right – the height of the probe is ~1.5 mm greater than specified.**

As a result of the erroneous manufacture of the ultrasound transducer, the thickness of the surfaces highlighted in Figure 5.5 had to be reduced by 1.5 mm. Additionally, the ultrasound transducer had to be attached to the chassis with epoxy adhesive instead of the fasteners.

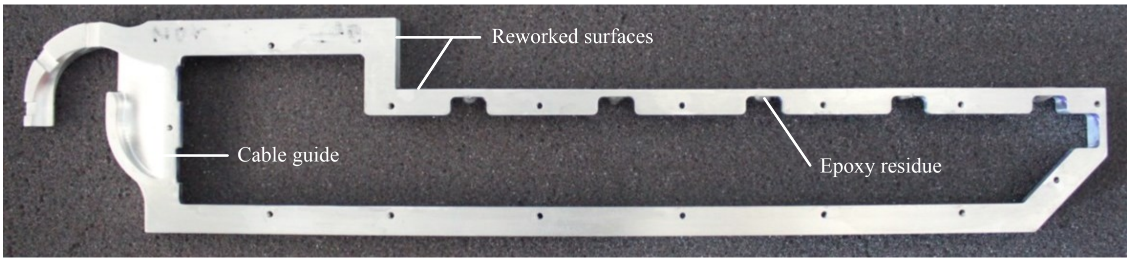

Figure 5.5: **Reworked Ultrasound Chassis**

The fully assembled ultrasound chassis is shown in Figure 5.6. Despite the problems with the transducer, the assembly functioned well. However, the cable management does not guide the cables quite as elegantly as expected and there is room for improvement.

Figure 5.6: **Assembled Ultrasound Chassis**

5.1.3 HSBP HOUSING

The HSBP housing suffered from several manufacturing and assembly challenges. Most of these issues were caused by the necessarily intricate design. In the following discussion, the manufacture of the TPX is considered first. This is followed by a discussion of the CFRP housing and finally the stitching process and general assembly are discussed.

TPX compression plate. The raw TPX was acquired from Port Plastics (Los Angeles, USA) as 10 mm thick sheet. Despite, making contact with several suppliers, 6 mm sheet could not be procured. Hence, as part of the machining process, the thickness of the TPX needed to be reduced by 40%.

In the first machining operation, the surface of the TPX was skimmed to remove surface imperfections. Also in the first operation, the fillet and step shown in Figure 5.7 (left) were machined. In the second machining operation, ~4 mm of material was removed from the second surface and the O-ring seat, and 1 mm holes were added (see Figure 5.7, right).

The removal of so much material, in the second machining operation, released internal stresses within the TPX. This in turn caused the TPX to deform by as much as 1 mm. As a result, the machining features on the top and bottom of the TPX did not align. The misalignment would have resulted in a poor CFRP-to-TPX seal and so the component was rejected.

A revised machining workflow was proposed wherein the thickness of the TPX was reduced to 6 mm in a first operation and, in a second and third operation the machining features were added to each side of the TPX. With this procedure, the necessary precision was achieved. However, the internal fillet, designed to assist with bubble management, was forfeited. With the machining operation resolved, the manufacture of the TPX compression plate was relatively straightforward.

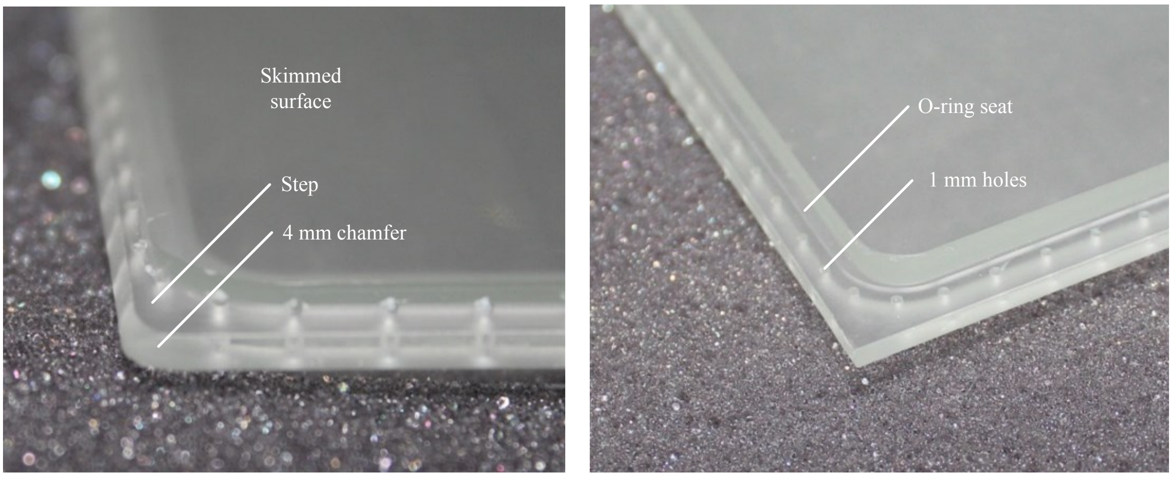

Figure 5.7: TPX Machining Operations. Left – the step and chamfer are machined in the first operation. Right – In the second operation, the thickness is reduced by 4 mm and the O-ring seat and 1 mm holes are added.

CFRP housing. The ambitious task of manufacturing the CFRP housing was taken up by Custom Works (Jeffreys Bay, South Africa). In the first iteration (see Figure 5.8, left), the 0.5 mm front-edge and 0.1 mm tolerances were easily achieved. However, the top surface, onto which the O-ring seals, required attention. Figure 5.8 (right) shows the two major issues: pitting around the 1 mm holes and a slight curvature in surface. These issues were expected to jeopardise the integrity of the seal. As a short term resolution, the pitting was filled with Loctite 401 adhesive and an oversized

O-ring was used to compensate for the curvature. These issues are expected to fall away as the manufacturing process is refined.

CFRP-to-TPX stitching and general assembly. In what may be considered a feat of manufacturing, all 200 1 mm holes in the TPX aligned perfectly with those in the CFRP. Despite this, the stitching of the CFRP-to-TPX bond, shown in Figure 5.9, proved to be a time consuming process. Because pliers were needed to pull the needle and thread through each hole, the nominal rate of stitching was ~2 minutes per stitch. At this rate, it took almost seven hours to stitch up the housing.

A large variety of stitching threads were tested, including polyester sutures. However, upholstery thread – the exact specifications of which remain unknown – provided the best combination of tensile strength and durability. The latter was an important factor as it was preferable to use a single thread to stich the entire bond.

Figure 5.8: CFRP Housing #1. Left – the CFRP housing is shown as delivered. Right – some of the manufacturing issues are highlighted.

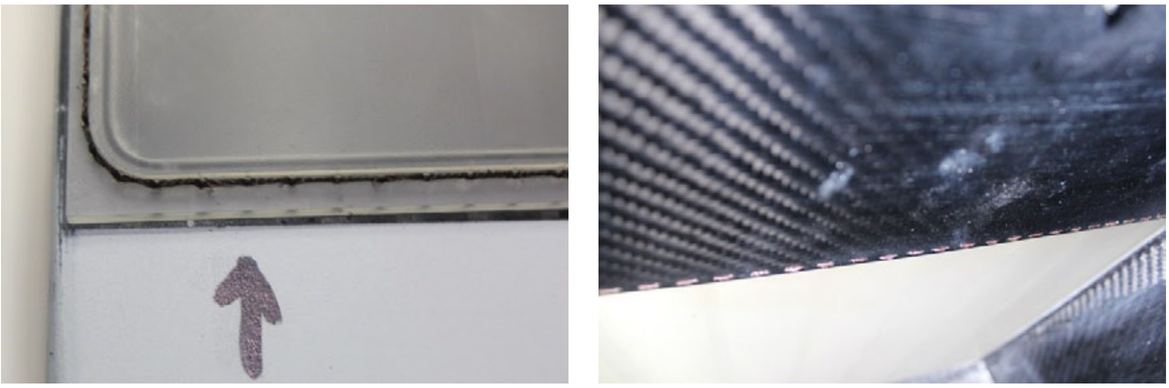

Figure 5.9: HSBP Stitching. Left – external stitching. Right – internal stitching prior to sealing.

A method was developed to repair snapped threads. However, the blemish resulting from the repair could only be hidden on the lateral and back edges of the seal. As such, if the thread snapped on the front-edge the stitching process was restarted. Hence, the stitching began at the front and centre of the HSBP and progressed in both directions toward the back.

When the stitching was complete, epoxy resin was applied to the threads from inside the housing. The assembly was then baked at ~60° C for four hours to cure the resin. Only at this stage could the performance of the seal be evaluated for the first time. The seal was tested by placing the housing front-edge down and filling it with water. Even though the O-ring was visibly compressed at the end of the stitching process, the compression appeared to have released and water seeped from the housing. This is illustrated respectively, in Figure 5.10.

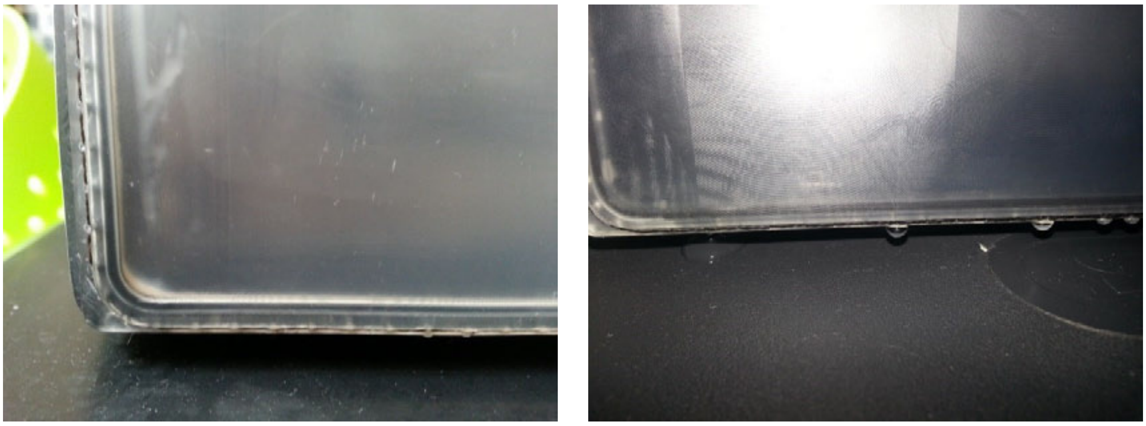

Figure 5.10: HSBP Seal Testing. Left – the O-ring compression is clearly visibly in the dry housing. Right – water is shown leaking from the housing.

In an effort to repeat the assembly process, the TPX was removed from the CFRP by cutting the stiches on the outside of the housing. However, owing to the use of epoxy resin, the 1 mm holes in the CFRP could not be cleared and this first CFRP housing had to be scrapped. At this stage it was decided that urethane rubber (Vytaflex) would be used to seal the holes and thread. This change allowed the TPX and CFRP to be reused in the event of a sealing failure.

Paying closer attention to the compression of the O-ring, a second TPX-CFRP assembly was stitched up. After sealing the threads with urethane, the assembly was once again baked at ~60° C for four hours to cure the glue. Before testing the seal, it was discovered that the O-ring compression had once again been released.

At this point, it was hypothesised that the baking process was the cause of the sealing failure. A series of tests showed this was indeed the case. A consultation with the manufacturer revealed that the softening point of the epoxy resin used in the manufacture of the CFRP was ~40°C. As a result, at high temperatures the 0.5 mm thick front-edge deformed, under the strain of the O-ring compression.

To mitigate this phenomenon, several procedural and design changes were instigated. Firstly, the baking process was removed from the assembly procedure. Secondly, the manufacturer began investigating the feasibility of using a resin with a higher thermal rating. Thirdly, the decision was made to thicken the front-edge of future housings to 0.8 mm. This last modification was also motivated by concerns that deflections of the flexible front-edge would result in fluid volume changes under compression and hence larger deflections of the compression plate. Additionally, the planned thermal testing of the HSBP and Aceso was postponed so as not to jeopardise the functionality of Aceso.

In a third stitching attempt, the O-ring appeared to remain compressed, even after the application of the urethane sealant. However, in leak testing, small amounts of fluid still leaked from the housing. Coloured liquid was used to identify the source of the leak. It was traced to one of the 1 mm holes, and it was caused by poor impregnation of the CFRP surrounding the carbon fibre. Loctite 401, which cures in the presence of water, was successfully used to seal this leak. After three attempts, a successfully sealed HSBP was achieved.

To evaluate the strength of the seal, leak testing was performed at 5°C, 10°C and 40°C as per HSCO5. Although the seal held, above 30°C the thermal expansion of the TPX became significant, and it bowed outward by as much as 3 mm at 40°C.

Based on the aforementioned issues with epoxy resin, urethane rubber was used to bond the seal rim to the housing and epoxy resin was used to attach the cross-brace and mount plates.

5.1.4 CABLE MANAGEMENT

The cable management chassis is shown partially assembled, in Figure 5.11. Mechanically, the cable management chassis performed as expected. However, there were two unforeseen issues with the system. The resolution of these is discussed below.

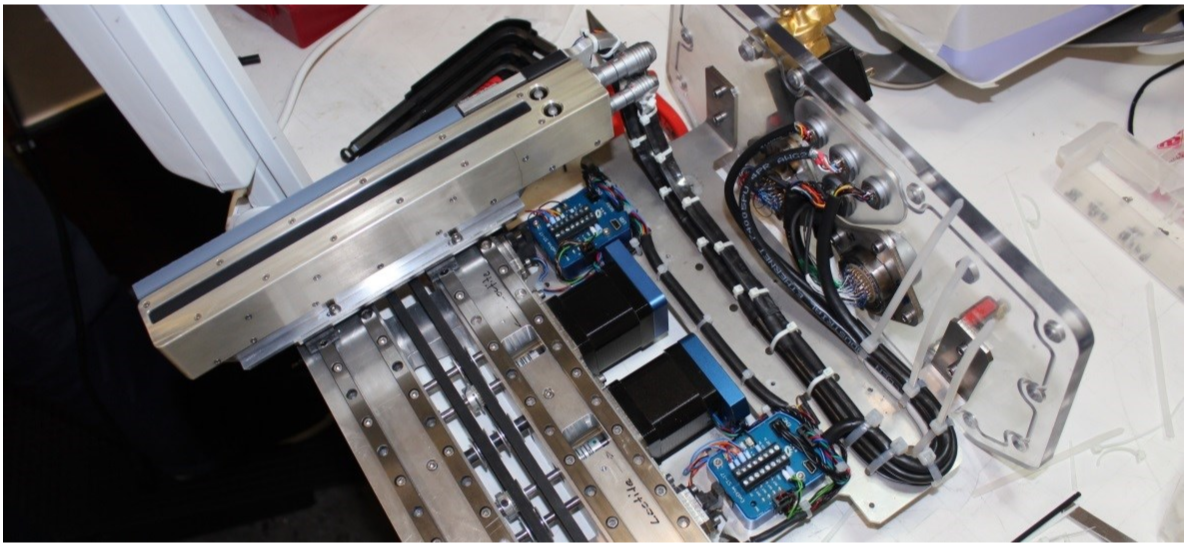

Figure 5.11: Cable Management Chassis

It is well known that electrical cables degrade in the presence of mineral oil. In anticipation of this effect, cables that were resistant to mineral oil were procured for use within the HSBP. Despite the suitability of the selected cables, preliminary testing showed that they became rigid when submerged in mineral oil. Upon closer inspection of the cable sheaths, it was discovered that only the outer layer of the sheath was mineral oil resistant. Because the cables are fully submerged in the HSBP, the inside of the sheath is also exposed to the oil.

The rigidity of cables did not jeopardise the integrity of the insulation in the case of the static cables. However, it was feared that, over time, the insulation of the dynamic portion of the cables would fail. Hence, the outer sheaths of the dynamic Pandia and ultrasound cables were stripped and replaced with heat shrink. The heat shrink did not deteriorate in mineral oil, and was found to provide the required flexibility.

The second issue was the longevity of the Pandia's CAT 7 Ethernet cable. The CAT 7 standard requires each of the 4 twisted-pairs to be separately shielded. In commercially available cables this is achieved with foil shielding. However, over time the foil shielding cut into the individual lines, eventually causing the cable to fail. This issue was resolved by constructing a custom cable using a metallic braid to shield each twisted pair, rather than foil. To date, this solution has performed well.

5.1.5 FILLING AND BLEEDING THE HSBP

Figure 5.12 shows the filling process under way. Much experience was gained from the filling and bleeding of prototype 3 and as a result, the filling and bleeding process was relatively straightforward.

One issue was the persistence of bubbles inside the HSBP. This was caused by the slow release of air, trapped throughout the drive assembly. Despite an extensive bleeding effort, a significant amount of air was released when the submerged mechatronics were exercised for the first time. Although untested, it is assumed that all the air can be removed by repeating the bleeding process over a period of time. Alternatively, a large vacuum chamber could be used to bleed the HSBP. However, this has implications for the integrity of the Pandia.

Figure 5.12: Filling the HSBP

In the preceding sections, the important HSBP manufacturing and assembly challenges and the resolutions thereof were discussed. Like the rail carriage, most components were easily manufactured and assembled (CR04, CR05). Although, some design changes have been recommended to improve the ease of manufacture and assembly of these components. The manufacture of the TPX and CFRP proved more complex. Many of the issues relate to the novelty of the design, and are likely to be resolved over time. However, the stitching process remains difficult and time consuming. In the following section, the operational performance of the HSBP is evaluated through laboratory testing.

5.2 PART II – LABORATORY TESTING

The laboratory testing of the HSBP is specified by the Aceso HSBP Verification Test Procedure (Smith, 2013). The assessment is divided into the following 6 tests: (1) metrological testing; (2) mechatronics testing; (3) compression testing; (4) integration testing; and (5) thermal testing. In this section, the methods and results of tests 1-4 are documented and discussed. However, as mentioned in the preceding section, the thermal testing was postponed until the thermal sensitivity of the CFRP was resolved.

5.2.1 METROLOGICAL TESTING

In the metrological testing, several critical measurements were made pertaining to the imaging coverage and dead space. With the exception of the front-edge dead space, all measurements were made with a metre rule having a resolution of 1 mm. The measurement process was complicated by the geometry of the system and hence there is a tolerance of ±1 mm on all measurements.

The measured coverage and dead space are given in Figure 5.13[1]. Importantly, the width of the dual-modality coverage is 235 mm. As discussed in section 2.5, the active imaging width of mammography machines typically varies from 24-30 cm. Hence, the dual-modality coverage of Aceso is slightly below the lower limit of this range. However, the HSBP contributes only 6 mm to lateral dead space; the Pandia dead space and the high level constraint on the width of the compression plate have a more substantial effect on the active imaging area.

Another important measurement is the lateral dual-modality dead-space of 30 mm (left) and 42 mm (right). This is on par with the General Electric system mentioned in section 2.5. Once again, the contribution of the HSBP (8.3%) is insignificant in comparison with the contributions of the Pandia (70.8%) and ultrasound transducer (20.8%). It is therefore concluded that the HSBP has performed well with respect to imaging dead space criterion (CR02).

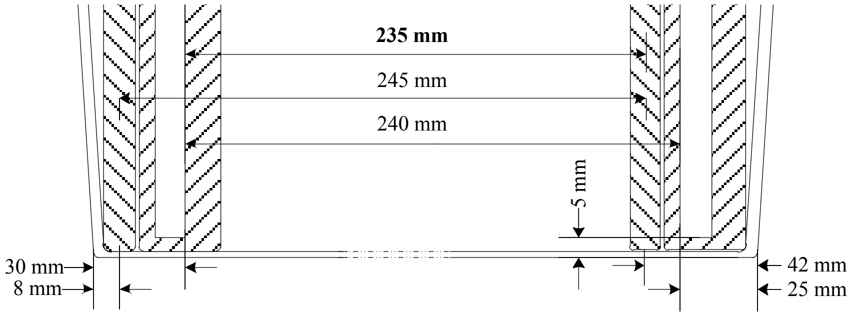

Figure 5.13: Imaging Coverage and Dead Space

The front-edge dead space was measured by X-raying a 0.8 mm thick stainless-steel plate, placed precisely 5±0.1 mm from the outside front-edge of the HSBP housing. Figure 5.14 shows the resulting image which has been expanded to make the individual pixels visible. The Pandia dead space is shown to the left and the corner of the plate is shown to the right. There is three pixels worth of clearance between the two. For this image, two-by-two binning was used, and hence the effective pixel size is 54 µm. From this a clearance of ~0.162 mm may be inferred. This clearance is greater

---

[1] The imaging window shown on the Pandia is the 4 mm post-collimator gap.

than the uncertainty in the position of the test piece. Therefore, the front-edge dead space has been shown to meet the 5 mm requirement (CO03).

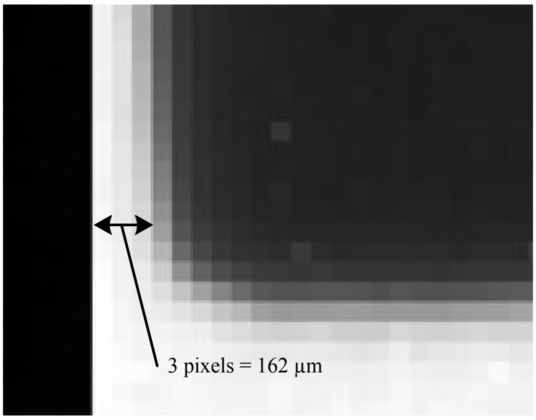

Figure 5.14: Front-Edge Imaging Dead Space

5.2.2 MECHATRONICS TESTING

The purpose of the mechatronics testing was to assess the general functionality of the rail carriage and precision and accuracy of the scanning system.

General functionality. When the rail carriage was in the design phase the Pandia scan speed was specified at 46 mm/s. However, it was later disclosed that the Pandia was capable of scanning at up to 65 mm/s. The subsequent implementation of this scan speed placed an increased demand on the performance on the rail carriage. Nevertheless, as discussed in section 4.4.2 this was expected to be well within the limits of the ST-17 stepper motors.

To validate this assumption, both carriages were driven at 65 mm/s with the C-arm at -90°, 0° and +90°, respectively. The rail carriage successfully translated the carriages at this speed, in all three positions. However, at ±90° an issue with the control algorithm on the Evo controllers caused the carriages to fall under their own weight when reaching the end of their travel. It is assumed that this issue can be easily resolved by modifying the control algorithm. Nevertheless, it falls within the Aceso software domain and is hence outside the scope of this research.

In wetted testing of the HSBP's general functionality, the optical light-gates were found to fail intermittently. In subsequent bench tests this phenomenon could not be replicated. This indicates that the light attenuation of the oil was not in and of itself the cause of the problem. As an interim solution, the Pandia was driven to the end of its travel to obtain an absolute reference point. To date, the resolution of this issue is on-going.

Spatial precision and accuracy. The absolute position accuracy of the rail carriage was assessed in three ways. In the first test, the Pandia was driven to its home position and a clock gauge[1] was zeroed on the Pandia's trailing face. Five X-rays were then acquired and the variation of the Pandia's home position was measured for each scan. These measurements, tabulated in Table 5.1, show a deflection of no more than 15 µm, which is within the 20µm limit (RCCO2).

---

[1] The resolution of the clock gauge was 10µm.

Table 5.1: Position Accuracy Measurements for the Pandia

Measuring No.	Value ± 5 [µm]
1	0
2	5
3	10
4	15
5	5
6	10

In a second test, a thin wire was X-rayed three times. The position of the wire was then measured in the resulting images. The image-to-image variation was found to be within two pixels or 108 µm (two-by-two binning). Although this is outside the allowable limits, there was some observer uncertainty in this measurement. Additionally, non-deterministic synchronisation of the Pandia acquisition and the motor translation may have contributed to the discrepancy.

In the third test, an X-ray was taken with the collimator fixed in the centre of the imaging window. The C-arm was then rotated through 90° and a second X-ray was acquired. The histograms of the resulting images were then plotted. The peaks of the respective histograms were found to be within 1-pixel or 54 µm of one another.

Based on the agreement of the first and third tests, and the uncertainty in the second test, it was concluded that the absolute position accuracy is within the acceptable limits (RCCO2).

Having ascertained the absolute accuracy of the rail carriage, the testing progressed to an evaluation of the Pandia-collimator alignment during scanning. To assess this, the collimator and Pandia were precisely aligned and their scanning velocities were synchronised. This calibration procedure is described in Appendix E. The collimator gap was set to 3 mm and an X-ray image was acquired. This gap width corresponds to a fan beam which is 22.5 mm wide at the detector[1]. The gap width was then incrementally narrowed until stripes appeared in the images. An example of said stripes is shown in the windowed X-ray of a hand in Figure 5.15.

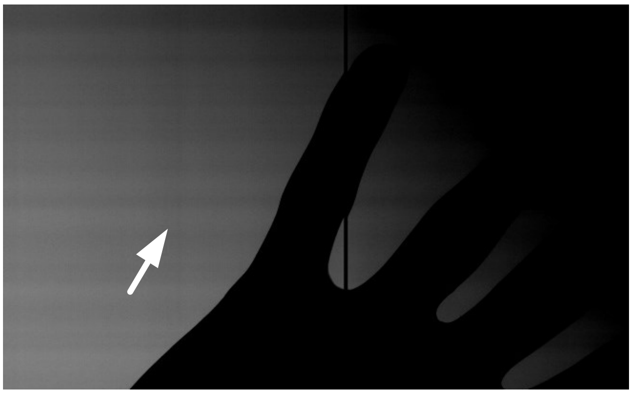

Figure 5.15: X-ray Image Striping. The horizontal striping is caused by time varying misalignment of the Pandia and the collimator.

The striping is caused by time varying misalignment of the Pandia and collimator. Ultimately, this is a mechatronics control problem caused by oscillating errors in the set-point tracking. The Evo

---

[1] To measure the beam width, an X-ray was acquired with a static collimator. Using a histogram of the resulting image, the beam width was then computed from the width of the histogram, at the point where the grayscale intensity was half of its maximum value.

controllers (used for the rail carriage and collimator) implement closed-loop PID[1] control. Despite efforts to tune the PID gains using an iterative method and the Ziegler-Nichols method (Palm, 2000), adequate control has not yet been achieved. The task of tuning the PID gains is complicated by the cumulative uncertainty of the Pandia and collimator controllers. Nevertheless, adequate control was achieved in Soteria and prototype 2 and should hence be achievable in Aceso. However, the tuning of the gains – a complex task in and of itself – is outside the scope of this research.

As an interim solution, the feedback was disabled and an open-loop control algorithm was used. Using open-loop control, the collimator gap-width was reduced to 1 mm (~7.5 mm at the detector) without causing striping.

The most pertinent outcome of this testing was that the spatial frequency of the striping was a function of the PID gains. Further, the spatial frequency was not a harmonic of the intrinsic stepper motor vibrations, the rpm of the belt drive system or the pitch of the toothed belts. Hence, it was concluded that the performance of the rail carriage is satisfactory. That said, the Pandia's post-collimator is only 4 mm wide. The beam-width is therefore oversized by ~ 88%. The implications of this are discussed further in section 0.

5.2.3 COMPRESSION TESTING

The compression testing comprises static deflection testing and fatigue compression testing; the purpose being to quantify the deflection of the compression plate and verify the strength of the stitched CFRP-to-TPX bond, respectively.

Deflection testing. To measure the deflection of the compression plate, a clock gauge[2] was placed inside the dry HSBP and zeroed on the centre of the compression plate. A stereotactic breast phantom[3] was then compressed to 200 N as shown in Figure 5.16. The resulting deflection was 0.30 mm. This process was repeated for MLO compression and a deflection of 0.15 mm was measured. This deflection was well below the expected value of 0.8 mm (see Table 4.6). This is attributed to two factors. Firstly, the measurements were performed at ~17°C while the material properties used in the FEA computation were for TPX at 22°C. Secondly, the vertical edges of the CFRP housing appear to support a large portion of the compression load. This was not properly accounted for in the FEA modelling.

As previously indicated, thermal testing of the HSBP was curtailed. However, during the baking process of the failed housings, some relevant observations were made. An increase in temperature caused the compression plate to bow outward rather than inward. Additionally, even at 40°C, the stiffness of the 6 mm thick TPX was not significantly reduced. Interestingly, this contrasts strongly with the observations made in the testing of prototype 3. Nevertheless, based on these observations, downward deflection of the compression plate is not expected to be an issue. However, outward deflection of the platform, due to thermal expansion, may increase the Pandia-to-compression-plate and transducer-to-compression-plate clearance. This has implications in terms of attenuation and geometric magnification which highlights the importance of the outstanding thermal testing.

---

[1] PID controllers are feedback controllers, the output of which is the sum of the proportional, integral and derivative transfer functions.

[2] The resolution of the clock gauge was 10µm.

[3] Model 013 from CIRS, Virginia USA.

Fatigue testing. The HSBP was filled and bled for this test; however, to stress-test the system the solenoid valve was not closed. In each cycle the stereotactic phantom was compressed to 200N, held compressed for five seconds and then fully released. 100 cycles each were executed for the CC and MLO positions. There was no apparent degradation of the bond.

In conclusion, the compression plate deflections have been shown to be significantly less than the required 2 mm. This indicates that there is room to optimise the compression plate thickness. Additionally, the thermal performance of the compression plate is an important consideration, yet to be evaluated. The longevity of the stitched seal was successfully verified through fatigue testing. However, production versions will require higher count fatigue testing.

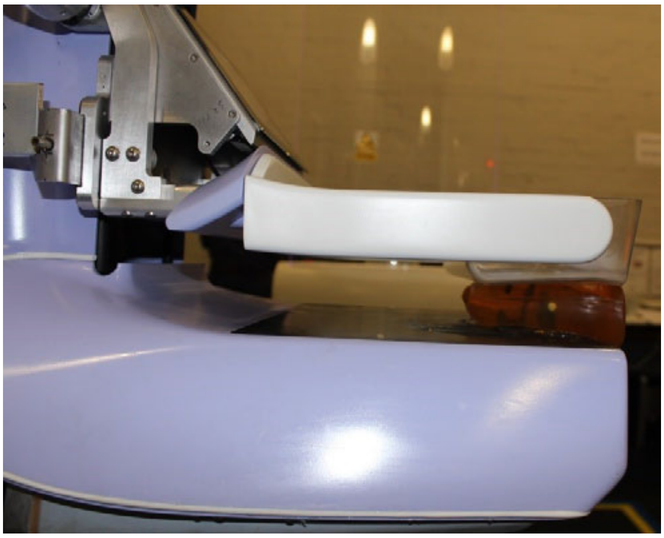

Figure 5.16: Compression Testing

5.2.4 INTEGRATION TESTING

The integration testing addresses: (1) the attachment of the HSBP to the C-arm; (2) the mounting of the flexible bladder; (3) the attachment of the aesthetic skirt; and finally (4) the poor performance of the ultrasound system.

C-arm attachment. The HSBP is mounted to the C-arm with 19 M6 fasteners which pass through the C-arm into the mount plates. The mounting was significantly over-engineered to ensure there was no flexion of the housing relative to the C-arm. This was necessary to maintain the Pandia-to-collimator alignment for all C-arm positions. The performance of the attachment exceeded expectations in that the HSBP could be removed from the C-arm and remounted without the collimator needing to be realigned.

Mounting of the flexible bladder. The C-arm features a depression below the HSBP for the elegant mounting of the flexible bladder. However, the TPX platform deflected downwards by ~1 mm, when the bladder was installed in this location. This in turn caused the stitching at the rear of the compression plate to touch the Pandia preventing it from translating.

This discovery led to the realisation that because the bladder was flexible, the platform was being subjected to a negative hydraulic head. The magnitude of the head was calculated from $P=\rho gh$, where ρ was the density of the mineral oil (~800 kg/m^3), g was gravitational acceleration (~9.81 m/s^2) and h was the distance from the underside of the compression plate to the base of the bladder (~200 mm). This gives a negative gauge pressure of ~1570 Pa. The net downward force on the upper surface of the 300 x 340 mm housing is hence ~160 N. This force deflection relationship is in reasonably good agreement with the FEA results reported in Table 4.6. This issue was easily resolved by repositioning the bladder higher up in the C-arm such that there was no deflection of the compression plate.

Attaching the aesthetic skirt. The aesthetic skirt along with the rest of the Aceso covers was designed by industrial designer John Harverson. He is shown fitting the skirt in Figure 5.17. The skirt provides an aesthetic, ergonomic and hygienic cover for the HSBP. At present the TPX is left without an aesthetic treatment because of the adhesion challenges and the anticipated increase in X-ray and ultrasound attenuation. In Figure 5.18 the Aceso and HSBP are shown both with and without the aesthetic covers. As explained below, the ergonomics of the HSBP and Aceso have not yet been studied in a clinical trial.

Figure 5.17: Fitment of the Aesthetic Skirt

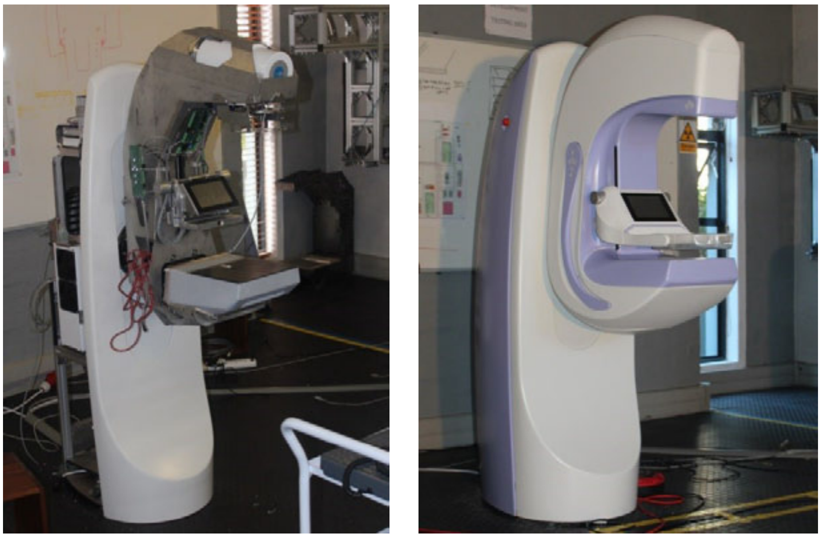

Figure 5.18: HSBP Integration. Left – the Aceso is shown with no aesthetic covers. Right – the Aceso is shown fully clad.

The poor performance of the ultrasound system. In addition to the problems discussed in section 5.1.2, the ultrasound transducer was plagued by dead elements. This degraded the performance of the entire transducer by causing a loss in transmission power and intensity drops in the acquired images. Figure 5.19 shows an ultrasound scan of a wedge-shaped gel-pad in which the aforementioned degradation is highlighted.

Additionally, the ultrasound system was susceptible to electrical noise interference. This is also shown in Figure 5.19. The source of this susceptibility is difficult to identify, although it was assumed that the FPCs, multiplexer and hermetically sealed connectors all contributed.

Ultimately, the decision was made that the ultrasound images were not of a sufficiently high quality for a clinical trial. Hence, the trial was postponed until a functional ultrasound system could be implemented.

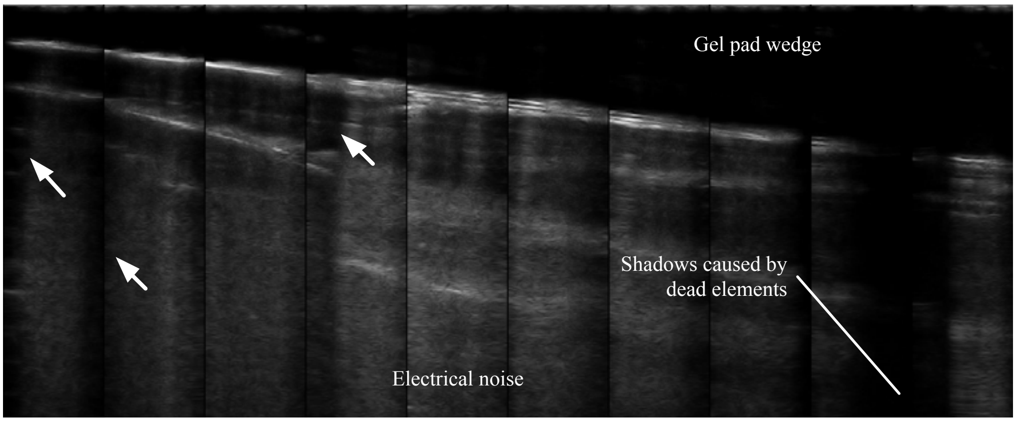

Figure 5.19: Reconstructed Ultrasound Slice. The ultrasound slice is generated by stitching together the frames acquired from each of the 10 multiplexed 64-element transducers that make up the 640 element transducer. Some of the dead element artefacts are marked with arrows.

5.2.5 CONCLUSION

In the laboratory testing of the HSBP, the active imaging area was measured and the contribution of the HSBP to the imaging dead space was shown to be inconsequential. The functionality of the rail carriage was also verified (RE03, RE05). However, the sporadic behaviour of the light-gates is yet to be resolved.

The strength of the stitched CFRP-TPX bond was fatigue tested without failure and the deflection of the compression plate was found to be well within the allowable limits (RE02, CO04). The testing also highlighted several integration issues. These issues were subsequently resolved and the relevant HSBP performance specifications were achieved. However, the thermal performance of the HSBP was not fully tested so as to avoid damaging the system. Hence, constraints CO05 and CO06 could not be verified although some concerns were raised about outward deflection of the compression plate, due to thermal expansion.

The poor performance of the ultrasound transducer prevented some aspects of the integration from being fully characterised (RE01, RE04). Owing to the postponement of the clinical trial, some criteria also could not be evaluated (CR01, CR04).

Postponements in the arrival of the multiplexer and the failure of the ultrasound system significantly delayed the project schedule. Although the design and manufacturing processes were completed on time (CO07, CO08), the HSBP (with the Pandia and ultrasound chassis) was first commissioned on 6 December 2013, two-months behind schedule (CO09).

In the next section, the effect of the HSBP on the X-ray image quality is characterised as per RE04 and CR01. Similarly, in section 0 the performance of the HSBP, with respect to the ultrasound image quality, is analysed through equivalency testing, conducted with a HHUS transducer.

5.3 PART III – X-RAY IMAGE QUALITY TESTING

Figure 5.20 shows two examples of X-rays acquired with Aceso. In this section the effect of the HSBP on the X-ray image quality is quantitatively evaluated through a difference study of the system MTF, NPS and DQE. Additionally, the effect of the rail carriage performance on the dose efficiency of the system is discussed. Finally, the theoretical best-case X-ray image quality is compared to that of an equivalent system.

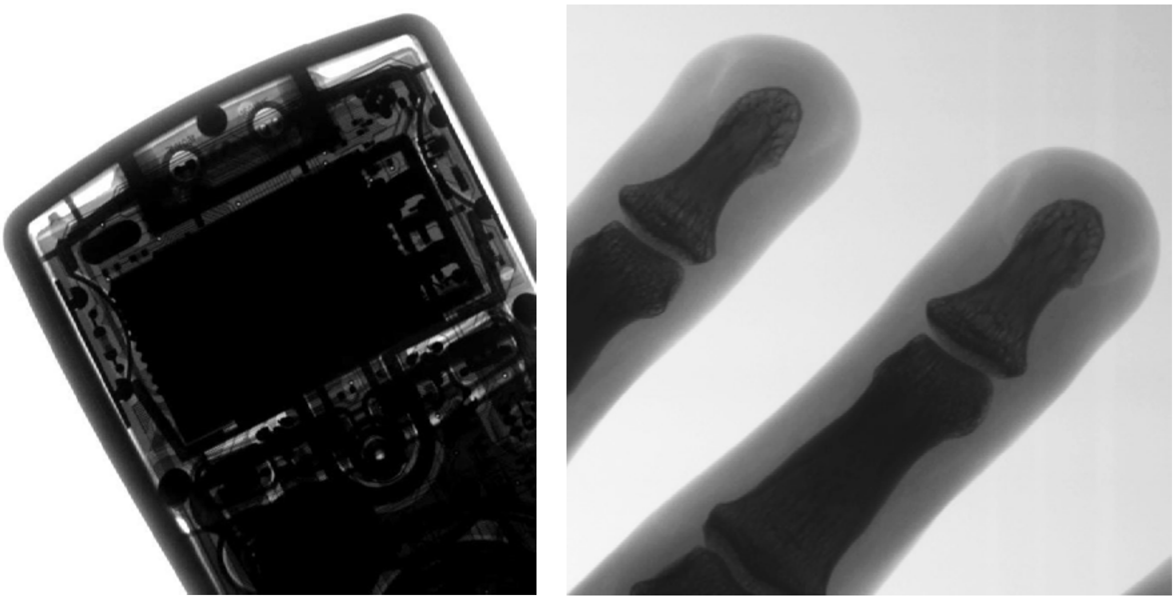

Figure 5.20: Example X-rays Acquired with Aceso. Left – an X-ray of a multi-meter. Right – an enlarged, but otherwise unprocessed, X-ray image of a hand. Note the visibility of the finger nails.

5.3.1 METHODOLOGY, EQUIPMENT AND INSTRUMENTATION

The MTF, NPS and DQE were computed and compared for three cases, as illustrated in Figure 5.21. A 3 mm thick PMMA compression paddle was used as a control in case 1. In case 2 the TPX compression plate was added to the imaging stack and in case 3 the HSBP was filled, thereby adding mineral oil to the imaging stack.

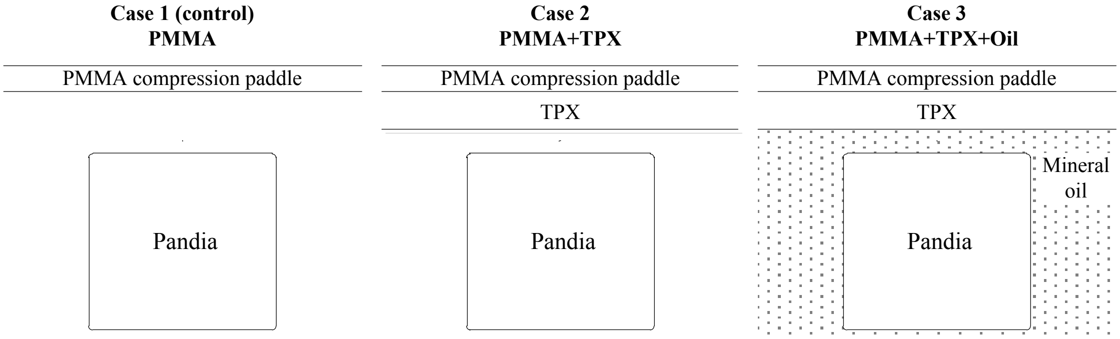

Figure 5.21: X-ray Image Quality Testing Cases

The MTF, NPS and DQE were measured and computed according to the methods prescribed by the IEC (IEC, 2007). To start, a calibration measurement was made for the computation of the conversion function. Subsequently, 9 X-ray images were acquired, 3 for each of the cases 1-3.

Unless otherwise indicated all measurements were performed at 28kV and 98mA with a 2.5 mm aluminium filter (99.999% pure). The Aceso is fitted with a C341-V X-ray tube with a tungsten source, from IAE (Milano, Italy). Importantly, all images were acquired with two-by-two binning, yielding a resolution of 54 µm. Finally, all images were appropriately corrected using the linear and image-independent flat-fielding script, included in Appendix F.

Conversion function measurements. This function – which is linear for the Pandia – defines the relationship between radiation dose and the resulting image greyscale value. The inverse of conversion function is used to convert the greyscale value of each pixel to units of dose (µGy). This is used in the computation of the NPS.

To compute the conversion function, the radiation dose for various mA values was measured. After removing the dosimeter[1], gain images[2] were obtained for the same set of mA values.

The position of the dosimeter, for the dose measurements, is shown in Figure 5.22. The top surface of the PMMA is 3 mm above the TPX. The inverse square law may be used to correct for this offset. However, the necessary change in dose was found to be less than 0.01%[3]. Therefore, the correction was deemed insignificant and neglected. The gain images were acquired *without* PMMA, TPX or oil in the imaging field. The measured dose and corresponding greyscale values are tabulated in Table 5.2, and the conversion function is shown in Figure 5.23. As shown, the r^2 value is greater than the lower limit of 0.99, set by the IEC.

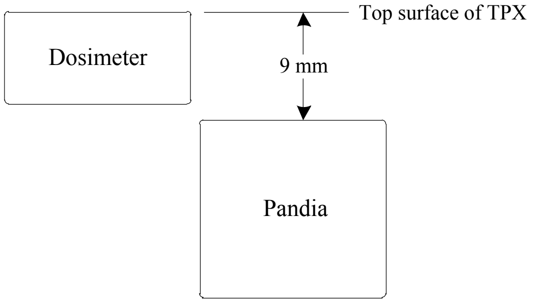

Figure 5.22: Dosimeter Position for the calculation of the conversion function

mA	Dose [µGy]	Greyscale
0	0	6.308
50	73.77	2681
74	103.7	4041
98	135.7	5382
122	170.7	6696
146	204.2	7964
170	239.4	9140

Table 5.2: Conversion Function Data

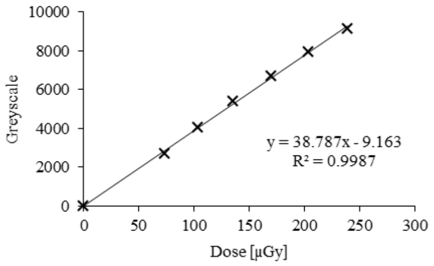

Figure 5.23: Conversion Function Plot

NPS measurements. For the measurement of NPS, a single gain image was acquired for each of the 3 cases shown in Figure 5.21.

---

[1] An Unfors Xi dosimeter (Raysafe™, Sweden) was used for all dose measurements.

[2] Gain images are blank images acquired with no imaging subject.

[3] The source-to-TPX distance is 640 mm.

MTF measurements. For the measurement of MTF, two images were acquired for each of the three setups. A 0.8x120x60 mm stainless steel test-piece was placed on the surface of the PMMA compression paddle. With respect to Figure 5.24, the test piece was placed in position A (transverse axis) for the first acquisition, and position B (lateral axis) for the second acquisition.

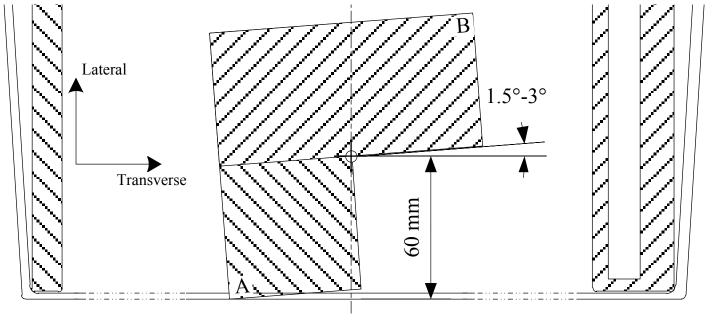

Figure 5.24: MTF Test Piece Position. The positioning of the test piece is shown for the transverse (A) and lateral (B) directions.

With the necessary data acquired, a script – written for CapeRay by the contractor Benjamin Irving – was used to compute the MTF, NPS and DQE. The script implements the computations laid out in the IEC standard. The contributions of Nielen Venter (CapeRay staff), Granton (2010) and Fredenberg (2012) to the script are also acknowledged.

For the conversion function, the coefficients given in Figure 5.23 were used. Additionally, an input dose of 135.7 µGy and a SNR_{in}^2 value of 6575 $(mm^2 \cdot \mu Gy)^{-1}$ were used, as per the IEC standard. The resulting plots are presented in the following section. Sample NPS and transverse and lateral MTF images are included in Appendix G.

5.3.2 RESULTS

The raw MTF, NPS and DQE results are plotted below. Said results are analysed and discussed in section 5.3.3.

Figure 5.25 shows the transverse (A) and lateral (B) MTF for case 2 (left) and case 3 (right), overlaid with case 1 (the control). The plots show a marginal decrease in MTF for cases 2 and 3 at midrange spatial frequencies.

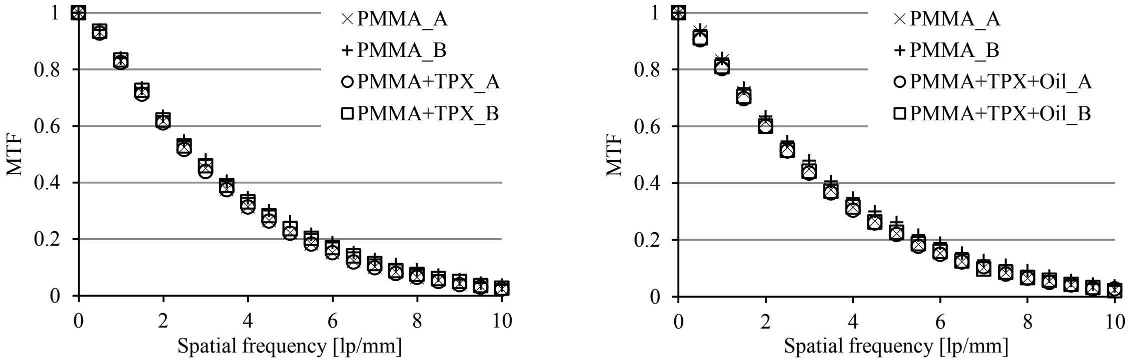

Figure 5.25: Plot of MTF versus Spatial Frequency. Left – the PMMA+TPX case is overlaid with the control PMMA case for the transverse (A) and lateral (B) directions. Right – The PMMA+TPX+Oil case is overlaid with the control.

Figure 5.26 shows the transverse (A) and lateral (B) NPS for case 2 (left) and case 3 (right), overlaid with case 1 (the control). A slight decrease in NPS is noted for case 2 and a significant decrease is noted for case 3. Additionally, a slight decrease in NPS for the lateral case when compared to the transverse case is observed.

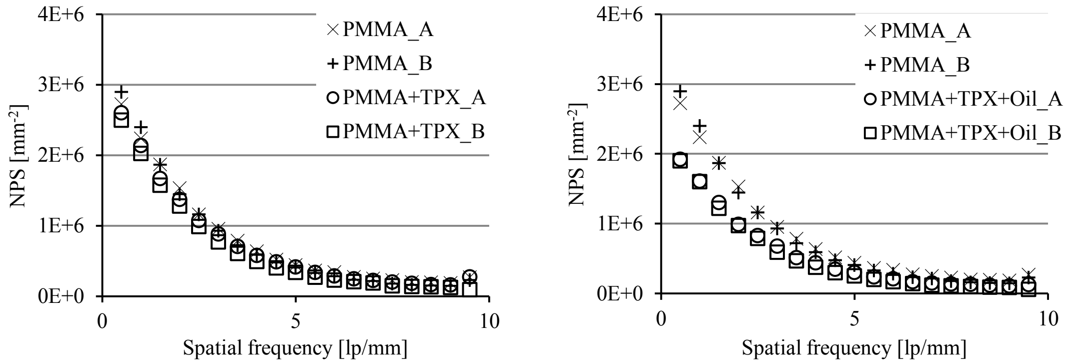

Figure 5.26: **Plot of NPS versus Spatial Frequency. Left – the PMMA+TPX case is overlaid with the control PMMA case for the transverse (A) and lateral (B) directions. Right – The PMMA+TPX+Oil case is overlaid with the control.**

Figure 5.27 shows the transverse (A) and lateral (B) DQE for case 2 (left) and case 3 (right), overlaid with case 1 (the control). A slight increase in transverse and lateral DQE is noted for case 2 (left) and a significant increase is noted for case 3 (right). In general, at midrange frequencies the transverse DQE is less than the lateral DQE.

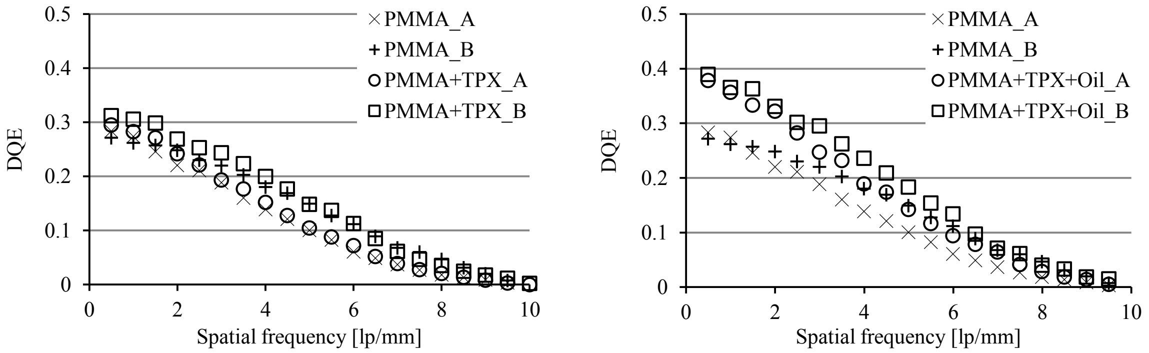

Figure 5.27: **Plot of DQE versus Spatial Frequency. Left – the PMMA+TPX case is overlaid with the control PMMA case for the transverse (A) and lateral (B) directions. Right – The PMMA+TPX+Oil case is overlaid with the control.**

5.3.3 ANALYSIS AND INTERIM CONCLUSIONS

Figure 5.25 shows that – for cases 1 and 2 – the transverse MTF is marginally higher than the lateral MTF. However, this trend is reversed in case 2. No logical conclusion – pertaining to the performance of the HSBP – could be drawn from this result. Hence, the variation in MTF between the transverse and lateral cases is assumed to lack significance.

Figure 5.28 shows the difference in transverse and lateral MTF for cases 2 and 3 with respect to case 1 (the control). More specifically, $\Delta MTF_i \equiv MTF_i - MTF_1,\ i = 2, 3$.

Considering first the transverse case 2 (PMMA+TPX_A), a marginal decrease in MTF (<0.015) is observed. For the lateral case, the decrease in MTF reaches a maximum of 0.025. For case 3

(PMMA+TPX+Oil), a maximum decrease of 0.03 and 0.04 is observed for the transverse and lateral cases, respectively. For cases 2 and 3, the decrease in MTF is most pronounced at midrange spatial frequencies.

For both case 2 and 3 the decrease in MTF is more pronounced in the lateral direction. No logical mechanism for this trend could be identified. Hence, it is assumed that some small offset error exists in the control MTF measurements.

In conclusion, the HSBP has caused a decrease in MTF in the lateral direction of 0.035 or 13% at 5 lp/mm. In the transverse direction this number is reduced to 0.003 or 1.7%. However, the validity of these variations is made somewhat questionable by the lack of a logical explanation, other than the presence of offset error in the control measurement/s of MTF.

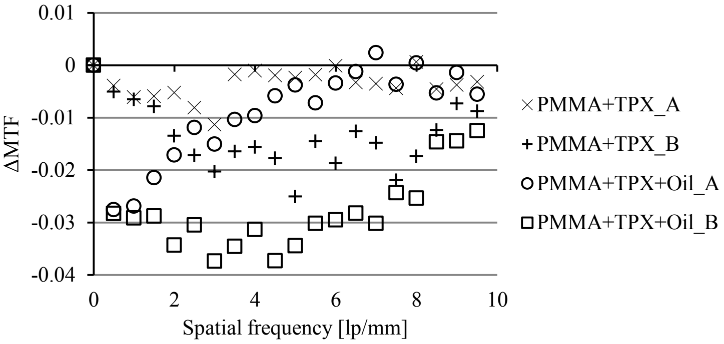

Figure 5.28: Plot of ΔMTF versus Spatial Frequency. The change in MTF resulting from the addition of TPX and TPX+Oil is shown for the transverse (A) and lateral (B) directions.

Figure 5.29 shows the difference in transverse and lateral NPS for cases 2 and 3, with respect to case 1. More specifically, $\Delta NPS_i \equiv NPS_i - NPS_1,\ i = 2, 3$.

Both the addition of TPX and more so, the addition of TPX+Oil results in a decrease in NPS. This decrease is most pronounced at low spatial frequencies. Additionally, for cases 2 and 3, the decrease is more pronounced in the lateral direction.

At 5 lp/mm the decrease in NPS is ~ $1.56 \cdot 10^5$ mm^{-2} or 38% for the transverse and lateral directions.

In conclusion, the HSBP has caused a substantial decrease in NPS of 38% at 5 lp/mm. This unexpected result is assumed to be caused by the TPX and mineral oil acting as radiographic noise filters.

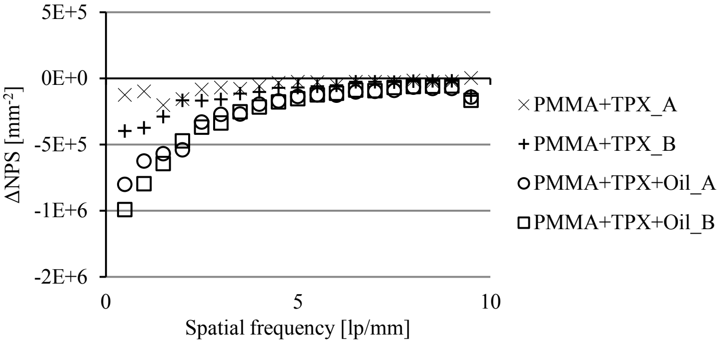

Figure 5.29: Plot of ΔNPS versus Spatial Frequency. The change in NPS resulting from the addition of TPX and TPX+Oil is shown for the transverse (A) and lateral (B) directions.

Figure 5.30 shows the difference in transverse and lateral DQE for cases 2 and 3, with respect to case 1. More specifically, $\Delta DQE_i \equiv DQE_i - DQE_1, i = 2, 3$.

The change in DQE is shown to follow the trend set by the NPS. That is to say, the increase in DQE is more pronounced for case 3 than for case 2. Also, the DQE is higher and more improved in the lateral direction. Despite DQE being proportional to the square of MTF, the small decrease in MTF is dominated by the significant improvement in NPS.

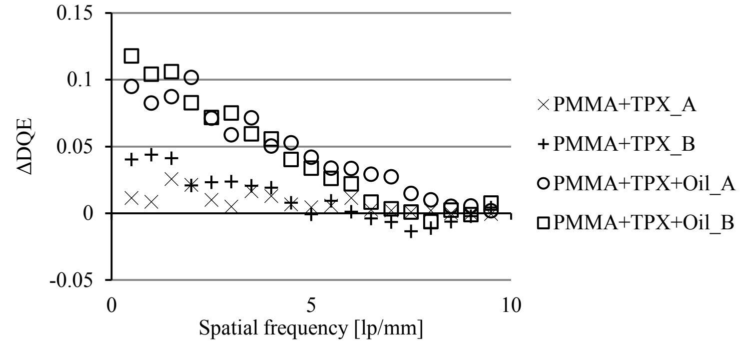

Figure 5.30: **Plot of ΔDQE versus Spatial Frequency. The change in DQE resulting from the addition of TPX and TPX+Oil is shown for the transverse (A) and lateral (B) directions.**

Figure 5.31 shows the DQE and ΔDQE values at 5 lp/mm. The change in DQE with the addition of TPX was marginal. This is attributed to the small, but squared, decrease in MTF counterbalancing the more marked improvement in NPS. An increase in DQE of ~4% at 5 lp/mm was observed for case 3 and this is due to the substantial improvement in NPS.

In conclusion, the HSBP has resulted in an ~4% increase in DQE at 5 lp/mm. Although the HSBP caused a decrease in the MTF, this was outweighed by the improvements in NPS. These are attributed to the apparent radiographic noise filtering properties of the TPX and mineral oil.

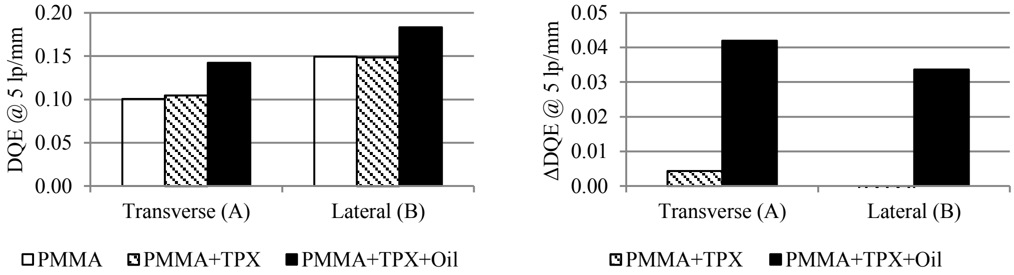

Figure 5.31: **DQE at 5 lp/mm. Left – the DQE at 5 lp/mm is shown for cases 1, 2 and 3. Right – the change in DQE resulting from the addition of TPX and TPX+Oil is also shown.**

Despite the increase in DQE caused by the HSBP, the *system* DQE measurements were well below typical *detector* DQE measurements. For example, Smith (2003) reports a DQE of 0.2 at 5 lp/mm for an equivalent CCD detector. This discrepancy is caused by the difference in the width of the fan-beam at the detector and the width of the Pandia post collimator (Nishikawa, 2003).

The dosimeter used in the measurement of the DQE measured the dose corresponding to the fan-beam width rather than the dose of the Pandia, which is curtailed by the post-collimator. The theoretical *detector* DQE may be obtained by scaling the dose measurements by the ratio of the fan-beam width to the post-collimator width. Similarly, the DQE of the *system* can be made to approach the DQE of the detector by reducing the collimator-gap and hence the fan-beam width at the detector.

Figure 5.32 shows the resulting theoretical NPS and DQE for various fan-beam widths[1] (for case 1 above). By simply scaling the dose measurements, two assumptions are made: (1) the dose is linearly related to the collimator-gap; and (2) the X-ray spectrum, and hence the SNR_{in}^2 value, are independent of the collimator-gap (see Figure 5.32, left). No attempt has been made to validate these assumptions, and the DQE data under discussion is purely theoretical.

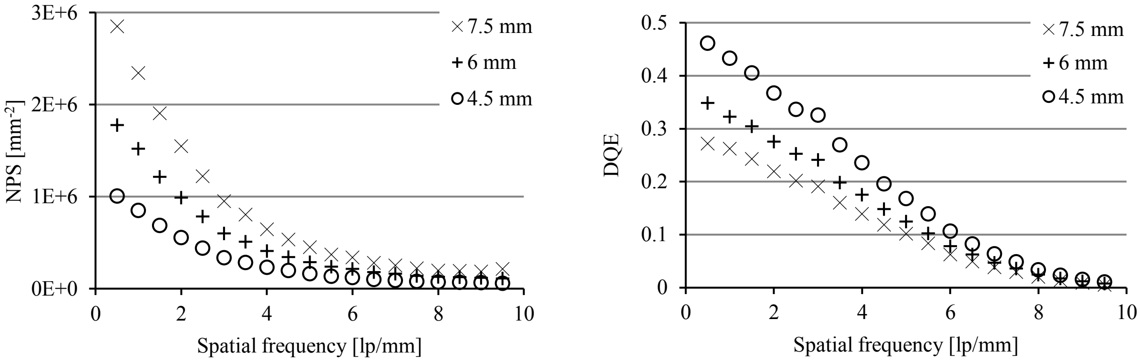

Figure 5.32: **Theoretical variation of NPS and DQE with Fan-Beam Width at the Detector. Left - the variation in NPS. Right – the variation in DQE (for case 1) is shown for the theoretical scaling of the fan-beam width.**

Nevertheless, the trends do allow some useful conclusions to be drawn. Specifically, the scanning performance of the rail carriage (and the collimator) is of critical importance to the system dose efficiency of Aceso. This is because the collimator-gap width is directly dependent on the dynamic alignment of the Pandia and collimator. However, at present the closed-loop control algorithm is the limiting factor rather than the mechanical performance of the rail carriage (see section 5.2.2).

In Figure 5.33 the theoretical system DQE for the Aceso is overlaid with the DQE for the Fischer FFDM+ABUS system, reported by Suri et al. (2005). Prior to comparing the DQE for the two systems, it is worth noting the differences in the experimental conditions, the effect of which is difficult to quantify. The Aceso DQE was computed for case 3 with the fan-beam width theoretically scaled to 4.5 mm. All other setup parameters are as per section 5.3.1. The Fischer DQE was computed for 27 kV and 150 mA with a 4.5 cm PMMA filter. A CCD scanning detector with a resolution of 54 μm was used.

Under the assumption that the experimental conditions warrant direct comparison, the theoretical performance of the Aceso is shown to exceed that of the Fischer FFDM+ABUS system by a substantial margin. Suri et al. (2005) found the Fischer FFDM+ABUS system to have a marginally higher DQE than the commercial SenoScan ® system. Therefore, it may be concluded that the theoretical DQE performance of Aceso also exceeds that of the commercial SenoScan® system. At 5 lp/mm the theoretical Aceso DQE is ~80% greater than that of the Fischer FFDM+ABUS system. This result highlights the potential of the Aceso system and once again confirms the need to optimise the collimator-gap width.

---

[1] MTF is unaffected by the scaling of the dose measurements.

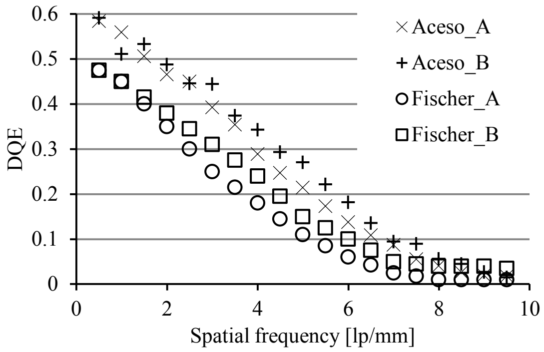

Figure 5.33: Plot of System DQE versus Spatial Frequency for the Aceso and Fischer FFDM+ABUS Systems. The Aceso DQE is based on the theoretical scaling of the fan-beam width to 4.5 mm. The Aceso DQE was computed for case 3 at 28 kV and 98 mA with a 2.5 mm aluminium filter and a resolution of 54 µm. The Fischer DQE was computed at 27 kV and 150 mA with a 4.5 cm PMMA filter and a resolution of 54 µm (Suri et al., 2005).

To conclude the X-ray image quality analysis, the HSBP caused a marginal reduction in MTF which was counteracted by a substantial decrease in NPS. This culminated in a ~4% increase in DQE at 5 lp/mm. Additionally, the need to narrow the collimator-gap to maximise the dose efficiency of Aceso has been highlighted. In particular, if the gap width can be reduced by ~60%, the DQE of the Aceso could exceed that of its competitors by up to 80% at 5 lp/mm. However, this latter result requires experimental verification through the testing of various competitor systems, under equivalent experimental conditions.

In terms of the HSBP SRS, the integration of ABUS (RE02) has led to an increase in the DQE performance of the X-ray system (CR01). However, the clinical image quality (RE04) has not yet been evaluated owing to the postponement of the clinical trial. That said, based on the theoretical detector DQE, the X-ray images are expected to be of diagnostic quality.

5.4 PART IV – ULTRASOUND IMAGE QUALITY TESTING

Figure 5.34 shows the first set of dual-modality images acquired with the HSBP and Aceso. The X-ray image is shown above the 3D ultrasound reconstruction. Although several lesions are seen in the X-ray, only two of these could be isolated in the ultrasound volume. Also, as was the case in Figure 5.19, there is a significant absence of tissue grain (see section 2.4.3). Nevertheless, these two images represent a significant step forward in the development of the Aceso and the field of FFDM+ABUS as a whole.

Ultimately, the performance of the ultrasound system was found to be less than acceptable. This was true for both the clinical trial and the testing of the HSBP. Hence, it was decided that the effect of the HSBP on the ultrasound image quality should be studied using an alternate ultrasound system.

In testing the effect of the HSBP on the ultrasound image quality, it was decided to evaluate the effect of TPX thickness and ultrasound frequency. The effect of the TPX thickness was studied to validate the current design and also to inform any future optimisation of the compression plate (see section 5.2.3). The effect of ultrasound frequency was studied to inform the on-going review of the ultrasound system design and to predict the performance of the HSBP for the range of possible frequencies.

In this section the methods, results and analysis, and conclusions of the ultrasound image quality analysis are presented in turn.

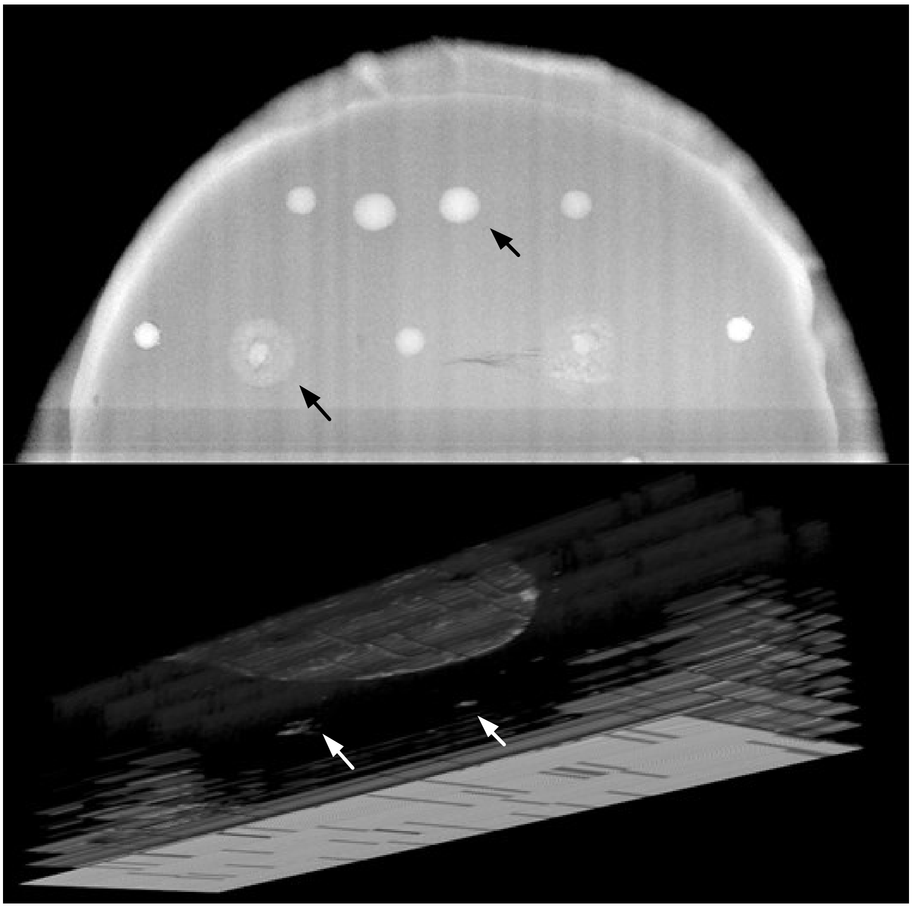

Figure 5.34: First Dual-Modality Image Acquired with Aceso. Top – X-ray of the stereotactic phantom. Bottom – bottom-right view of the simultaneously acquired 3D ultrasound. Two of the phantom lesions are discernible in the ultrasound volume. These are also marked in the X-ray image.

5.4.1 METHODOLOGY, EQUIPMENT AND INSTRUMENTATION

As discussed in section 2.4.3, the ultrasound image quality was measured and analysed using the methods and computational tools provided in the QA4US software package (MUSIC, 2012). As such, a detailed description of the image acquisition methods and computational processing are available from the reference above. Consequently, only a brief description of the experimental methods is given here.

Experimental cases. To study the effect of TPX thickness, the image quality was evaluated for 0, 2, 4 and 6 mm of TPX. To evaluate the effect of ultrasonic frequency, the image quality was evaluated at 2.5, 3.5, 5.5 and 8.5 MHz for each of the four TPX thicknesses. Hence, a total of 16 experimental cases resulted.

Image acquisition. Figure 5.35 shows the experimental setup for the image acquisition. With this setup the following four phantom targets were imaged for each experimental case: (1) greyscale targets; (2) vertical and horizontal line targets; (3) uniform portion of the phantom; and (4) vertical line targets, with the transducer rotated through 45° about its axial axis. Sample ultrasound images are included in Appendix H.

When no TPX was used, the transducer was placed directly on the skin-mimicking layer. When TPX was used, the transducer was offset from the TPX by 3 mm.

All measurements were performed using a WED-3100 ultrasound beam-former (Shenzhen Well. D, China). The 2.5 and 3.5 MHz measurements were made with a C1-11/50R/3.5MHz transducer and the 5.5 and 8.5 MHz images were acquired with a L1-5/7.5MHz linear transducer. The full specifications of the ultrasound equipment are given in Appendix I. The experimental results and analysis are presented in the following section.

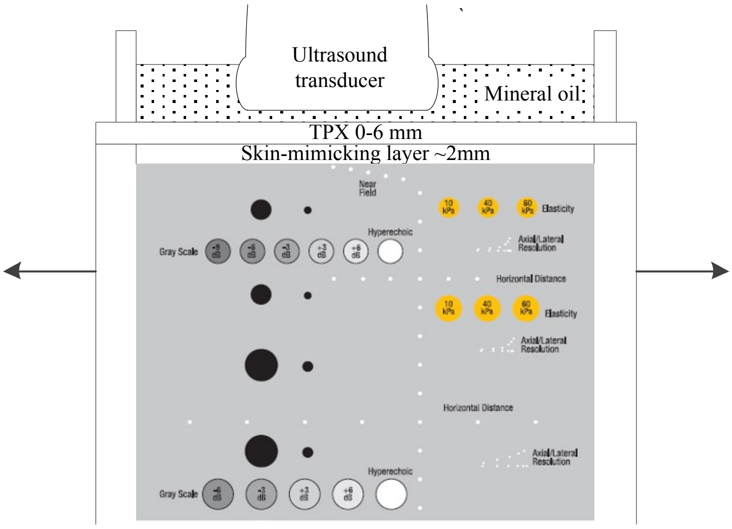

Figure 5.35: Ultrasound Image Quality Experimental Setup

5.4.2 RESULTS AND ANALYSIS

Prior to the presentation of the experimental results, the graphing system, necessitated by the 16 experimental cases, is introduced. Wherever possible, the experimental results were collated into *bubble plots*.

Figure 5.36 shows an example bubble plot for a pseudo measurement, with units of mm. The ultrasound frequency is shown on the vertical axis and the TPX thickness is shown on the horizontal axis. The measurement of interest for each case is represented by a bubble. The diameter of the bubble is scaled to the value printed at its centre. This value is the measurement of interest. Additionally, the units of the measurement are given in the bottom left bubble. Finally, the shaded region around the bubble represents the ±1 standard deviation of the measurement. This representation of the data allows trends with respect to the two control variables – TPX thickness and ultrasound frequency – to be easily identified. Additionally, a visual indication of the spread of the data is provided for. In the case of the geometric conformity data, negative values are represented by a shaded circle.

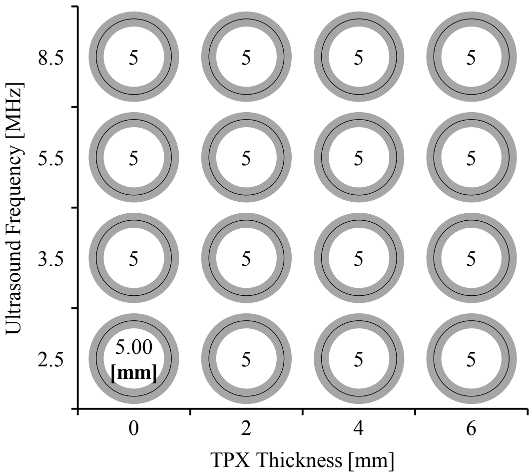

Figure 5.36: Example Bubble Plot. The diameter of each circle is scaled to the value printed at its centre and the units of the measurement are shown in the bottom left bubble. The shaded region gives the ±1 standard deviation of the measurement.

Below, each of the following ultrasound image quality parameters are presented and discussed in turn: (1) transverse resolution (elevation focus); (2) contrast resolution; (3) penetration depth; (4) dead zone; (5) spatial resolution; and (5) geometric conformity. The reader is referred to section 2.4.3 for the definition of these terms and the definition of the transverse, axial and lateral directions.

In the results that follow, the effect of TPX thickness is shown to be a function of frequency. For the purposes of conciseness and to remain relevant, the effect of TPX thickness is sometimes only discussed for the 3.5 MHz case. This is because the following analysis shows that this best represents the most likely frequency case for the future Aceso ultrasound system.

Transverse resolution. The mean of the FWHM for all 16 experimental cases is plotted in Figure 5.37. As detailed in section 2.4.3, the FWHM is the width of the PSF at the -6dB drop off and is the inverse of the resolution. An increase in the transverse FWHM with decreasing frequency is observed. There is also a step change in the transverse FWHM between the high frequency (HF) and low frequency (LF) ultrasound transducers. The transverse FWHM is shown to decrease slightly with increasing TPX thickness from 5.31 mm to 5.02 mm at 3.5 MHz (5.5%) and from 3.8 mm to 3.3 mm at 8.5 MHz (13%).

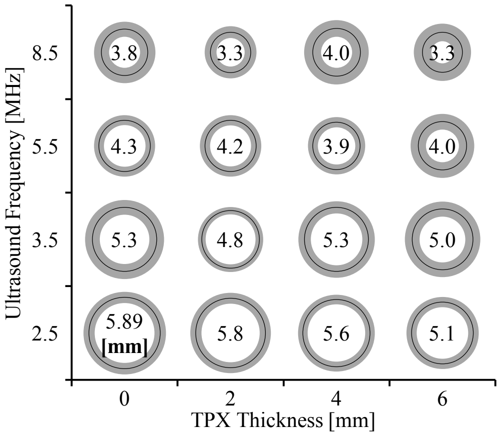

Figure 5.37: Bubble Plot of Transverse FWHM versus Ultrasound Frequency and TPX Thickness

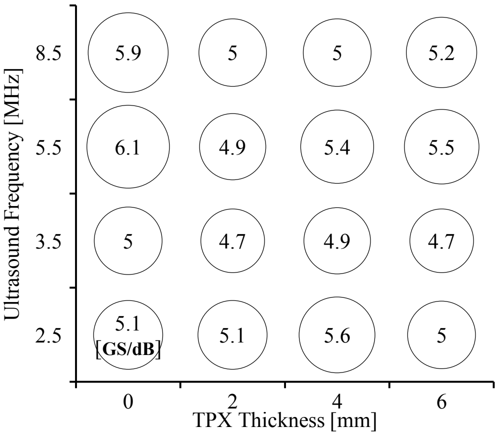

Figure 5.38: Bubble Plot of Contrast Resolution versus Ultrasound Frequency and TPX Thickness

Contrast resolution. Figure 5.38 shows the variation of contrast resolution for the experimental cases. There is no discernible pattern to the data distribution and it is hence concluded that the variation is within the uncertainty of the measurement. The standard deviations of the measurements are not plotted because they are not provided by the QA4US software. Nevertheless, an inspection of the linear curve fittings indicated the presence of some uncertainty. A representative example of the fitting is included in Appendix J.

Penetration Depth. As per RE05, the ultrasound system must be capable of imaging breasts up to 80 mm thick (when compressed). Taking into account the thickness of the imaging stack, the total ultrasound penetration must be in the region of 90 mm.

The penetration depth measurements produced a voluminous set of data which is plotted in Figure 5.39. For practical reasons, only the upper and lower plots for the HF and LF transducers are labelled. Nevertheless, it is clear that the penetration depth is heavily dependent on frequency and in particular, the centre frequency and/or other characteristics of the transducer.

The QA4US definition of penetration depth was found to be a poor indicator of the effective imaging depth, due to the variation in the peak greyscale level across the 16 cases[1]. Instead a minimum threshold was set for the acceptable grayscale level. Above this level the tissue grain, or rather phantom grain, was deemed to be of diagnostic quality[2]. This threshold was set at 70 (70 GS), and is represented by a dashed line in Figure 5.39. From this analysis, two things are immediately clear: (1) the HF transducer does not achieve an acceptable penetration depth; and (2) the LF transducer produces poor image quality in the near field. The latter is the result of the low grayscale level in the near field.

---

[1] QA4US defines the penetration depth as the axial distance at which the average greyscale level has decreased by 6dB from the maximum.

[2] Grey levels are compared directly because all images were acquired with the same gain settings, and the contrast resolution of all cases is assumed equal as previously discussed.

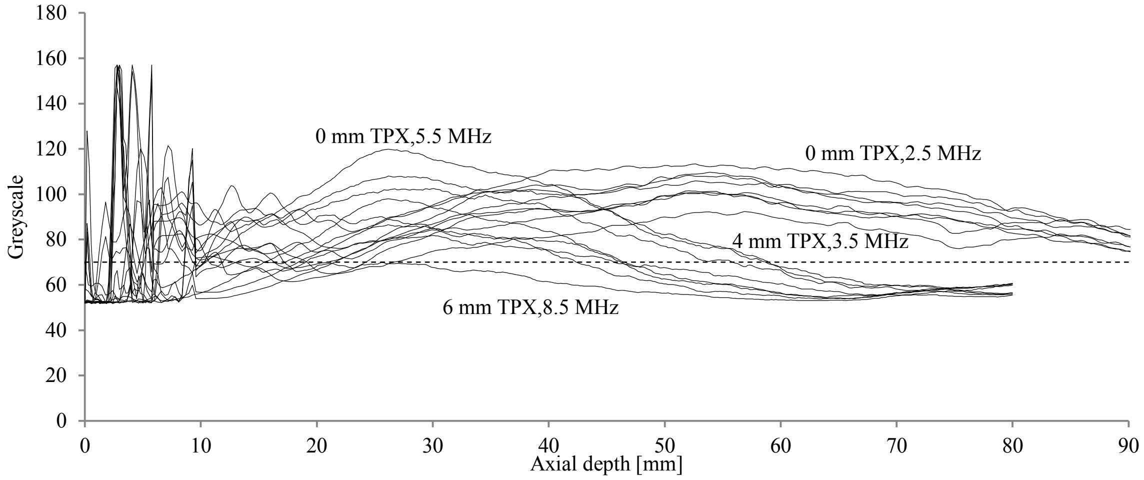

Figure 5.39: **Variation of Penetration Depth with Ultrasound Frequency and TPX Thickness. The acceptable grey level of 70 is shown with a dashed line. For the purposes of clarity, only the extremes of the data distribution are labelled. The 8.5 & 5.5 MHz measurements were performed with the HF transducer while the 3.5 & 2.5 MHz measurements were performed with the LF transducer.**

In Figure 5.39, the large amplitude spikes in the 0-10 mm range give an indication of the reflective losses of the coupling stack. The total reflective losses were estimated by computing the sum of the greyscale levels for each case. These were then normalised to unity. The results, plotted in Figure 5.40, agree well with those predicted by ultrasound transmission theory (see section 2.4.2). That is to say, the addition of TPX caused a step change in the reflective losses. Additionally, the reflective losses appear to be independent of frequency. However, there is a slight decrease in the reflective losses with increasing TPX thickness. This is more likely caused by an increase in attenuation losses than a thickness-dependent change in reflective losses.

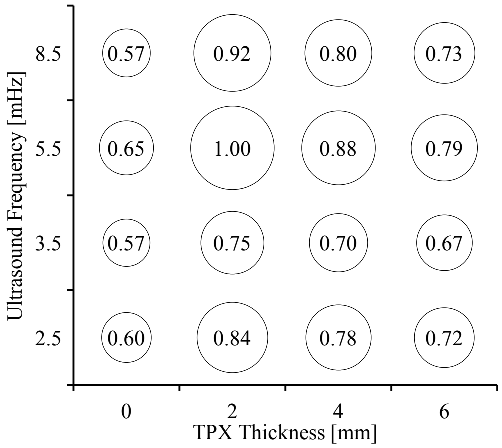

Figure 5.40: **Bubble Plot of Normalised Cumulative Greyscale Level versus Ultrasound Frequency and TPX Thickness**

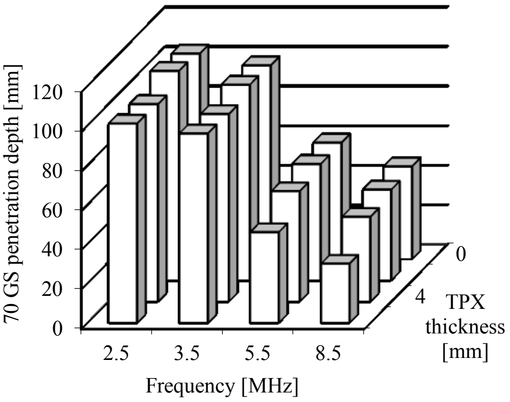

Figure 5.41: **Variation of 70 GS Penetration Depth with Ultrasound Frequency and TPX Thickness**

Figure 5.41 summarises the penetration depth for the 16 cases. The threshold is the 70 GS level as discussed above. Two important trends are highlighted by this plot: (1) frequency has a far greater effect on penetration depth than TPX thickness; and (2) the reduction in penetration depth caused by TPX increases with increasing frequency. This second point is attributed to the attenuation of TPX increasing with frequency. The decrease in transmission depth with 6 mm of TPX is 3 mm and 17 mm for the 3.5 MHz and 8.5 MHz cases, respectively. And the resulting penetration with 6 mm of TPX is 96 mm at 3.5 MHz and 30 mm at 8.5 MHz.

In conclusion, acceptable penetration depth could not be achieved at frequencies above 3.5MHz. The centre frequency of the transducer appears to be significant in this regard. Additionally, the effect of TPX on penetration depth is reduced with decreasing frequency. At 3.5 MHz, the TPX caused only a 3 mm decrease in penetration depth. It is based on these results that the earlier recommendation of a LF transducer was made. However, the degradation in near field image quality should also be taken into consideration in the specification of the Aceso ultrasound system.

Dead zone. Even though the near-field image intensity is decreased at low frequencies, the dead zone was a constant 2 mm in all 16 experimental setups. It is hence concluded that the offset created by the skin and/or TPX and oil improved the dead zone performance, but that the first two dead zone targets were lost in the skin-phantom reflections.

Axial resolution. The axial FWHM is plotted in Figure 5.42. The axial FWHM is shown to be most dependent on the transducer type (increasing for the LF case) with the thickness of TPX having no definitive effect.

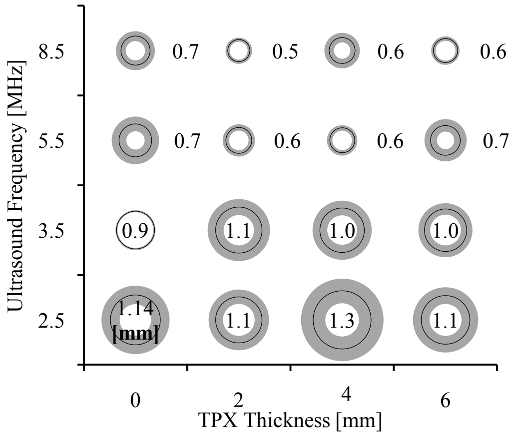

Figure 5.42: Bubble Plot of Axial FWHM versus Ultrasound Frequency and TPX Thickness

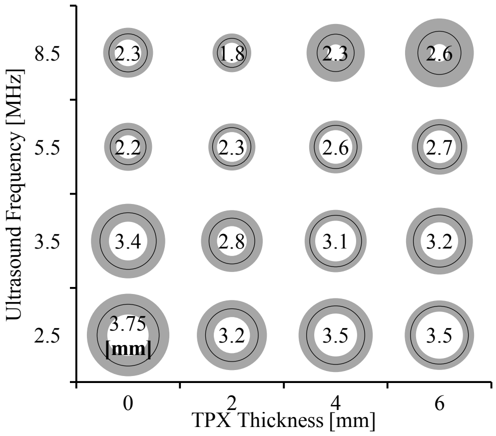

Figure 5.43: Bubble Plot of Lateral FWHM versus Ultrasound Frequency and TPX Thickness

Lateral resolution. The lateral FWHM results are plotted in Figure 5.43. The results show that the lateral FWHM increases with decreasing frequency. Additionally, at high frequencies, the TPX increases the FWHM; whereas, at low frequencies it appears to have a focusing effect, slightly reducing the lateral FWHM. At 3.5 MHz, a 6% decrease in lateral FWHM is caused by TPX, and at 8.5 MHz, a 13% increase results.

Axial geometric conformity. Figure 5.44 shows the axial geometric conformity results. Note that negative errors are shown greyed out. The geometric conformity is the percentage error in distances measured on the ultrasound image using, for example, digital callipers. The results show the axial conformity to be a function of the transducer. The TPX caused a negative change in the percentage error of ~3% at 3.5 and 8.5 MHz. This change does not appear to be a function of TPX thickness or frequency.

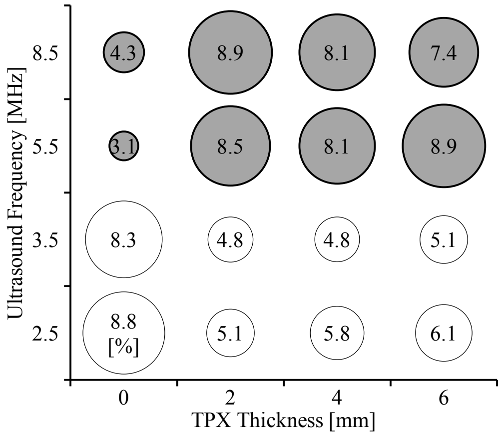

Figure 5.44: **Bubble plot of Axial Geometric Conformity versus Ultrasound Frequency and TPX Thickness**

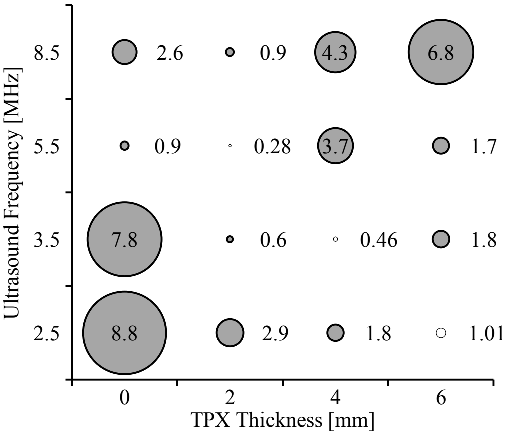

Figure 5.45: **Bubble Plot of Lateral Geometric Conformity versus Ultrasound Frequency and TPX Thickness**

Lateral geometric conformity. Figure 5.45 shows the lateral geometric conformity results. No logical trends can be identified from the plot. However, it is noted that the length of the measurement for this case was 20-30 mm versus 70-100 mm for the axial measurements. This is a possible explanation for the large variation in the measurements.

5.4.3 INTERIM CONCLUSIONS

It is clear from the results that – for the LF and HF ultrasound transducers used here – it is not possible to achieve an acceptable penetration depth at or above 5.5MHz. However, sufficient penetration was achieved at both 2.5 and 3.5 MHz. Because FWHM decreases as a function of frequency, it is nevertheless preferable to use a frequency that is as high as possible (see section 2.4.2). For this reason the effect of the HSBP coupling stack on the ultrasound image quality is summarised for the 3.5 MHz case in Table 5.3. Additionally, in the unlikely event that some other HF transducer is able to achieve acceptable penetration, the effects of the coupling stack at 8.5 MHz are also summarised.

Table 5.3 shows that the effect of the coupling stack on the ultrasound image quality is limited, but worsens with increasing frequency. At 3.5 MHz the stack had a marginally negative effect on the transverse resolution, causing an increase of 5.5% in the transverse FWHM. Similarly, the penetration depth was reduced by 3 mm and a 3% error was measured in the axial geometric conformity. In contrast, the coupling stack improved the lateral resolution by 6% but the mechanism for this is unknown.

Considering the SRS for the HSBP, the success of the ABUS integration (RE01) cannot be fully quantified owing to the failure of the ultrasound system. However, in the integration testing of the HSBP the ultrasound transducer was successfully coupled to the compression plate. Additionally, the ultrasound image quality tests indicate that the HSBP should have minimal effect on the image quality at low frequencies. On this basis, it may be concluded that ABUS has been successfully integrated with FFDM, as illustrated by the acquisition of a first dual-modality image (see Figure 5.34). That being said, the diagnostic quality of the Aceso dual-modality system and the performance of the HSBP (RE04 & CR01) can only be fully assessed through clinical testing of a functional ultrasound system. This is especially true with respect to the reduction in ultrasound frequency, necessitated by the coupling stack losses.

Table 5.3: Summary of the Effect of the HSBP on the Ultrasound Image Quality

Variable	Effect of HSBP on the ultrasound image quality	
	3.5 MHz	8.5 MHz
Transverse FWHM	5.5% increase	13% increase
Contrast resolution	No change	No change
Penetration depth[1]	3 mm decrease	17 mm decrease
Dead zone	No change	No change
Axial FWHM	No change	No change
Lateral FWHM	6% decrease	13 % increase
Axial geometric conformity	3% negative error	3% negative error
Lateral geometric conformity	Inconclusive	Inconclusive

---

[1] Because the nominal measurements vary significantly for the 3.5 MHz and 8.5 MHz cases, this measurement is not reported as a percentage.

Chapter 6: DISCUSSION AND CONCLUSIONS

6.1 DISCUSSION

In this section the work of this thesis is summarised and the major results are discussed for the purposes of drawing conclusions.

The topic of this thesis is: (1) the design; (2) the construction; and (3) the testing of a hermetically sealed breast platform (HSBP) for dual-modality mammography (FFDM+ABUS). These three objectives were executed in five stages:

i. The contextualisation and specification of the design task (Chapter 1)
ii. A review of the relevant literature and existing design solutions (Chapter 2)
iii. The drawing up of design specifications, the development and selection of theoretical design concepts and the development and testing of design prototypes (Chapter 3)
iv. The detailed design of the HSBP (Chapter 4)
v. The evaluation of the performance of the HSBP (Chapter 5)

This discussion addresses the relevant aspects of each of these five stages in turn.

Breast cancer claims nearly half a million lives annually. At present, early detection and treatment are the most effective means of reducing mortality. Even though mammography is the gold standard in breast cancer screening, it does not perform well in the case of dense breasts. Conversely, ultrasound is well suited to the imaging of dense breasts, and has been shown to significantly improve the sensitivity and specificity of breast cancer screening.

However, ultrasound is normally used only as an adjunct to X-ray mammography. The disadvantages of this approach include: variable image quality; poor co-registration of X-ray and ultrasound images; and increased costs and patient anxiety. In response to these shortcomings, the Aceso FFDM+ABUS system aims to acquire both X-ray and 3D ultrasound simultaneously.

The architecture of the Aceso was detailed in section 1.1.4. The scanning X-ray and ultrasound architectures were introduced along with the Pandia, a CCD X-ray detector. The importance of the dynamic alignment of the collimator and Pandia was also discussed. Similarly, the importance of matching the Pandia's scan speed to its CCD clocking speed was highlighted.

Importantly the architecture of the scanning X-ray and ultrasound systems were defined as input constraints to the design and were hence outside the scope of this research. However, as discussed in section 0, the opportunity later arose to contribute to the design of the next iteration of the ultrasound system.

The most significant challenge in the development of a FFDM+ABUS system is that of coupling the ultrasound transducer to the breast. This is further complicated by the myriad of design constraints, which stem from four sources: (1) the aforementioned architecture of the mammographic arrangement and the Aceso; (2) the clinical requirements of breast imaging; (3) the transmission characteristics of ultrasound; and (4) the ergonomic and regulatory requirements of mammography.

With (1) in the previous paragraph already characterised, Chapter 2 sets about defining (2) through (4). The chapter begins with an introduction to the anatomy of the breast and the pathology of breast cancer. From this, the importance of X-ray spatial and contrast resolution is established, while the importance of imaging the axillary lymph nodes is also shown.

In section 2.3, MTF, NPS and DQE are introduced as measures of the aforementioned spatial and contrast resolution. Their use is endorsed and enforced by several regulatory authorities included the IEC. MTF is used to quantify the spatial resolution while NPS quantifies the noise of the system and hence its contrast resolution. DQE combines MTF and NPS in a single measurement that quantifies the overall performance of the X-ray imaging system. Additionally, DQE is a useful indicator of the dose efficiency of a system. In Part III of Chapter 5 these three metrics are used to evaluate the effect of the HSBP on the X-ray image quality.

In section 2.4, several themes pertaining to the ultrasound system were addressed. The first of these was the need for a *coupling stack* to acoustically couple the ultrasound transducer to the breast (see section 2.4.1). The purpose of the coupling stack is to: support the compression of the breast and take up any deflection in the compression plate, while maintaining the acoustic coupling between the ultrasound transducer and the breast.

Additionally, the need for coupling fluid/gel to lubricate the coupling-stack-to-transducer interface was shown. This fluid represents one of the most significant challenges of FFDM+ABUS. The presence of fluid in the breast platform poses a risk to the integrity of the Pandia (the X-ray detector) and the scanning mechatronics. Additionally, any irregular build-up of fluid on the underside of the compression plate would result in unacceptable X-ray artefacts. The resolution of this issue forms the basis of the design problem.

In section 2.4.2, the role of attenuation, reflection and refraction in the degradation of ultrasound image quality is discussed. Additionally, the importance of selecting a suitable ultrasound frequency was highlighted. Specifically, it was shown that although attenuation decreases with decreasing frequency, there is a corresponding increase in the FWHM. That is to say the resolution performance is degraded. This information proved useful in the selection of the compression plate material and the optimisation of the coupling stack.

Section 2.4 concludes with a study of the six ultrasound image quality metrics:

i. Transverse resolution defines the beam width in the scan direction and hence has important implications for ABUS.
ii. Contrast resolution is similar to NPS and gives an indication of the ultrasound sensitivity.
iii. Penetration depth is an important measure for FFDM+ABUS as it defines the maximum depth at which ultrasound, of diagnostic quality, can be obtained. For the Aceso the lower limit of the penetration depth is 80 mm of breast tissue or 90 mm when the coupling stack is taken into consideration.
iv. The dead zone defines the near-field performance of the ultrasound system.
v. The spatial resolution is akin to MTF and is defined by the -6dB spread of a point target or the FWHM.
vi. The geometric conformity is the error in measurements made on the image using digital callipers, when compared to their real-world values.

In part IV of Chapter 5, these metrics are used to evaluate the effect of the coupling stack on the ultrasound image quality.

In section 2.5, the fourth set of constraints – which stem from the ergonomic and regulatory requirements – is detailed. Here the importance of minimising the imaging dead space is shown. This is especially true for the front-edge dead space which is limited by the IEC to no more than 5 mm. This design constraint was a dominant factor in the selection of the final design concept.

With the design constraints fully characterised, section 2.6 sets about reviewing the attempts of others to solve the challenges of FFDM+ABUS. The review of these approaches and the implementation thereof provided much useful information. In particular, the prevalent use of TPX as a compression plate material was highlighted. And additionally, the ultrasonic implications of the use of TPX were also revealed. These included attenuation of the ultrasound and the introduction of refraction artefacts.

Although several prototype FFDM+ABUS system have been developed, only the work done under the guise of Fischer attempts to implement FFDM+ABUS using an architecture similar to that of the Aceso. They make use of a fluid-filled coupling chamber to achieve compression-plate-to-transducer coupling. The coupling chamber, patented by Philips, implements a compliant sliding seal around its periphery. Coupling fluid is sucked through the coupling chamber to ensure the absence of air bubbles and maintain an effective seal.

The failure of Fischer to develop this concept beyond the working prototype stage is evidence of some unsolved and fundamental issues. It is suspected that residual fluid on the underside of the compression plate and the management thereof is one such issue.

In a review of innovative ultrasonic coupling solutions, from outside the sphere of mammography, a pertinent design patent was discovered. This patent illustrates the use of a hermetically sealed coupling chamber, wherein a scanning ultrasound transducer is fully submerged, for the purpose of finger print recognition.

With the background to the design fully characterised, the SRS for the system was defined in the first section of Chapter 3. Subsequently, four design concepts were developed and critically evaluated. This led to concept 2 – a variation of the Fischer-Philips design – being selected for prototyping. The prototype (prototype 1) demonstrated many of the suspected issues with the sliding seal arrangement. That is to say, fluid leaked out of the seal and air leaked into the seal. Additionally, the sliding seal significantly increased the imaging dead space. Based on this result the decision was made to reconsider the concept selection phase.

After discounting the first and third concepts, the decision was made to more carefully evaluate the feasibility of the fourth concept. Concept 4 involved the submerging of the ultrasound transducer, the Pandia and the scanning mechatronics, in a hermetically sealed breast platform or HSBP. The HSBP would then be entirely filled with a non-conductive coupling fluid. In theory, this concept had the potential to elegantly address the imaging dead space requirements and the coupling problem. It is worth noting that, despite the similarities, concept 4 was developed prior to the unearthing of the aforementioned patent for a finger print scanner.

After successfully de-risking this concept it progressed to the prototyping stage. In all, three prototypes were made. The first (prototype 2) served to demonstrate the feasibility of the design. While the second and third prototypes (3 and 4) served to optimise the mechanical and acoustic aspects of the design, respectively.

Having successfully demonstrated the feasibility of the concept and having resolved the preliminary design issues, the final design of the HSBP was begun. In Chapter 4 the detailed design is presented.

It begins with the development and design of the rail carriage (see section 4.2). For this system the focus was ensuring precision control of the Pandia and minimising the imaging dead space and overall size of the HSBP. This was ultimately achieved through the innovative use of a belt drive system and a precision gantry.

The design of the hermetically sealed housing and specifically the coupling stack was considered next (see section 4.3). White pharmaceutical oil 15 (or mineral oil) was selected as the coupling fluid. This selection was based on experimental testing of its electrical non-conductivity, sonolucency and radiolucency.

A thorough study of potential compression plate materials revealed TPX as the only viable option. Although several other materials exhibited suitable X-ray and mechanical properties, only TPX demonstrated the necessary ultrasonic characteristics. Specifically, the acoustic impedance of TPX is well matched to that of breast tissue. This alleviated the problem of acoustic reverberations.

With the compression plate material defined, the task of bonding it to the CFRP portion of the housing was addressed. The notion of bonding the TPX to the CFRP with an adhesive of sorts was discounted in the testing of prototype 3. Additionally, many other solutions were excluded based on the timeline of the Aceso project and lengthy lead-time of such solutions. It was therefore decided that a mechanical seal was the most viable option.

The implementation of the mechanical seal necessitated a means of clamping the TPX to the CFRP. However, the list of suitable clamping solutions was quickly curtailed by the 5 mm front-edge dead space. This was exacerbated by the consideration of geometric magnification. Ultimately, several concepts were prototyped before settling on the *stitched bond* solution. With this approach, an O-ring is placed between the TPX and CFRP and the two materials are stitched together, thereby compressing the O-ring.

In section 4.4, the design of the ultrasound carriage and more specifically the chassis is detailed. Again the importance of minimizing the imaging dead space and the overall size of the HSBP is emphasised. Finally, in section 4.5 the cable management system and the general assembly of the HSBP are presented.

With the design phase complete, the work entered into the manufacture and assembly stage. The performance of the design in this regard is evaluated in Part I of Chapter 5. The manufacturing and assembly performance of the rail carriage were found to be exemplary. However, there is room to improve the serviceability of the motors and light-gates.

The manufacture of the ultrasound chassis proved more complex. However, the machining challenges were ultimately overcome and the component was manufactured to specification.

The manufacture and assembly of the HSBP housing proved a significant challenge. Specifically, internal stresses in the TPX resulted in the rejection of the first compression plate. However, after more carefully designing the machining workflow, this issue was resolved and the manufacture of the TPX compression plate was easily achieved.

An array of manufacturing challenges was overcome in the production of the CFRP portion of the HSBP housing. Specifically a front-edge thickness of just 0.5 mm was achieved, as was a tolerance of 0.1 mm on the respective reference surfaces. Nevertheless, the top surface of the housing – onto which the O-ring seals – featured some imperfections. As a temporary solution these imperfections were filled with adhesive and an oversized O-ring was used. However, it is expected that this issue will be easily resolved in the future by modifying the manufacturing process to ensure proper impregnation of the CFRP surrounding the stitching holes.

The process of stitching the TPX to the CFRP was found to be labour intensive and time consuming. Additionally, the integrity of the seal was found to be thermally sensitive. That is to say, at temperatures above 40°C the CFRP was found to soften, releasing the O-ring compression and causing the seal to fail. This latter issue is expected to be resolved in later versions through the use of a more thermally stable CFRP resin.

Despite the complications of the stitched bond, at present, it is the only known means of creating a hermetic seal that does not violate the restriction on the front edge imaging space. And, in this regard it may be considered a significant achievement of this design. However, future work should focus on a study of alternate solutions. Special attention should be paid to solutions such as the development of a custom adhesive and the use of innovative manufacturing techniques such as in-moulding and sonic welding. All of these solutions were rejected based purely on the project timeline rather than a proper evaluation of their potential.

Section 5.1.4 discloses the success of the cable management system as well as the two issues with the performance of the cables themselves. In particular, the mineral oil caused the outer sheaths of the cables to stiffen. This was resolved by replacing the sheath with heat-shrink, for the dynamic portion of the cables. Additionally, it was necessary to construct a custom Ethernet cable for the Pandia wherein braiding was used as shielding rather than foil. Although foil is used in commercially available cables, repeated bending of the cable caused the foil to damage the electrical integrity of the cable.

The filling and bleeding of the HSBP was relatively uncomplicated. One remaining issue is the removal of bubbles. This issue arises from the slow release of air held captive within the scanning assembly and the stepper motors. Although untested, it is assumed that this will be easily resolved by bleeding the system after exercising the mechatronics for a period of a few hours or days. Nevertheless, if this fails to remove all the air, the HSBP can be bled in a vacuum chamber. Hence this outstanding consideration is not considered to be significant.

In Part II of Chapter 5, the performance of the HSBP in terms of the SRS is evaluated through a series of laboratory tests. The tests are divided into four laboratory categories: (1) metrological testing; (2) mechatronics testing; (3) compression testing; and (4) integration testing.

In the metrological testing the width of the dual-modality imaging area was found to be 235 mm. Being narrower than small mammographic films, this may be considered to be on the lower limit of acceptability. Nevertheless, the HSBP contributes just 6 mm or 8.3% to the lateral dead space. This is considered to be a major achievement of this design.

Also in the metrological testing, the ability to capture X-rays within 5 mm of the outside front-edge of the HSBP was verified. This represents yet another significant achievement of the HSBP design and serves to validate the stitched bond.

In section 5.2.2 the performance of the rail carriage was evaluated. It was found to provide the necessary precision and mechanical drive power. Although outside the scope of this research, the testing highlighted some pertinent issues with the stability of the PID motor controllers. Specifically, the closed-loop control had to be disabled so as to achieve an acceptable dynamic alignment of the

Pandia and the collimator. The implications of this for the dose efficiency of the Aceso are discussed later in this chapter.

One on-going issue with the rail carriage is the intermittent failure of the optical light-gates. However, because this behaviour could not be replicated in bench tests, the assumption is made that it will be easily resolved when the HSBP is next serviced. As an interim solution the Pandia is driven into the CFRP housing to obtain an absolute position reference.

In section 5.2.3 the performance of the HSBP under compression was studied. Under 200 N of compression the deflection of the HSBP was found to be just 0.3 mm. This was significantly less than the design limit of 2 mm. This is attributed in part to differences between the physical loading case and the case modelled in the FEA.

The other consideration is the thermal variation of the TPX stiffness. It was shown with prototype 2 that the stiffness of TPX reduces significantly at ~40°C. As such, any optimisation of the TPX thickness should be preceded by a study of its performance across the operational temperature range of the Aceso. Although such testing was a planned part of this research, it was curtailed owing to the current thermal sensitivity of the CFRP-TPX bond.

The integrity of the stitched CFRP-TPX bond was evaluated through fatigue testing. The testing verified the strength of the bond. This represents another major design achievement. However, for production versions it is recommended that the number of cycles should be increased in accordance with the expected longevity of the HSBP.

In section 5.2.4 the high-level integration of the ultrasound and X-ray systems into the HSBP and the integration of the HSBP into the Aceso were evaluated. The C-arm attachment was found to perform better than expected – precisely locating the HSBP relative to the collimator. However, it was necessary to change the mounting position of the flexible bladder so as to prevent the downward deflection of the compression plate. The deflection was found to be the result of the hydraulic head generated by placing the bladder below the HSBP. Finally, the HSBP integrated well with the cosmetic and ergonomic skirt.

Although the Pandia was successfully integrated with the HSBP, the integration of the ultrasound system could not be properly evaluated. In preliminary testing, the ultrasound system and specifically the ultrasound transducer were found to be faulty. Specifically, the resulting image quality was not suitable for a clinical trial or even evaluating the performance of the HSBP. Based on this result it was decided to evaluate the effect of the HSBP on the ultrasound system through an equivalent study of the coupling stack, using a HHUS system.

In Part III of Chapter 5 the effect of the HSBP on the X-ray system was quantified. To achieve this, the system MTF, NPS and DQE were measured for three experimental cases, using the methods and computations prescribed by the IEC. In the first case the, a 3 mm thick PMMA compression plate was used as a control. In the second case the TPX compression plate was added below the PMMA and in the third case the full HSBP coupling stack was added below the PMMA. More specifically, in the second case an empty HSBP was used and in the third case it was filled with mineral oil. The resulting MTF, NPS and DQE curves are presented in section 5.3.2 with a subsequent analysis and interim conclusions presented in section 5.3.3. Also in section 5.3.3, the theoretical best case performance of the Aceso was computed and compared to that of the Fischer FFDM+ABUS system and the Fischer SenoScan® commercial system.

In the MTF, NPS and DQE analysis, the HSBP and more specifically the coupling stack resulted in a small decrease in MTF (13% at 5 lp/mm). However, a significant decrease in NPS also resulted (38% at 5 lp/mm). Cumulatively, this led to an increase in DQE of ~4% at 5 lp/mm. Based on these results, it is concluded that the coupling stack has a filtering effect on the X-ray system. Although this leads to some degradation in MTF and hence spatial resolution, the contrast resolution of the system is significantly improved. Thus, as indicated by the increase in DQE, the overall imaging performance has been enhanced by the HSBP.

In the comparison of the Aceso and Fischer systems, the theoretical DQE for the Aceso was computed by scaling the dose measurements to simulate a beam-beam width of 4.5 mm. In the subsequent analysis, the theoretical DQE of the Aceso was found to be ~80% higher than both Fischer systems at 5 lp/mm. This comparison was purely theoretical and future work should focus on experimentally comparing the performance of the Aceso to that of other systems. Nevertheless, this result highlights the potential of the Aceso to outperform its competitors as well as the need to optimise the collimator-gap width.

It is important to note that the clinical X-ray image quality of the system is yet to be evaluated in a clinical trial. Nonetheless, the results of the analysis presented here are a promising indication for the X-ray imaging performance of the HSBP.

In Part IV of Chapter 5, the effect of the HSBP on the ultrasound image quality was studied. Despite the poor performance of the ultrasound system, dual-modality images of a stereotactic breast phantom were acquired with the HSBP and Aceso. Although the ultrasound was not of diagnostic quality, the acquisition served to verify the functional integration of ABUS into the Aceso. This demonstrated the success of the HSBP design in this regard. It is hence concluded that the HSBP has successfully integrated ABUS and FFDM. This represents a significant step forward in the development of a clinically viable FFDM+ABUS system. However, the performance of this integration can only be fully tested with a functional ultrasound system.

To this end, the effect of the HSBP, or more specifically the coupling stack, on the ultrasound image quality was studied using a HHUS system. Using the QA4US ultrasound image quality software, and the experimental setup detailed in section 5.4.1, a total of 16 experimental cases were evaluated.

Because the ultrasound system was under review at the time of this study, the intended ultrasound frequency was yet to be determined. Since ultrasound attenuation is a function of frequency, it was therefore necessary to evaluate the effect of the coupling stack across a range of potential frequencies. This had the added advantage of providing valuable feedback for the design of the ultrasound system.

Additionally, the effect of TPX thickness on the ultrasound image quality was also evaluated. This was done to validate the design of the compression plate and inform any future optimisation of the TPX thickness.

Hence, the image quality was analysed for 0, 2, 4 and 6 mm of TPX at 2.5, 3.5, 5.5 and 8.5 MHz. Importantly, a LF transducer was used for the 2.5 and 3.5 MHz measurements and a HF transducer was used for the 5.5 and 8.5 MHz measurements. The resulting data is presented and analysed in section 5.4.2.

The most significant result of the ultrasound image quality testing relates to the relationship between frequency and penetration depth. The results showed that the penetration depth was just 30 mm at 8.5

MHz compared to 96 mm at 3.5 MHz. The attenuation of the coupling stack (with 6 mm TPX) contributes 17 mm at 8.5 MHz and 3 mm at 3.5 MHz.

For the ultrasound transducers used here, it is clear that even without TPX the necessary penetration of 90 mm could not be achieved at 8.5 MHz or even at 5.5 MHz. Acceptable penetration was however achieved using the LF transducer at 3.5 MHz. This result has important implications for the design of the ultrasound system.

The performance of any ultrasound system is dependent on the ultrasound transducer. Hence it is reasonable to assume that a different transducer may produce better penetration even at high frequencies. However, such a transducer would need to double the penetration measured here. The likelihood of this is somewhat questionable. Nevertheless, the effect of the coupling stack is analysed at both 3.5 MHz and 8.5 MHz in section 0.

As was the case with penetration depth, this analysis shows the effect of the coupling stack on the ultrasound image quality is marginal at low frequencies but becomes more significant with increasing frequency. Additionally, the impact of the TPX thickness is also marginal at low frequencies becoming more important with increasing frequency.

The specific effect of the coupling stack on the remaining image quality metrics is now discussed. The contrast resolution, dead zone, axial resolution and lateral geometric conformity were unaffected by the addition of the coupling stack.

In contrast, the coupling stack increased the transverse FWHM by 5.5% at 3.5 MHz. In practice this equates to a slight reduction in the resolution in the scan direction. The stack caused a small increase in the lateral FWHM of 6% at 3.5 MHz; thereby improving the lateral resolution slightly. Finally, the addition of the coupling stack causes a -3% error in axial measurements made using digital callipers.

It is difficult to draw definitive conclusions regarding the clinical significance of these small gains and losses in image quality. While it may prove useful to evaluate the performance of the ultrasound system using an anthropomorphic ultrasound phantom, such a phantom is not commercially available and the construction of one represents a significant body of work (Madsen et al., 1982). This highlights the importance of testing the ultrasound image quality in the clinical setting.

It is therefore concluded that the HSBP has successfully integrated ABUS and FFDM. Additionally, phantom testing has shown that the HSBP has a marginal effect on the ultrasound image quality at low ultrasonic frequencies. Such frequencies are necessitated by the penetration depth required by the Aceso ultrasound architecture. There exists the possibility that higher frequency ultrasound may be used, in which case the effect of the HSBP will become more significant and efforts should be made to reduce the TPX thickness. Although phantom testing produces useful quantitative information, future work should aim to analyse the effect of the HSBP on the clinical image quality.

6.2 CONCLUSIONS AND RECOMMENDATIONS FOR FUTURE WORK

Based on the discussion in the preceding section the following conclusions are made.

i. In this work a novel hermetically sealed breast platform (HSBP) was designed, constructed and tested.

ii. It has been shown through laboratory testing, X-ray image quality testing and ultrasound image quality testing that the goal of combing ABUS and FFDM in a single system has been achieved.
iii. Importantly it has been achieved in a clinically viable package which abides by the various regulatory and ergonomic requirements of FFDM.
iv. Additionally HSBP has been shown to improve the X-ray image quality through its radiographic noise filtering attributes.
v. In theoretical testing, it was shown that the Aceso could potentially exceed the DQE performance of its competitors by up to 80%
vi. The HSBP has been shown to degrade the ultrasound image quality only slightly.
vii. However, at higher ultrasonic frequencies this degradation becomes more significant.
viii. Such frequencies are unlikely to be implemented as they do not provide for sufficient depth penetration.
ix. Although the X-ray and ultrasound image quality has been evaluated using appropriate and quantitative measures, no determination of the clinical image quality has been made here.

Additionally, the following recommendations for future work are made.

i. Future design work should focus on the optimisation of the TPX thickness and the TPX-CFRP bond.
ii. Additionally, a more in-depth study of the non-conductive coupling fluid may yield a more efficient coupling stack.
iii. The Aceso X-ray image quality should be compared to that of its competitors through an experimental study of MTF, NPS and DQE under equivalent experimental conditions.
iv. Finally, the validation of the clinical performance of the HSBP is of primary importance. It is hence recommended that all aspects of the HSBP are tested in a clinical setting. This is particularly pertinent in the case of the X-ray and ultrasound image quality.

APPENDICES

Appendix A: MOTOR SIZING PYTHON SCRIPT

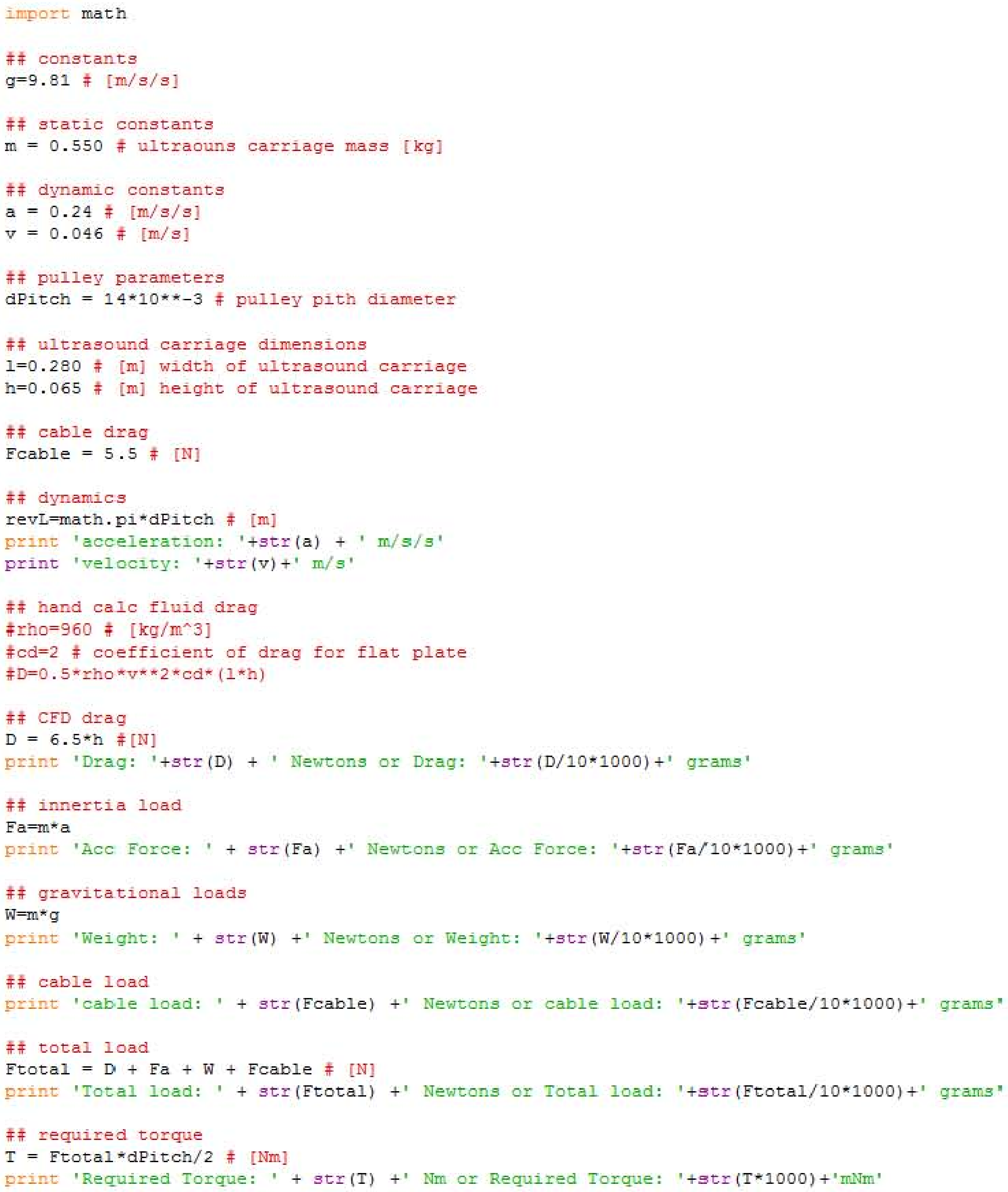

```
import math

## constants
g=9.81 # [m/s/s]

## static constants
m = 0.550 # ultraouns carriage mass [kg]

## dynamic constants
a = 0.24 # [m/s/s]
v = 0.046 # [m/s]

## pulley parameters
dPitch = 14*10**-3 # pulley pith diameter

## ultrasound carriage dimensions
l=0.280 #  [m] width of ultrasound carriage
h=0.065 #  [m] height of ultrasound carriage

## cable drag
Fcable = 5.5 # [N]

## dynamics
revL=math.pi*dPitch # [m]
print 'acceleration: '+str(a) + ' m/s/s'
print 'velocity: '+str(v)+' m/s'

## hand calc fluid drag
#rho=960 #  [kg/m^3]
#cd=2 # coefficient of drag for flat plate
#D=0.5*rho*v**2*cd*(l*h)

## CFD drag
D = 6.5*h #[N]
print 'Drag: '+str(D) + ' Newtons or Drag: '+str(D/10*1000)+' grams'

## innertia load
Fa=m*a
print 'Acc Force: ' + str(Fa) +' Newtons or Acc Force: '+str(Fa/10*1000)+' grams'

## gravitational loads
W=m*g
print 'Weight: ' + str(W) +' Newtons or Weight: '+str(W/10*1000)+' grams'

## cable load
print 'cable load: ' + str(Fcable) +' Newtons or cable load: '+str(Fcable/10*1000)+' grams'

## total load
Ftotal = D + Fa + W + Fcable # [N]
print 'Total load: ' + str(Ftotal) +' Newtons or Total load: '+str(Ftotal/10*1000)+' grams'

## required torque
T = Ftotal*dPitch/2 # [Nm]
print 'Required Torque: ' + str(T) +' Nm or Required Torque: '+str(T*1000)+'mNm'
```

Appendix B: CUSTOM CIRS 040GSE ULTRASOUND PHANTOM

Table B.1: Custom CIRS 040GSE Ultrasound Phantom Acoustic Properties

Acoustic properties		
Variable		Value
Background material I (II)	Material	Zerdine
	Speed of sound	1540 m/s ±10 m/s
	Attenuation coefficient	0.5 (0.7) dB/cm/MHz
Wire targets	Material	Nylon monofilament
Near field group	Number of targets	5
	Diameter	100 µm
	Depth range	1-5 mm
	Vertical spacing	1 mm
Vertical distance group	Number of targets	16
	Diameter	100 µm
	Depth range	1-16 cm
	Vertical spacing	10 mm
Horizontal distance group	Number of groups	2
	Diameter	100 µm
	Depths	4 & 9 cm
	Number of targets	4 & 7 respectively
	Horizontal spacing	10 & 20 mm respectively
Grey Scale Targets	Depth	3 cm
	Diameter	8 mm
	Contrast	-9; -6; -3; +3; +6; >15 dB

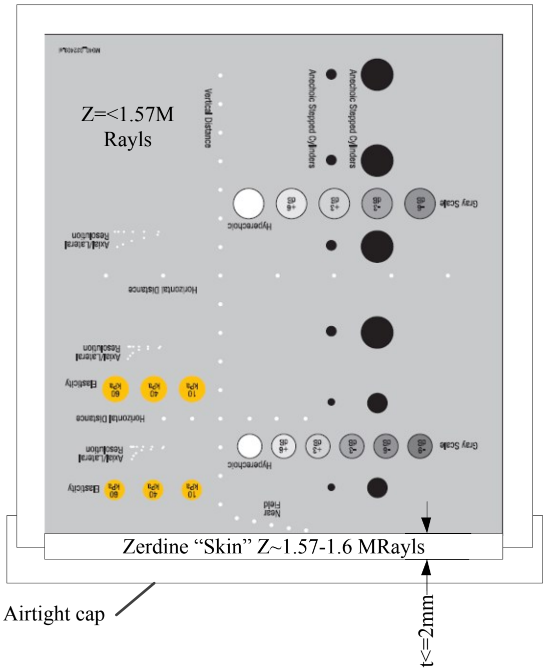

Figure B.1: Custom CIRS 040GSE Ultrasound Phantom

Appendix C: SELECTED MANUFACTURING DRAWINGS

All components were manufactured from the 3D models. Hence the included manufacturing drawings only contain critical tolerances and nominal dimensions.

2. HSBP housing

3rd Angle Projection

6	flange bearing 3x8x3 [SDP a_7y_5mf0803]
7	flange bearing 5x13x4 [SDP a_7y_5mf1305]
9	spacer
11	idler
11.1	needle roller bearing 5x9x9 SDP S99NH2MBN0509
11.2	stock sleeve SDP a_6a50m022gt10
11.3	pulley flange SDP a_6a50m022fa
12	idler
12.1	needle roller bearing 5x9x9 SDP S99NH2MBN0509
12.2	pulley flange SDP a_6a50m022fa
12.3	blank stock
16	tensioning shaft
17	idler shaft
18	shaft extension
20	belt clamp spacer
21	belt clamp
28	B27.7M - 3AM1-5

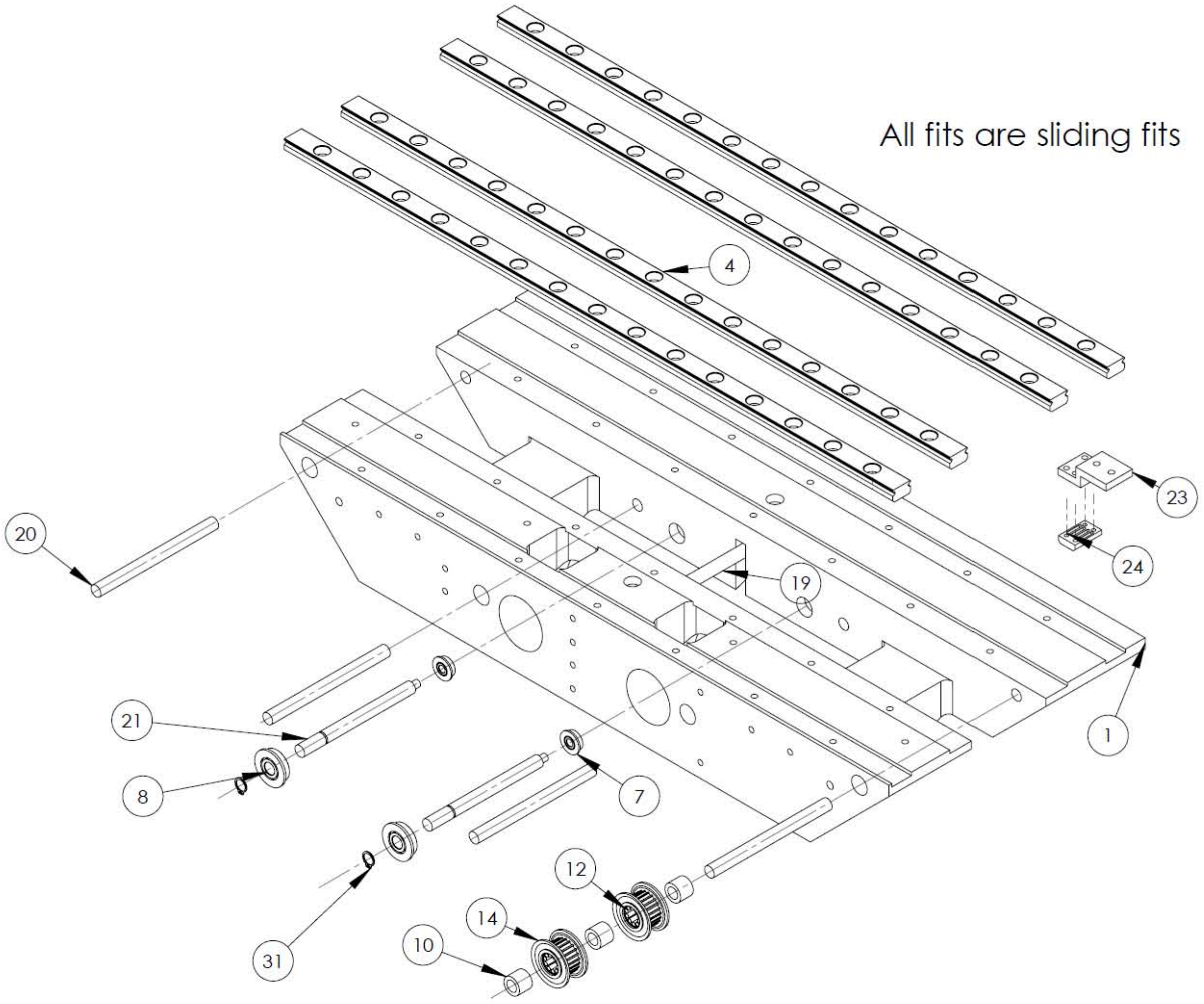

All fits are sliding fits

Scale 2:3	Material	General Assembly	Tolerance General ±0.5 X.X ±0.2 X.XX ±0.1 Hole Centres ±0.1 Angle ±0.5° All dimensions in mm	Remove All Burrs & Sharp Edges Drawn By: Raphael Smith Checked By: James Boonzaier Sheet 1 of 1
A3	Finish	NA		

CapeRay

Date		Rev.		
	17 July 2013	A	Name	HSBP\ **rail carriage**
			Part no.	N/A
			Drawing no.	N/A

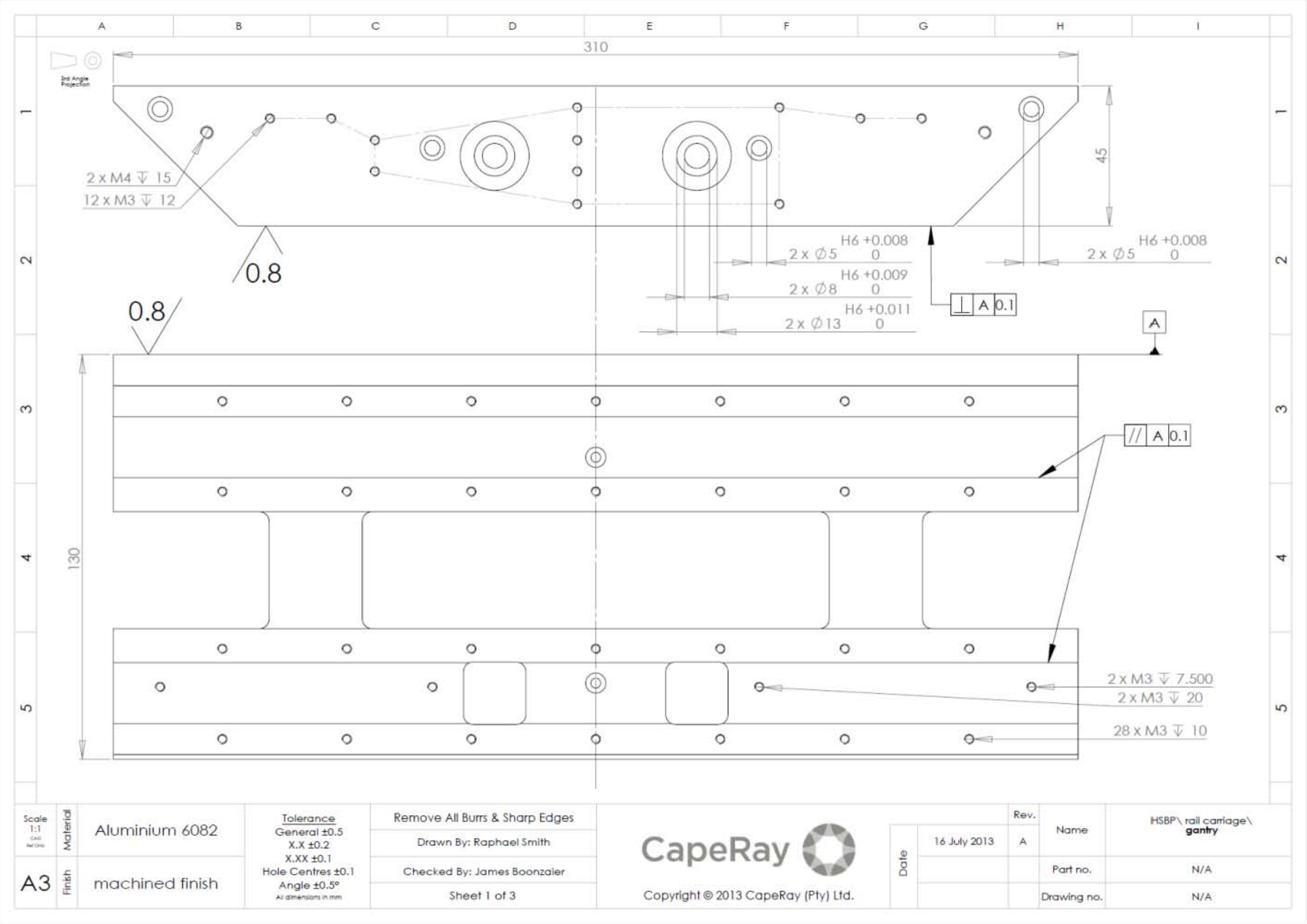
A
B
C
D
E
F
G
H
I
1
2
3
4
5
3rd Angle Projection
310
45
130
2 x M4 ↧ 15
12 x M3 ↧ 12
0.8
0.8
2 x ∅5 H6 +0.008 0
2 x ∅8 H6 +0.009 0
2 x ∅13 H6 +0.011 0
2 x ∅5 H6 +0.008 0
⊥ A 0.1
A
// A 0.1
2 x M3 ↧ 7.500
2 x M3 ↧ 20
28 x M3 ↧ 10
Scale 1:1
Material
Aluminium 6082
A3
Finish
machined finish
Tolerance
General ±0.5
X.X ±0.2
X.XX ±0.1
Hole Centres ±0.1
Angle ±0.5°
All dimensions in mm
Remove All Burrs & Sharp Edges
Drawn By: Raphael Smith
Checked By: James Boonzaier
Sheet 1 of 3
CapeRay
Copyright © 2013 CapeRay (Pty) Ltd.
Date
16 July 2013
Rev.
A
Name
HSBP\ rail carriage\ gantry
Part no.
N/A
Drawing no.
N/A

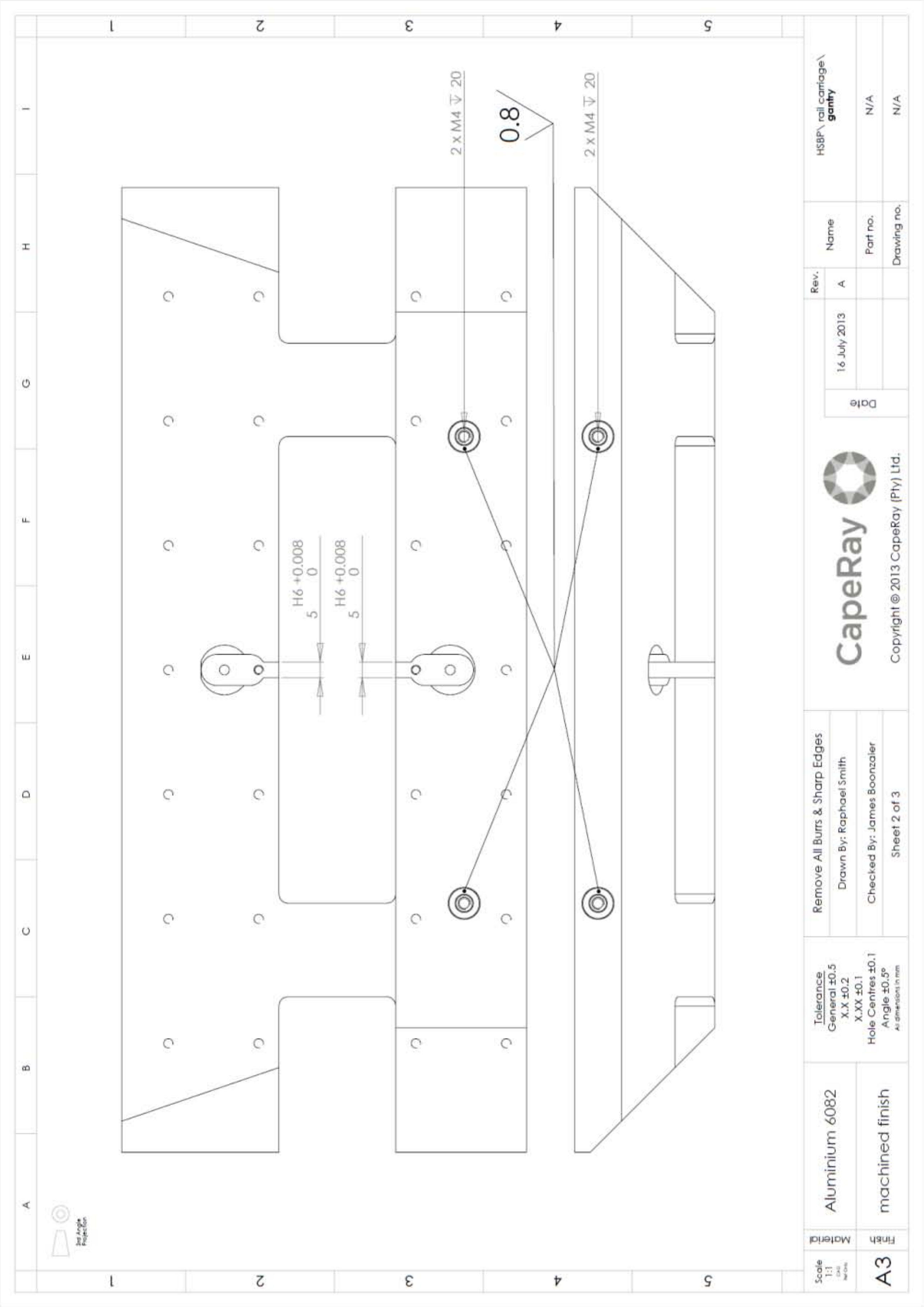
2 x M4 ⊽ 20
0.8
2 x M4 ⊽ 20
5 H6 +0.008 0
5 H6 +0.008 0
HSBP\ rail carriage\ gantry
Name
Rev.
A
16 July 2013
Date
Part no.
N/A
Drawing no.
N/A
CapeRay
Copyright © 2013 CapeRay (Pty) Ltd.
Remove All Burrs & Sharp Edges
Drawn By: Raphael Smith
Checked By: James Boonzaier
Sheet 2 of 3
Tolerance
General ±0.5
X.X ±0.2
X.XX ±0.1
Hole Centres ±0.1
Angle ±0.5°
All dimensions in mm
Material
Aluminium 6082
Finish
machined finish
Scale 1:1
A3
3rd Angle Projection
1
2
3
4
5
A
B
C
D
E
F
G
H
I

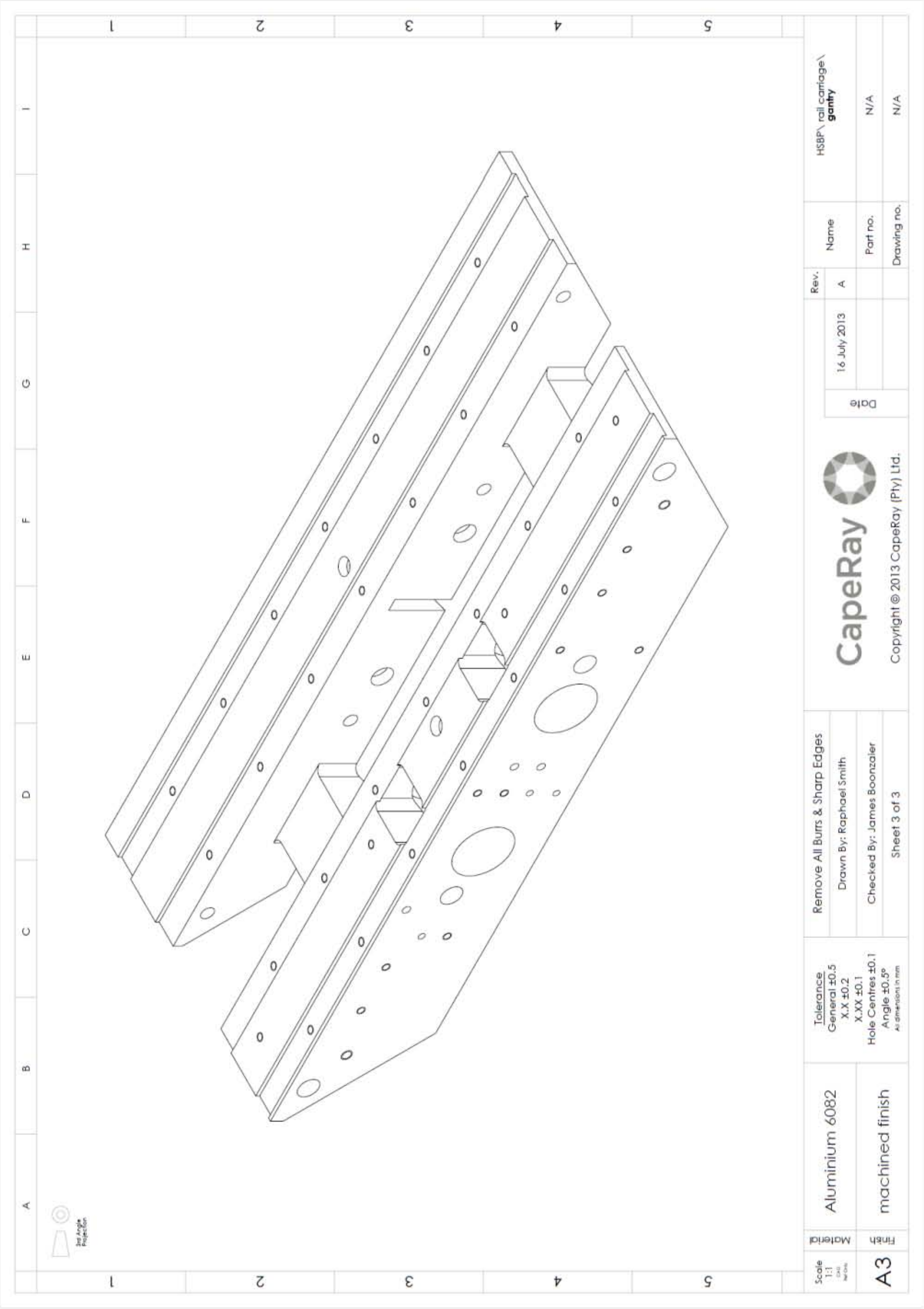

HSBP\ rail carriage\ **gantry**

Name: HSBP\ rail carriage\ gantry
Part no.: N/A
Drawing no.: N/A
Rev.: A
Date: 16 July 2013

CapeRay

Copyright © 2013 CapeRay (Pty) Ltd.

Remove All Burrs & Sharp Edges
Drawn By: Raphael Smith
Checked By: James Boonzaier
Sheet 3 of 3

Tolerance
General ±0.5
X.X ±0.2
X.XX ±0.1
Hole Centres ±0.1
Angle ±0.5°
All dimensions in mm

Material: Aluminium 6082
Finish: machined finish
A3

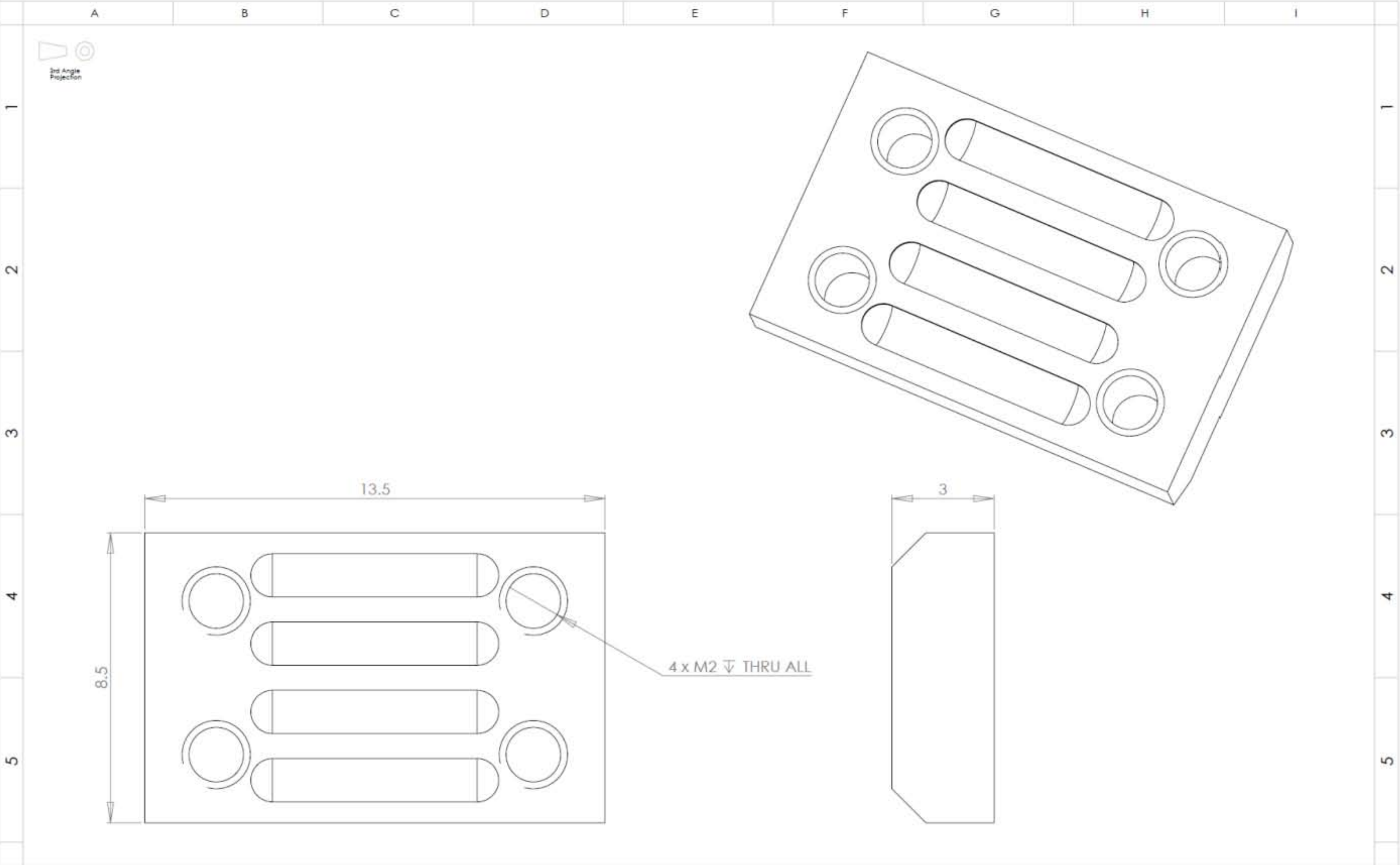

Scale 5:1 CAD Ref Only	Material	Stainless Steel 304	Tolerance General ±0.5 X.X ±0.2 X.XX ±0.1 Hole Centres ±0.1 Angle ±0.5° All dimensions in mm	Remove All Burrs & Sharp Edges	CapeRay	Date		Rev.	Name	HSBP\rail carriage\ **belt clamp**
				Drawn By: Raphael Smith			17 July 2013	A		
A3	Finish	machined finish		Checked By: James Boonzaier					Part no.	N/A
				Sheet 1 of 1	Copyright © 2013 CapeRay (Pty) Ltd.				Drawing no.	N/A

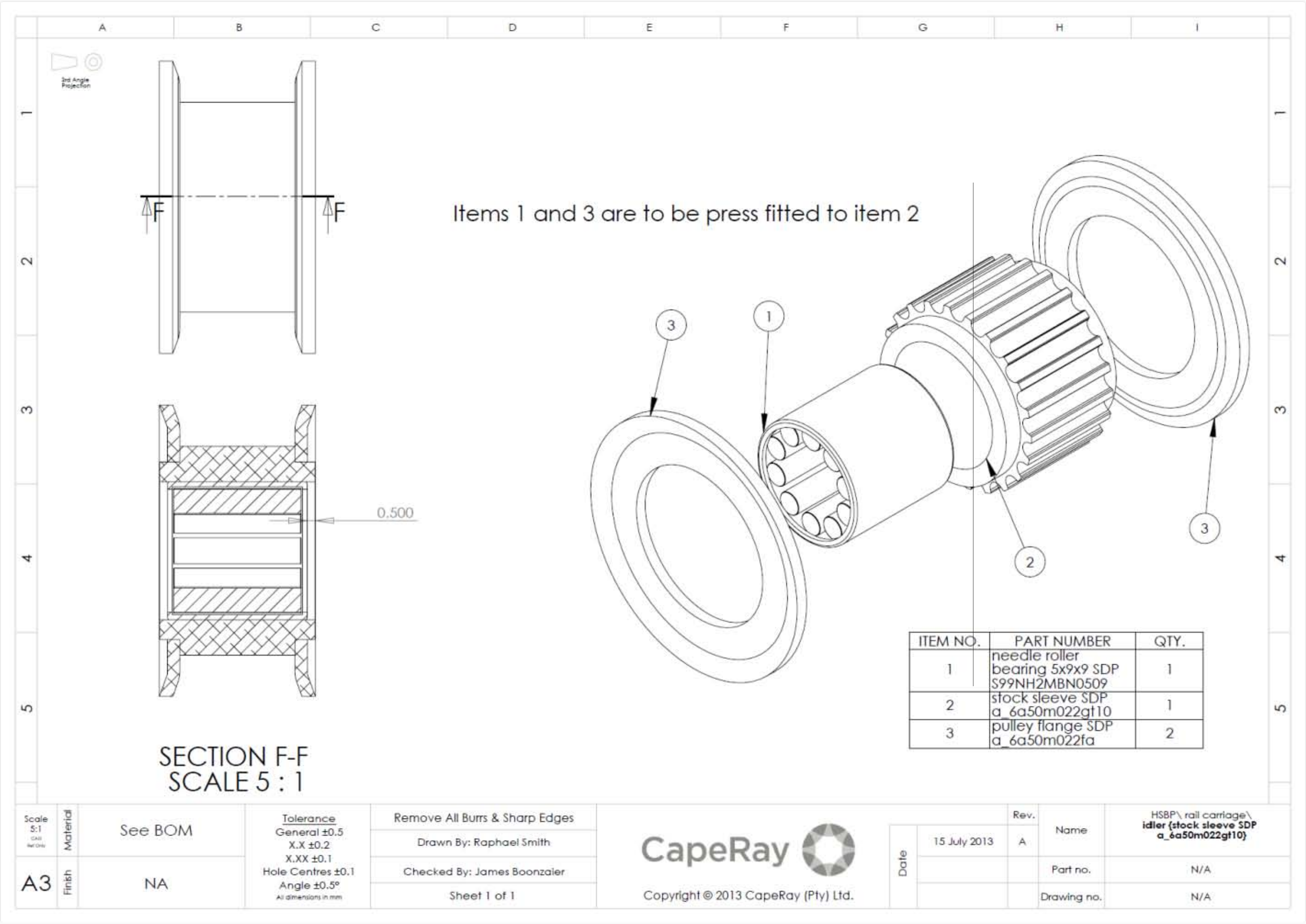

Items 1 and 3 are to be press fitted to item 2

ITEM NO.	PART NUMBER	QTY.
1	needle roller bearing 5x9x9 SDP S99NH2MBN0509	1
2	stock sleeve SDP a_6a50m022gt10	1
3	pulley flange SDP a_6a50m022fa	2

Scale 5:1	Material: See BOM	Tolerance General ±0.5 X.X ±0.2 X.XX ±0.1 Hole Centres ±0.1 Angle ±0.5° All dimensions in mm	Remove All Burrs & Sharp Edges	CapeRay	Date: 15 July 2013	Rev.: A	Name: HSBP\ rail carriage\ **idler (stock sleeve SDP a_6a50m022gt10)**
			Drawn By: Raphael Smith				Part no.: N/A
A3	Finish: NA		Checked By: James Boonzaier				
			Sheet 1 of 1	Copyright © 2013 CapeRay (Pty) Ltd.			Drawing no.: N/A

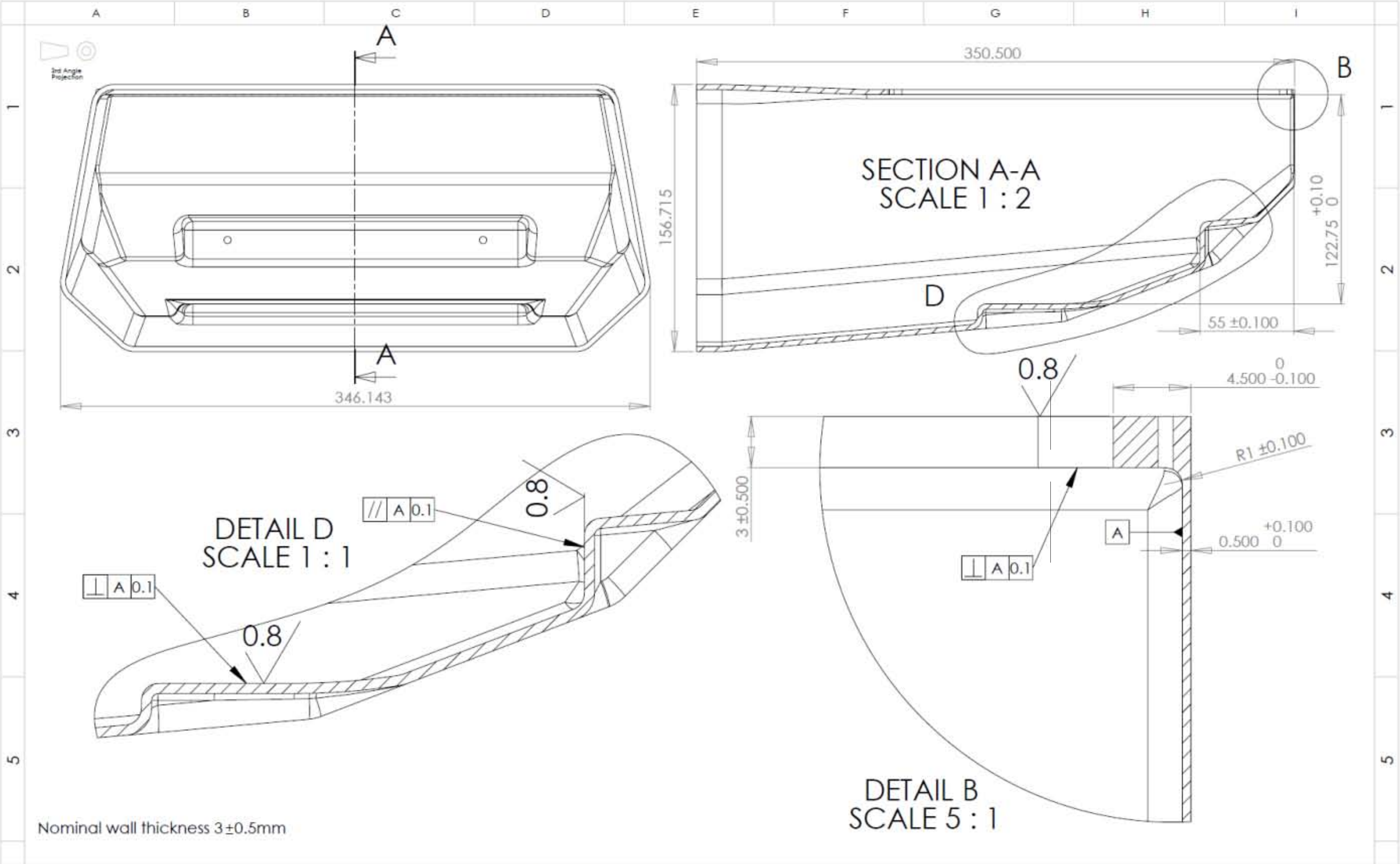

Scale 1:2 CAD Ref Only

A3

Material: CFRP

Finish: 0.5mm nominal, 0.8 microns on sealing faces

Tolerance
General ±0.5
X.X ±0.2
X.XX ±0.1
Hole Centres ±0.1
Angle ±0.5°
All dimensions in mm

Remove All Burrs & Sharp Edges

Drawn By: Raphael Smith

Checked By: John Harverson

Sheet 1 of 1

CapeRay

Date	Rev.	
08 July 2013	V1.0	Name
16 July 2013	V1.1	Part no.
		Drawing no.

HSBP/
CFRP V1.1

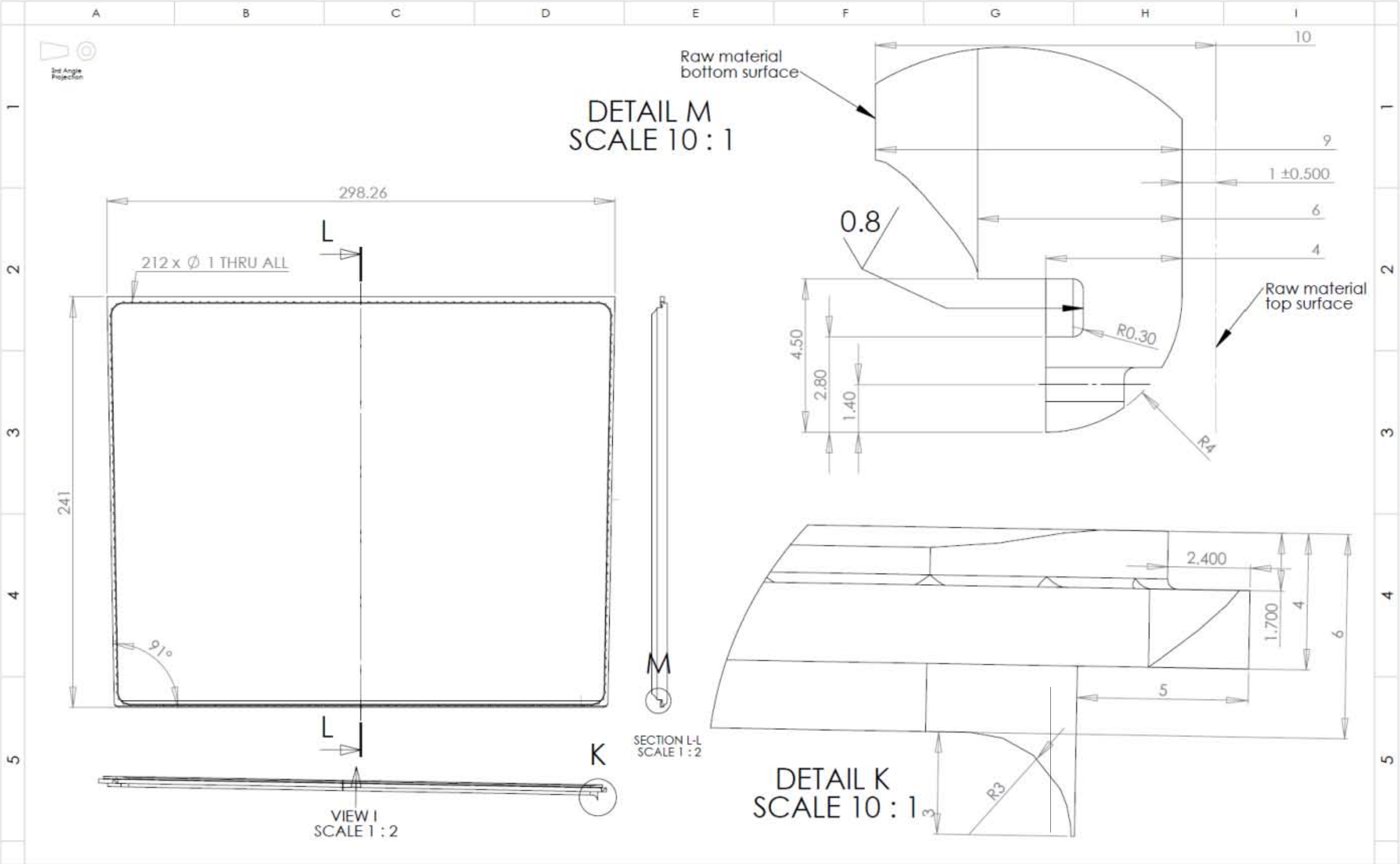

Scale 1:2 CAD Ref Only	Material	**Provided** TPX sheet 10±0.5 x 355 x 355	Tolerance General ±0.5 X.X ±0.2 X.XX ±0.1 Hole Centres ±0.1 Angle ±0.5° All dimensions in mm	Remove All Burrs & Sharp Edges
				Drawn By: Raphael Smith
A3	Finish	flat surfaces to be polished		Checked By: James Boonzaier
				Sheet 1 of 1

CapeRay

Date		Rev.		
	17 July 2013	A	Name	HSBP\ housing\ **TPX**
			Part no.	N/A
			Drawing no.	N/A

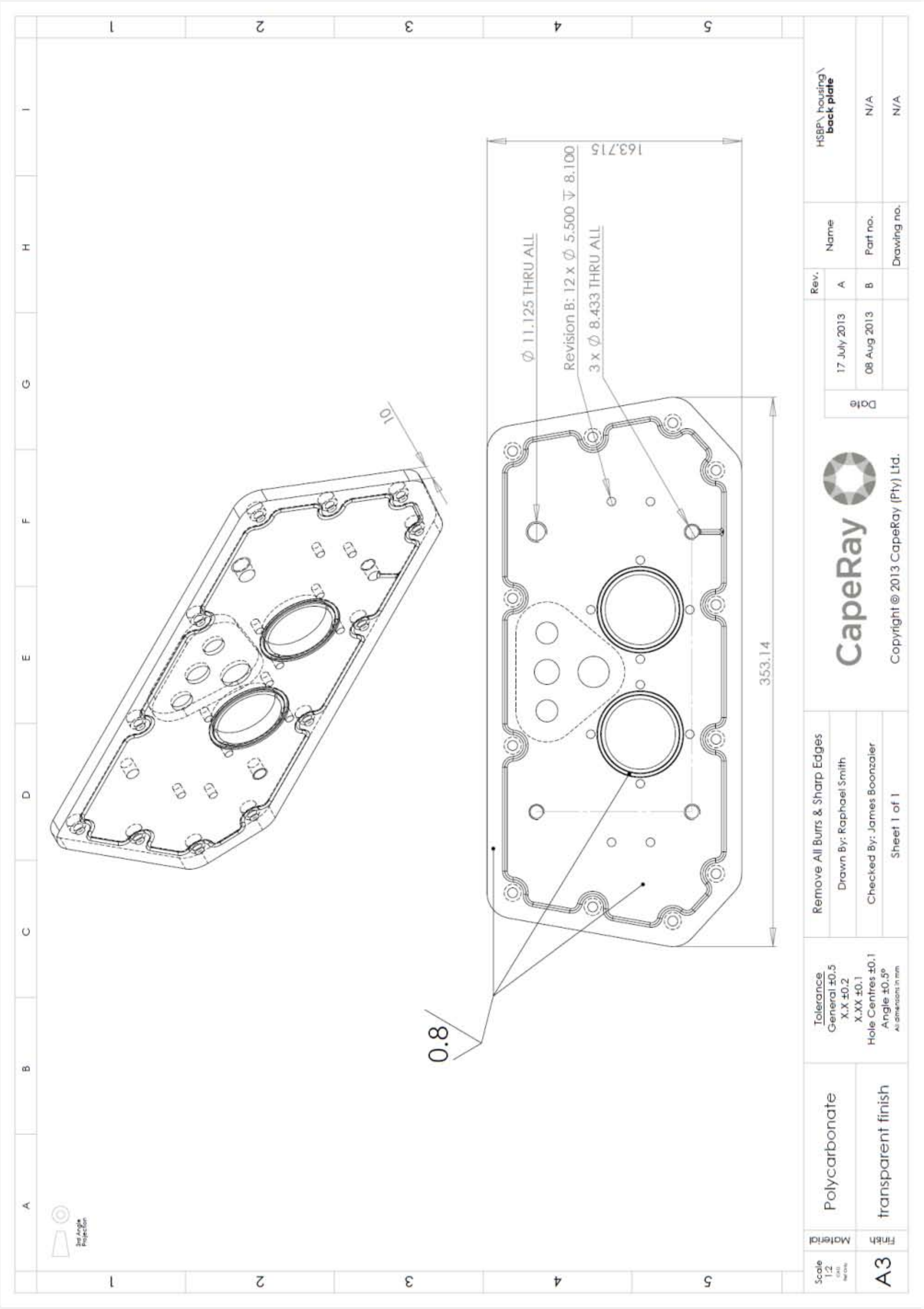
163.715
∅ 11.125 THRU ALL
Revision B: 12 x ∅ 5.500 ↧ 8.100
3 x ∅ 8.433 THRU ALL
10
353.14
0.8
HSBP\ housing\ back plate
Name
Rev.
A
17 July 2013
B
08 Aug 2013
Date
Part no.
N/A
Drawing no.
N/A
CapeRay
Copyright © 2013 CapeRay (Pty) Ltd.
Remove All Burrs & Sharp Edges
Drawn By: Raphael Smith
Checked By: James Boonzaier
Sheet 1 of 1
Tolerance
General ±0.5
X.X ±0.2
X.XX ±0.1
Hole Centres ±0.1
Angle ±0.5°
All dimensions in mm
Material
Polycarbonate
Finish
transparent finish
Scale
1:2
A3
3rd Angle Projection
1
2
3
4
5
A
B
C
D
E
F
G
H
I

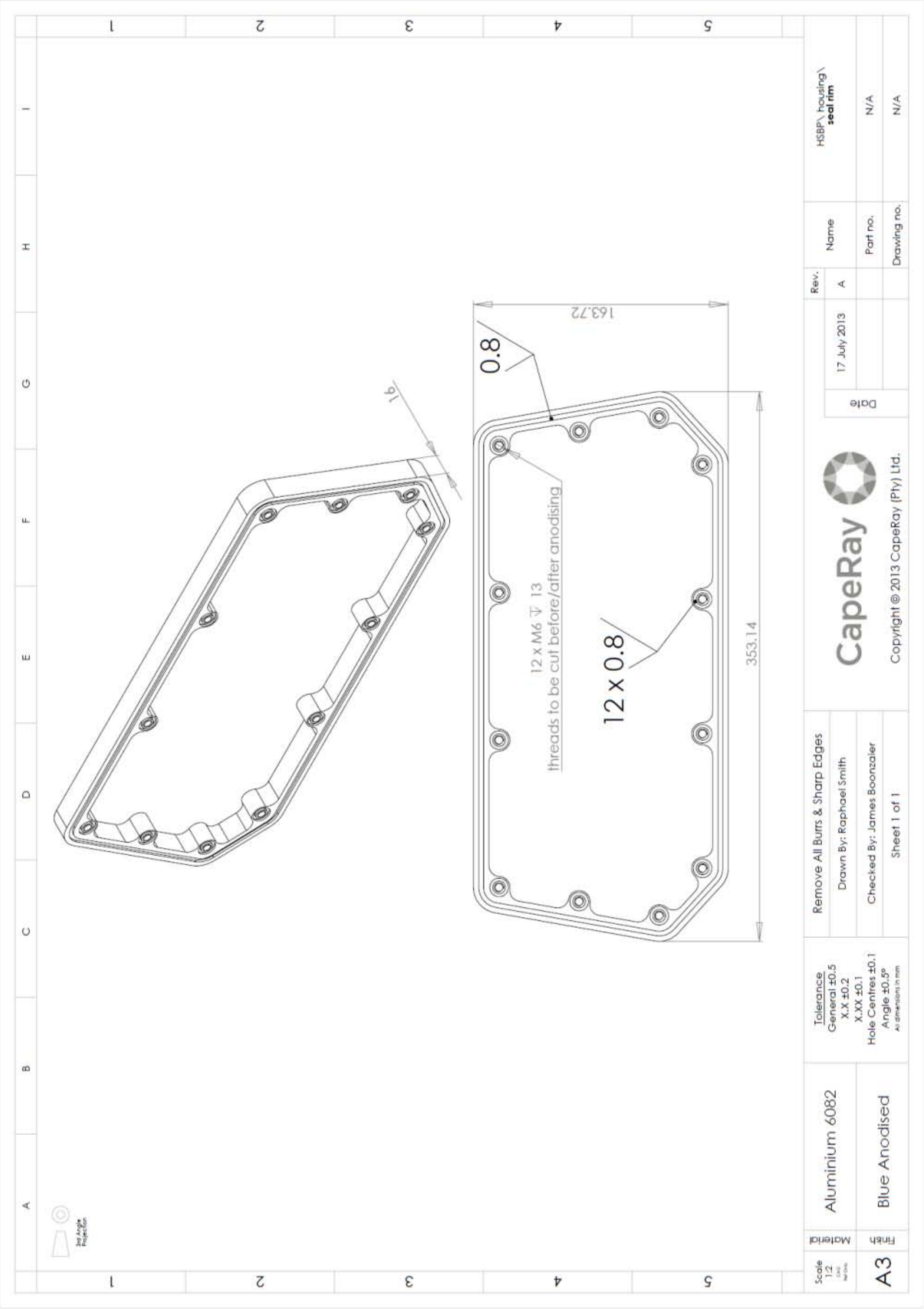
163.72
0.8
16
12 x M6 ↧ 13
threads to be cut before/after anodising
12 x 0.8
353.14
HSBP\ housing\ seal rim
Name
Part no.
N/A
Drawing no.
N/A
Rev.
A
17 July 2013
Date
CapeRay
Copyright © 2013 CapeRay (Pty) Ltd.
Remove All Burrs & Sharp Edges
Drawn By: Raphael Smith
Checked By: James Boonzaier
Sheet 1 of 1
Tolerance
General ±0.5
X.X ±0.2
X.XX ±0.1
Hole Centres ±0.1
Angle ±0.5°
All dimensions in mm
Material
Aluminium 6082
Finish
Blue Anodised
Scale
1:2
A3
3rd Angle Projection
1
2
3
4
5
A
B
C
D
E
F
G
H
I

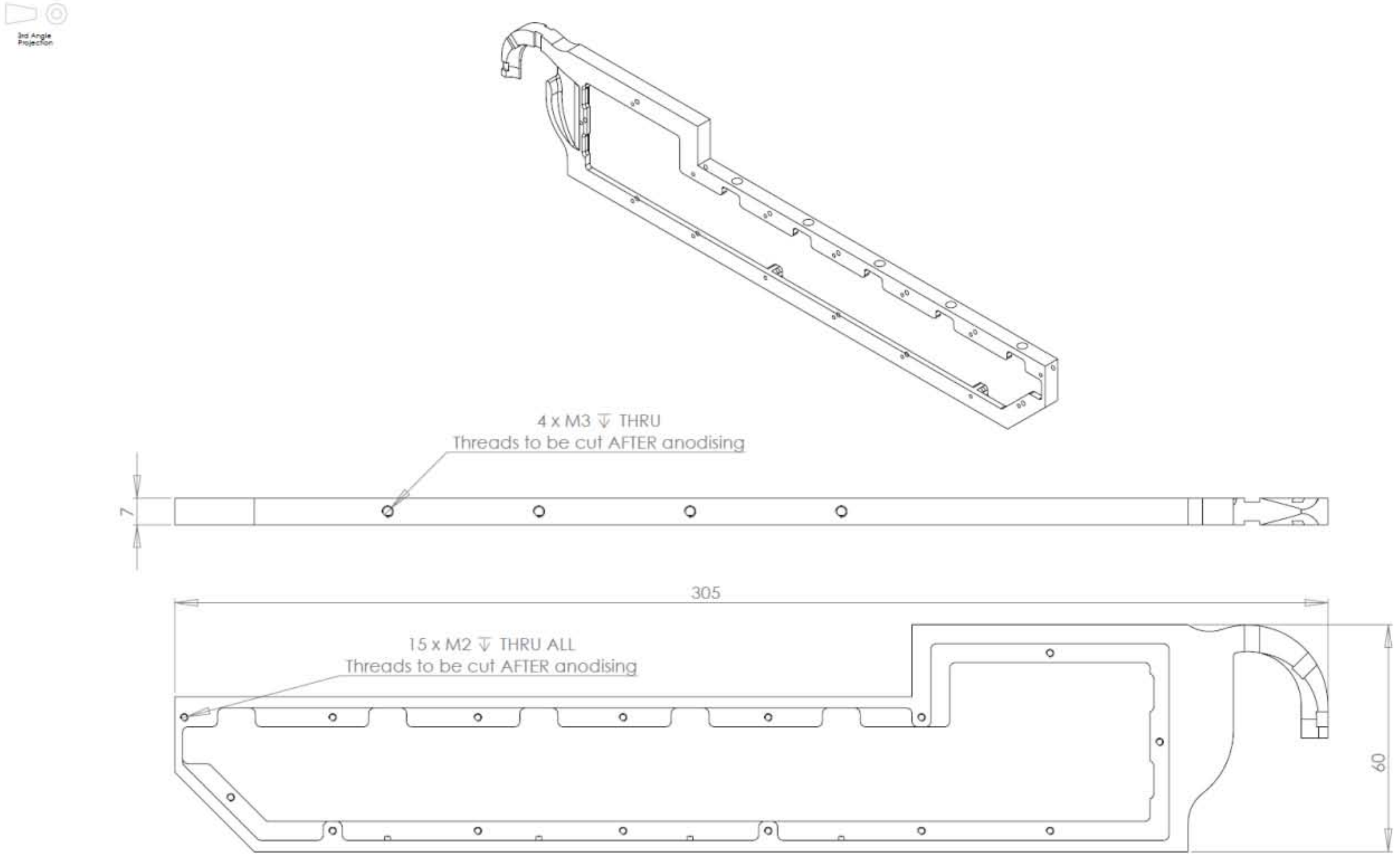

Scale 1:1
A3
Material: Aluminium 6082
Finish: Blue Anodised

Tolerance
General ±0.5
X.X ±0.2
X.XX ±0.1
Hole Centres ±0.1
Angle ±0.5°
All dimensions in mm

Remove All Burrs & Sharp Edges
Drawn By: Raphael Smith
Checked By: James Boonzaier
Sheet 1 of 1

CapeRay

Date: 17 July 2013
Rev.: A
Name: HSBP\ Ultrasound carriage \ **ultrasound chassis**
Part no.: N/A
Drawing no.: N/A

Appendix D: Selected Photographs of the Rail Carriage Assembly

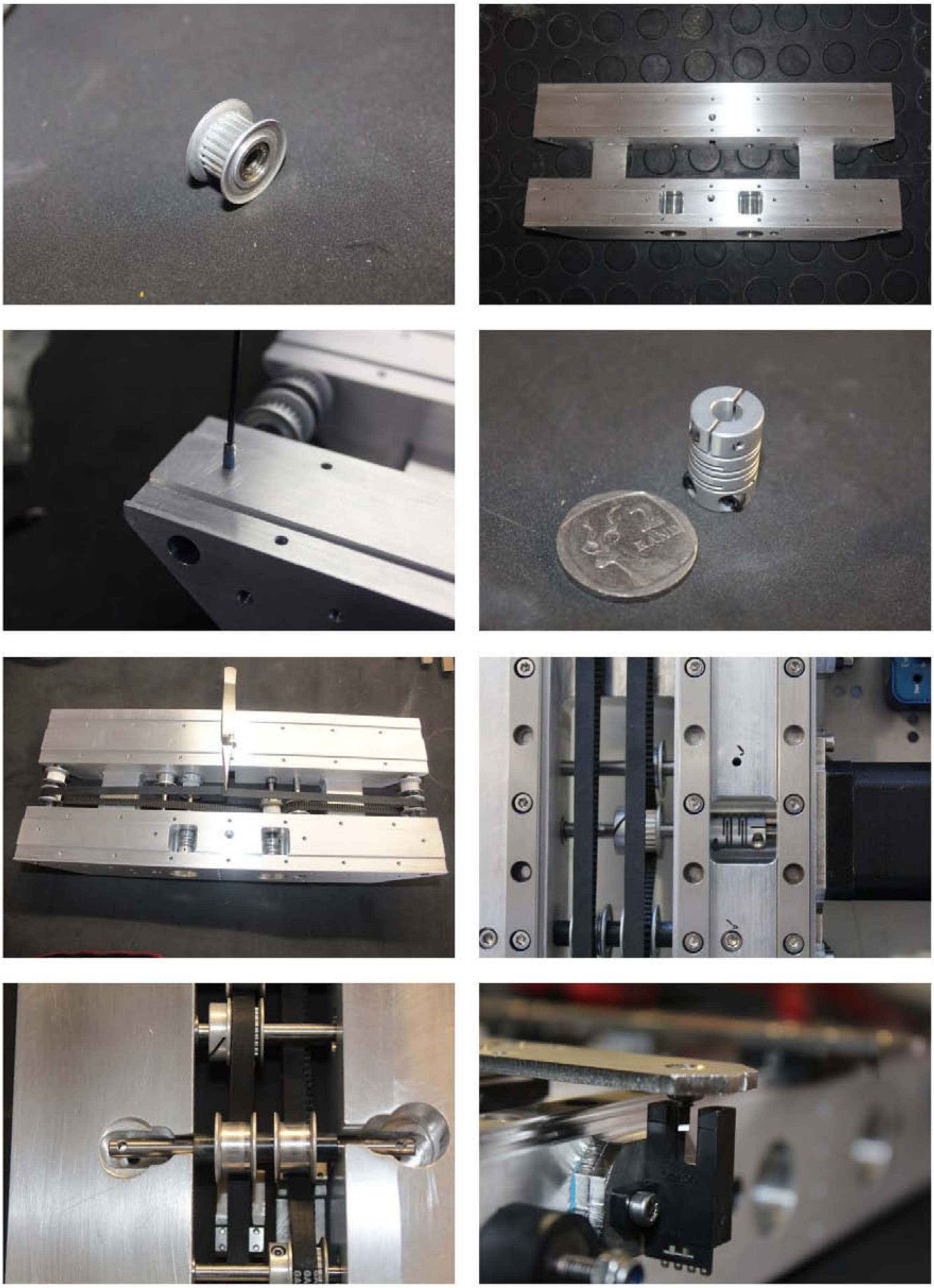

Figure D.1: **Selected Pictures of the Rail Carriage Assembly. From top left to bottom right: a toothed idler; the gantry; the assembly of an idler shaft, a flexible couple, the drive belt pathway, the assembly of a drive shaft, installation of the tensioning shaft; the light gate and trigger-screw.**

Appendix E: PANDIA-COLLIMATOR CALIBRATION TECHNIQUE

The following steps describe the process for calibrating the position and velocity of the Pandia and collimator.

Start position calibration

i. Roughly align the Pandia and collimator.
ii. Acquire an X-ray.
iii. Measure the average greyscale value on the right of the image i.e. close to the starting position of the Pandia.
iv. Add an offset to the starting position of the Pandia and repeat steps ii and iii.
v. Plot the greyscale values against the starting position offset. A 2nd order polynomial should result.
vi. Set the starting position offset equal to the turning point of the polynomial i.e. the offset value for which the greyscale value is a maximum.
vii. Acquire a further scan to validate the maximum and the shape of the polynomial.
viii. This process may be repeated across a decreasing range of offsets to ensure the absolute maximum exposure is achieved.

Velocity calibration

i. Execute steps i through viii above with the following differences: (1) the grey scale region of interest should be from the latter portion of the image, (2) the velocity of the *collimator* must be varied rather than the X-ray offset.
ii. If a large change in velocity is required, the start position calibration and velocity calibration should be repeated until the greyscale measurements reach a global maximum.

Appendix F: FLAT-FIELDING SCRIPT

```
%% Author:  Raphael Smith
%% Date:    January 2014

clc
%% file paths

ffFiles = { '28kV 50mA_01.pgm','28kV 50mA_02.pgm',...
            '28kV 74mA_01.pgm','28kV 74mA_02.pgm',...
            '28kV 98mA_01.pgm','28kV 98mA_02.pgm',...
            '28kV 122mA_01.pgm','28kV 122mA_02.pgm',...
            '28kV 146mA_01.pgm','28kV 146mA_02.pgm',...
            '28kV 170mA_01.pgm','28kV 170mA_02.pgm'};

%targetFile = 'MTF_01.pgm';
%targetFile = 'MTF_03.pgm';
%targetFile = 'NPS_01.pgm';

%% import target image
display 'importing target images';
targetImg = double(importdata(targetFile))+1;

%% generate dark image
display 'generating dark image';
darkSlice = [targetImg(5500:5900,10:2045), targetImg(5500:5900,2071:4078)];
darkRow = mean(darkSlice,1);
darkImg = repmat(darkRow,4001,1);

%% import flat field images, averaging & remove dark
display 'importing & generating flat field images';
if ~exist('ffImg')
    display 'generating flat field image';
    ffImg = zeros(size(targetImg));
    for i = 1:length(ffFiles) %(mAlevel*2-1):mAlevel*2
        tempImg = double(importdata(ffFiles{i}))+1;
        tempdarkSlice = tempImg(5500:5900,:);
        tempdarkRow = mean(tempdarkSlice,1);
        tempdarkImg = repmat(tempdarkRow,6000,1);
        tempdarkImg = tempImg - tempdarkImg;
        ffImg = (ffImg + tempdarkImg)./2;
        display('.');
    end
    ffImg = [ffImg(500:4500,10:2045), ffImg(500:4500,2071:4078)];
end

%% crop images
targetImg = [targetImg(500:4500,10:2045), targetImg(500:4500,2071:4078)];

%% flat field
display 'flat fiellding';
finalImg = (targetImg-darkImg).*mean(mean(ffImg))./ffImg;

%% convert to 16bit
display 'converting to 16bit';
finalImg = uint16(finalImg - 1);

%% save file
display 'saving';
imwrite(finalImg,['ff ' targetFile '.tiff']);

%% cleanup
clear 'darkFile' 'ffFile' 'imgFile' 'i';
display 'done';
```

Appendix G: SAMPLE X-RAY IMAGE QUALITY IMAGES

The images below are sample NPS and transverse and lateral MTF X-rays. Specifically, these images were acquired for the PMMA+TPX+Oil case.

Figure G.1: Sample NPS and MTF Images. Top – NPS, middle –transverse MTF, bottom – lateral MTF.

Appendix H: SAMPLE ULTRASOUND IMAGE QUALITY IMAGES

A sample set of ultrasound images acquired for the ultrasound image quality testing is shown below. The images were acquired at 3.5 MHz through 3 mm of mineral oil, 6 mm of TPX and a 2 mm thick skin-mimicking layer of Zerdine.

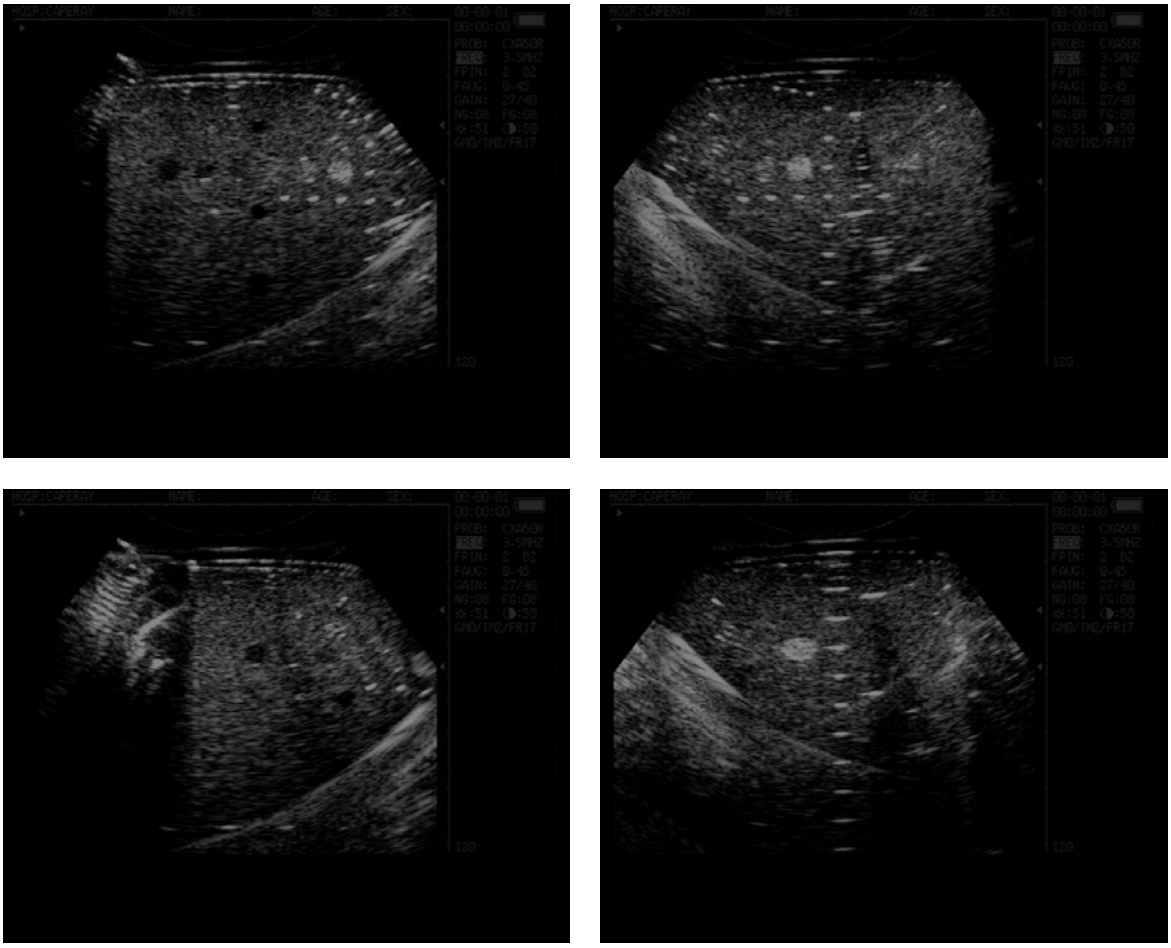

Figure H.1: **Sample Ultrasound Image Quality Images. From top left to bottom right: greyscale targets; vertical and horizontal line targets; uniform portion of the phantom; and vertical line target with the transducer rotated through 45° about its axis.**

Appendix I: ULTRASOUND SYSTEM SPECIFICATIONS

The specifications of the WED-3100 ultrasound beam-former (Shezhen Well. D, China), the C1-11/50R/3.5MHz transducer and the L1-5/7.5MHz transducer are given below. The table is an excerpt from the user manual.

Table I.1: Ultrasound Beam-former and Transducer Specifications

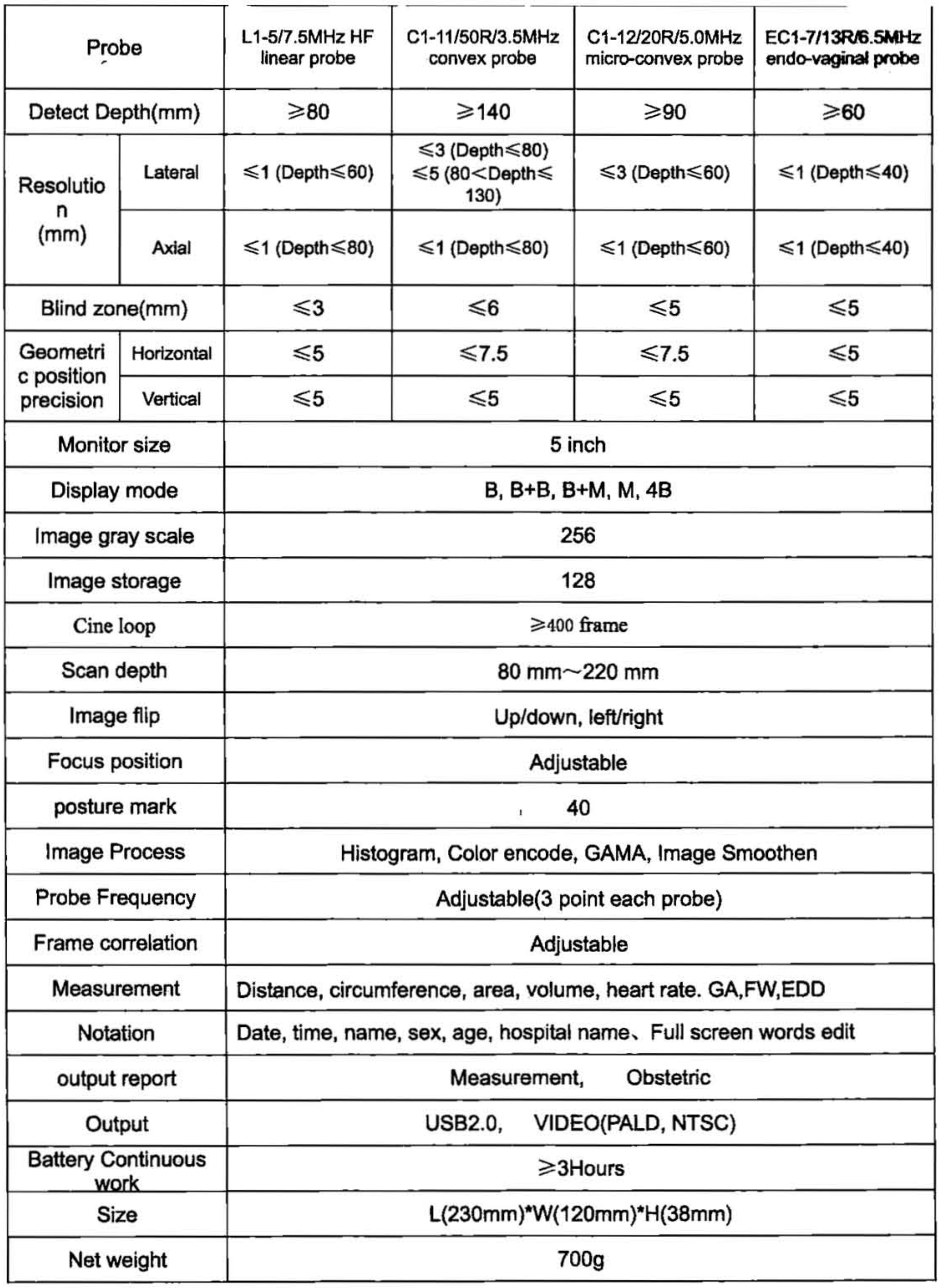

Probe		L1-5/7.5MHz HF linear probe	C1-11/50R/3.5MHz convex probe	C1-12/20R/5.0MHz micro-convex probe	EC1-7/13R/6.5MHz endo-vaginal probe
Detect Depth(mm)		⩾80	⩾140	⩾90	⩾60
Resolution (mm)	Lateral	⩽1 (Depth⩽60)	⩽3 (Depth⩽80) ⩽5 (80<Depth⩽ 130)	⩽3 (Depth⩽60)	⩽1 (Depth⩽40)
	Axial	⩽1 (Depth⩽80)	⩽1 (Depth⩽80)	⩽1 (Depth⩽60)	⩽1 (Depth⩽40)
Blind zone(mm)		⩽3	⩽6	⩽5	⩽5
Geometric position precision	Horizontal	⩽5	⩽7.5	⩽7.5	⩽5
	Vertical	⩽5	⩽5	⩽5	⩽5
Monitor size		5 inch			
Display mode		B, B+B, B+M, M, 4B			
Image gray scale		256			
Image storage		128			
Cine loop		⩾400 frame			
Scan depth		80 mm～220 mm			
Image flip		Up/down, left/right			
Focus position		Adjustable			
posture mark		40			
Image Process		Histogram, Color encode, GAMA, Image Smoothen			
Probe Frequency		Adjustable(3 point each probe)			
Frame correlation		Adjustable			
Measurement		Distance, circumference, area, volume, heart rate. GA,FW,EDD			
Notation		Date, time, name, sex, age, hospital name、Full screen words edit			
output report		Measurement, Obstetric			
Output		USB2.0, VIDEO(PALD, NTSC)			
Battery Continuous work		⩾3Hours			
Size		L(230mm)*W(120mm)*H(38mm)			
Net weight		700g			

Appendix J: EXAMPLE OF THE QA4US CONTRAST RESOLUTION LINEAR FITTING

The greyscale values are plotted against the echo level of the greyscale targets (-9, -6, -3, 0, 3 and 6 dB). The contrast resolution is given by the gradient of the linear fit of these data. As shown, there is some uncertainty in the fitting.

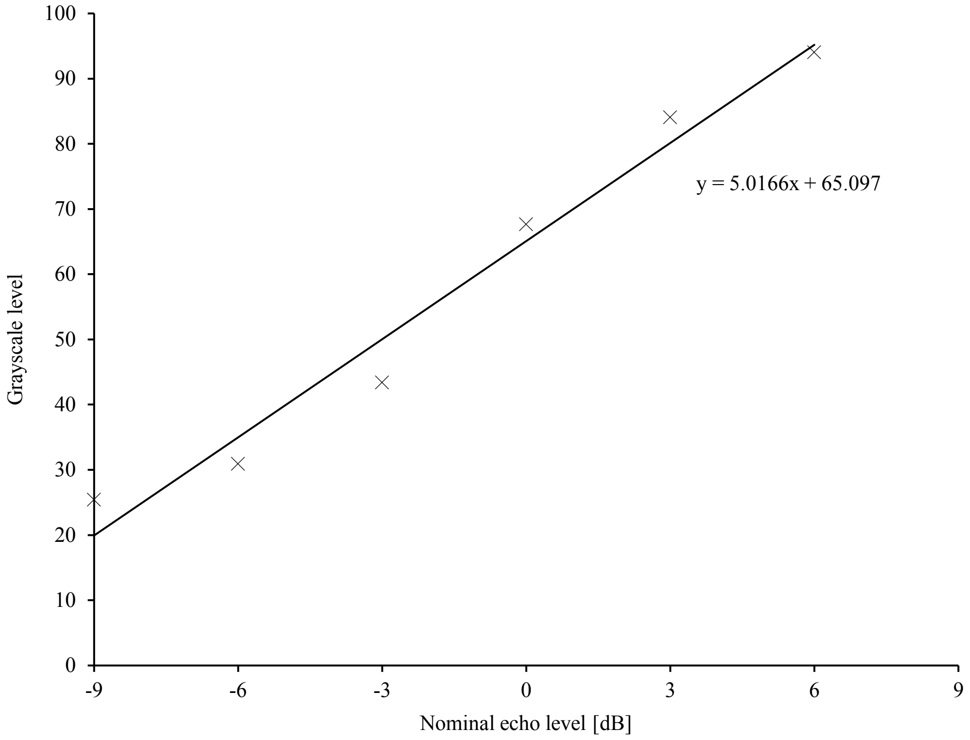

Figure J.1: **Sample of the Contrast Resolution Linear Curve Fitting.This is the curve for 6 mm of TPX at 2.5 MHz.**

REFERENCES

Albert, U.-S., & Schulz, K.-D. (2004). Short version of the Guideline: Early Detection of Breast Cancer in Germany. An evidence-, consensus-, and outcome-based guideline according to the German Association of the Scientific Medical Societies (AWMF) and the German Agency for Quality in Medicine. *Journal of Cancer Research and Clinical Oncology*, *130*(9), 527–536.

Amara, A. (2012). Method and a system for medical imaging. United States Patent Application, US 20120022376, January 26, 2012.

Anderson, T., Hautala, R., & Mar, J. (2006). Apparatus and method for full-field breast ultrasound scanning. United States Patent Application, US 20060241423, October 26, 2006.

Åslund, M., Cederström, B., Lundqvist, M., & Danielsson, M. (2006). Scatter rejection in multislit digital mammography. *Medical Physics*, *33*(4), 933–940.

Aufrichtig, R., & Xue, P. (2000). Dose efficiency and low-contrast detectability of an amorphous silicon x-ray detector for digital radiography. *Physics in Medicine and Biology*, *45*(9), 2653–2669.

Azhari, H. (2010). *Basics of Biomedical Ultrasound for Engineers*. Hoboken, New Jersey: Wiley & Sons.

Baasch, R. (2013a). *AC-SRS-002 Aceso System Requirements Specification*. CapeRay Medical (Pty) Ltd.

Baasch, R. (2013b). *AC-URS-001-Aceso User Requirements Specification*. CapeRay Medical (Pty) Ltd.

Baert, A., Reiser, M., Hricak, H., & Knauth, M. (2010). *Digital Mammography*. Heidelberg: Springer.

Baldelli, P., McCullagh, J., Phelan, N., & Flanagan, F. (2011). Comprehensive dose survey of breast screening in Ireland. *Radiation Protection Dosimetry*, *145*(1), 52–60.

Bar-Cohen, A., Arik, M., & Ohadi, M. (2006). Direct liquid cooling of high flux micro and nano electronic components. *Proceedings of the IEEE*, *94*(8), 1549–1570.

Bassett, L. W., Hoyt, A. C., & Oshiro, T. (2010). Digital mammography: clinical image evaluation. *Radiologic Clinics of North America*, *48*(5), 903–915.

Berg, W. A., Blume, J. D., Cormack, J. B., Mendelson, E. B., Lehrer, D., Böhm-Vélez, M., Pisano, E. D., Jong, R. A., Evans, W. P., Morton, M. J., Mahoney, M. C., Larsen, L. H., Barr, R. G., Farria, D. M., Marques, H. S., & Boparai, K. (2008). Combined screening with ultrasound and mammography vs mammography alone in women at elevated risk of breast cancer. *The Journal of the American Medical Association*, *299*(18), 2151–2163.

Besson, G., & Nields, M. (2005). Integrated X-ray and ultrasound medical imaging system. United States Patent, US 6,846,289, January 25, 2005.

Beyer, J., & Derndinger, W. (1984). Ultrasonic applicator. United States Patent, US 4,483,343, November 20, 1984.

Bleyer, A., & Welch, H. G. (2012). Effect of three decades of screening mammography on breast-cancer incidence. *The New England Journal of Medicine*, *367*(21), 1998–2005.

Booi, R. C., Krücker, J. F., Goodsitt, M. M., O'Donnell, M., Kapur, A., LeCarpentier, G. L., Roubidoux, M. A., Fowlkes, J. B., & Carson, P. L. (2007). Evaluating thin compression paddles for mammographically compatible ultrasound. *Ultrasound in Medicine & Biology*, *33*(3), 472–482.

Boyd, N. F., Martin, L. J., Yaffe, M. J., & Minkin, S. (2011). Mammographic density and breast cancer risk: current understanding and future prospects. *Breast Cancer Research*, *13*(6), 223–244.

Browne, J. E., Watson, A. J., Gibson, N. M., Dudley, N. J., & Elliott, A. T. (2004). Objective measurements of image quality. *Ultrasound in Medicine & Biology*, *30*(2), 229–237.

Carney, P. A., Miglioretti, D. L., Yankaskas, B. C., Kerlikowske, K., Rosenberg, R., Rutter, C. M., Geller, B. M., Abraham, L. A., Taplin, S. H., Dignan, M., Cutter, G., & Ballard-Barbash, R. (2003). Individual and combined effects of age, breast density, and hormone replacement therapy use on the accuracy of screening mammography. *Annals of Internal Medicine*, *138*(3), 168–175.

Carter, C. L., Allen, C., & Henson, D. E. (1989). Relation of tumor size, lymph node status, and survival in 24,740 breast cancer cases. *Cancer*, *63*(1), 181–187.

Chan, V., & Perlas, A. (2011). Basics of Ultrasound Imaging. In *Atlas of Ultrasound-Guided Procedures in Interventional Pain Management* (pp. 13–20). New York: Springer.

Crosby, P. A., & Shmulewitz, A. (1998a). Sonography and biopsy apparatus. United States Patent, US 5,820,552, October 13, 1998.

Crosby, P. A., & Shmulewitz, A. (1998b). Traction-inducing compression assembly for enhanced tissue imaging. United States Patent, US 5,851,180, December 22, 1998.

D & L Graphics. (2014). Breast Lymphatic System. Retrieved January 18, 2013, from http://fineartamerica.com/featured/breast-lymphatic-system-artwork-d-l-graphics.html

D'Orsi, C. J. (2010). Imaging for the diagnosis and management of ductal carcinoma in situ. *Journal of the National Cancer Institute Monographs*, *2010*(41), 214–217.

Delphinus Medical Technologies. (2014). Delphinus Softvue. Retrieved February 02, 2014, from http://www.delphinusmt.com/

Dempsey, P. J. (2004). The history of breast ultrasound. *Journal of Ultrasound in Medicine*, *23*(7), 887–894.

Dines, K. A., Kelly-Fry, E., & Romilly, A. P. (2005). Mammography method and apparatus. United States Patent, US 6,876,879, April 05, 2005.

Dudley, N., & Griffith, K. (2001). A review of two alternative ultrasound quality assurance programmes. *European Journal of Ultrasound*, *12*, 233–245.

Entrekin, R. R. (2011). Transducer unit incorporating an acoustic coupler. United States Patent Application, US 20110105900, May 05, 2011.

Erikson, K. R., Carson, P. L., & Stewart, H. F. (1976). Field Evaluation of the AIUM Standard 100 mm Test Object. In *Ultrasound in Medicine* (pp. 445–451). New York & London: Plenum Press.

EVA Robotics. (2013). EVA Robotics. Retrieved January 31, 2014, from http://www.evarobotics.com.au/

Evans, M., Smith, R., & Vaughan, C. (2013a). Dual-modality mammography. United Kingdom Patent Application, GB 1311124.0, June 21, 2013.

Evans, M., Smith, R., & Vaughan, C. (2013b). Dual-modality mammography. United States Patent Application, US 14136775, December 20, 2013.

Ferlay, J., Shin, H.-R., Bray, F., Forman, D., Mathers, C., & Parkin, D. M. (2010). Estimates of worldwide burden of cancer in 2008: GLOBOCAN 2008. *International Journal of Cancer*, *127*(12), 2893–2917.

Fischer, D., & Mertelmeier, T. (2011). Mammography system and method for sonographic and radiographic examination of a breast. United States Patent Application, US 20110087098, April 14, 2011.

Flaherty, J. J., Clark, J. W., & Rosauer, P. J. (1969). Medical diagnostic system. United States Patent, US 3,448,606, June 10, 1969.

Flaherty, J. J., & O'Connor, D. T. (1969). Medical ultrasonic scanning system. United States Patent, US 3,480,002, November 25, 1969.

Fredenberg, E. (2012). Noise-power spectrum. Retrieved February 02, 2014, from http://www.mathworks.com/matlabcentral/fileexchange/36462-noise-power-spectrum

Gale, A. G., Hunter, N., Lawton, C., & Purdy, K. (2007). *Ergonomic Assessment of Mammography Units*. Sheffield: National Health Service Breast Screening Programme.

Giuliano, V., & Giuliano, C. (2012). Improved breast cancer detection in asymptomatic women using 3D-automated breast ultrasound in mammographically dense breasts. *Clinical Imaging*, *37*(3), 480–486.

Goemans, B. (2013). *AC-RRR-006 Aceso Regulatory Requirements Review*. CapeRay Medical (Pty) Ltd.

Goodsitt, M. M., Carson, P. L., Witt, S., Hykes, D. L., & Kofler, J. M. (1998). Real-time B-mode ultrasound quality control test procedures. Report of AAPM Ultrasound Task Group No. 1. *Medical Physics*, *25*(8), 1385–1406.

Granton, P. (2010). Slant edge script. Retrieved February 02, 2014, from http://www.mathworks.com/matlabcentral/fileexchange/28631-slant-edge-script/content/MATHWORKS_MTF/MTFscript.m

Green, P. S., & Taenzer, J. C. (1984). Compact ultrasound apparatus for medical examination. United States Patent, US 4,433,690, February 28, 1984.

Greiter, M. B., & Hoeschen, C. (2010). Mobile measurement setup according to IEC 62220-1-2 for DQE determination on digital mammography systems. *Medical Imaging*, *7622*(4P), 1–12.

Guangxian, W., Zhi, C., & Hirobumi, S. (2002). The vibration characteristic and saturation effect of the 2-phase hybrid stepping motor. In *Electrical Machines and Systems. Proceedings of the Fifth International Conference* (pp. 404–407). Shenyang.

Guyton, A. C. (1982). *Physiology of the Human Body* (5th ed.). Philadelphia: Saunders College Publishing.

Harper, P., & Kelly-Fry, E. (1980). Ultrasound visualization of the breast in symptomatic patients. *Radiology*, *137*(2), 465–469.

Hayakawa, K., & Matsui, K. (1996). Ultrasonic coupler. United States Patent, US 5,575,291, November 19, 1996.

Hirshaut, Y., & Pressman, P. (2009). *Breast Cancer: The Complete Guide* (4th ed.). New York: Random House Digital, Inc.

Hoctor, R. T., & Thomenius, K. E. (2003). Focus correction for ultrasound imaging through mammography compression plate. United States Patent, US 6,607,489, August 19, 2003.

Hologic. (2013). Hologic. Retrieved from http://www.hologic.com/

IEC. (2007). *International Standard IEC 62220-1-2: Medical electrical equipment – Characteristics of digital X-ray imaging devices* (1st ed.). Switzerland: International Electrotechnical Commission.

IEC. (2011). *International Standard IEC 60601-2-45: Medical electrical equipment – Particular requirements for the basic safety and essential performance of mammographic X-ray equipment and mammographic stereotactic devices* (3.0 ed.). Switzerland: International Electrotechnical Commission.

Ishiyama, K., & Takano, M. (1987). Ultrasonic probe device. United States Patent, US 4,688,578, August 25, 1987.

Jellins, J., Kossoff, G., & Reeve, T. S. (1977). Detection and classification of liquid-filled masses in the breast by gray scale echography. *Radiology*, *125*(1), 205–212.

Jones, H. S. (1971). Breast holder for mammograph. United States Patent, US 3,556,081, January 19, 1971.

Kailes, J. I., & Lee, M. (2009). *Mammography: Addressing Equipment Design*. California: Center for Disability Issues and the Health Professions.

Kapur, A., Carson, P. L., Eberhard, J., Goodsitt, M. M., Thomenius, K., Lokhandwalla, M., Buckley, D., Roubidoux, M. A., Helvie, M. A., Booi, R. C., LeCarpentier, G. L., Erkamp, R. Q., Chan, H.-P., Fowlkes, J. B., Thomas, J. A., & Landberg, C. E. (2004). Combination of digital mammography with semi-automated 3D breast ultrasound. *Technology in Cancer Research & Treatment*, *3*(4), 325–334.

Kapur, A., & Thomenius, K. (2005). Acoustic coupling gel for combined mammography and ultrasound image acquisition and methods thereof. United States Patent Application, US 20050288581, December 29, 2005.

Kelly-Fry, E., Kossoff, G., & Hindman Jr., H. A. (1972). The potential of ultrasound visualization for detecting the presence of abnormal structures within the female breast. *Ultrasonics Symposium*, 25–30.

Kossoff, G., & Robinson, D. E. (1983). Apparatus for ultrasonic examination of deformable objects. World Intellectual Property Organisation Patent Application, WO 8302053, June 23, 1983.

Kuhl, C. K., Kuhn, W., & Schild, H. (2005). Management of women at high risk for breast cancer: new imaging beyond mammography. *The Breast*, *14*(6), 480–486.

Lai, C.-J., Shaw, C. C., Geiser, W., Chen, L., Arribas, E., Stephens, T., Davis, P. L., Ayyar, G. P., Dogan, B. E., Nguyen, V. A., Whitman, G. J., & Yang, W. T. (2008). Comparison of slot scanning digital mammography system with full-field digital mammography system. *Medical Physics*, *35*(6), 2339–2346.

Lasser, R. S., Lasser, M. E., & Gurney, J. W. (2005). Apparatus for multimodal plane wave ultrasound imaging. United States Patent, US 6,971,991, December 06, 2005.

Lease, A., Vaughan, C., Beningfield, S., Potgieter, H., & Booysen, A. (2002). Feasibility of using LODOX technology for mammography. In *SPIE 4682, Medical Imaging 2002: Physics of Medical Imaging* (Vol. 4682, pp. 656–664). San Diego.

Lokhandwalla, M., & Kapur, A. (2007). Compliant probe interface assembly. United States Patent, US 7,299,806, November 27, 2007.

Lynch, P. J. (2006). Medial Section of Left Breast. Retrieved December 11, 2013, from http://commons.wikimedia.org/wiki/File:Breast_anatomy_normal.jpg#metadata

Madsen, E., Zagzebski, J., & Frank, G. (1982). An anthropomorphic ultrasound breast phantom containing intermediate-sized scatterers. *Ultrasound in Medicine & Biology*, *8*(4), 381–392.

MUSIC. (2012). QA4US. Retrieved December 30, 2013, from http://music.runmc-radiology.nl/index.php/MUSIC_qa4us

National Cancer Institute. (2013). Stages of Breast Cancer. Retrieved January 09, 2013, from http://www.cancer.gov/cancertopics/pdq/treatment/breast/Patient/page2#Keypoint18

National Cancer Registry. (2006). *Cancer Statistics, 2006*. South Africa: National Health Laboratory Service.

NHS Breast Screening Programme. (2009). *Calculation Of Quantitative Image Quality Parameters*. Sheffield: NHS Cancer Screening Programmes.

Nields, M. W., & Ulatowski, B. R. (2000). Enhanced breast imaging/biopsy system employing targeted ultrasound. United States Patent, US 6,102,866, August 15, 2000.

Nishikawa, R. (2003). The Effect of Scatter Radiation and its Removal on the DQE of Digital Mammography Systems (abstract only). In *Digital Mammography* (pp. 59–63). Berlin: Springer.

Nothacker, M., Duda, V., Hahn, M., Warm, M., Degenhardt, F., Madjar, H., Weinbrenner, S., & Albert, U.-S. (2009). Early detection of breast cancer: benefits and risks of supplemental breast ultrasound in asymptomatic women with mammographically dense breast tissue. A systematic review. *BioMed Central Cancer*, *9*, 335–363.

Novak, D. (1983). Indications for and comparative diagnostic value of combined ultrasound and X-ray mammography. *European Journal of Radiology*, *3*(1), 299–302.

Palm, W. J. (2000). *Modeling, Analysis, and Control of Dynamic Systems* (2nd ed.). New York: Wiley & Sons Inc.

Pedersen, L. (1999). Tables of Acoustic Properties of Materials. Retrieved January 12, 2013, from http://www.ondacorp.com/tecref_acoustictable.shtml

Pretlow, R. A. (2005). Coupling pad for medical ultrasound devices. United States Patent, US 5,782,767, August 10, 2005.

Revolution Cooling. (2014). Liquid Submersion Cooling. Retrieved January 21, 2014, from http://www.grcooling.com/

Richards, M. A., Westcombe, A. M., Love, S. B., Littlejohns, P., & Ramirez, A. J. (1999). Influence of delay on survival in patients with breast cancer: a systematic review. *Lancet*, *353*(9159), 1119–1126.

Richter, K. (1998). Method for imaging display of a part of the human body. United States Patent, US 5,840,022, November 24, 1998.

Romilly-Harper, A. P., Kelly-Fry, E., & Dines, K. A. (1995). Clinical evaluation of manual, automated and 3-D ultrasound imaging of breasts compressed in the same position modes applied in X-ray mammography. In *Ninth International Congress on the Ultrasonic Examination of the Breast*. Indianapolis.

Rose, A. (1948). The sensitivity performance of the human eye on an absolute scale. *Journal of the Optical Society of America*, *38*(2), 196–208.

Russell, W. O. (2010). *Design of a Breast Platform with Optimal Acoustic and Mechanical Properties for a Dual Modality Mammography Unit*. CapeRay Medical (Pty) Ltd.

Samei, E. (2003). Performance of digital radiographic detectors: quantification and assessment methods. *Advances in Digital Radiography: RSNA*, 37–47.

Sant, M., Allemani, C., Capocaccia, R., Hakulinen, T., Aareleid, T., Coebergh, J. W., Coleman, M. P., Grosclaude, P., Martinez, C., Bell, J., Youngson, J., & Berrino, F. (2003). Stage at diagnosis is a key explanation of differences in breast cancer survival across Europe. *International Journal of Cancer*, *106*(3), 416–422.

Schaefer, F. K. W., Waldmann, A., Katalinic, A., Wefelnberg, C., Heller, M., Jonat, W., & Schreer, I. (2010). Influence of additional breast ultrasound on cancer detection in a cohort study for quality assurance in breast diagnosis-analysis of 102,577 diagnostic procedures. *European Radiology*, *20*(5), 1085–1092.

Schilling, K., Narayanan, D., Kalinyak, J. E., The, J., Velasquez, M. V., Kahn, S., Saady, M., Mahal, R., & Chrystal, L. (2011). Positron emission mammography in breast cancer presurgical planning: comparisons with magnetic resonance imaging. *European Journal of Nuclear Medicine and Molecular Imaging*, *38*(1), 23–36.

Schneider, J. K., Kitchens, J. C., & Baker, J. T. (2010). Ultrasonic fingerprint scanning using a plane wave. United States Patent Application, US 20100251824, October 07, 2010.

Schopper, D., & de Wolf, C. (2009). How effective are breast cancer screening programmes by mammography? Review of the current evidence. *European Journal of Cancer*, *45*(11), 1916–1923.

Sendai, T. (2012). Multi-modality mammography imaging device for improved imaging conditions. United States Patent, US 8,192,361, June 05, 2012.

Shmulewitz, A. (1996). Methods and apparatus for performing sonomammography and enhanced x-ray imaging. United States Patent, US 5,479,927, January 02, 1996.

SIGN. (2013). *SIGN 134: Treatment of Primary Breast Cancer*. Edinburgh: Scottish Intercollegiate Guidelines Network.

Simmons, M. A., Chavez, J., & Barke, L. D. (2013). Patient Positioning and Mammography. Retrieved December 26, 2013, from http://www.eradimaging.com/site/article.cfm?ID=787

Simpson, W. L., Hermann, G., Rausch, D. R., Sherman, J., Feig, S. A., Bleiweiss, I. J., Jaffer, S., & Port, A. (2008). Ultrasound detection of nonpalpable mammographically occult malignancy. *Canadian Association of Radiologists Journal*, *59*(2), 70–76.

Sinha, S. P., Goodsitt, M. M., Roubidoux, M. A., Booi, R. C., LeCarpentier, G. L., Lashbrook, C. R., Thomenius, K. E., Chalek, C. L., & Carson, P. L. (2007a). Automated ultrasound scanning on a dual-modality breast imaging system: coverage and motion issues and solutions. *Journal of Ultrasound in Medicine*, *26*(5), 645–655.

Sinha, S. P., Roubidoux, M. A., Helvie, M. A., Nees, A. V, Goodsitt, M. M., LeCarpentier, G. L., Fowlkes, J. B., Chalek, C. L., & Carson, P. L. (2007b). Multi-modality 3D breast imaging with X-ray tomosynthesis and automated ultrasound. In *Annual International Conference of the IEEE Engineering in Medicine and Biology Society* (pp. 1335–1338). Lyon.

Sipilä, O., Mannila, V., & Vartiainen, E. (2011). Quality assurance in diagnostic ultrasound. *European Journal of Radiology*, *80*(2), 519–525.

Smith, A. (2003). Fundamentals of digital mammography: physics, technology and practical considerations. *Radiology Management*, *25*(5), 18–24, 26–31.

Smith, R. (2013). *AC-HVT-032 Aceso Hermetically Sealed Breast Platform Verification Test Procedure*. CapeRay Medical (Pty) Ltd.

Smith, R., & Saslow, D. (2003). American Cancer Society guidelines for breast cancer screening: update 2003. *CA: A Cancer Journal for Clinicians*, *53*, 141–169.

Stierstorfer, K., & Spahn, M. (1999). Self-normalizing method to measure the detective quantum efficiency of a wide range of x-ray detectors. *Medical Physics*, *26*(7), 1312–1319.

Suri, J. S., Danielson, T., Guo, Y., & Janer, R. (2005). Fischer's fused full field digital mammography and ultrasound system (FFDMUS). *Studies in Health Technology and Informatics*, *114*, 177–200.

Suri, J. S., Janer, R., Guo, Y., & Elbakri, I. A. (2011). Diagnostic system for multimodality mammography. United States Patent, US 7,916,918, March 29, 2011.

Suri, J. S., Sun, Y., & Janer, R. (2013). Method for breast screening in fused mammography. United States Patent Application, US 20130251103, September 26, 2013.

Thijssen, J. M., van Wijk, M. C., & Cuypers, M. H. M. (2002). Performance testing of medical echo/doppler equipment. *European Journal of Ultrasound*, *15*(3), 151–164.

Thijssen, J. M., Weijers, G., & de Korte, C. L. (2007). Objective performance testing and quality assurance of medical ultrasound equipment. *Ultrasound in Medicine & Biology*, *33*(3), 460–471.

Towfiq, F., Busse, L. J., Douglas, S. J., & Stribling, M. L. (2013). System and method for three-dimensional ultrasound imaging. United States Patent Application, US 13673987, June 20, 2013.

Tradup, D. J., Hangiandreou, N. J., & Taubel, J. P. (2003). Comparison of ultrasound quality assurance phantom measurements from matched and mixed scanner-transducer combinations. *American College of Medical Physics*, *4*(3), 239–247.

Vaughan, C. L. (2011). New developments in medical imaging to detect breast cancer. *Continuing Medical Education*, *29*(3), 122–125.

Vaughan, C. L., & Evans, M. D. (2013). Dual-modality scanning system for detecting breast cancer. United States Patent Application, US 20130281840, October 24, 2013.

Wang, S. P., Chen, J., & Summers, D. G. (2013). Breast ultrasound scanning template. United States Patent, US 8,579,817, November 12, 2013.

Weinberg, R. (2013). *The Biology of Cancer* (2nd ed.). New York: Garland Science.

Wendelken, M. E., & Pope, C. (2006). Standoff holder and standoff pad for ultrasound probe. United States Patent, US 7,029,446, April 18, 2006.

Williams, M. B., Mangiafico, P. a, & Simoni, P. U. (1999). Noise power spectra of images from digital mammography detectors. *Medical Physics*, *26*(7), 1279–1293.

Yokouchi, K., Kamehara, N., & Niwa, K. (1987). Immersion cooling for high-density packaging. *IEEE Transactions on Components, Hybrids, and Manufacturing Technology*, *10*(4), 643–646.